Research Frontiers 2022

SPring-8
SACLA

ISSN 2433-5126
SPring-8 Document D2023-010

SPring-8/SACLA
Research Frontiers 2022

CONTENTS

Reviews

Life Science

Physical Science

Chemical Science

Earth & Planetary Science

Industrial Applications

SPring-8

SACLA

New Apparatus, Upgrades & Methodology

SPring-8

SACLA

SPring-8/SACLA

Note: The principal publication(s) concerning each article is indicated with all author's names in italics in the list of references.

PREFACE

We are pleased to announce the publication of SPring-8/SACLA Research Frontiers 2022. As a user promotion organization for SPring-8 and SACLA registered with the Ministry of Education, Culture, Sports, Science and Technology of Japan (MEXT), JASRI's mission is to support users and ensure the transparent and fair selection of experimental proposals. JASRI also manages SPring-8 and SACLA, which are owned by RIKEN. In other words, JASRI works closely with RIKEN to operate and maintain SPring-8 and SACLA and develop technologies related to synchrotron radiation science.

Despite the continued COVID-19 pandemic, the activity of SPring-8 and SACLA in FY2022 recovered to the level before COVID-19, except for restrictions on users from abroad according to the regulations of the Japanese government. Many precautionary measures have been implemented on-site for users. In FY2022, SPring-8 welcomed approximately 16,000 researchers. They performed more than 2,000 experiments and published approximately 1,000 research papers .

In 2022, a number of SPring-8 and SACLA users were awarded prestigious prizes for their scientific and technological achievements. The Commendation for Science and Technology by the Minister of Education, Culture, Sports, Science and Technology (Research Category) was awarded to the following three researchers: Professor Teruo Ono (Kyoto University) for research on the magnetization control of nanoscale magnetic materials. Professor Keiji Tanaka (Kyushu University) for the research on interfacial nanophysical properties of polymer functionalization. Professor Atsushi Wakamiya (Kyoto University) for research on high-performance solar cells using coated semiconductor materials

This volume contains two comprehensive review articles. The first review is by Professor Akira Tsuchiyama (Ritsumeikan University) and Dr. Megumi Matsumoto (Tohoku University), who examined samples collected from the surface of the C-type asteroid 162173 Ryugu by the Japan Aerospace Exploration Agency (JAXA) spacecraft Hayabusa-2 and brought back to Earth in December 2020. This review describes the progress of research on the formation and evolution of 162173 Ryugu. The experiments were conducted using X-ray computed tomography (XCT) at SPring-8 BL20XU and BL47XU. The second review, presented by Dr. Shinji Kohara of the National Institute for Materials Science (NIMS), describes his recent work using high-energy X-ray diffraction at SPring-8 BL04B2 to extract order from disordered materials.

In the main part of this volume, the active users of SPring-8 describe the essence of their results in various fields, including life science, physical science, chemical science, earth & planetary science, and industrial applications. In addition, principal activity reports on the SPring-8/SACLA facilities are included in the sections of Accelerators & Beamlines Frontiers and Facility Status.

I am very grateful to the many authors and experts who contributed their articles to this volume. Special thanks to Dr. Toyohiko Kinoshita, Ms. Marcia M. Obuti-Daté, and the members of the editorial board for their continuous efforts.

Y. Amemiya

Yoshiyuki Amemiya
President
Japan Synchrotron Radiation Research Institute (JASRI)

EDITOR'S NOTE

This is the 2022 issue of SPring-8/SACLA Research Frontiers, which covers the outstanding scientific outcomes of SPring-8 and SACLA in 2021 and 2022. This was the period during which we were recovering from the influence of COVID-19. After the retirement of the previous editor in chief, Dr. Naoto Yagi, I assumed the position for this issue.

The best scientific achievements are collected from more than 1,000 papers published each year using SPring-8 or SACLA. Protein crystallography is very active, and the investigation of a variety of functional materials towards sustainable development goals (SDGs) is ongoing.

There are two review articles on this issue. One is written by Professor Akira Tsuchiyama (Ritsumeikan University) and Dr. Megumi Matsumoto (Tohoku University). They review the achievements of the Hayabusa 2 Project, which attracted considerable attention worldwide. Hayabusa 2 is an asteroid exploration project of the Japan Aerospace Exploration Agency (JAXA), and the spacecraft successfully returned a capsule containing sample materials from the asteroid Ryugu on December 6, 2020. This review is an example of how SPring-8 is playing an important role in a variety of research projects being performed in the worldwide. The other review is reported by Dr. Shinji Kohara (National Institute for Materials Science) who worked at SPring-8 previously as a member of the beamline staff. He introduces high-energy X-ray diffraction analyses for disordered materials. Combining theoretical simulations such as density functional theory (DFT), molecular dynamics (MD), and reverse Monte Carlo (RMC) modeling, pair distribution function (PDF) diffraction data are analyzed. Some interesting examples of ordered structures within disordered glass are introduced.

In addition to the scientific results (Scientific Frontiers), there is some information on hard and soft infrastructures that support scientific research. Although important data, such as operation time, are included in this part, additional information and more complete statistical numbers on the operation of SPring-8 and SACLA are available on the website so that more updated information can be accessed (http://www.spring8.or.jp/en/about_us/spring8data/).

The full text of SPring-8/SACLA Research Frontiers is also available on the SPring-8 website (http://www.spring8.or.jp/en). For the list of publications produced by SPring-8 users and staff, please visit the publication database at http://www.spring8.or.jp/en/science/publication_database/.

On behalf of all the editors, I would like to thank those who helped us by recommending excellent research results suitable for publication in this issue, and the users and staff of SPring-8 who contributed their reports to this issue despite this pandemic.

Toyohiko Kinoshita
Japan Synchrotron Radiation Research Institute (JASRI)

EDITORIAL BOARD

SCIENTIFIC FRONTIERS

Review Article

Formation and evolution of the C-type asteroid 162173 Ryugu: Evidence from returned samples analyzed by X-ray micro- and nano-tomographies

1. Introduction

The samples collected from the surface of the C-type asteroid 162173 Ryugu were successfully brought back to Earth on 6th December 2020 by the Hayabusa2 spacecraft of Japan Aerospace Exploration Agency (JAXA) [1]. The initial analytical campaign was performed for one year from June 2021 after noninvasive and nondestructive curatorial works at JAXA. Further detailed analyses by JAXA "International Announcement of Opportunity (AO) for Hayabusa2 Sample Investigation" are under way. Our research group performed a series of multiscale nondestructive three-dimensional (3D) analyses by combining different types of X-ray tomography (XCT) as the initial analysis [2,3] and advanced curatorial work [4]. Through these analyses, we revealed the features of the returned samples and their relation to known meteorites. We also performed further analyses to understand the origin and evolution of Ryugu and the evolution processes on the asteroid surface. The results were also useful for cutting cross sections appropriate for later analyses such as electron microscopy.

The returned samples are composed of particles of <~10 mm size [1,5] (Fig. 1). The total amount of the samples is ~5.42 g. To perform appropriate and systematic analyses, we used two different beamlines using different XCT imaging systems for different particle size ranges: large particles of >~100 μm size at SPring-8 BL20XU and small particles of <~100 μm size at SPring-8 BL47XU. In this review, we described the features of the two beamlines and the results obtained thus far separately.

2. Analysis at SPring-8 BL20XU for large samples

The integrated XCT system using 30 keV X-ray beams equipped at beamline BL20XU was used for large samples (>~100 μm). This system is composed of three types of XCT: absorption X-ray tomography (absorption-CT), X-ray diffraction tomography (XRD-CT), and differential phase contrast tomography (phase-CT) with a common sample stage that can be used by moving the optical devices of the three CT types [2,4], enabling us to compare their CT images easily. In the absorption-CT mode, we obtained 3D-CT images of high spatial resolution (>~0.85 μm/voxel) in a wide field of view (<~3 mm) by using a 4K camera. In the XRD-CT mode, mineral phases were identified from the obtained XRD pattern and 2D mineral maps were constructed in arbitrary cross sections. In the phase-CT mode, low-element materials with low absorption, such as carbonaceous materials, were observed. Through these modes, we performed not only textural observation but also the identification of constituent mineral phases.

Extraterrestrial samples such as Ryugu samples might undergo alterations such as oxidation and hydration through contact with the terrestrial atmosphere. Each Ryugu sample, which was set in a container filled with dry and pure N_2 gas, was transferred from the JAXA curation facility. To exclude atmospheric exposure, we prepared a special glove box filled with dry and pure N_2 gas. The sample was moved to a sample holder for CT and the holder was sealed (Fig. 2) in the glove box [6].

We examined 24 Ryugu particles (1.8–8.7 mm in size or 0.8–93.5 mg

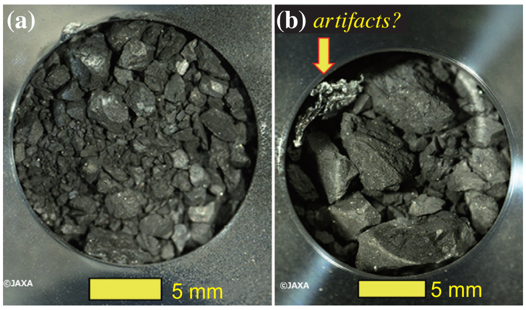

Fig. 1. All samples returned from the asteroid Ryugu (courtesy of JAXA). Samples in Chambers A **(a)** and C **(b)** were collected during the first and second touch-down operations (TD1 and TD2), respectively [5]. TD2 was performed near the artificial crater excavated using the small carry-on impactor (SCI) [1].

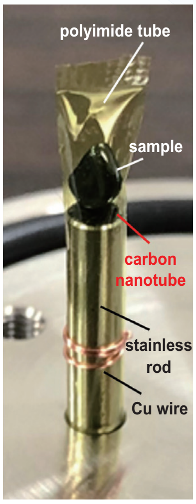

Fig. 2. Sample holder for CT at BL20XU. A sample particle placed on a carbon nanotube sheet is sealed with a polyimide tube and a Cu wire. The polyimide tube is filled with dry and pure N_2 gas.

in weight) [2,4]. The optical and absorption-CT slice images of a typical sample particle are shown in Figs. 3(a,b). The contrast of the CT image corresponds to the linear absorption coefficient of the material, which is determined by the chemical composition and density. In Ryugu samples, regions with bright and dark contrasts generally correspond to Fe-rich and Fe-poor materials, respectively. However, Ca-rich phases also show some bright contrasts, and porous regions have dark contrasts. Therefore, we used XRD-CT to confirm their mineral phases. As shown in Fig. 3(b), Ryugu samples are generally composed of mineral grains of pyrrhotite ($Fe_{1-x}S$), magnetite (Fe_3O_4), dolomite ($CaMg(CO_3)_2$), and breunnerite ($(Mg,Fe)CO_3$) embedded in a fine matrix of phyllosilicates (saponite: $(Ca/2,Na)_{0.3}(Mg,Fe)_3((Si,Al)_4O_{10}(OH)_2\cdot nH_2O$ and serpentine: $(Mg,Fe)_3Si_2O_5(OH)_4$). The mineral assemblage and its texture clearly showed that Ryugu samples correspond to Ivuna-type carbonaceous chondrites (CI) (e.g., [7]) or related material [2,4]. We observed heterogenous contrasts with a spatial scale of 1 mm or less in the matrix (Fig. 3(b)). On the basis of these results, the samples were prepared using a wire saw to obtain designated areas for later destructive analyses, and then many scientific outcomes were obtained efficiently [2,4].

The volumes of the sample particles were obtained from the absorption-CT images. The bulk densities of 16 particles were determined together with their masses separately measured using a precise electric balance. It is difficult to measure the volume of relatively small and fragile samples such as Ryugu particles. However, the present method of using XCT would be most reliable. The value ranges from 1.65 to 1.93 g/cm^3 with an average of 1.79±0.08 g/cm^3 [2]. The bulk density of large CI chondrite grains varies from 1.58 to 1.91 g/cm^3, which should be the result of alteration on Earth (terrestrial weathering). The bulk density of Ryugu particles determined in the present study is one of the most important physical properties and the present value was used to discuss dynamical processes, such as the formation and impact fragmentation of Ryugu, and physicochemical processes, such as aqueous alteration in Ryugu [2].

Cracks were observed in most of the samples (e.g., Fig. 3(b)). Some flat particles have many cracks almost parallel to the flat surfaces (Figs. 3(c,d)), as a compressive deformation caused by the impact of asteroids on Ryugu's parent body. The rubble pile asteroid of Ryugu was formed by the accumulation of such impact-induced fragments. These samples are fossils of the impact responsible for Ryugu formation [2,8].

3. Analysis at SPring-8 BL47XU for small samples

We used an analytical X-ray nanotomography (XnCT) system for small particles (<~100 µm) in BL47XU, where dual-energy tomography (DET) and scanning-imaging X-ray microscopy (SIXM) were combined (e.g., [9]). In DET, we used an imaging-absorption CT system with a voxel size of ~50 nm. Samples were imaged at two different X-ray energies (7 and 7.35 keV) near the *K*-edge energy of Fe (7.11 keV), enabling us to discriminate many minerals because the images at 7 and 7.35 keV roughly correspond to the *z* (average atomic number) and Fe contrasts, respectively. We also obtained enlarged images for ROI in 17 samples with higher resolution (~10 nm/voxel) using a common sample stage for local CT. In SIXM, we obtained differential phase shift images corresponding to density-contrast images at 8 keV with a voxel size of ~100 nm. These images are suitable for observing low-element materials, such as water and organic materials. By combining these sets of CT images, we obtained 3-color CT images (R: absorption image

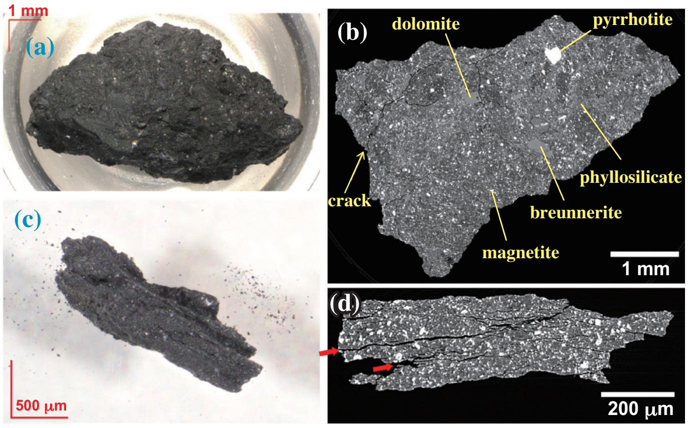

Fig. 3. Optical and absorption CT images of large Ryugu particles. **(a,b)** Sample: C0002. **(c,d)** Sample: C0055.

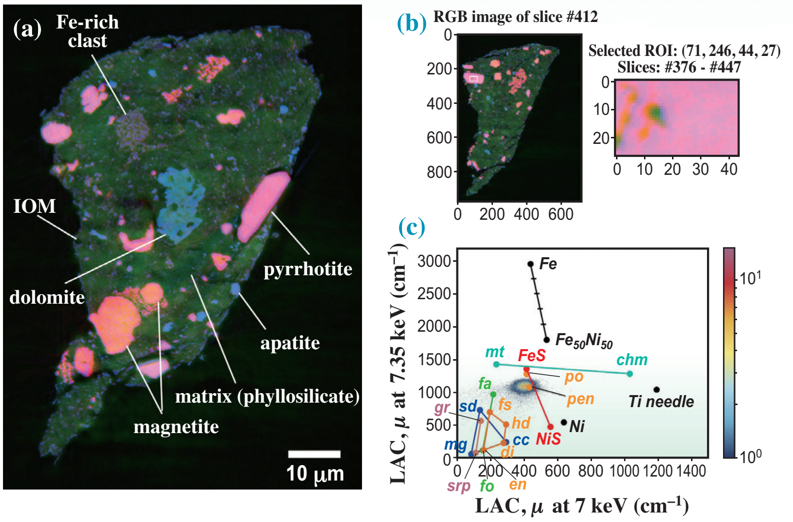

Fig. 4. 3-color CT images of small Ryugu particles (sample: C0103-FC007) and method of quantitative mineral discrimination. **(a)** 3-color CT image of R (LAC at 7 keV = 0-950 cm^{-1}), G (RID = 0-20×10^{-6}), and B (LAC at 7.35 keV = 0-450 cm^{-1}). **(b)** ROI for pink mineral used for the mineral discrimination. **(c)** 2D histogram of LAC at 7 keV *vs* LAC at 7.35 keV for ROI in (b), indicating the pink mineral is pyrrhotite. The other 2D histograms of LAC at 7 keV *vs* RID and LAC at 7.35 keV *vs* RID were also considered but are not shown here. LAC: linear attenuation coefficient. RID: refractive index decrement (= 1 – refractive index ∝ ~density). *mt*: magnetite, *chm*: chromite, *po*: pyrrhotite, *pen*: pentlandite, *fa*: fayalite, *fo*: forsterite, *fs*: ferrosilite, *hd*: hedenbergite, *di*: diopside, *en*: enstatite, *gr*: greenalite, *srp*: serpentine, *sd*: siderite, *cc*: calcite, and *mg*: magnesite.

at 7.35 keV, G: phase image, and B: absorption image at 7 keV), and the distributions of different minerals, organic materials, pores, and cracks are easily recognized in 3D (Fig. 4(a)). Quantitative phase discrimination was based on the contrast histograms of the three sets of CT images (Figs. 4(b,c)).

We examined 54 samples (9–103 µm in sphere-equivalent diameter) [2,4,10]. Most of them were small particles recovered, and some were extracted from large particles. The 3-color CT slice image of a typical sample is shown in Fig. 4(a). Different mineral grains (pyrrhotite, magnetite, dolomite, and apatite: $Ca_5(PO_4)_3(F,Cl,OH)$) were embedded in a fine-grained matrix of phyllosilicates. Organic materials (insoluble organic matter: IOM) and voids were also seen. The mineral assemblages and textures are also consistent with those of CI chondrites and related materials. We, however, have not completed the observation of some minerals such as sulphates in CI, and this can be explained by the terrestrial weathering of CI.

Pyrrhotite and carbonate (dolomite and breunnerite) grains, which precipitated from aqueous fluid during aqueous alteration in Ryugu is parent body, contained a large number of pores in CT images, some of which would be occupied by low-density materials (Figs. 5(a,b)). A relatively large inclusion (~3 µm) in pyrrhotite (Fig. 5(a)) was exposed by an ion beam at –120°C below the freezing temperature of the fluid and analyzed by time-of-flight secondary ion mass spectroscopy (TOF-SIMS). Ion signals from H_2O and CO_2 indicated that this inclusion was filled with H_2O–CO_2 fluid (or liquid) (Fig. 5(c)) [2]. Aqueous fluid has been found in a carbonaceous chondrite [11], but this is the first discovery of aqueous fluid in a known asteroid. The presence of CO_2 strongly suggests that Ryugu's parent body was formed outside of the CO_2 snow line in the outer region of the Solar System beyond the Jupiter orbit and transferred to the asteroid belts between Mars and Jupiter. The TOF-SIMS signals also indicate that the fluid is brine like ocean water. IOM was observed in pyrrhotite and carbonates (Fig. 5(b)), suggesting that IOM particles were dispersed in an aqueous fluid.

Crystal morphologies of minerals in 3D were examined. Magnetites have a large variety of morphologies (e.g., spherulite, framboid (Fig. 6(a)), plaquette, bar, and equant), while

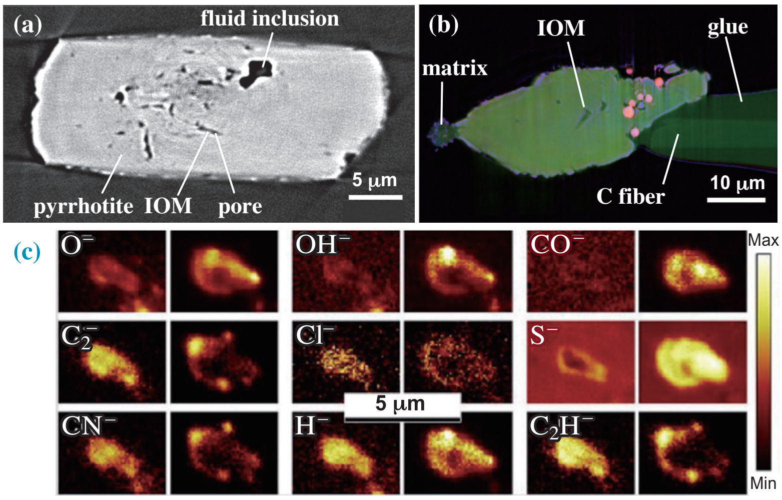

Fig. 5. Fluid and IOM inclusions. **(a)** Absorption CT image (7 keV) of pyrrhotite grain containing fluid and IOM inclusions (sample: C0002-FC012). **(b)** 3-color CT image of breunnerite grain containing IOM inclusions (LAC and RID ranges are the same as those in Fig. 4(a) (sample: A0067-FC0003). **(c)** TOF-SIMS ion maps of fluid inclusion in (a) [2].

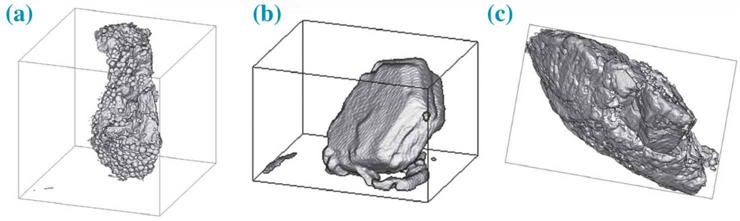

Fig. 6. Bird's-eye views of mineral grains created from 3D absorption CT images. **(a)** Framboidal magnetite crystals covering on a sample particle surface, ~45 μm in length (sample: A0104-00000900). **(b)** Hexagonal plate grain of pyrrhotite, 8×5.5×2.5 μm in size (sample: A0104-00000900). **(c)** Flat rhombohedral grain of breunnerite, 49×42.5×17 μm in size (sample: A0067-FC003).

other minerals have rather simple morphologies with facets (pyrrhotite: hexagonal plate (Fig. 6(b)), dolomite and breunnerite: flat rhombohedron (Fig. 6(c)), and apatite: hexagonal prism). From the included and enclosed relations among these minerals in 3D, their order of precipitation was estimated. On the basis of the obtained results, we proposed a model for the formation and evolution of Ryugu's parent body: formation by the accumulation of CO_2–H_2O ice, minerals (mainly amorphous silicate and Fe sulfide), and IOM, and the subsequent aqueous alteration by the reaction of the minerals with melted ice, where magnetite with irregular morphologies (e.g., spherulite, framboid, and plaquette) and poorly crystalline phyllosilicates precipitated first from a highly supersaturated aqueous fluid formed by the rapid dissolution of amorphous silicates, followed by the precipitation minerals with simple morphologies and coarse phyllosilicates from a slightly supersaturated aqueous fluid [10].

We also observed amorphization in a "smooth layer" [3], melts (glasses) (Fig. 7) in a "frothy layer" [3], and craters on the surfaces of Ryugu particles [2,3]. They are the results of space weathering caused by the exposure of solar wind and micrometeoroid bombardments. The absorption of the 2.7 μm hydroxyl (–OH) band in the reflectance IR spectrum of the Ryugu sample was determined to be stronger than that of the Ryugu surface determined by Hayabusa2 remote sensing observation [2]. This discrepancy can be explained by the dehydration of the outermost surface of space-weathered grains on the Ryugu surface, which contributes to the weakening of the 2.7 μm band [3].

4. Summary

We performed the 3D analysis of returned samples from the asteroid Ryugu by combining different types of XCT systems at SPring-8 BL20XU and BL47XU for 24 large (>~100 μm) and 54 small (<~100 μm) particles, respectively. We revealed that the returned samples correspond to CI chondrites or related materials [2,4,5]. This is consistent with the results of other mineralogical, petrological, and geochemical analyses (e.g., [2,4,12]). CI chondrites are one of the most important meteorites because they exhibit a representative chemical composition of the Solar System (e.g., [7]). We revealed physical, mineralogical, and petrological characteristics of these important Ryugu samples, such as bulk density, impact features, space weathering, crystal morphology, and mineral precipitation order during aqueous alteration. We discovered CO_2–H_2O fluid, suggesting the formation of Ryugu's parent body in the outer region of the Solar System. Detailed analyses by AO are now still under way.

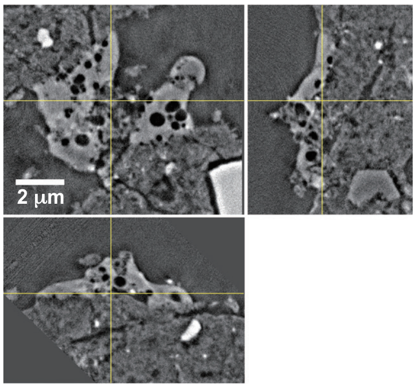

Fig. 7. Absorption CT image (7.35 keV) of melt splash (vesiculated glass) on particle surface (sample: C0105-04300900).

Akira Tsuchiyama[a,b,c,*]
and Megumi Matsumoto[d]

[a] Research Organization of Science and Technology, Ritsumeikan University
[b] CAS Key Laboratory of Mineralogy and Metallogeny/Guangdong Provincial Key Laboratory of Mineral Physics and Materials, Guangzhou Institute of Geochemistry, China
[c] CAS Center for Excellence in Deep Earth Science, China
[d] Department of Earth and Planetary Materials Sciences, Tohoku University

*Email: atsuchi@fc.ritsumei.ac.jp

References

[1] S. Tachibana *et al.*: Science **375** (2022) 1011.
[2] T. Nakamura *et al.*: Science **379** (2023) 787.
[3] T. Noguchi *et al.*: Nat. Astron. **7** (2023) 170.
[4] M. Ito *et al.*: Nat. Astron. **6** (2022) 1163.
[5] T. Yada *et al.*: Nat. Astron. **6** (2022) 214.
[6] M. Uesugi *et al.*: Rev. Sci. Instrum. **91** (2020) 035107.
[7] D. S. Lauretta and H. Y. McSween Jr.: Eds. "Meteorites and the Early Solar System II," p.942 (2006), The University of Arizona Space Science Series.
[8] M. Kikuiri *et al.*: MetSoc 2022 (2022) Abstract #6199.
[9] M. Matsumoto *et al.*: Science Adv. **5** (2019) eaax5078.
[10] A. Tsuchiyama *et al.*: MetSoc 2022 (2022) Abstract #6221.
[11] A. Tsuchiyama *et al.*: Science Adv. **7** (2021) eabg9707.
[12] T. Yokoyama *et al.*: Science **379** (2023) 786.

Review Article

Extracting order within disorder in disordered materials by high-energy X-ray diffraction

The structure of disordered materials is not highly disorganized: these materials have some degree of intermediate-range ordering [1]. The advent of third-generation synchrotron radiation sources, which can generate high-flux, high-energy X-rays, and the development of advanced instruments allow probing atomic arrangements in disordered materials with high real-space resolution. A combination of quantum beam (X-ray and neutron) diffraction, theoretical simulations (such as density functional theory (DFT) and molecular dynamics (MD)), and data-driven structural modeling (such as reverse Monte Carlo (RMC) modeling [2]) facilitates ordering within disorder in disordered materials. In this article, a dedicated high-energy X-ray diffractometer installed at SPring-8 BL04B2 [3] is introduced and, recent studies on probing the intermediate ordering in disordered materials are reviewed. In particular, recently discovered extraordinarily ordered oxide glasses and liquids are addressed to discuss the relationship between diffraction peaks and intermediate-range ordering in disordered materials.

High-energy X-ray diffractometer

A dedicated X-ray pair distribution function (PDF) diffractometer for disordered materials was developed at SPring-8 BL04B2 in 1999. The light source of BL04B2 is a bending magnet with a critical energy of 28.9 keV; additionally, the single-bounce bent Si 220 and Si 511 crystals with a Bragg angle fixed at 3° provide 61.7 and 113.3 keV X-rays, respectively. The beamline details are described in a previous study [3]. The advantages of our dedicated diffractometer are the extremely low background and high reliability of the diffraction data, which are important factors for obtaining accurate PDF data.

A dedicated diffractometer for disordered materials has been operating for over 20 years at BL04B2. The first- and second-generation detectors were intrinsic germanium (Ge) and triple-cadmium telluride (CdTe), respectively. The advantage of a Ge detector is its supersensitivity, which is important in the high-diffraction-angle region, because the diffraction intensity is weak in the high-scattering-vector *Q* (high diffraction angle) region owing to the decay of the *Q*-dependent atomic form factors. The efficiency of the Ge detector is comparable to that of the CdTe detector at 61.7 keV; however, it is 1.8 times higher at 113.3 keV. In addition, the size of the Ge detector element is much larger than that of CdTe. Previous studies confirmed that approximately twice the gain is obtained with a Ge detector compared with a CdTe detector at 61.7 keV, thus suggesting that an approximately four-fold higher gain is achieved at 113.3 keV. Another advantage of a semiconductor detector is its high energy resolution for discriminating fluorescence from the sample and the signal of the higher harmonic reflections of the monochromator crystal. The energy resolution (FWHM) of CdTe detectors is better than 3.1 keV,

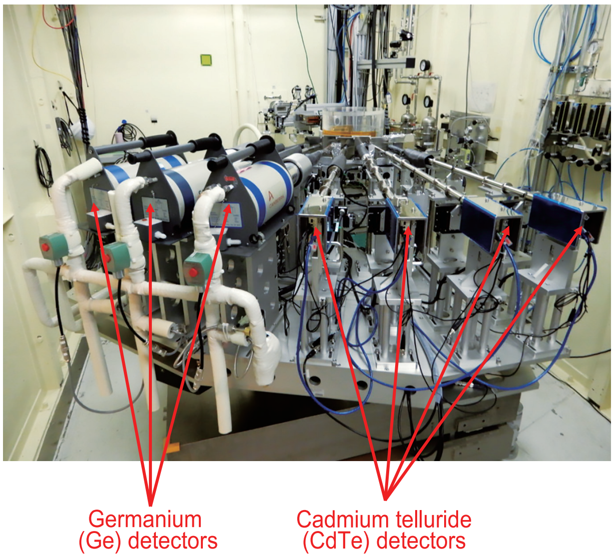

Fig. 1. High-energy X-ray PDF diffractometer installed BL04B2 [3].

whereas that of Ge detectors is better than 1.0 keV. The primary disadvantage of the Ge detector is the necessity to replenish liquid nitrogen, which interrupts the measurement. On the other hand, the advantage of a CdTe detector is its small size, which renders it suitable for covering low-diffraction-angle regions where space is limited. Another advantage of the CdTe detector is that it uses a Peltier device cooling system owing to its small detector elements. In a recent upgrade, four CdTe detectors were installed for low-diffraction-angle regions and three Ge detectors with an automated liquid nitrogen filling system were installed for high-diffraction-angle regions. The typical setup of the upgraded diffractometer is shown in Fig. 1.

Analysis of diffraction data by structure modeling techniques

Important quantitative structural information on short- and intermediate-range orders in glasses can be obtained from the atom distribution functions derived using X-ray and neutron diffraction. Modeling techniques are necessary to obtain more realistic and useful structural information from diffraction data, particularly for intermediate-range orders. RMC modeling allows for a quantitative fit of the experimental data without the use of potential functions. Compared with MD and/or standard Monte Carlo simulation techniques, RMC is particularly useful for the study of multicomponent glasses, for which the determination of interatomic potential functions for chemical bonding is difficult. The combination of RMC modeling and MD simulations has become popular for obtaining more reliable structural models [2].

Structure of oxide glasses and liquids

Oxide glasses, such as window glass, fiber glass, and optical glass, are essential daily-use materials. The most conventional glass formation method is melt quenching, in which the glass-forming ability (GFA) is governed by the viscosity of a high-temperature melt. In the last century, Angell proposed the concept of “fragility” based on the temperature–dependent behavior of viscosity to understand the relationship between viscosity and GFA [4]. The basic concept underlying glass formation is a corner-sharing tetrahedral motif proposed by Zachariasen in 1932 [5]. Fifteen years later, Sun classified single-component oxides as glass formers, glass modifiers, and intermediates [6]. Silica (SiO_2) is a prototypical glass former in which the silicon–oxygen coordination number is four, and the glass network is formed by corner-sharing oxygen atoms. In alkali and alkali earth silicate glasses, alkali and alkali earth oxides are typical glass modifiers; they cannot solely form glass but rather modify the network formed by a network former by breaking the silicon–oxygen bonds in the network and/or occupying cavities.

Densified silica glass

Figure 2(a) shows the *in situ* neutron structure $S(Q)$ of silica glass under high pressure [7]. The first sharp diffraction peak (FSDP) and principal peak (PP) were observed in the ambient pressure data (black curve) at Q of approximately 1.5 and 3 $Å^{-1}$, respectively. The formation of the FSDP was owing to atomic ordering along the cavities by corner-sharing SiO_4 tetrahedra. The origin of the second PP appeared to be a type of orientational correlation among the oxygen atoms occupying the corners of the tetrahedra, thus suggesting that the PP reflects the packing of oxygen atoms. Upon the application of pressure at room temperature, the FSDP shifted to a high Q and diminishes. By contrast, the PP became very sharp (see Fig. 2(a)), which is associated with a cavity volume reduction. This sharp PP is a signature of orientational correlations formed by oxygen atoms under high pressure.

Figure 2(b) shows the X-ray total structure factors $S(Q)$ of the densified silica glasses obtained by hot compression. These data were not *in situ* diffraction data; however, the FSDP was the sharpest in the sample recovered at 1200 °C/7.7 GPa. This behavior is very different from the *in situ* neutron diffraction data shown in Fig. 2(a). Thus, 1200 °C/7.7 GPa glass was demonstrated as the most ordered silica glass in the world.

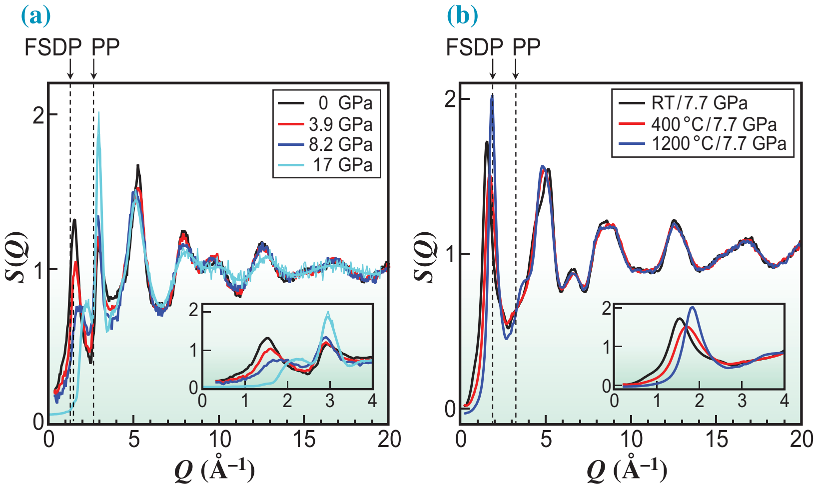

Fig. 2. **(a)** *In situ* neutron $S(Q)$ of silica glass under high pressure and room temperature [7]. **(b)** X-ray structure factor $S(Q)$ of densified silica glass recovered at high temperature and high pressure [8].

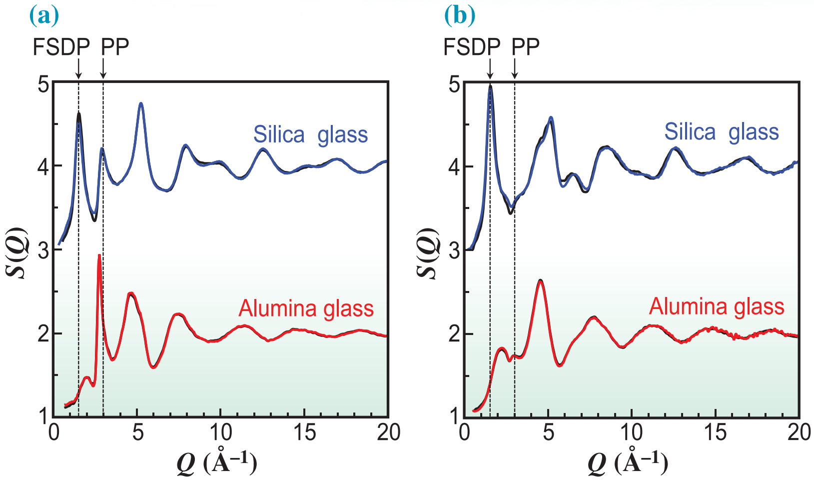

Fig. 3. **(a)** Neutron and **(b)** X-ray total structure factors $S(Q)$ of silica and alumina glasses [9]. Blue and red curves: experimental data, black curves: MD–RMC model.

Intermediate alumina glass

Silica is a good glass former, as mentioned above, whereas alumina (Al_2O_3) is not a glass former and is classified as an intermediate according to Sun [6]. Alumina glass cannot be formed using conventional melt-quenching techniques. However, Hashimoto *et al*. recently reported that amorphous alumina synthesized by the anodization of aluminum metal exhibits a glass transition [9]. Figures 3(a) and 3(b) show the neutron and X-ray total structure factors $S(Q)$, respectively, of the silica and alumina glasses. Silica glass exhibited a distinct FSDP owing to its high glass-forming ability. By contrast, alumina glass exhibited an extraordinarily sharp PP in the neutron $S(Q)$ data, similar to the *in situ* high-pressure data of silica glass shown in Fig. 2(a), thus suggesting that the packing density of oxygen atoms is very high in alumina glass. Figure 4 illustrates the atomic arrangement of the alumina glass in a stick representation (a) and cavity visualization (b), where the lattice (crystal)-like atomic arrangement formed by edge-sharing of the AlO_n polyhedra is highlighted by black dotted lines. In addition, numerous sparser regions formed by the tetrahedral corner-sharing motif were observed (Fig. 4(a)). The cavity volume ratio of alumina glass was 4.5%, which is comparable to those of densified silica glasses recovered at 1200 °C/7.7 GPa. Further, the average Al–O coordination number was 4.7, which is much higher than that in silica glass (4), and the formation of AlO_4, AlO_5, and AlO_6 was confirmed. This variation in Al–O coordination is the reason for the formation of edge-sharing Al–O polyhedra, which can disturb the evolution of the intermediate-range ordering detected as an FSDP.

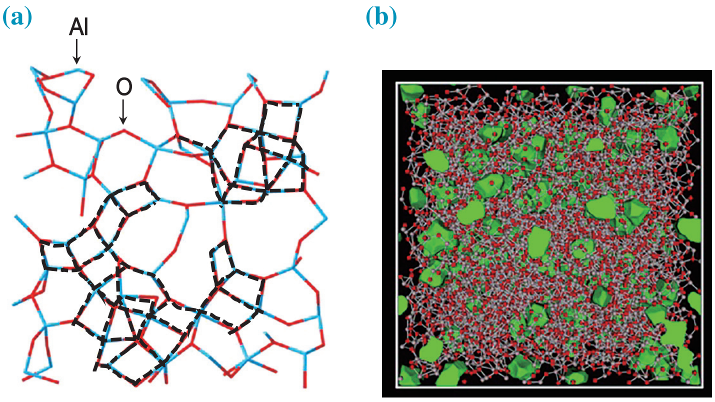

Fig. 4. Atomic arrangements of alumina glass in: **(a)** stick representation and **(b)** with cavity visualization [9].

Levitated erbia liquid

Erbia (Er_2O_3) is a nonglass-forming material with an extremely high melting point (T_m = 2430 °C). To perform diffraction measurements of such high-temperature liquids, several containerless techniques that enable holding a liquid droplet without a container have been developed [2]. A previous study employed an aerodynamic levitation technique for X-ray measurements, in which a sample is levitated using dry air from a conical nozzle.

Figure 5 shows the X-ray structure factors $S(Q)$ of the erbia liquid (2650 °C) [10] (a) and zirconia (ZrO_2) liquid (2800 °C) [11] (b), together with those obtained using several simulation techniques. No FSDP were observed in either dataset because they are nonglass-forming materials. However, they exhibited a PP at a Q of approximately 2 $Å^{-1}$. The FWHMs of PP for the zirconia and erbia liquids were 0.7669 and 0.4299, respectively. In the case of zirconia liquid, the RMC–DF/MD model of 501 particles (magenta curve) reproduced the experimental data. However, the RMC–MD model of 5000 particles (red curve) was required to reproduce the extraordinarily sharp PP of the erbia liquid. As a benchmark, the number of particles in the standard RMC approach was reduced, and

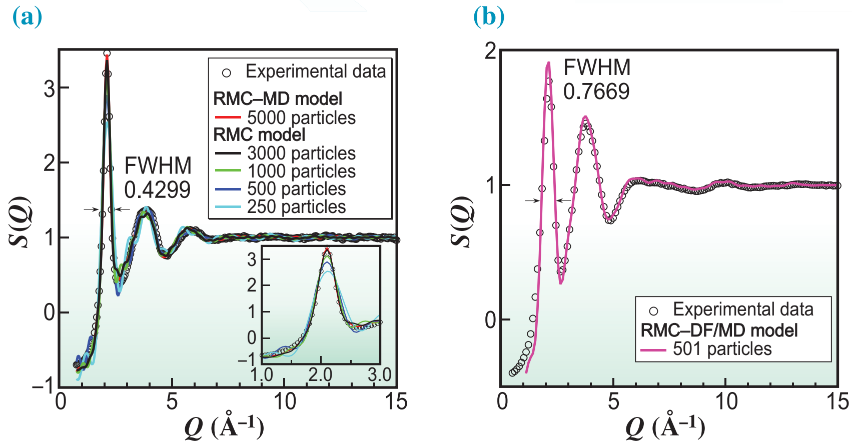

Fig. 5. X-ray structure factors $S(Q)$ of: **(a)** erbia liquid (2650°C) [10] and **(b)** zirconia liquid (2800°C) [11], along with those obtained by RMC–MD, RMC, and RMC–DF/MD modeling.

500 particles (blue) were confirmed to be insufficient for reproducing such an extraordinarily sharp PP.

The cation–oxygen coordination number was approximately 6 for both liquids, which is extremely larger than 3.9 for silica SiO_2 liquid (2100°C) and 4.4 for alumina liquid (2127°C). Moreover, the oxygen–cation coordination number was 3.0 for zirconia liquid and 4.1 for erbia liquid, thus suggesting that a large fraction of an OEr_4 tetracluster, which cannot be observed in other liquids, was observed.

Figure 6 illustrates the atomic arrangement of the erbia liquid in the stick representation. Evidently, an extraordinarily densely packed atomic arrangement, as that found in alumina glass, was observed; however, a sparse region, as that observed in alumina glass, was not observed. This extraordinarily densely packed atomic arrangement, highlighted by the dotted lines, was formed by the edge-sharing ErO_n polydra associated with the formation of OEr_4 tetraclusters and is the origin of the extremely low glass-forming ability and extraordinarily sharp PP.

We review several unusual oxide glasses and liquid structures with respect to. Their structures are significantly different from those of conventional oxide glasses and liquids. The characteristic features of these glasses and liquids are variations in the polyhedra in terms of coordination number and polyhedral connections (corner, edge, and face).

In this article, the high-energy X-ray PDF diffractometer was briefly introduced for disordered materials developed at SPring-8 BL04B2. Combining quantum beam measurements and advanced simulations is a promising method for extracting the hidden order in disordered materials. The results of the advanced analysis can help to forge a new path or designing novel functional disordered materials.

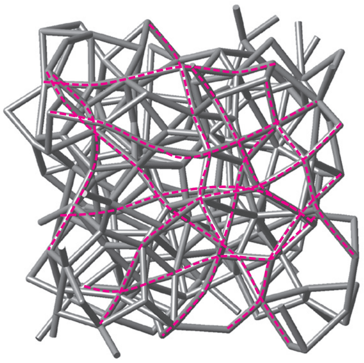

Fig. 6. Atomic arrangement of erbia liquid in stick representation [10].

Shinji Kohara[a,b]

[a] National Institute for Materials Science
[b] Tokyo University of Science

Email: KOHARA.Shinji@nims.go.jp

References

[1] P. S. Salmon: Nat. Mater. **1** (2002) 87.
[2] S. Kohara and L. Pusztai: "Atomistic Simulation of Glasses," Ed. by J. Du and A. N. Cormack, Wiley-American Ceramic Society, Hoboken p.60 (2022).
[3] K. Ohara *et al*.: J. Phys.: Condens. Matter **33** (2021) 383001.
[4] C. A. Angell: Science **267** (1995) 1924.
[5] W. H. Zachariasen: J. Am. Chem. Soc. **54** (1932) 3841.
[6] K.-H. Sun: J. Am. Ceram. Soc. **30** (1947) 277.
[7] A. Zeidler *et al*.: Phys. Rev. Lett. **113** (2014) 135501.
[8] Y. Onodera *et al*.: NPG Asia Mater. **12** (2020) 85.
[9] H. Hashimoto *et al*.: Sci. Rep. **12** (2022) 516.
[10] C. Koyama *et al*.: NPG Asia Mater. **12** (2020) 43.
[11] S. Kohara *et al*.: Nat. Commun. **5** (2014) 5892.

Crystal and cryo-EM structures of the gastric proton pump bound with potassium-competitive acid blockers

Acid-related gastric diseases are associated with disorders of the digestive tract, such as peptic ulcers or gastroesophageal reflux disease (GERD). Gastric mucosal injury induced by the continuous use of non-steroidal anti-inflammatory drugs (NSAIDs) or gastrin-producing tumors may also cause peptic ulcers [1]. Current therapies to treat these conditions either prevent the stimulation of parietal cells or inhibit the final step in acid production. The former is accomplished by antagonizing histamine H2 receptors, and the latter by targeting the gastric proton pump, H$^+$,K$^+$-ATPase. The suppression of gastric acid secretion in combination with antimicrobial agents has also been used for the eradication of *Helicobacter pylori*, which is recognized as the main cause of gastric ulcers and gastric cancers [2]. Proton pump inhibitors (PPIs) such as omeprazole have been utilized for acid suppression. The PPI drug itself is a prodrug, requiring acid activation in the secretory canaliculus to inhibit H$^+$,K$^+$-ATPase. Once activated, the PPI forms a covalent bond with Cys813 of H$^+$,K$^+$-ATPase and irreversibly inhibits acid secretion. However, given its relatively short plasma half-life and the need for an acidic pH to convert the prodrug to the active compound, considerable effort has been expended to develop different types of H$^+$,K$^+$-ATPase inhibitor [3]. K$^+$-competitive acid blockers (P-CABs) differ from the PPIs in that they do not depend on acid activation, are relatively stable in the acidic canaliculus, and bind directly to the proton pump, thereby providing a more rapid onset and better inhibition of acid secretion. They are currently in clinical use in some Asian countries. However, as these compounds have been developed by phenotypic screening, their detailed binding poses and interactions are unknown, except for two previously reported crystal structures of H$^+$,K$^+$-ATPase [4] bound to SCH28080 (a prototypical P-CAB) or vonoprazan (approved for the clinical treatment in Japan).

We determined new crystal (at SPring-8 **BL41XU** and **BL45XU**) and cryo-EM (**EM01CT**) structures of H$^+$,K$^+$-ATPase in complexes with four different P-CABs, tegoprazan, soraprazan, PF-03716556 and revaprazan, at resolutions reaching 2.8 Å [5]. The structures reveal molecular details of their interactions (Figs. 1 and 2) and are supported by the results of functional analyses of tailored mutations. As expected, the three SCH28080-related P-CABs show similar but distinguishable binding modes to the prototypic compound. On the other hand, revaprazan has a

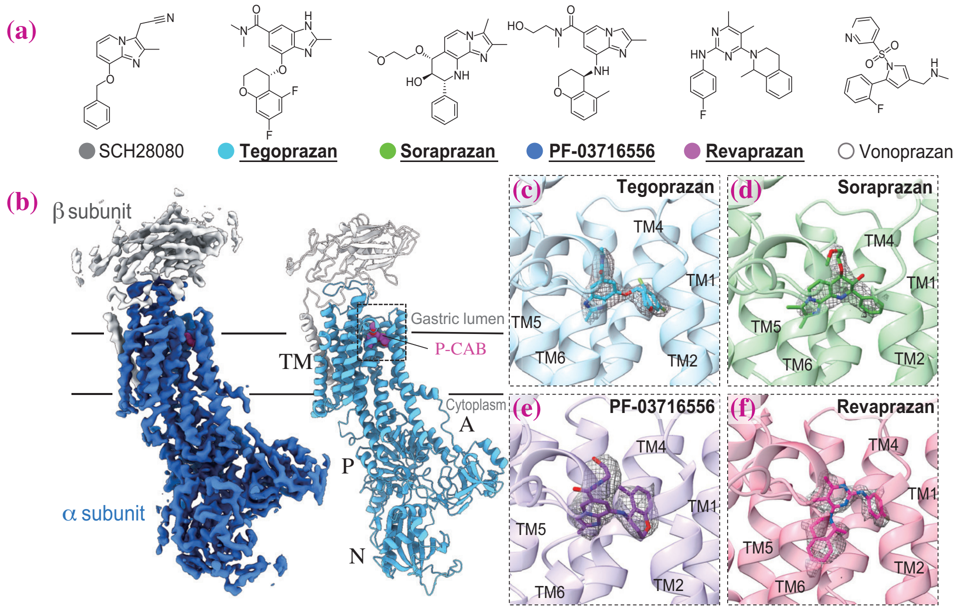

Fig. 1. Structure of P-CABs bound to H$^+$,K$^+$-ATPase. **(a)** Chemical structures of P-CABs. The four P-CABs used for structural determination are highlighted. **(b)** Overall structure of revaprazan-bound form of H$^+$,K$^+$-ATPase composed of α- and β-subunits. Three cytoplasmic domains (A, P and N domains) and TM helices are indicated. **(c–f)** Close-up view of P-CAB binding site (indicated by dotted box in **b**) for tegoprazan (**c**, blue), soraprazan (**d**, green), PF-03716556 (**e**, purple) and revaprazan (**f**, magenta), with their electron or EM density maps (mesh). Figures are viewed along the membrane plane with luminal-side up.

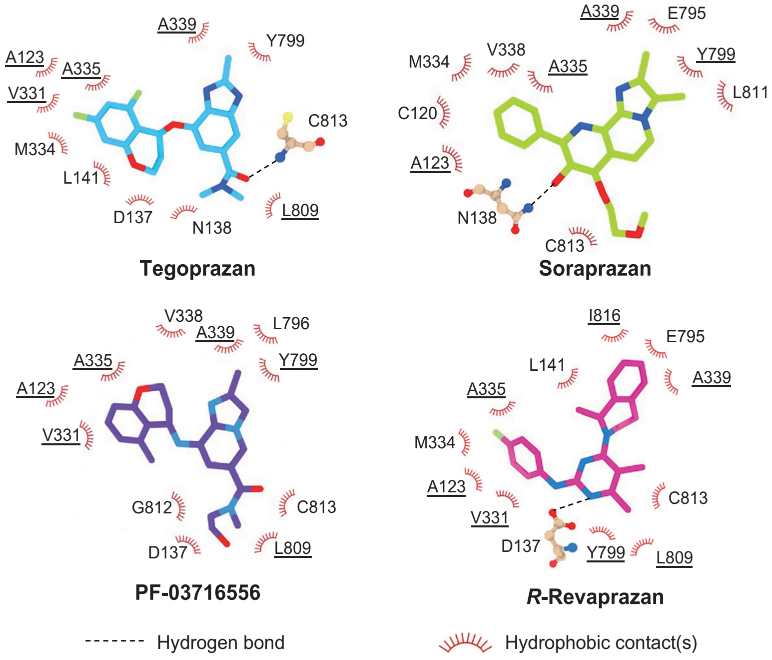

Fig. 2. Schematic representation of P-CAB binding. Schematics of the molecular interactions between H^+,K^+-ATPase and each P-CABs. The hydrophobic residues located within 3.9 Å from bound P-CAB are shown. Expected hydrogen bonds within 3.3 Å are shown as dotted lines. The mutant residues evaluated in Ref. 5 are highlighted with an underbar.

novel binding mode, in which its tetrahydroisoquinoline moiety binds deep in the pocket; such biding is thus clearly distinct from the binding of SCH28080-related compounds. To our knowledge, vonoprazan shows the most potent binding affinity for H^+,K^+-ATPase *in vitro* ($IC_{50,\mathrm{vonoprazan}}$ = 0.015 μM), and this compound is exceptional among P-CABs, because it binds deep in the binding pocket. Our structural analysis reveals that revaprazan directs its tetrahydroisoquinoline moiety toward the cation binding site similar to the vonoprazan binding pose (Fig. 3). According to a previous report, compounds with methoxy substitution in the tetrahydroisoquinoline group of revaprazan, which is facing the cation binding site, show a significant improvement in binding affinity. Our structural and mutagenesis studies suggest that the binding state of revaprazan is somewhat loose, but further optimization of the tetrahydroisoquinoline moiety, especially on the side that faces the cation binding site, may further improve the binding affinity of this type of P-CAB.

The mechanism of action of these P-CABs can now be evaluated at the molecular level, which will facilitate the rational development and improvement of currently available P-CABs, leading to a better treatment of acid-related gastrointestinal diseases and a possible eradication of their main cause, namely, *H. pylori*.

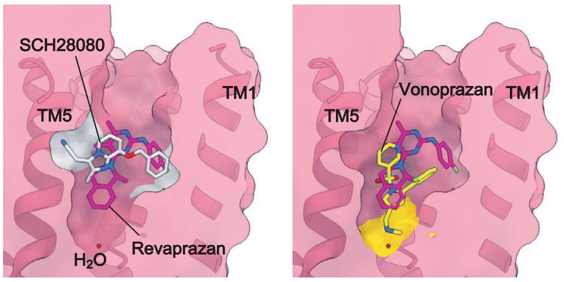

Fig. 3. Binding modes of revaprazan and other representative P-CABs. Cross section of the TM helices at the P-ACB binding site of revaprazan-bound H^+,K^+-ATPase (surface), with superimposed SCH28080 (left, gray) and vonoprazan (right, yellow), viewed approximately parallel to the membrane plane. A red sphere indicates a likely water molecule bound at the cation binding site. Binding surfaces of SCH28080 and vonoprazan are indicated in gray and yellow, respectively.

Kazuhiro Abe

Cellular and Structural Physiology Institute,
Nagoya University

Email: kabe@cespi.nagoya-u.ac.jp

References

[1] J. L. Wallace: Best Pract. Res. Clin. Gastroenterol. **14** (2000) 147.
[2] G. Sachs *et al.*: Yale J. Biol. Med. **69** (1996) 301.
[3] J. M. Shin *et al.*: J. Am. Chem. Soc. **126** (2004) 7800.
[4] K. Abe *et al.*: Nature **556** (2018) 214.
[5] *S. Tanaka, M. Morita, T. Yamagishi, H. V. Madapally, K. Hayashida, H. Khandelia, C. Gerle, H. Shigematsu, A. Oshima and K. Abe: J. Med. Chem.* ***65*** *(2022) 7843.*

Structural basis for substrate discrimination and accommodation in bacterial site-2 protease homologue RseP

Intramembrane proteolysis is a unique cellular process wherein a polypeptide chain is hydrolyzed within the lipid bilayer [1]. Intramembrane proteolysis maintains the quality of the membrane by removing unnecessary and potentially cytotoxic membrane proteins. In addition, intramembrane proteolysis mediates signal transduction by cleaving the membrane-anchored precursor of signaling molecules such as transcription factors and secretory proteins. The deregulation of intramembrane proteolysis is also associated with human diseases such as cancer, Alzheimer's disease, and Parkinson's disease, while the signal transduction through the cleavage is implicated in pathogenic infections. Thus, how the substrates are cleaved within the lipid bilayer is an important biochemical and medical issue that must be addressed.

Intramembrane proteolysis is catalyzed by intramembrane proteases (IMPs) whose active center is within the transmembrane (TM) region. To date, four distinct families of IMPs (site-2 protease (S2P), presenilin/signal peptide peptidase, rhomboid, and Ras-converting enzyme1) have been identified across three domains of life [2]. Out of the four families, S2P was the first IMP to be isolated and classified as a zinc metalloprotease. As their names suggest, many of the S2P family members perform intramembrane proteolysis after the cleavage of their substrates in the soluble regions (site-1 cleavage). S2Ps activate transcription factors involved in the lipid metabolism and ER stress response in eukaryotes, while their prokaryotic homolog mediate signal transduction in extracytoplasmic stress responses and cell envelope biosynthesis. Each S2P cleaves several membrane proteins without apparent consensus on the primary structures. However, the cleavage is not promiscuous and its efficiency obviously varies depending on the substrate. Structural analysis is indispensable for understanding the molecular mechanism underlying the substrate discrimination by S2Ps, but the structural analysis of S2Ps had lagged behind that of other IMP families [3].

In this study, we performed crystallographic analysis on the *E. coli* S2P homolog RseP (*Ec*RseP) and its ortholog from the marine bacterium *Kangiella koreensis* (*Kk*RseP). *Ec*RseP was identified as an IMP to cleave a suppressor of the transcription factor and was further shown to remove remnant signal peptides from secretory proteins (Fig. 1). We purified *Ec*RseP using an immuno-affinity purification system termed the PAtag system to avoid denaturation. *Kk*RseP was discovered as the orthologue suitable for structural analysis. For phasing, we prepared selenomethionine (SeMet)-substituted *Kk*RseP. Diffraction-quality crystals were successfully obtained for both *Ec*RseP and SeMet-substituted *Kk*RseP in the lipidic cubic phase by adding an inhibitor batimastat. X-ray diffraction data were collected from microcrystals using the automated data collection system ZOO and processed by the KAMO system at SPring-8 **BL32XU**. Finally, we determined the crystal structures of *Ec*RseP and SeMet-substituted *Kk*RseP at 3.2 and 3.1 Å resolutions, respectively (Figs. 2(a,b)) [4].

Crystallographic analysis has revealed that the TM region of *Ec*RseP contains four membrane-spanning helices with a four-stranded membrane-reentrant β(MREβ)-sheet inserted between TM1 and TM2. The MREβ-sheet contains several charged residues on the cytoplasmic side and likely assists the recruitment of water molecules into the active center by excluding lipid molecules. The fourth strand of the MREβ-sheet is referred to as the edge strand and is located close to the active center. The peptide-mimetic inhibitor batimastat assumed an extended conformation and docked to the edge strand via hydrogen bonding between the main chains (Fig. 2(c)). Batimastat also forms hydrogen bonds with the side chain of Asn-394 on TM3. Structure-based mutational analysis suggested that the TM segment of the substrate should also be extended by the edge strand and clamped by Asn-394 for cleavage.

In addition, *Ec*RseP possesses two tandemly arranged PDZ domains (PDZ tandem) and the PDZ C-terminal (PCT) region between TM2 and TM3 on the periplasmic side. The PCT region contains two α-helices (PCT-H1 and H2) attached to the membrane surface and a loop connecting these two helices (PCT-loop). It has been proposed that the PDZ tandem suppresses the entry of bulky membrane protein into the active center [5]. PCT-H1 is also presumed to be involved in this size exclusion process. In fact, the PDZ tandem and PCT region lie just above the TM region and appear to restrict access to the active center. More specifically, PCT-H2 and PCT-loop surround the active center by interacting with TM4 via Asp-446 (Fig. 2(d)). The substitution of Asp-446 to residues other than glutamic acid substantially

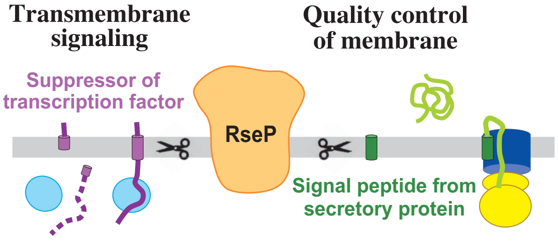

Fig. 1. Examples of the physiological roles of RseP in *E. coli*.

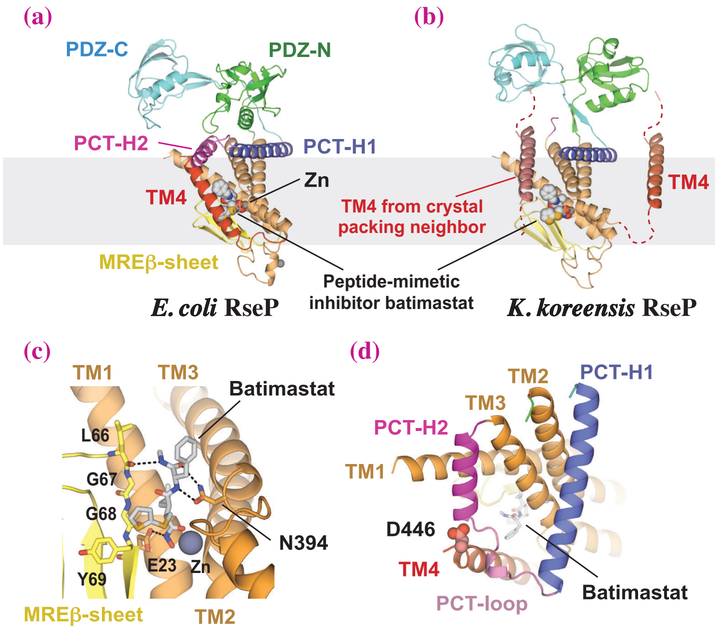

Fig. 2. Crystal structures of *Ec*RseP and *Kk*RseP. **(a)** *E. coli* RseP (*Ec*RseP). Polypeptide chains are shown as ribbon models. Batimastat and zinc ions (Zn) are shown as sphere models. **(b)** *K. koreensis* RseP orthologue (*Kk*RseP). The TM4 segment from the crystal packing neighbor is also shown in the ribbon diagram. **(c)** Close-up view of the batimastat binding site in *Ec*RseP. Batimastat, the residues forming hydrogen bonds with batimastat (Glu-23, Leu-66, Asn-394), and the three residues on the edge strand (Gly-67, Gly-68, Tyr-69) are shown as stick models. TM4 is omitted to visualize the binding site. **(d)** View of the *Ec*RseP model from an outside-in perspective relative to the membrane. The PDZ tandem is omitted to visualize the PCT region and TM domain. Asp-446 is shown as a sphere model.

reduces the substrate cleavage efficiency, indicating the importance of the electrostatic interaction between TM4 and the PCT region in the proteolytic reaction.

Furthermore, a structural comparison between *Ec*RseP and *Kk*RseP provided clues to help us understand the mechanism underlying the substrate accommodation. Despite the structural conservation of individual domains, *Kk*RseP showed marked conformational changes relative to *Ec*RseP (Figs. 2(a,b)). For instance, the PDZ tandem is positioned further away from the TM region, while the PCT-loop and PCT-H2 are unstructured. In *Kk*RseP, TM4 also moves away from the active center and docks to the cleft between TM1 and TM3 of the crystal packing neighbor, reminiscent of the binding mode with the substrates. These observations raised the possibility that the rearrangement of the domains surrounding the active center occurs during the substrate accommodation. In fact, we observed that intramolecular cross-links to fix the position of the PCT region reduced the proteolytic activity in *Ec*RseP.

From the results of our structural and biochemical analyses, we infer that the substrate discrimination and accommodation in *Ec*RseP are controlled by multiple processes, as summarized in Fig. 3. (1) Size exclusion process: The PDZ tandem suppresses the entry of bulky intact substrates by steric hindrance. After the cleavage of the periplasmic region (site-1 cleavage), the size-reduced substrates become accessible to the TM domain containing the active center. (2) Gating process: The PDZ tandem, PCT-H2, and TM4 undergo conformational changes to accommodate the substrate into the active center. Asp-446 may play a pivotal role in the cooperative movement of PCT-H2 and TM4. (3) Unwinding process: The edge strand of the MREβ-sheet extends the TM segment of the substrate and the side chain of Asn-394 clamps it for efficient cleavage. Our findings are expected to deepen our understanding of the mechanism underlying the substrate accommodation and cleavage in other IMPs including presenilin and rhomboid as they share common properties despite the difference in catalytic mechanism.

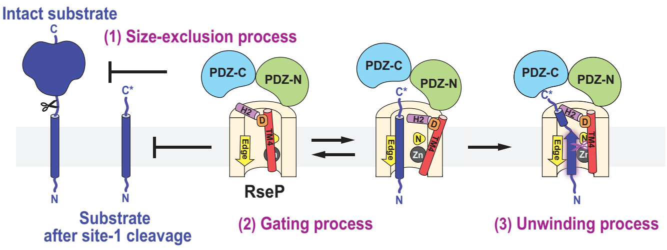

Fig. 3. Proposed model for substrate discrimination and accommodation in *Ec*RseP.

Yuki Imaizumi, Kazunori Takanuki and Terukazu Nogi*

Graduate School of Medical Life Science,
Yokohama City University

*Email: nogi@yokohama-cu.ac.jp

References

[1] M. S. Brown *et al.*: Cell **100** (2000) 391.
[2] N. Kühnle *et al.*: J. Cell Sci. **132** (2019) jcs217745.
[3] L. Sun *et al.*: Curr. Opin. Struct. Biol. **37** (2016) 97.
[4] *Y. Imaizumi, K. Takanuki, T. Miyake, M. Takemoto, K. Hirata, M. Hirose, R. Oi, T. Kobayashi, K. Miyoshi, R. Aruga, T. Yokoyama, S. Katagiri, H. Matsuura, K. Iwasaki, T. Kato, M. K. Kaneko, Y. Kato, M. Tajiri, S. Akashi, O. Nureki, Y. Hizukuri, Y. Akiyama, T. Nogi: Sci. Adv.* **8** *(2022) eabp9011.*
[5] Y. Hizukuri *et al.*: Structure **22** (2014) 326.

Crystal structure of the small-molecule-bound apelin receptor

Apelin receptor (APJR) belongs to the class A G-protein coupled receptor (GPCR) group, which is closely related to cardiac development, cardiovascular homeostasis and cardiac contraction [1,2]. The activation of the APJR signaling pathway can alleviate or treat many cardiovascular-related diseases such as heart failure and hypertension (Fig. 1). Many pharmaceutical companies, such as AMGEN, BMS and Sanofi, are trying to develop effective APJR agonist ligands; however, no drug has been successfully marketed until now. To develop new agonists of APJR, especially small-molecule drugs, understanding the molecular mechanism of the small-molecule binding mode is of critical importance.

To investigate the molecular mechanism of a small-molecule ligand, we chose a potent small-molecule agonist, (1S,2R)-N-(4-(2,6-dimethoxyphenyl)-5-(6-methylpyridin-2-yl)-4H-1,2,4-triazol-3-yl)-1-hydroxy-1-(5-methylpyrimidin-2-yl) propane-2-sulfonamide (termed cmpd644), which is similar to a clinical-stage drug candidate developed for treating heart failure (US patent WO2016187308A1, Amgen Inc.). After several rounds of optimization, we obtained cmpd644-bound APJR structures in a complex with its downstream heterotrimeric $G\alpha_i G\beta\gamma$ by cryo-EM methods [3]. Interestingly, we observed two types of APJR-Gi coupling stoichiometry from one cryo-EM dataset. Dimeric APJR and monomeric APJR adopt 2:1 and 1:1 (receptor: G protein) stoichiometric ratios, respectively (Fig. 2). This provides the first direct structural evidence of the coexistence of homodimers and monomers in the ligand-bound and G protein-coupled APJR signaling complexes.

To understand the small-molecule ligand binding mode for APJR in greater detail, we also solved the co-crystal structure of APJR in a complex with cmpd644 at a high resolution (2.7 Å) in the absence of Gi protein by X-ray crystallography. To obtain a stable APJR protein for structural determination, we first back-mutated W261K to the wild type employing the previous construct used for obtaining the APJR-peptide co-crystal structure [4]. Then, we generated and screened multiple constructs and finally introduced three new mutations (i.e., E174C, M217C, and I250C) based on the wild-type APJR sequence to further stabilize the receptor, and conducted crystallization trials by the LCP method. Finally, with the help of beamline scientists at SPring-8 **BL41XU**, we obtained high-quality X-ray diffraction data sufficient for solving the structure.

This is the first reported small-molecule-bound APJR co-crystal structure and we named it $_{\mathrm{xtal}}\mathrm{APJ}^{\mathrm{cmpd644}}$ (Fig. 3(a)). Alignment with our previously solved peptide-bound AMG3054-APJR co-crystal structure revealed an almost identical receptor conformation (r.m.s.d. 0.529Å) [4]. We are curious about the distinction between peptide and small-molecule binding modes. Upon close examination of the binding pocket, we found that cmpd644 only occupied "site 1" of the pocket and inserted itself deeper when aligning with the C-terminal portion of the peptide ligand, which is different from the two-site binding mode for the peptide ligand (Fig. 3(b)). Moreover, the dimethoxyphenyl group of cmpd644 simulates the phenyl ring of F17 in AMG3054, interacting with W85$^{2.60}$, I109$^{3.32}$, F110$^{3.33}$, and F291$^{7.35}$ (Fig. 3(c)). There is an extended subpocket formed by the interaction between the methylpyridine ring in

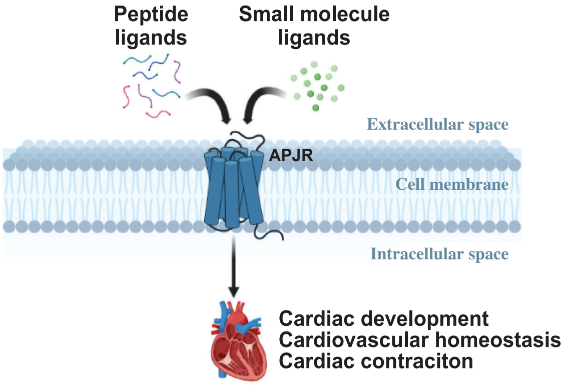

Fig. 1. Simplified illustration of APJR functional pathway. Peptide and small-molecule ligands can activate APJR signaling, which leads to cardiac development, cardiovascular homeostasis and cardiac contraction [1,2]. This figure was created at BioRender.com.

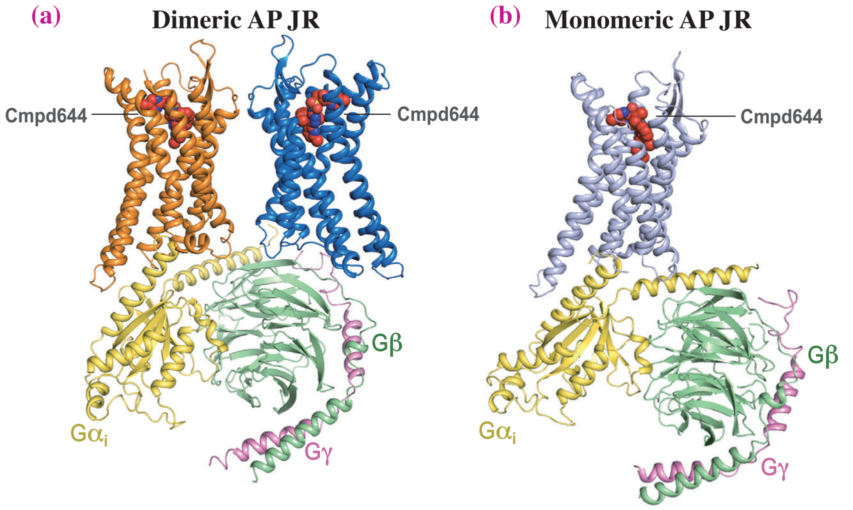

Fig. 2. Cryo-EM structures of the dimeric APJR-Gi (**a**) and monomeric APJR-Gi (**b**) complexes in the presence of cmpd644.

cmpd644 and the surrounding hydrophobic residues of F78$^{2.53}$, F110$^{3.33}$, Y264$^{6.51}$, and Y299$^{7.43}$ (Fig. 3(c)). The interacting residues W85$^{2.60}$, F110$^{3.33}$, K268$^{6.55}$, Y271$^{6.58}$, M288$^{7.32}$, and F291$^{7.35}$ are consistent with the reported functional assay for the small-molecule AM-8123, which shares a similar scaffold with cmpd644 [5].

We report the first co-crystal structure of APJR in a complex with the drug-candidate small-molecule compound, providing a precise molecular template for further pharmacology studies on treating cardiovascular disease. Additionally, together with the G-protein-bound cryo-EM structures in both 2:1 and 1:1 stoichiometric ratios, we provide a different, exciting view of the class A GPCR signaling mechanism.

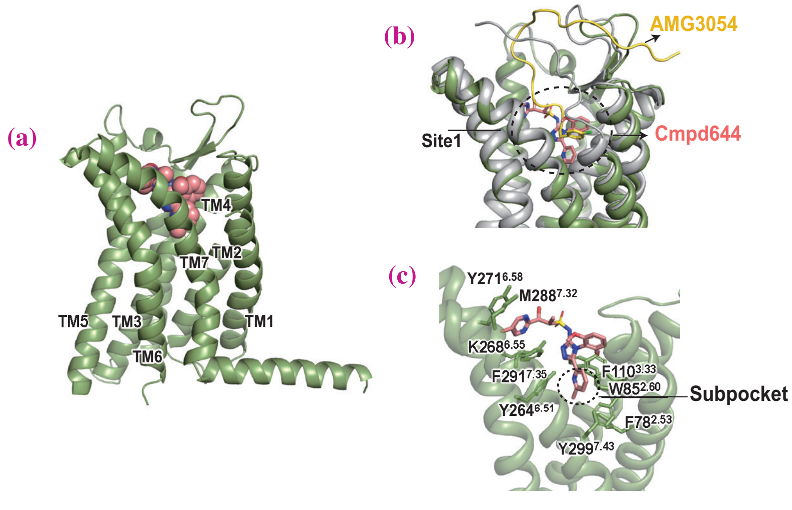

Fig. 3. (**a**) Overall structure of $_{\text{xtal}}$APJ$^{\text{cmpd644}}$. APJR is colored green and cmpd644 pink. (**b**) Comparison of $_{\text{xtal}}$APJ$^{\text{cmpd644}}$ with AMG3054-APJR co-crystal structure (PDB ID: 5VBL, AMG3054 is colored yellow and APJR gray). Site 1 is circled with dashed lines. (**c**) Binding pocket of cmpd644 in $_{\text{xtal}}$APJ$^{\text{cmpd644}}$. Interacting residues of APJR are shown as sticks. The subpocket is circled with dashed lines.

Yang Yue[a] and Fei Xu[a,b,*]

[a] iHuman Institute, ShanghaiTech University, China
[b] School of Life Science and Technology,
ShanghaiTech University, China

*Email: xufei@shanghaitech.edu.cn

References

[1] B. F. O'Dowd *et al*.: Gene **136** (1993) 355.
[2] S. C. Chng *et al*.: Dev. Cell **27** (2013) 672.
[3] *Y. Yue, L. Liu, L.-J. Wu, Y. Wu, L. Wang, F. Li, J. Liu, G.-W. Han, B. Chen, X. Lin, R. L. Brouillette, É. Breault, J.-M. Longpré, S. Shi, H. Lei, P. Sarret, R. C. Stevens, M. A. Hanson and F. Xu: Nat. Struct. Mol. Biol.* ***29*** *(2022) 688.*
[4] Y. Ma *et al*.: Structure **25** (2017) 858.
[5] B. Ason *et al*.: JCI Insight **5** (2020) e132898.

Structural basis for neutralization of SARS-CoV-2 Omicron variant using engineered ACE2 decoy

The coronavirus disease (COVID-19) caused by sever acute respiratory syndrome coronavirus 2 (SARS-CoV-2) emerged in Wuhan, China, at the end of 2019 and then spread worldwide. Coronaviruses have large trimeric membrane proteins called spike proteins on their surface. The spike protein binds to angiotensin-converting enzyme 2 (ACE2) on the surface of human cells via its receptor binding domain (RBD), triggering viral infection. Therefore, inhibiting the binding of spike proteins to ACE2 is one of the most promising therapeutic strategies for COVID-19. Following this concept, multiple vaccines and therapeutic agents have been developed to date. However, the pandemic is still ongoing three years after the outbreak and many cases are reported every day, causing a significant impact on our lives. One reason for this is the high mutation rate of SARS-CoV-2 ($\sim 1\times10^{-3}$ substitutions per site per year) [1]. Since the first SARS-CoV-2 appeared in Wuhan, various mutants of the virus have emerged over the past three years, and there is concern that spike protein-based vaccines and monoclonal antibody therapeutics targeting the RBD may reduce or nullify their efficacy because of the mutations.

We previously developed a therapeutic candidate that neutralizes SARS-CoV-2 using the extracellular region of ACE2, soluble ACE2 (sACE2) (Fig. 1) [2]. The main advantage of using an sACE2-based decoy receptor is its resistance to virus escape mutations. The virus mutant escaping from the sACE2 decoy should also have a limited binding affinity toward native ACE2 receptors on the cell surface, resulting in diminished or eliminated infectivity. Since the affinity of wild type (WT) sACE2 for the RBD is relatively low, we first attempted to increase the affinity by directed evolution. Random mutations were introduced to the amino acid residues 18–102 of ACE2, which form the RBD-binding interface by error-prone PCR. They were then expressed on human cells and ACE2 mutants with increased affinity were selected by flow cytometry. After repeating these procedures three times, we obtained a high-affinity ACE2 mutant, ACE2(3N39), with seven mutations, A25V, K26E, K31N, E35K, N64I, L79F, and N90H. Quantitative measurements of binding affinity to the Wuhan RBD showed that sACE2(3N39) has an approximately 100-fold increased affinity compared with WT (K_D values of WT and the 3N39 variant are 17.63 nM and 0.29 nM, respectively). We further characterized each mutation and found that only four of the seven mutations (A25V, K31N, E35K, and L79F) were sufficient to achieve high affinity comparable to those of conventional antibody drugs (K_D value of the A25V/K31N/E35K/L79F mutant is 0.64 nM). We next conducted the structural analysis of sACE2(3N39) complexed with the Wuhan RBD. Initial crystallization screening yielded thin rod-shaped crystals, and the optimization of crystallization conditions resulted in thick hexagonal plate-shaped crystals. X-ray diffraction data were collected at SPring-8 **BL44XU**, and the complex structure was solved at a resolution of 3.2 Å. The crystal structure revealed how the mutated residues in 3N39 contribute to the affinity enhancement for the Wuhan RBD [2].

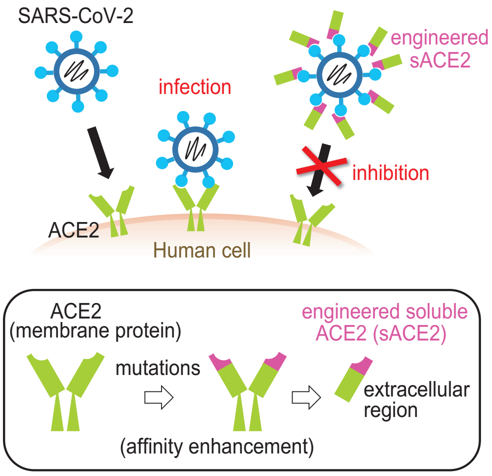

Fig. 1. Strategy for SARS-CoV-2 neutralization using engineered sACE2 decoy.

However, as mentioned above, SARS-CoV-2 rapidly undergoes mutations, and various variants of concern (VOCs) have emerged thus far. The Omicron variant of SARS-CoV-2, which was detected for the first time in South Africa in November 2021, has a high number of mutations in the spike gene. More than 30 amino acid residues are mutated in the Omicron spike protein, 15 of which are in the RBD (Fig. 2). These mutations significantly reduced the activity of several therapeutic antibodies developed to target the Wuhan strain [3,4]. The complex structure of the Omicron RBD and WT ACE2 was first deposited in the PDB in December 2021 and has since been reported by several research groups. The structures showed that multiple Omicron mutations are located at the binding interface of these molecules (Fig. 3(a)). To understand the difference in interaction mechanism among the RBD/ACE2 pairs, we compared the structures of Omicron RBD-WT ACE2, Wuhan RBD-WT ACE2, and Wuhan RBD-ACE2(3N39) complexes [5]. In WT ACE2, K31 and

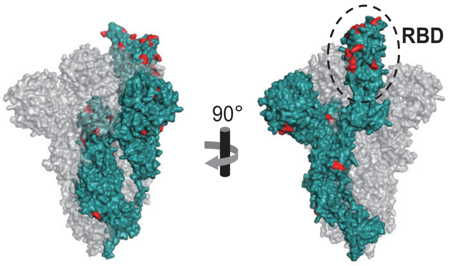

Fig. 2. Mapping of the mutation sites introduced in the Omicron spike protein. One subunit within the trimeric Omicron spike protein (PDB: 7wvn) is shown as a dark cyan surface, and the other two subunits are shown as gray transparent surfaces. Omicron mutations are highlighted in red.

E35 form an intramolecular salt bridge (Fig. 3(b)), whereas in our mutant, the simultaneous mutation of K31N and E35K disrupts this interaction, allowing E35K to exclusively form a hydrogen bond with Q493 of the Wuhan RBD (Fig. 3(c)). We speculated that this is one of the reasons for the improved affinity in 3N39. On the other hand, in the Omicron RBD, Q493 was substituted with arginine, which forms a salt bridge with E35 of WT ACE2 (Fig. 3(d)). This salt bridge may contribute to the affinity enhancement of the Omicron RBD for WT ACE2. However, when ACE2(3N39) binds to the Omicron RBD, there is concern that electrostatic repulsion between the E35K mutation site of ACE2(3N39) and R493 of the Omicron RBD could occur. To predict the effect of the Omicron mutations on ACE2(3N39) binding, we built a homology model of the Omicron RBD-ACE2(3N39) complex using structures of PDB IDs 7t9l and 7dmu. The complex model suggested that the electrostatic clash between K35 and R493 can be easily avoided by the rotation of their side chains. It was also found that the side chain of R493 could form a direct hydrogen bond with N31 of ACE2(3N39) instead of K35 (Fig. 3(e)). Thus, it was structurally predicted that 3N39 could retain a high affinity for the Omicron RBD.

In later studies, we evaluated various aspects of ACE2 decoys and attempted to optimize the design of ACE2 mutants. Finally, we succeeded in designing ACE2(3N39v4) with improved stability and reduced potential immunogenicity while maintaining the high affinity of the original ACE2(3N39). The degree to which sACE2(3N39v4) neutralized Omicron was comparable to the case of the Wuhan strain and showed a therapeutic effect against Omicron infection in hamster and human ACE2 transgenic mice [5]. These facts indicate that the decoy strategy is more effective against viruses with a high mutation rate than antibody-based therapeutics. The ACE2 decoy developed in this study is expected to show high neutralizing activity against any SARS-CoV-2 VOCs that may emerge in the future.

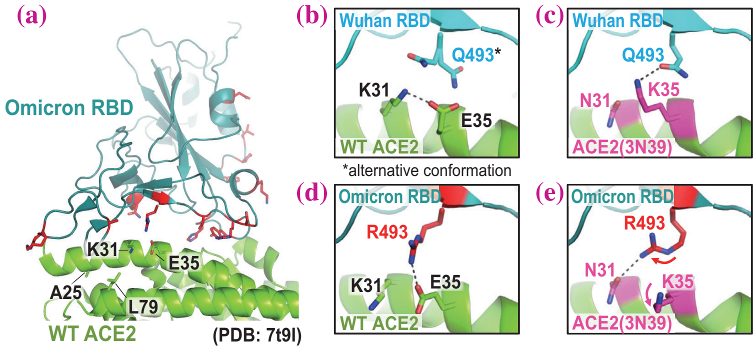

Fig. 3. Difference in interaction mode among the RBD/ACE2 pairs. **(a)** Cryo-electron microscopy structure of the Omicron RBD-WT ACE2 complex (PDB ID: 7t9l). Residues mutated in Omicron are shown as red sticks. Four residues (A25, K31, E35, and L79) of which mutations are essential for enhancement of affinity in the ACE2(3N39) variant are shown as sticks. **(b** to **e)** Close-up views of the interface between **(b)** Wuhan RBD and WT ACE2 (PDB ID: 6m0j), **(c)** Wuhan RBD and ACE2(3N39) (PDB ID: 7dmu), **(d)** Omicron RBD and WT ACE2 (PDB ID: 7t9l), and **(e)** Omicron RBD and ACE2(3N39) (simulated model) are shown. Potential hydrogen-bonding and salt-bridge interactions are indicated by dashed lines.

Takao Arimori* and Junichi Takagi

Institute for Protein Research, Osaka University

*Email: arimori@protein.osaka-u.ac.jp

References

[1] L. van Dorp *et al*.: Nat. Commun. **11** (2020) 5986.
[2] *Y. Higuchi, T. Suzuki, T. Arimori, N. Ikemura, E. Mihara, Y. Kirita, E. Ohgitani, O. Mazda, D. Motooka, S. Nakamura, Y. Sakai, Y. Itoh, F. Sugihara, Y. Matsuura, S. Matoba, T. Okamoto, J. Takagi, A. Hoshino: Nat. Commun.* ***12*** *(2021) 3802.*
[3] M. Hoffmann *et al*.: Cell **185** (2021) 447.
[4] D. Planas *et al*.: Nature **602** (2022) 671.
[5] *N. Ikemura, S. Taminishi, T. Inaba, T. Arimori, D. Motooka, K. Katoh, Y. Kirita, Y. Higuchi, S. Li, T. Suzuki, Y. Itoh, Y. Ozaki, S. Nakamura, S. Matoba, D. M. Standley, T. Okamoto, J. Takagi, A. Hoshino: Sci Transl Med.* ***14*** *(2022) eabn7737.*

Cell-free protein crystallization for structural analysis

In nature, some proteins spontaneously crystallize in living cells. Such crystals are known to have biological functions such as protein storage, virus protection, heterogeneous catalysis, and immune system activation [1,2]. Since the structure of polyhedra, one of the in-cell protein crystals, was determined in 2007 [3], in-cell protein crystallization (ICPC) has attracted attention as a next-generation structural biology tool because it does not require multistep purification processes or large-scale crystallization screening. Several ICPC methods have been developed, including high-throughput screening and the optimization of the cell culture process. However, significant issues remain to be resolved in obtaining various protein crystals in sufficient amounts and quality for structure determination by ICPC because crystals are often formed incidentally in the cells. Therefore, several technical challenges must be overcome to apply this method to protein structural analysis. If a new ICPC method can be established, it will be expected to become a more accessible structural analysis technique.

Cell-free protein synthesis (CFPS), a protein preparation technique used in synthetic biology, is very effective for rapidly screening protein synthesis [4]. However, it has been considered unsuitable for structural biology efforts that require large amounts of protein, such as crystallization. Here, we report the development of cell-free protein crystallization (CFPC), a direct protein crystallization method using CFPS [5]. We have (1) established small-scale and rapid crystallization using CFPS and (2) manipulated crystallization by adding chemical reagents. The polyhedra crystal (PhC), produced in insect cells by infection with cytoplasmic polyhedrosis virus (CPV), is one of the most studied in-cell protein crystals. The most crucial advantages of CFPC are that the reaction scale and time can be minimized and that various reagents can be added during the reaction.

The crystallization of polyhedrin monomers (PhMs) was performed using the Wheat Germ Protein Synthesis kit (WEPRO7240 Expression Kit) because these extracts have been identified as having the highest protein expression activity among eukaryotic systems. Translation reactions were performed by the bilayer method. A 20 μL reaction mixture containing 10 μL of WEPRO7240 and 10 μL of mRNA solution was placed in a 1.5 mL microtube, overlaid with 200 μL of SUB-AMIX SGC solution, and incubated at 20°C for 24 h (Fig. 1(a)). The reaction mixture was centrifuged, and a white precipitate was collected (Fig. 1(b)). The crystalline precipitate was observed under an optical microscope (Fig. 1(c)). The crystals prepared from the CFPC reaction (PhC_CF) have the same cubic morphology as PhC synthesized in insect cells (PhC_IC). The average size of PhC_CF (580 nm) measured by scanning electron microscopy (SEM) is about one-fifth that of PhC_IC (2700 nm) (Fig. 1(d)).

To collect diffraction data of nanosized PhC_CF isolated from the reaction mixture, a micro-X-ray beam at SPring-8 **BL32XU** equipped with Serial Synchrotron Rotation Crystallography (SS-ROX) was used for diffraction. PhC_CF was refined with a resolution of 1.80 Å and has a space group ($I23$) and lattice parameters identical to those of PhC_IC (Fig. 2). The significant difference between PhC_CF and PhC_IC is the absence of the electron density of nucleotide triphosphate (NTP) bound to the monomer interface observed in PhC_IC. The result indicates that NTP binding is not essential for the crystallization of PhMs. After the elucidation of the translation time, it was found that the CFPC reaction of PhC produces nanocrystals of sufficient quality to obtain a high-resolution structure in only 6 h. This reaction time is markedly shorter than the incubation time (>3 days) required to obtain equivalent high-quality crystals using insect cells. By the dialysis method for CFPC, the crystal that gives a resolution of 1.95 Å was obtained with only 20 μL of the reaction mixture.

We applied this method to the structure determination of crystalline inclusion protein A (CipA) with the addition of chemical reagents to the reaction solution to suppress twin crystal formation. CipA, a hydrophobic protein

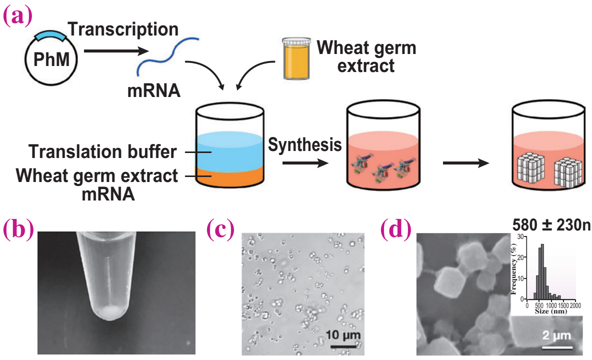

Fig. 1. **(a)** Schematic illustration of cell-free protein crystallization (CFPC) of polyhedrin monomer (PhM) using the Wheat Germ Protein Synthesis kit. **(b)** Photograph of the tube after CFPC. **(c)** Differential interference contrast (DIC) image of PhC_CF. **(d)** Scanning electron micrograph of PhC_CF. Size distribution of PhC_CF determined from the SEM image.

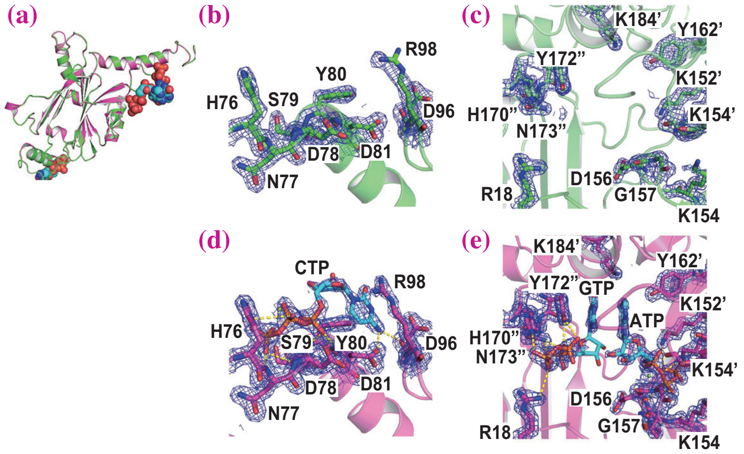

Fig. 2. Crystal structures of PhC_CF20°C/24h and PhC_IC (PDB ID: 5 gqm). **(a)** Superimposed structures of PhC_CF 20°C/24 h (green) and PhC_IC (magenta). **(b,c)** Close-up views of (b) CTP and (c) ATP/GTP binding sites in PhC_CF20°C/24h, **(d,e)** Close-up views of (d) CTP and (e) ATP/GTP binding sites in PhC_IC. The selected $2|Fo| - |Fc|$ electron density maps at 1.0σ are shown in blue. Hydrogen bonds are indicated with yellow dotted lines.

of 104 amino acid residues, spontaneously forms crystalline particles in *Photorhabdus luminescens*, an entomopathogenic bacterium. When CipA was expressed in CFPC by the dialysis method, a white precipitate appeared in the solution mixture after 24 h. The structural analysis of CipA_CF was attempted with 1.61 Å resolution data obtained by the small wedge method at SPring-8 BL32XU. However, the structure could not be determined because the twin fraction was high. Therefore, we attempted to overcome this problem by adding a reagent that inhibits twinning to the reaction mixture of CFPC. X-ray diffraction experiments of the crystal show that CipA_CF crystallized in the presence of 3 v/v% 1,4-dioxane had a markedly reduced twinning fraction of 0.10 with a resolution of 2.11 Å. The structure was determined by molecular replacement using the search model created by AlphaFold2 (Fig. 3). The monomer structure of CipA is a typical oligonucleotide/oligosaccharide-binding (OB) fold, consisting of an α-helix and a β-strand. In the lattice structure, the four α-helices from each monomer form a four-helix bundle and exist as a tetramer. This tetramer is considered to be the basic unit of crystal growth. The interactions between the edges of each tetramer form the crystal lattice, which is further stabilized by embedding the neighboring monomer's N-terminal arm in the cleft that forms between the tetramer-tetramer interface.

We have established a CFPC method to rapidly obtain protein crystals in microliter volumes within a few hours without the need for purification and crystallization procedures. This technology, which integrates in-cell and *in vitro* crystallization, significantly expands the tools available for high throughput protein structure determination, particularly in unstable, low-yield, or substrate-binding proteins, which are difficult to analyze by conventional methods.

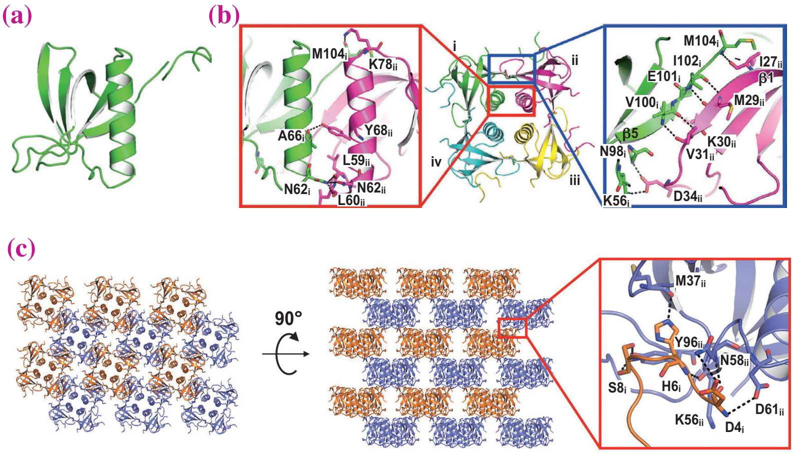

Fig. 3. Crystal structure of CipAC-CF with 1,4-dioxane. Structures of **(a)** monomer and **(b)** tetramer. **(a)** The CipA monomer consists of the N-terminal arm followed by three β-strands (β1, β2, and β3), an α-helix, and two β-strands (β4 and β5). **(b)** Interactions between monomers (i, ii, iii, and iv) in the tetramer. **(c)** Lattice structure and interactions between tetramers. Hydrogen bonds are indicated with black dotted lines.

Satoshi Abe* and Takafumi Ueno

Tokyo Institute of Technology

*Email: saabe@bio.titech.ac.jp

References

[1] M. Kojima *et al.*: Biomater. Sci. **10** (2022) 354.
[2] R. Schonherr *et al.*: Biol. Chem. **399** (2018) 751.
[3] F. Coulibaly *et al.*: Nature **446** (2007) 97.
[4] M. Harbers: FEBS Lett. **588** (2014) 2762.
[5] *S. Abe, J. Tanaka, M. Kojima, S. Kanamaru, K. Hirata, K. Yamashita, A. Kobayashi and T. Ueno: Sci. Rep.* ***12*** *(2022) 16031.*

Master allostery in clock protein KaiC orchestrates circadian rhythm

Allostery, a biological (or ubiquitous) event in which a chemical process occurring at one site of a protein or enzyme affects the catalytic activity of another site, is the basis of non-linear cellular responses. The circadian rhythm, a major example of such regulatory phenomena, is a biological timekeeping system that enables organisms to adapt to environmental fluctuations caused by Earth's rotation. Efforts have been dedicated to understanding the mechanisms by which activities and structures of molecules, complexes, and cells autonomously oscillate with a 24-hour period. However, the precise relationship between protein allostery and rhythmicity remains to be elucidated.

The core oscillator of circadian rhythms in cyanobacteria consists of three clock proteins, KaiA, KaiB, and KaiC (Fig. 1(a)). The three Kai proteins repeatedly associate and disassociate *in vitro* in the presence of adenosine triphosphate (ATP). KaiC, a component with the highest molecular mass among the three, orchestrates the assembly states of KaiA and KaiB through autonomous activation and deactivation of its own catalytic activities.

The cyanobacterial circadian rhythm is generated by two reaction cycles in KaiC (Fig. 1(b)). The KaiC hexamer hydrolyzes ATP in its N-terminal domain (C1) to determine the period length of the rhythm (C1-ATPase cycle). In its C-terminal domain (C2), phosphorylation and dephosphorylation of S431 and T432 configure the cycle with a circadian period (C2-phospho cycle) (ST→SpT→pSpT→pST: S for S431, T for T432, p for phosphorylated states). Although the active sites of C1 and C2 are 4 nm distant, they function cooperatively through mutual allosteric regulations. The importance of this cooperativity is evident from the fact that the loss of function of either C1 or C2 results in arrhythmicity, but the mechanisms of the rhythm emergence via C1-C2 coupling and the transmission of temporal information to KaiA and KaiB are still unresolved. To address this issue, we conducted comprehensive structural analyses of KaiC.

To gain insights into the structural basis of the rhythmicity, we crystallized KaiC in different phosphorylation states and obtained electron density maps at 2.2–3.1 Å resolutions through diffraction experiments at SPring-8 **BL44XU** [1][2][3]. Our structure library consisting of 13 KaiC coordinates covered the entire C2-phospho cycle via KaiC-ST, KaiC-SpT, KaiC-pSpT, and KaiC-pST. Similarly, for C1, we identified ATP, nucleophilic water molecules, and adenosine diphosphate (ADP) in the active sites and confirmed that pre- and post-hydrolysis states in C1-ATPase cycle were captured.

The KaiC structure library captured three conformational changes in C1 and C2. First, a secondary structural transition associated with the C2-phospho cycle was identified (C2-PSw, phosphorylation switch) (Fig. 2(a)). The upstream region of the phosphosites adopted helical and coiled conformations due to differences in the volumes and charges around S431/pS431 [1]. This dynamic structural change was also confirmed in the solution phase during the *in vitro* oscillation [3]. The C2-phospho cycle through the biochemical 4-state was nearly a conformational switch between the two structural states.

The second was a whole domain positional rearrangement in which the neighboring C1 shifts systematically at the protomer-protomer interfaces (C1-domain slide) (Fig. 2(b)). This was related to the oscillation of the ATP hydrolysis activity, through ADP-ATP exchange process and the regulation of lytic water positions (Fig. 2(c)) [2].

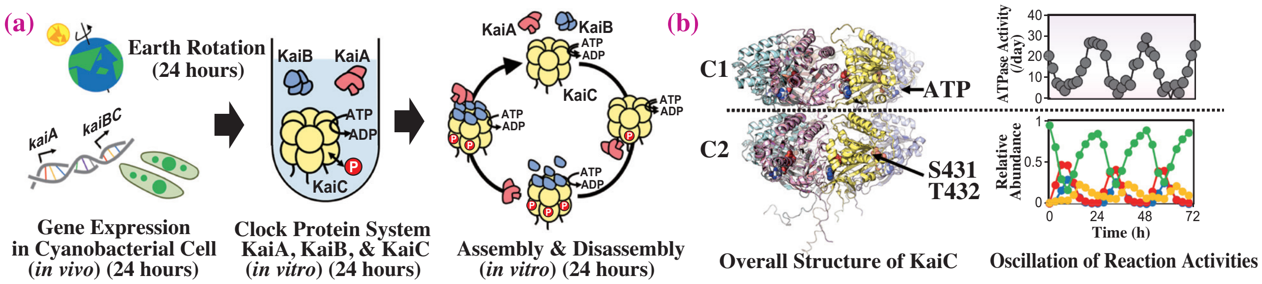

Fig. 1. Clock protein KaiC mastering the cyanobacterial circadian rhythm. **(a)** Cross-scale relationships between the oscillation *in vitro*, the rhythm *in vivo*, and Earth's rotation. **(b)** The overall architecture of KaiC and the oscillations of states in C1 and C2. KaiC-ST, KaiC-SpT, KaiC-pSpT, and KaiC-pST, are distinguished by green, red, blue, and orange, respectively.

Third, the above structural alternations in C1 and C2 were mediated by the hydrogen bond rearrangements in their interface (Fig. 2(d)). The neutral Q394 was the key residue for the functional and structural C1-C2 communication, which is accomplished by switching its hydrogen bonding partner between the basic R217 and the acidic E214 (ERQ triad) [1].

KaiC integrates elementary reactions of C1-ATPase cycle and C2-phospho cycle through these secondary, tertiary, and quaternary structural arrangements to generate the circadian rhythm. This observation was experimentally verified through the examination of a mutant with the single phosphorylation at S432 (KaiC-SV). Despite the mutation of T432 into valine, KaiC-SV still retained a rhythmicity based on C2-PSw. Furthermore, its prolonged period could be *allosterically* shortened by activating C1-ATPase (Fig. 2(e)) [1].

The C1-C2 allostery is indeed a core of the clock that transmits the time information throughout the cell. The disassembly of KaiA-KaiB-KaiC complexes formed during the cycle is essentially suppressed with an extremely low dissociation rate constant [4]. The cue for the disassembly is provided by the activation of ATP hydrolysis accompanied by C1-domain slide [2]. Moreover, the circadian rhythm is known as a temperature-insensitive phenomenon, in which the period length is almost constant in the range of physiological temperature, and this ability referred to as temperature compensation also relies on C1-C2 allostery [5].

For understanding biological phenomena such as the circadian rhythm that span a wide range of spatio-temporal scales (from fast atomic dynamics to slow complex disassembly dynamics), it is important to observe the structural changes of biomolecules underlying the cellular events. Slight structural changes in the active sites can be particularly significant in these systems, so it is still necessary to solve the crystal structures as demonstrated in this study.

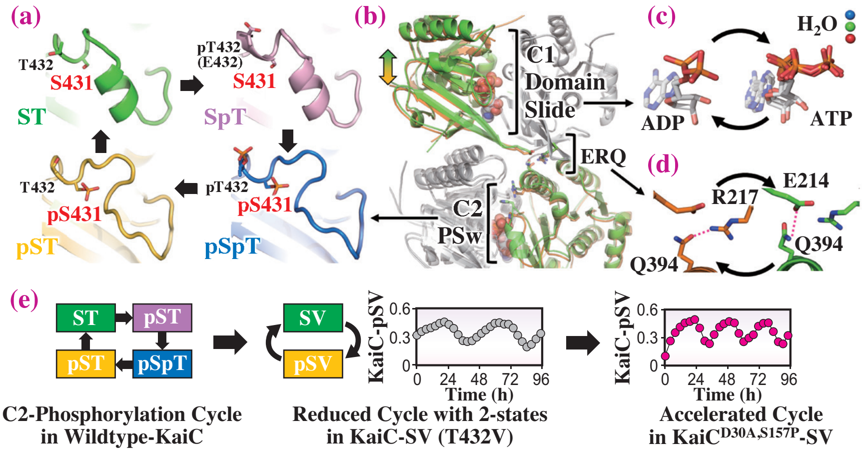

Fig. 2. Master allostery integrating C1-ATPase cycle and C2-phospho cycle in KaiC. **(a)** Helical and coiled structures found at the upstream region of S431. **(b)** Structural coupling between C1-domain slide and C2-phosphorylation switch. The direction of C1-domain slide is indicated by an arrow. **(c)** ATP, nucleophilic water molecules, and ADP found in C1-ATPase cycle. The positional rearrangements of the waters are represented by red (high activity), green (middle activity), and blue (low activity) spheres. **(d)** Hydrogen-bond switch among E214, R217, and Q394. **(e)** Scheme of the experiments verifying the identified allostery. The period length of KaiC-SV oscillation was 47 hours in the presence of KaiA and KaiB. The mutations, D30A and S157P introduced into C1, resulted in the reduction of the period length down to 29 hours.

Yoshihiko Furuike[a,b,*], Atsushi Mukaiyama[a,b,c]
and Shuji Akiyama[a,b]

[a] Research Center of Integrative Molecular Systems (CIMoS), Institute for Molecular Science
[b] Department of Functional Molecular Science, SOKENDAI, The Graduate University for Advanced Studies
[c] Department of Bioscience and Biotechnology, Fukui Prefectural University

*Email: furuike@ims.ac.jp

References

[1] *Y. Furuike, A. Mukaiyama, D. Ouyang, K. Ito-Miwa, D. Simon, E. Yamashita, T. Kondo and S. Akiyama: Sci. Adv.* **8** *(2022) eabm8990.*
[2] *Y. Furuike, A. Mukaiyama, S. Koda, D. Simon, D. Ouyang, K. Ito-Miwa, S. Saito, E. Yamashita, T. Nishiwaki-Ohkawa, K. Terauchi, T. Kondo and S. Akiyama: Proc. Natl. Acad. Sci. USA* **119** *(2022) e2119627119.*
[3] *A. Mukaiyama, Y. Furuike, E. Yamashita and S. Akiyama: Biochem. J.* **479** *(2022) 1505.*
[4] D. Simon *et al*.: Biophys. Physicobiol. **19** (2022) e190008.
[5] Y. Furuike *et al*.: Comm. Phys. **5** (2022) s42005-022-00852-z.

Time-resolved X-ray crystallography of enzymatic reaction that degrades a mutagenic nucleotide

Time-resolved X-ray crystallography is a methodology to observe intermediate structures during enzymatic reactions and reveals reaction mechanisms at atomic resolution. To perform the time-resolved X-ray crystallography of enzymes, it is essential to establish reaction conditions in a crystalline state, i.e., to prepare crystals of an enzyme-substrate complex in its active form and control the entire reaction process on a time scale that can be followed while maintaining its crystalline state. We previously followed the nucleotidyl-transfer reaction in DNA polymerase [1,2]. The reaction in the crystals of DNA polymerase was initiated by soaking the crystals in a solution containing Mg^{2+} ions, active metal ions for the reaction, and stopped by freezing the crystals at desired time points. The intermediate structures captured by this freeze-trap method allowed us to observe the process of phosphodiester bond formation by DNA polymerase at a neutral pH of 7.0 in a time scale of 40 to 300 s. In this study, we have followed the course of the enzymatic reaction of *E. coli* MutT, which degrades a mutagenic nucleotide 8-oxo-dGTP and suppresses transversion mutations. We have visualized the entire reaction process of *E. coli* MutT by the freeze-trap method with a lower reaction rate at a lower pH of 5.8 [3].

8-Oxo-dGTP, which is produced by the oxidation of dGTP, is a mutagenic nucleotide because it is misincorporated into DNA by a DNA polymerase and the 8-oxoguanine (8-oxoG) base can mispair with adenine (Fig. 1). *E. coli* MutT hydrolyzes 8-oxo-dGTP to 8-oxo-dGMP and pyrophosphate (PPi) through the nucleophilic attack by a water molecule in the presence of Mg^{2+} or Mn^{2+} [4]. We previously determined the crystal structure of MutT in a complex with 8-oxo-dGMP (a product) and revealed the recognition mechanism of the 8-oxoG nucleotide through the large conformational change of MutT [5]. To follow the hydrolytic reaction of 8-oxo-dGTP by MutT, the complex of MutT and 8-oxo-dGTP was crystallized. The complex structure showed that 8-oxo-dGTP is bound to the active site (enzyme-substrate complex structure: ES, Fig. 2), and the hydrolysis of 8-oxo-dGTP during crystallization without Mg^{2+} or Mn^{2+} ions was not observed. The crystals of ES were soaked in Mg^{2+} or Mn^{2+} solutions to trigger the hydrolytic reaction and then incubated for several hours. We confirmed that 8-oxo-dGTP is hydrolyzed to 8-oxo-dGMP (enzyme-product complex structure: EP) while maintaining its crystalline state. Next, the reaction conditions were screened to capture intermediate structures including an important step: nucleophilic attack by a water molecule. More than a hundred crystals were prepared under different reaction conditions of Mn^{2+} concentration (1 to 20 mM), reaction time (minutes to hours), and pH (5.6 to 6.0), and X-ray diffraction data were collected at SPring-8 **BL44XU** and **BL41XU**. The Mn^{2+} ion was used as an active metal ion because the anomalous signal derived from Mn^{2+} is used for the calculation of its occupancy, which is important information for the refinement of the intermediate structures. The reaction condition of 5 mM Mn^{2+} was suitable for observing the reaction processes immediately before nucleophilic attack, i.e., the sequential binding of metal ions, the structural change of the active site for catalysis, and the motion of nucleophilic water, whereas the reaction condition of 20 mM Mn^{2+} was suitable for visualizing the gradual hydrolysis of 8-oxo-dGTP to 8-oxo-dGMP and the release of PPi and Mn^{2+} ions. Finally, six types of intermediate structure (including ES) were determined at 1.36–1.90 Å resolutions.

MutT belongs to the Nudix hydrolase superfamily, which is widely distributed in all species, and is one of the most studied Nudix hydrolases. A number of studies of the Nudix hydrolases including MutT indicated that the Nudix hydrolases require two or three metal ions for catalysis. The intermediate structures in this study have clearly shown that MutT requires three metal ions for catalysis (Fig. 3). In the structure of the MutT and 8-oxo-dGTP complex (ES), 8-oxo-dGTP binds to the active site through Na^{+} ions and a water molecule, and the triphosphate moiety

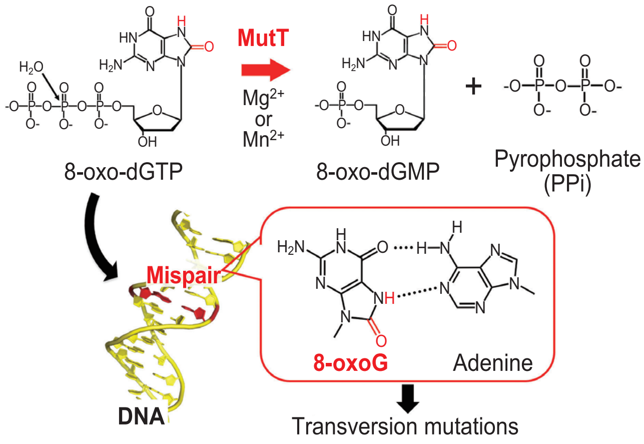

Fig. 1. MutT hydrolyzes 8-oxo-dGTP and prevents transversion mutations caused by the mispairing of 8-oxoG in DNA.

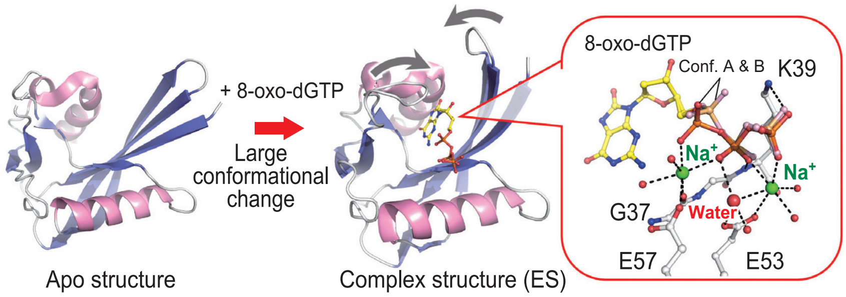

Fig. 2. Crystal structure of the MutT and 8-oxo-dGTP complex.

of 8-oxo-dGTP shows two alternate conformations (Fig. 2). Upon soaking in a solution containing Mn^{2+} ions, three Mn ions bind to the active site, and the triphosphate moiety is aligned for the reaction (left and middle of Fig. 3). Nucleophilic water bridges the two Mn^{2+} ions, at a position appropriate for nucleophilic attack on 8-oxo-dGTP (a red circle and an arrow in the middle of Fig. 3). After nucleophilic attack, 8-oxo-dGTP is hydrolyzed to 8-oxo-dGMP and PPi, and the generated PPi is released with two Mn^{2+} ions (right of Fig. 3). These intermediate structures suggested an activation mechanism of the nucleophilic water. When three Mn^{2+} ions bind to the active site, new electron densities are observed around the Mn^{2+} binding site (pink mesh on the left of Fig. 3). The electron densities would indicate the motion of the water molecule for nucleophilic attack, that is, a water molecule bound to Glu53 in ES (Fig. 2) moves to the position of nucleophilic attack by bridging the two newly arrived Mn^{2+} ions (left and middle of Fig. 3). The motion of the water molecule suggests that Glu53 is involved in the deprotonation of water before nucleophilic attack. Previous kinetic studies also suggested that Glu53 is a general base for catalysis. Alternatively, there is a possibility that water molecules in the bulk solvent are involved in the deprotonation of the nucleophilic water molecule. To further discuss the hydrolytic reaction mechanism in detail, the protonation/deprotonation states in the active site should be investigated by neutron crystallography and/or ultrahigh-resolution X-ray crystallography. In conclusion, MutT hydrolyzes 8-oxo-dGTP via nucleophilic attack by a water molecule activated through the sequential binding of three metal ions. The reaction mechanism of MutT proposed in this study would be shared among some of the Nudix hydrolases.

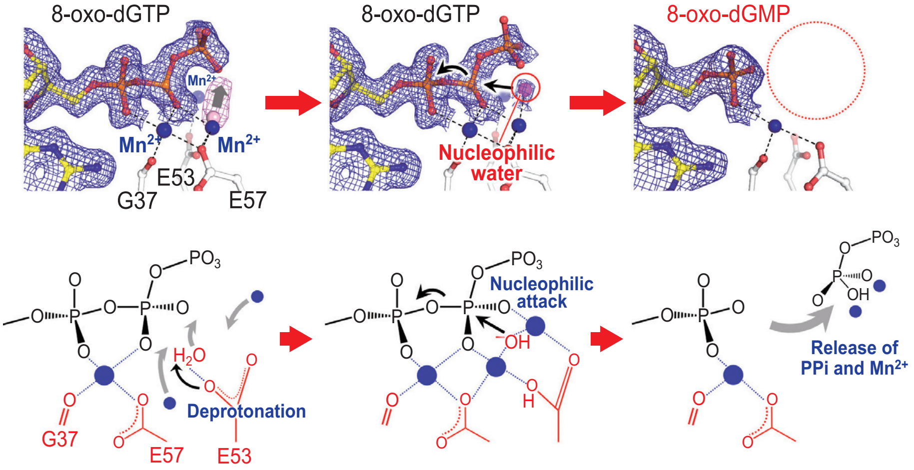

Fig. 3. Structures and electron density maps during the hydrolytic reaction of 8-oxo-dGTP and the proposed mechanism.

Teruya Nakamura

Graduate School of Pharmaceutical Sciences,
Kumamoto University

Email: tnaka@gpo.kumamoto-u.ac.jp

References

[1] T. Nakamura *et al.*: Nature **487** (2012) 196.
[2] T. Nakamura *et al.*: Biophysics **9** (2013) 31.
[3] *T. Nakamura and Y. Yamagata: Proc. Natl. Acad. Sci. USA* ***119*** *(2022) e2203118119.*
[4] H. Maki and M. Sekiguchi: Nature **355** (1992) 273.
[5] T. Nakamura *et al.*: J. Biol. Chem. **285** (2010) 444.

Flavin photoreduction mechanism in a DNA photolyase elucidated by time-resolved X-ray crystallography

DNA photolyases, members of the photolyase-cryptochrome family [1], are light-driven enzymes containing a flavin adenine dinucleotide (FAD) coenzyme (Fig. 1). In the process of photoactivation, two light-triggered single-electron photoreduction steps convert the oxidized chromophore (FAD_{ox}), via the radical semiquinone state ($\text{FAD}^{\bullet-}$ and its subsequently protonated form $\text{FADH}^{\bullet}$), to the reduced hydroquinone state (FADH^{-}) [2]. The electrons fueling the two photoreduction steps are provided by an electron transfer chain consisting of a tryptophan triad, which ultimately extracts an electron from the environment [3], although the precise identity of the *in vivo* electron donor is still unknown [4]. Upon photoactivation, DNA photolyases catalyze blue light-driven DNA repair of UV photolesions, such as cyclobutane pyrimidine dimers (CPD) [1] (Fig. 1).

We determined the 3D structures of reaction intermediates in the light-dependent reduction of a photolyase enzyme from *Methanosarcina mazei*, at atomic resolution [5] (Fig. 2). By using time-resolved crystallography at the SACLA **BL2** beamline, we collected snapshots at different times ranging from 10 ns to 5 ms, resulting in a 3D movie describing these FAD transformations in detail [5] (Fig. 3).

The 3D movie shows that, after the reaction is initiated by blue light, the flat geometry of FAD becomes distorted within nanoseconds, in a motion reminiscent of the fluttering wings of a butterfly (Fig. 2). Meanwhile, nearby amino-acids from the enzyme stabilize and support these movements, allowing the FAD_{ox} to settle into the first semi-stable intermediate, $\text{FAD}^{\bullet-}$, which is characterized by a strong twist (Fig. 3). Unless the protein environment quickly supports the strained geometry of $\text{FAD}^{\bullet-}$, by donating a proton and yielding $\text{FADH}^{\bullet}$, photolyase reverts back to its original FAD_{ox} state within milliseconds. However, if $\text{FADH}^{\bullet}$ is produced, then a second reaction cycle elicits renewed fluttering of the FAD, resulting in the final product, FADH^{-} (Fig. 3).

The protonation of $\text{FAD}^{\bullet-}$ at the *N5* position is essential for photoactivation, as only the neutral semiquinone $\text{FADH}^{\bullet}$ can be further reduced to the active FADH^{-} state (Fig. 3). However, the proton donor and molecular mechanism remain elusive [3]. Our structural data points toward the close involvement of the Arg378-Asp409 salt bridge in this step, as its geometry is strongly affected by the $\text{FAD}^{\bullet-}$ protonation. The Arg378 guanidinium moiety moves away from the isoalloxazine ring after the $\text{FAD}^{\bullet-}$ to $\text{FADH}^{\bullet}$ conversion, reverting to a position similar to the oxidized state (Fig. 2). However, the geometry of the bifurcated salt bridge is altered by this $\text{FAD}^{\bullet-}$ to $\text{FADH}^{\bullet}$ conversion, causing the Arg378 sidechain to break its salt bridge with Asp409 by a swivelling motion (Fig. 2). Our results also provide structural evidence for the stabilization of the protonated state by hydrogen bonding between isoalloxazine *N5* and Asn403 $O\delta 1$, supporting the unusually high pKa for the $\text{FADH}^{\bullet}$ *N5* position in photolyase (Fig. 3). Furthermore, the intensity of the above-mentioned negative difference map peak remained approximately constant, and additional positive and negative peaks surrounding the guanidinium-carboxylate salt bridge appeared. These results, along with the absence of other efficient proton donors or water molecules within 6.5 Å of the isoalloxazine *N5* nitrogen, suggest that Arg378 is the donor for the protonation of $\text{FAD}^{\bullet-}$ to $\text{FADH}^{\bullet}$ (Fig. 3).

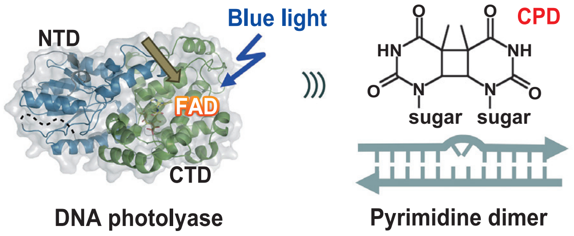

Fig. 1. Light-driven enzymatic catalysis of DNA repair by DNA photolyase. The FAD cofactor, located in the conserved folded structure of photolyase, should be fully reduced by photoreduction by the same blue light, prior to the DNA repair reaction.

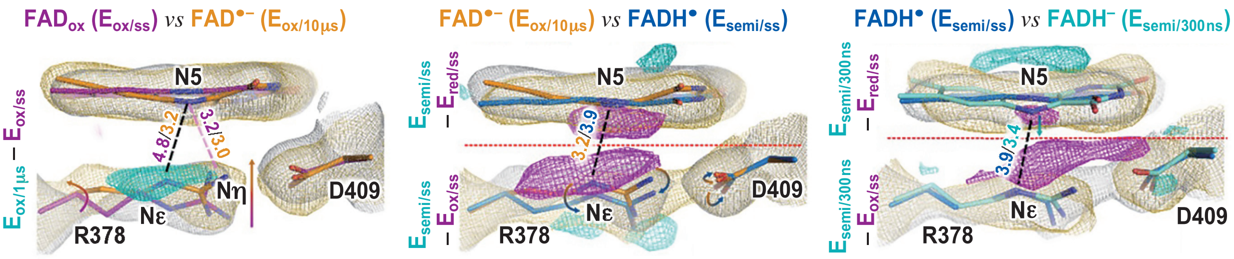

Fig. 2. Details of the FAD reaction in photolyase. Three frames of the 3D molecular movie are shown. Here, gray and yellow meshes represent the electron clouds surrounding the structures of the flavin and neighboring amino-acids, respectively. Meanwhile, the structures are shown as sticks with different colors (purple for the oxidized state, orange for the $FAD^{\bullet -}$ state, dark blue for the $FADH^{\bullet}$ state, and light blue for $FADH^{-}$). Differences between these structures are emphasized by superimpositions. Subtle differences are also highlighted by difference density clouds (magenta for negative clouds, cyan for positive clouds). Difference density clouds result from subtracting the simple electron clouds shown in yellow and gray. Thus, a negative difference density corresponds to regions where electrons disappear during the reaction, while in positive density regions, electrons appear.

Overall, our results show the atomic details of time-dependent structural changes in the photoreduction of FAD, mediated by an FAD redox sensor triad (Arg378, Asn403 and Asp409). The results also demonstrate that an enzyme-catalyzed redox reaction can take nano- to micro-seconds to complete the orbital re-hybridization processes, even though the electron transfer itself is usually faster by at least one order of magnitude. Both represent novel findings for photolyases and redox enzymes in general.

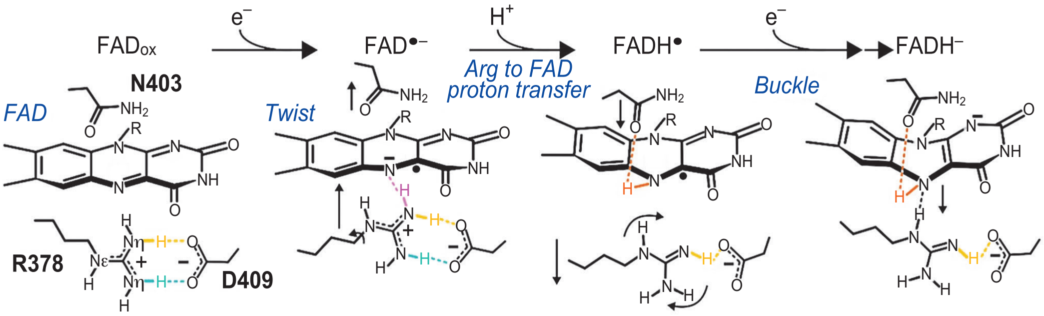

Fig. 3. Schematic representation of the 3D molecular movie. Structural formulas of the FAD and surrounding three amino-acids (R378, N403 and D409) are presented. Covalent interactions are shown as black lines, and non-covalent ones are dotted, colored lines. As the reaction progresses, note how the shape of FAD changes and its interaction network switches between different elements.

Y. Bessho[a,b,*], M. Maestre-Reyna[b,c], L.-O. Essen[d] and M.-D. Tsai[b]

[a] RIKEN SPring-8 Center
[b] Academia Sinica, Taiwan
[c] National Taiwan University, Taiwan
[d] Philipps University Marburg, Germany

*Email: bessho@spring8.or.jp

References

[1] A. Sancar: Angew. Chem. Int. Ed. Engl. (Nobel Lecture) **55** (2016) 8502.
[2] Y. T. Kao *et al.*: J. Am. Chem. Soc. **130** (2008) 13132.
[3] C. Aubert *et al.*: Nature **405** (2000) 586.
[4] E. Ignatz *et al.*: Photochem. Photobiol. **94** (2018) 81.
[5] *M. Maestre-Reyna, C. H. Yang, E. Nango, W. C. Huang, E. P. G. Ngurah-Putu, W. J. Wu, P. H. Wang, S. Franz-Badur, M. Saft, H. J. Emmerich, H. Y. Wu, C. C. Lee, K. F. Huang, Y. K. Chang, J. H. Liao, J. H. Weng, W. Gad, C. W. Chang, A. H. Pang, M. Sugahara, S. Owada, Y. Hosokawa, Y. Joti, A. Yamashita, R. Tanaka, T. Tanaka, F. Luo, K. Tono, K. C. Hsu, S. Kiontke, I. Schapiro, R. Spadaccini, A. Royant, J. Yamamoto, S. Iwata, L. O. Essen, Y. Bessho, M. D. Tsai: Nat. Chem.* ***14*** *(2022) 677.*

Lipid structure in stratum corneum of human skin

The top layer of human skin, stratum corneum (SC), serves as a barrier which protects human body from dehydration and penetration of unwanted substances. SC comprises of inactive cells (corneocytes) in which keratin filaments are densely packed and lipids such as ceramide, cholesterol, fatty acids and glycerides fill the space between the cells (brick-mortar model, Fig. 1). The barrier function is considered to mostly depend on the lipids that fill the gap of less than 50 nm wide. Many studies on the intercellular lipid structure have been carried out using electron microscopy, electron diffraction and X-ray diffraction. However, in most experiments SC was chemically treated to prepare specimens suitable for each technique. Therefore, we performed small-angle X-ray diffraction (SAXD) measurements of SC on intact human skin to examine structure of SC in our body [1].

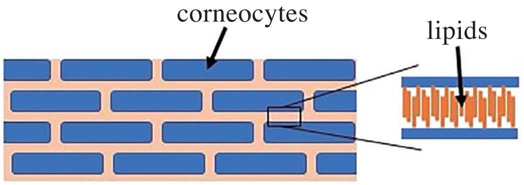

Fig. 1. The so-called brick-and-mortar model of stratum corneum which is 10–20 μm in thickness.

Human skin, obtained in a cosmetic surgery and provided by a supplier, was folded to form a pointed edge. An X-ray microbeam with a diameter of approximately 5 μm [2], obtained with a pinhole at SPring-8 **BL40XU**, was passed at the edge to obtain diffraction from SC so that we could study skin with X-rays under conditions as physiological as possible. The skin was moved so that diffraction patterns from different depths were recorded.

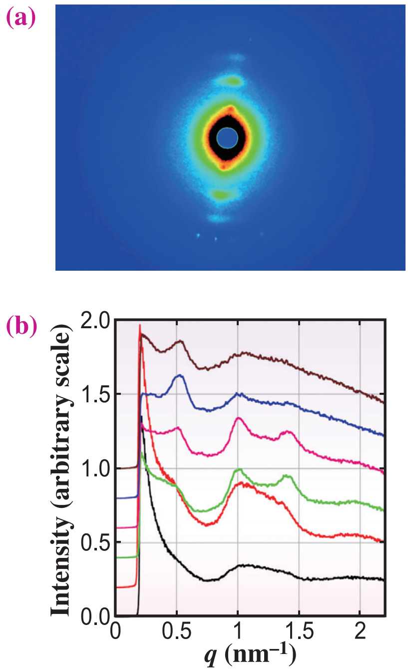

Fig. 2. **(a)** X-ray diffraction from human skin. Skin surface is horizontal. Diffraction spots arise from cholesterol crystals in skin. **(b)** Diffraction profiles at different depths. The sample was raised with 5 μm steps from the black to the brown curve so that the black curve is closest to the skin surface. The profiles are vertically displaced for clarity.

The diffraction pattern in Fig. 2(a) shows three major peaks at $q = 0.51$, 1.03 and 1.4 nm^{-1} ($q = (4\pi/\lambda)\sin(2\theta/2)$ where 2θ is the scattering angle). In most of the typical results obtained in this study, the peaks at $q = 1.03$ and 1.4 nm^{-1} are much stronger than that at $q = 0.51$ nm^{-1} in the region close to the skin surface, while the 0.51 nm^{-1} peak becomes stronger in deeper regions (Fig. 2(b)). When measured at the depth where the peaks are strongest, the ratio of the spacings of the two peaks is close to 2, suggesting that these are the first and second orders of the 12.3 nm periodicity (periodicity d is obtained by $d = 2\pi/q$). Additionally, there is a broad peak at around $q = 2$ nm^{-1} which may be the 4th order of this periodicity. Figure 2(b) clearly shows that the peak at $q = 1.4$ nm^{-1}, which was observed as a shoulder in a previous report on human skin [3], is indeed a separate peak. However, it cannot be indexed on the order of the peak at 1.03 nm^{-1}. The intensity ratios and widths of these peaks vary at different depths of skin.

Based on these experimental results, we attempted to explain them in terms of lipid structure models. To account for the observed diffraction profiles, models of electron density distribution were constructed. These are based on the electron micrographs of Swartzendruber *et al.* [4] but the distance between bands and their heights did not strictly follow the micrographs which were obtained from the sections of chemically fixed, dehydrated, and stained samples. The simplest unit in the model consists of a central density minimum and two minima that were at 5.0 nm on either side of the center with the same depth (Fig. 3(a)). Profiles of all minima were assumed to be Gaussians. Diffraction intensity expected from this unit gives broad peaks at around $q = 0.55$ and 1.1 nm^{-1} (Fig. 3(d)). When two such units were superposed with a separation of 13.0 nm (Fig. 3(b)), the resultant electron density profile resembles a model of tri-lamellar structure (the so-called Landmann unit). X-ray diffraction expected from this structure has peaks at $q = 0.5$, 1.0 and 1.3 nm^{-1} (Fig. 3(d)). With three units (Fig. 3(c)), there are small additional peaks other than the major three peaks (Fig. 3(d)). When the diffraction intensities from the one-, two- and three-unit models were added with a ratio of 3:3:1, the resultant profile (Fig. 3(e)) resembles the observed profile with peaks at $q = 0.56$, 1.04, 1.41 nm^{-1} and a broad baseline between the latter two peaks. This was found to be the best combination to match the experimental profile.

Based on the discussion by Swartzendruber *et al.* [4], the unit in our model represents the corneocyte lipid envelopes and their shared monolayer, while the two-unit model is made of two closely apposed bilayers. It has been shown by electron microscopy that intercellular spaces are mostly filled by either one, two, or three such units. It was indeed found in this study that the X-ray diffraction pattern from SC can be explained by summation of diffraction patterns from different numbers of units. A previous temperature-dependence study on porcine SC suggested that the peaks at $q = 1.0$ and 1.4 nm^{-1} originate from different lipid phases [5]. However, the present simulation demonstrates the possibility that they may arise from a single phase of lipids arranged with two and three repeats of the basic unit. This new interpretation may be used as a basic assumption in interpretation of X-ray diffraction from intact SC.

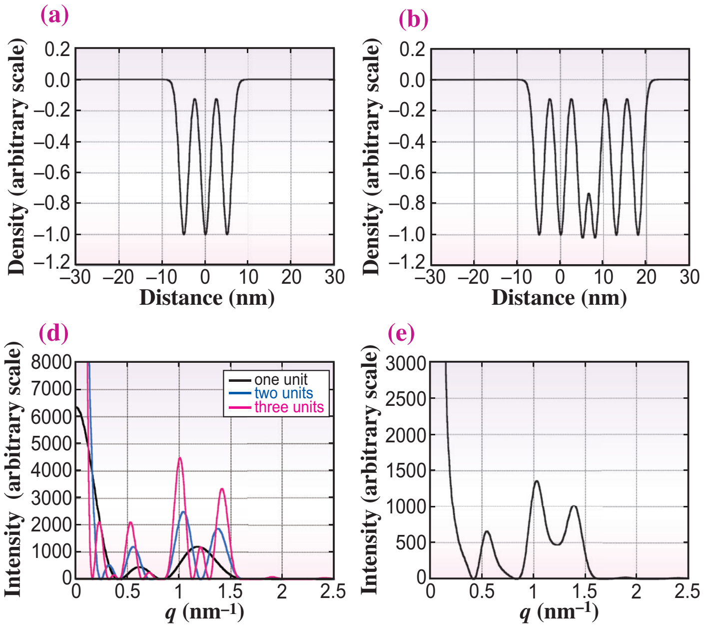

Fig. 3. Electron density models of lipids in SC and calculated diffraction from them. **(a)** An electron density model of one lamellar unit. There is an electron sparse region, corresponding hydrocarbon chains of lipids, in the center and there are two such regions at 5 nm on each side. All low electron density regions are simulated by a Gaussian with a full-width at half maximum of 3.5 nm. **(b)** A model in which the model (a) was duplicated in the right with a shift of 13 nm. **(c)** A model with three identical units. The third unit is shifted by –13 nm from the first unit. **(d)** X-ray diffraction expected from the one-unit model (black), two-unit model (blue) and three-unit model (red). **(e)** Mixture of one-, two-, and three-unit models with a ratio of 3:3:1.

Naoto Yagi*, Koki Aoyama and Noboru Ohta

Japan Synchrotron Radiation Research Institute (JASRI)

*Email: yagi@spring8.or.jp

References

[1] *N. Yagi, K. Aoyama and N. Ohta. PLoS ONE* ***15*** *(2020) e0233131.*
[2] N. Ohta *et al.*: J. Appl. Crystal. **38** (2005) 274.
[3] J. Doucet *et al.*: J. Lipid Res. **55** (2014) 2380.
[4] D. C. Swartzendruber *et al.*: J. Investigative Dermatology **92** (1989) 251.
[5] J. A. Bouwstra *et al.*: Lipid Res. **36** (1995) 685.

Water channel proteins and their role in lens optics and cataract

The eye lens provides one-third of the optical power of the human eye and has the capacity to alter its focus for a range of distances in eyes below the sixth decade of life. It also offers a high level of image quality because of its gradient index structure. The ability to alter focus decreases with age as does the amount and wavelength of light transmitted and the causal factors involved in these losses of function, whilst not conclusively clear, have been linked to changes in the lens proteins. These proteins, the crystallins, are distributed in varying concentrations within long fiber cells that accrue in layers over existing tissue. This concentration gradient creates a gradient of refractive index or GRIN with the highest refractive index in the center gradually decreasing towards the periphery. With age, the proteins alter in their formation and structural relationship with water and this can be detrimental to transparency of the lens, to the GRIN profile and ultimately can lead to cataract.

There is another class of proteins that are less prevalent in the lens, the aquaporins, but have been increasingly recognized as potentially key to lenticular maintenance of water and nutrient transportation [1]. These are membrane proteins and three types of aquaporins are expressed in the human lens: aquaporin 0: located in fiber cells of the lens and a major constituent of cell membrane proteins [1]; aquaporin 1: found in the lens epithelial cells [1] which are adjacent to the anterior surface of the lens capsule within which the lens sits and aquaporin 5 which has been detected in the outer layers of the lens, in the lens epithelium and in mature lens cells [1,2]. Aquaporin 0 proteins also have sub-classes: aquaporin 0a (Aqp0a) and aquaporin 0b (Aqp0b). The former has been shown to contribute to maintaining lens structure by stabilizing the sutures in the anterior lens in older lenses and keeping the nucleus centralized [3]. These structural factors are important for lens optics. However, it is not known whether and how Aqp0a and Aqp0b may to the development of the GRIN profile in the lens.

Recent research conducted at SPring-8 investigated optical properties of lenses with loss-of-function deletions of *aqp0a* and/or *aqp0b* in zebrafish generated using CRISPR/Cas9 gene editing [4]. Mutations considered were single *aqp0a*$^{-/-}$ and *aqp0b*$^{-/-}$ mutants as well as double *aqp0a*$^{-/-}$/*aqp0b*$^{-/-}$ mutants and wild type lenses matched for age. Samples were taken from very early embryonic life to elderly adult stages. The refractive index of each of the lenses was measured using X-ray phase tomography based on X-ray Talbot interferometry which is located at SPring-8 **BL20B2** [4].

Opacities in the lens, manifesting as disruptions to the GRIN profile were seen in lenses from all the aquaporin 0 mutants: *aqp0a*$^{-/-}$ and *aqp0b*$^{-/-}$ and double mutants *aqp0a*$^{-/-}$/*aqp0b*$^{-/-}$ as well as in lenses from very old wild type zebrafish. However, the opacities varied depending on the mutation or whether the lens was from an old wild type zebrafish. Single *aqp0a*$^{-/-}$ mutants had asymmetric GRIN profiles and a shift of the nuclear part of the GRIN towards the anterior of the lens (Fig. 1). In contrast, single *aqp0b*$^{-/-}$ mutants showed no difference in their GRIN profiles to those from wild type lenses in developing and young samples although disruptions to the GRIN were seen in very old *aqp0b*$^{-/-}$ mutant lenses (Fig. 2) and these were similar to features observed in wild type lenses of advanced age. In lenses from zebrafish with double *aqp0a*$^{-/-}$/*aqp0b*$^{-/-}$ mutations, the refractive index magnitudes in the GRIN profiles were lower than in wild type lenses of similar ages and dips in the refractive index were seen in the central plateau region of the GRIN (Fig. 3).

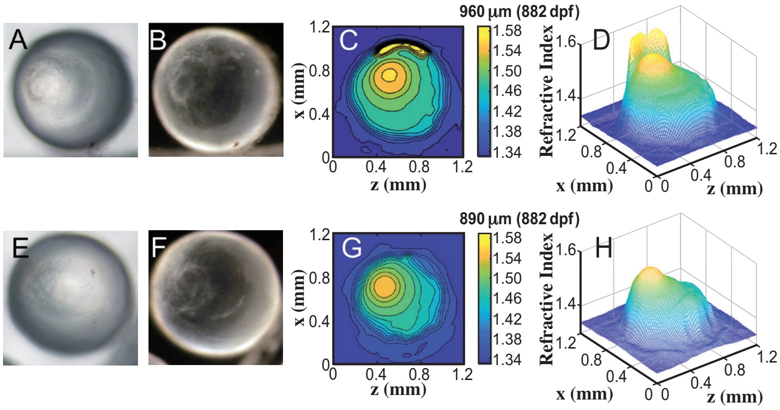

Fig. 1. Anterior polar opacity and asymmetric GRIN profiles in *aqp0a*$^{-/-}$ lens pairs: (A,E) show bright field images and (B,F) dark field images from zebrafish lenses aged 882 days post-fertilization with the corresponding 2D contours in (C,G) and 3D mesh plots of refractive index in (D,H).

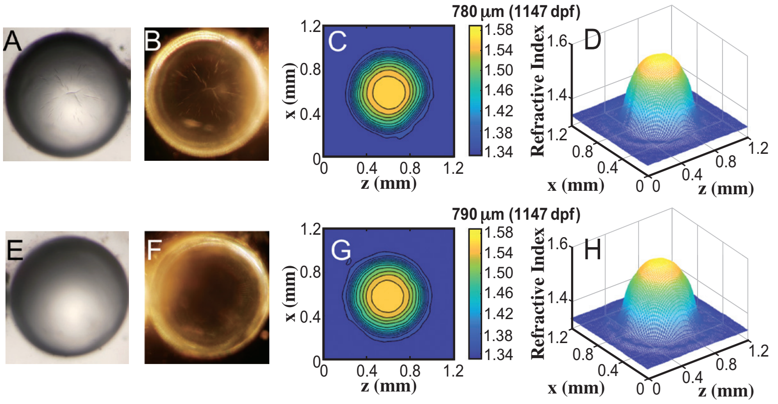

Fig. 2. Spoke cataract and disturbances to GRIN profiles in an old $aqp0b^{-/-}$ lens pairs: (A,E) show bright field images and (B,F) dark field images of lenses of a zebrafish aged 1147 days post-fertilization with the corresponding 2D contours in (C,G) and 3D mesh plots of refractive index in (D,H).

As the lens has no blood vessels, it is entirely reliant on circulation of water to ensure delivery of nutrients and waste removal [5]. This requires a gradient of hydrostatic pressure. The exact contribution of aquaporin 0 to maintaining the pressure gradient is as yet unclear, but the investigations conducted at SPring-8 confirms that this aquaporin has a vital role in ensuring the proper formation of the GRIN and hence is likely to have some impact on the pressure gradient. This research supports the previous findings that Aqp0a [3] plays a role in maintaining centralization of the lens nucleus and therefore symmetry of the GRIN profile. In double mutants, the refractive index magnitude in the center of the GRIN profiles was lower than age-matched wild type lenses, indicating that the high concentration of crystallin proteins critical for the appropriate magnitude of refractive index at the lens center requires presence of at least one of the two subtypes of aquaporin 0. Although aquaporins, as membrane proteins, are not involved in synthesis of the cytosolic crystallin proteins, any changes in water transport resulting from aquaporin absence could cause alterations in crystallin protein-water ratios in the lens center and hence affect the magnitude of refractive index.

The findings of this research indicate that aquaporins have an important role in optics of the lens by creating and maintaining its GRIN. There appear to be regional specificities in the roles of Aqp0a and Aqp0b. Whilst the presence of Aqp0a is needed in the peripheral lens to ensure a symmetrical GRIN profile, its role cannot be compensated by Aqp0b. However, in the lens center, Aqp0b can replace Aqp0a to ensure that the central part of the GRIN is maintained.

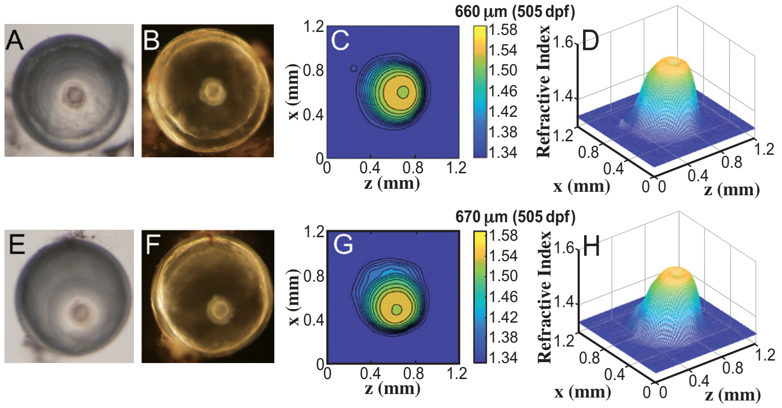

Fig. 3. Nuclear opacity and central dip to GRIN profiles in double $aqp0a^{-/-}/aqp0b^{-/-}$ lens pairs: (A,E) show bright field images and (B,F) dark field images of lenses of a zebrafish aged 505 days post-fertilization with the corresponding 2D contours in (C,G) and 3D mesh plots of refractive index in (D,H).

Barbara K. Pierscionek[a,*], Kehao Wang[b]
and Masato Hoshino[c]

[a] Faculty of Health Education Medicine and Social Care,
Medical Technology Research Centre,
Anglia Ruskin University, UK
[b] Beijing Advanced Innovation Centre for Biomedical Engineering, Beihang University, China
[c] Japan Synchrotron Radiation Research Institute (JASRI)

*Email: barbara.pierscionek@aru.ac.uk

References

[1] K. L. Schey *et al.*: Biochim. Biophys. Acta **1840** (2014) 1513.
[2] A. C. Grey *et al.*: Exp. Eye Res. **108** (2013) 94.
[3] I. Vorontsova *et al.*: Invest. Ophthalmol. Vis. Sci. **59** (2018) 2869.
[4] *K. Wang, I. Vorontsova, M. Hoshino, K. Uesugi, N. Yagi, J. E. Hall, T. F. Schilling and B. K. Pierscionek: Invest. Ophth. Vis. Sci.* ***62*** *(2021) 23.*
[5] R. T. Mathias *et al.*: J. Membr. Biol. **216** (2007) 1.

Nuclear resonance vibrational spectroscopy definition of intermediate Q in methane monooxygenase

Non-heme iron enzymes play a key role in the activation of dioxygen in Nature [1]. Among the strategies for the four-electron activation of O_2, some mononuclear enzymes (e.g., syringomycin halogenase SyrB2) use two electrons from the Fe^{II} center and two electrons from the cofactor α-ketoglutarate, producing a 5-coordinate $Fe^{IV}=O$ intermediate that cleaves the C–H bond of activated substrates (Fig. 1(a)). Alternatively, the two Fe^{II} centers of the binuclear enzyme soluble methane monooxygenase (sMMO) provide all four electrons, producing an Fe^{IV}_2 site able to cleave the strong C-H bond of methane to produce methanol. This high valent intermediate Q has been long studied as its structure informs the design of catalysts for methane oxygenation. Early results assigned Q as a closed core $Fe^{IV}_2(\mu\text{-}O)_2$, later supported by resonance Raman (rR) spectroscopy [2]. In 2010, an open core complex $O=Fe^{IV}–O–Fe^{IV}–OH$ was found to oxidize dihydroanthracene at a rate 100× higher than its closed core $Fe^{IV}_2(\mu\text{-}O)_2$ complex [3] and subsequent high energy resolution fluorescence detected X-ray absorption spectroscopy (HERFD-XAS) studies favored an open core structure [4]. Our study [5] utilized ^{57}Fe Nuclear Resonance Vibrational Spectroscopy (NRVS) to characterize the geometric and electronic structure of intermediate Q, providing insight into the closed vs. open core debate (Fig. 1(b)).

^{57}Fe NRVS is a synchrotron-based technique that detects vibrational modes containing iron motion. The NRVS data are interpreted using Density Functional Theory (DFT) to interrogate the structure of Q. ^{57}Fe NRVS was performed at SPring-8 **BL09XU**, Nuclear Resonant Scattering beamline, using a nuclear resonance energy of 14.4 keV, monochromated to 1.0 meV using both a high-heat-load and high-resolution monochromator. Vibrational sidebands were collected 100 meV above the elastic peak.

The NRVS spectrum of Q exhibited time-dependent changes in the beam. Using Mössbauer spectroscopy, we assigned this decay to cryoreduction of Q. Selective binning of scans from the first 10 hours and after 30 hours of measurement gave the vibrational spectra of Q (early) and cryoreduced Q (late). Figure 2 presents the NRVS spectra of early and late $^{16}O_2$ Q and late $^{18}O_2$ Q. The early Q spectrum shows features at 605, 420, 375, 330, 300 and 275 cm^{-1}, where late Q shows loss of the 605, 375 and 275 cm^{-1} features and growth of new features at 580, 365, 240 and 220 cm^{-1}. Further, two decay features 580 and 420 cm^{-1} show isotope sensitivity (Fig. 2(b) inset).

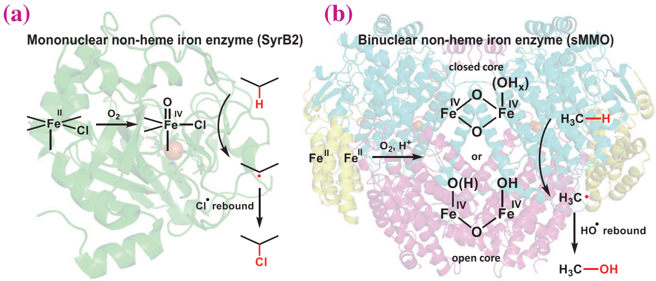

Fig. 1. Reactivity of mononuclear and binuclear non-heme iron enzymes.

90 closed and open core DFT optimized structures of Q were generated and used to simulate the NRVS and prior spectroscopic data. The closed core models contained two bridging $O(H)_x$ and one terminal ligand, while the open core models all contained one oxo bridge, with differing levels of protonation of carboxylate and oxygenic ligands. Comparison of the simulated vibrational spectra of each model to past rR data [2] showed that both open and closed core models could reproduce the experimental data, but eliminated some models. Further, time-dependent DFT analysis investigated which models would show rR enhancement of a 690 cm^{-1} feature by excitation at 351 nm. This analysis excluded all open core models except for those with two terminal hydroxides ($OH–Fe^{IV}–O–Fe^{IV}–OH$) or both a terminal hydroxide and an oxo ($O=Fe^{IV}–O–Fe^{IV}–OH$). For the remaining structural models, the full set of NRVS data (early and late $^{16}O_2$, late $^{18}O_2$) were simulated and compared to experimental NRVS data.

Figure 3 shows the NRVS simulations of open (a) and closed (b) core models that were the best simulations of the experimental data. The top panels display the experimental data, the middle panels show simulations of the early and late $^{16}O_2$ data, and the bottom panel compares simulations of the $^{16}O_2$ and $^{18}O_2$ late data. Figure 3(a) shows simulations for the closed core model containing a bis-μ-oxo core and a terminal hydroxide (bis(μO)–OH-12). Simulations to the low energy region (<450 cm^{-1}) are in good agreement with the experimental data. Further, the small $^{16/18}O_2$ isotope sensitivity of the experimental decay data is well reproduced due to the longer Fe-OH bond which dictates the magnitude of this isotope shift. Figure 3(b) displays simulations for the best open core model, $O=Fe^{IV}–O–Fe^{IV}–OH$ model (OC16). Comparison of the low energy region again shows good agreement to experiment, however, the simulations fail to reproduce

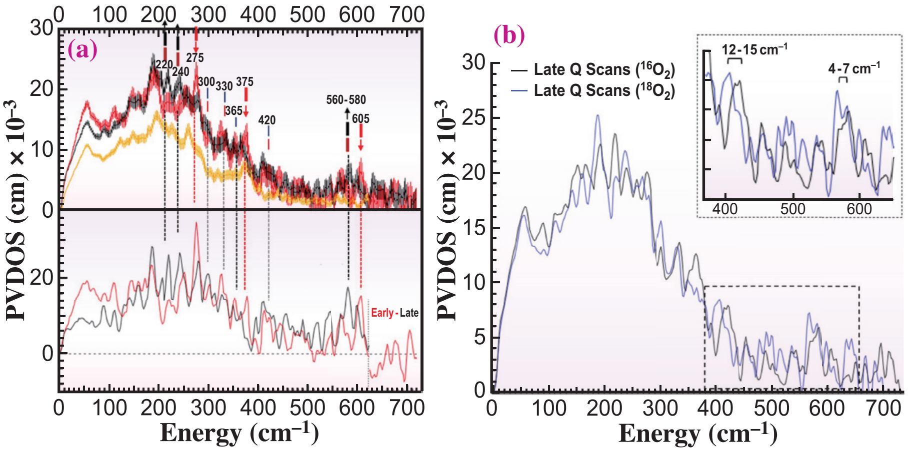

Fig. 2. NRVS spectra of Q: (**a** top) $^{16}O_2$ early (red), late (black) and $Fe^{II}Fe^{II}$ reactant species (yellow), (**a** bottom) spectra corrected for residual $Fe^{II}Fe^{II}$. (**b**) $^{16}O_2$ (black) and $^{18}O_2$ (blue) late Q with isotope sensitive features (inset).

the small magnitude of the isotope shift in the late data and this and other open core structural models were eliminated. Thus, the NRVS data on Q from SPring-8 show that the closed but not the open core structure is supported by the experiment.

Experimentally, intermediate Q in the binuclear sMMO enzyme performs hydrogen atom abstraction (HAA) from methane with a $\Delta G^‡$ of 10.3 kcal/mol, while the $Fe^{IV}O$ intermediate of the mononuclear enzyme SyrB2 has a $\Delta G^‡$ of 17.7 kcal/mol for its substrate threonine. Correcting for the difference in bond strength of the substrates, SyrB2's $\Delta G^‡$ for methane would be 24 kcal/mol. DFT calculations on the Q models give a barrier for a closed core of 12.4 kcal/mol (close to experiment), while the open core $O{=}Fe^{IV}{-}O{-}Fe^{IV}{-}OH$ and mononuclear $Fe^{IV}O$ sites are calculated to be 25.0 and 22.1 kcal/mol respectively. The low barrier for the closed core is due to the greater thermodynamic driving force associated with the reorganization of the resulting $Fe^{III}Fe^{IV}$(μ-O)(μ-OH) closed core, enabling efficient reactivity of sMMO in the conversion of methane to methanol.

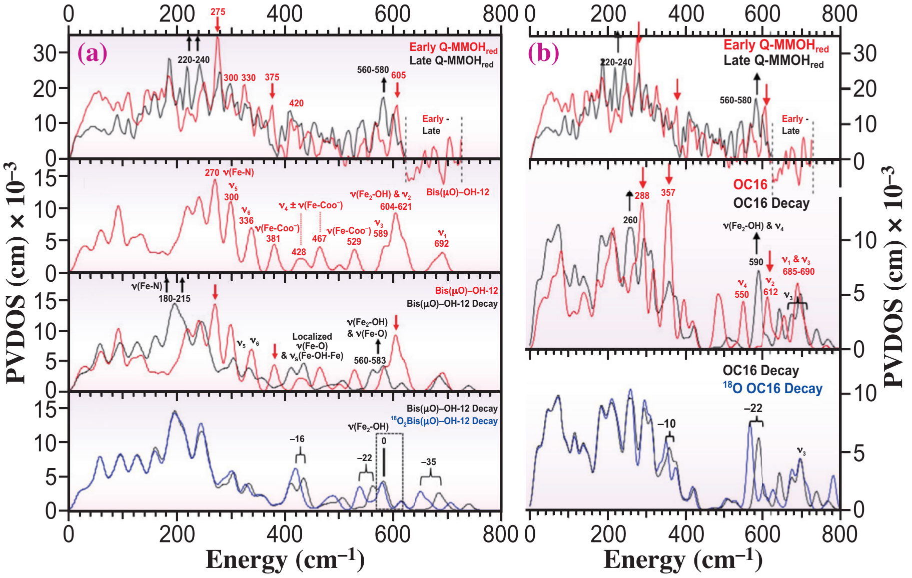

Fig. 3. Model simulations: top panel: experimental data, middle panels: simulations of the early (red) and late (black) $^{16}O_2$ data, bottom panel: simulations of the $^{16}O_2$ and $^{18}O_2$ late (blue) data (**a**) representative closed core model (bis(μO)–OH-12) (**b**) Best open core model (OC16).

Dory E. DeWeese, Augustin Braun and Edward I. Solomon*

Department of Chemistry Stanford University, USA

*Email: edward.solomon@stanford.edu

References

[1] E. I. Solomon *et al*.: Chem. Rev. **100** (2000) 235.
[2] R. Banerjee *et al*.: Nature **518** (2015) 431.
[3] G. Xue *et al*.: Nat. Chem. **2** (2010) 400.
[4] G. E. Cutsail *et al*.: J. Am. Chem. Soc. **140** (2018) 16807.
[5] *A. B. Jacobs, R. Banerjee, D. E. Deweese, A. Braun, J. T. Babicz Jr., L. B. Gee, K. D. Sutherlin, L. H. Böttger, Y. Yoda, M. Saito, S. Kitao, Y. Kobayashi, M. Seto, K. Tamasaku, J. D. Lipscomb, K. Park and E. I. Solomon: J. Am. Chem. Soc.* ***143*** *(2021) 16007.*

Unveiling an enigmatic fossil vertebrate from the Middle Devonian

The evolutionary history in deep time has long been the frontier of natural science. The fossil record provides the sole physical evidence for evolutionary processes and biodiversities in the past, but our understanding of fossil species is still far from sufficiency. It sometimes happens that an enigmatic fossil species cannot be compared with other known species owing to its very strange, incomprehensible body form. Such an enigma lasts for a long time until a breakthrough in paleontology.

Palaeospondylus gunni represents such an enigma. This species was first reported in 1890 [1] and is found in the Middle Devonian (about 390 million years ago) deep lacustrine deposits [2]. Thus far, thousands of specimens of *Palaeospondylus* have been collected, but this species remained mysterious, making its classification very difficult. This small (about 5 cm in body length) fishlike creature appears not to possess paired fins, unlike most extant fishes. Teeth are also lacking. In addition, the cranial dermal bones that cover the brain and sensory organs in most vertebrates are missing from *Palaeospondylus*. These features imply that this species possesses a "primitive" type of body and belongs to the lineage of cyclostomes, a jawless vertebrate group that diverged from the lineage of most vertebrates around 500 million years ago. On the other hand, *Palaeospondylus*, whose name stands for "ancient vertebrae", is furnished with well-developed vertebrae. Since distinct vertebrae are seen in evolutionarily new groups of vertebrates, such as teleost fishes and tetrapods, this feature contradicts a close relationship to cyclostomes.

The Devonian period was "the age of fishes", in which the early evolutions of, for example, sharks and bony fishes, ancestors of terrestrial vertebrates, proceeded to build the morphological diversity seen at the present time. Thus, if the enigmatic Middle Devonian *Palaeospondylus* belongs to any group, it will provide an important clue to understanding the early evolution of that group.

One reason for the lack of clarity regarding the phylogenetic position of *Palaeospondylus* is that, despite improvements in observation techniques, it has been unclear what parts the skull is divided into because the boundaries of the joints could not be clearly observed. We successfully solved this problem by strategically preparing the best specimens and ultrahigh-resolution, high-contrast conditions: we searched for extremely rare fossils where skulls were completely covered by the matrix rock, to observe the skeleton inside the rock by X-ray CT imaging. Normally, the rock is split up on the surface where the fossil is located, but in this case, we wanted to examine completely intact skulls, so we found two specimens with only the heads covered by rock (Fig. 1). We then performed synchrotron radiation X-ray micro-computed tomography (SRXμCT) at SPring-8 **BL20B2** [3].

The specimens were first scanned with conventional micro-CT to detect the positions of skulls within the rocks. Then, the specimens were trimmed stepwise to reduce their sizes to obtain higher resolutions at SRXμCT. As a result, we were able to observe complete skulls showing a detailed morphology inside the rock at resolutions of up to 1.46 μm per pixel (Fig. 2(a)). The valuable 3D morphological data obtained in this research has also been published in the database MorphoSource (https://www.morphosource.org) and made available to researchers around the world.

The key point of this research is that we were able to observe even the microstructures inside the skeletal elements in three dimensions. In particular, the spaces housing cells, or cell lacunae (Fig. 2(b)), were clearly recognizable. Detailed observations revealed that the histological features of the *Palaeospondylus* skull elements were comparable to those found in living bony fishes and tetrapods. By following the cell lacunae on the tomographic images, it was possible to determine the locations of boundaries between skeletal elements.

The morphology of each skeletal element of the *Palaeospondylus* skull can now be compared with that of other vertebrates. For example, a close examination of the occipital part of the skull revealed

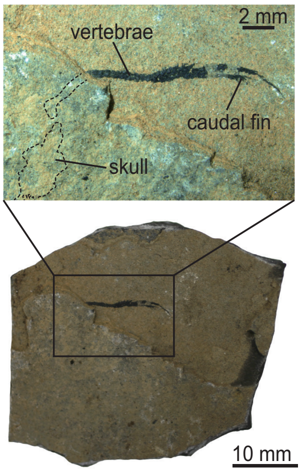

Fig. 1. Fossil specimen of *Palaeospondylus gunni*, NSMPV 24679, from the Middle Devonian of Scotland (now at the National Museum of Nature and Science, Tsukuba, Japan). Rare specimen with only the skull covered by rock.

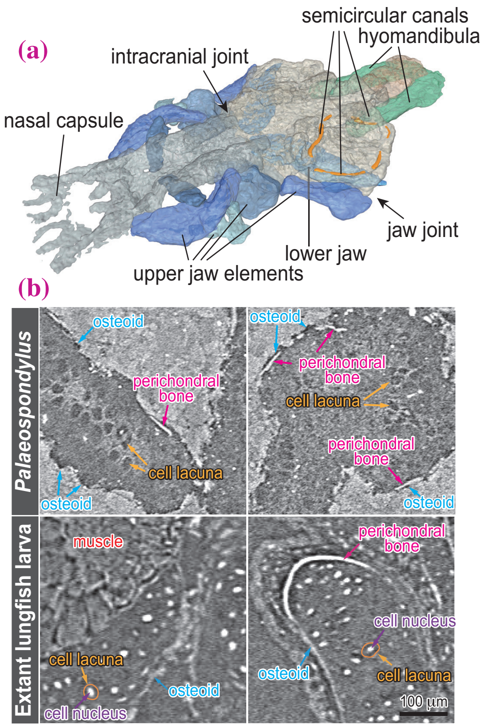

Fig. 2. (**a**) Skull of *Palaeospondylus*. (**b**) Skeletal histologies of *Palaeospondylus* and the extant sarcopterygian *Neoceratodus forsteri* (Australian lungfish).

three tubes where the three semicircular canals used to be housed (Fig. 2(a)), providing definitive evidence that *Palaeospondylus* is among the jawed, rather than jawless vertebrates. Among the many other morphological features revealed, one of the most surprising was the presence of an intracranial joint, which divided the skull into two (Fig. 2(a)). This intracranial joint is a feature shared with sarcopterygian vertebrates, the lineage consisting of coelacanths, lungfishes, and tetrapods. In addition, some other features of *Palaeospondylus* were shared with tetrapods among sarcopterygians.

These morphological characteristics enable the phylogenetic analyses of *Palaeospondylus* for the first time since its discovery in 1890, eventually placing this species within the lineage of tetrapods (Fig. 3). The Devonian period was a time when vertebrates began their forays onto land, and some tetrapods, such as *Eusthenopteron*, of this period possessed fins instead of limbs, despite the name of the group. The results of our phylogenetic analyses demonstrated that *Palaeospondylus* was likely closer to tetrapods possessing either limbs or limb-like fins, such as *Acanthostega*, *Elpistostege*, and *Tiktaalik*, than to tetrapods possessing fish fins, such as *Eusthenopteron*. The enigmatic *Palaeospondylus* was, to the best of our current knowledge, a member of the lineage of our ancestors expanding onto land. The absence of teeth, cranial dermal bones, and paired appendages in *Palaeospondylus* suggests that the morphotype of this species is comparable to that of the larvae of tetrapods. The combination of the larval-like body plan and the relatively short jaw resulted in the retracted mouth opening of *Palaeospondylus* (Fig. 3), the latter of which is seen in only limited species of tetrapods (among living tetrapods, some caecilians have a similar proportion), had probably been an obstacle to the classification of *Palaeospondylus*, as it rendered a very strange, incomprehensible impression.

Although the question of whether *Palaeospondylus* was a true larva or merely a larval-like form remains, our finding is expected to make a significant contribution to the overall picture of the evolutionary history of vertebrates over a period of 500 million years.

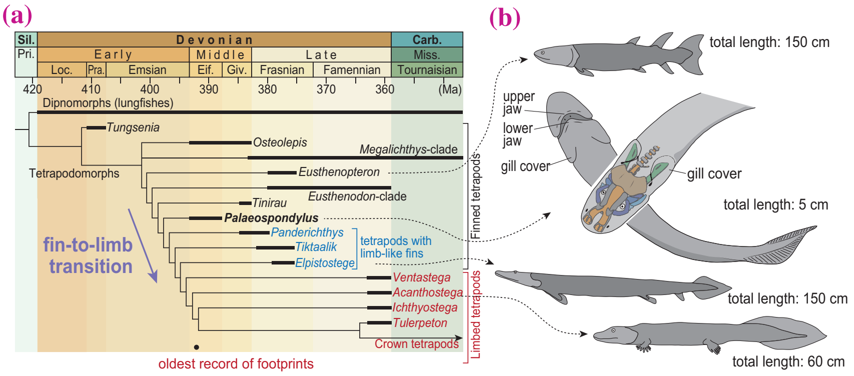

Fig. 3. (**a**) Phylogenetic position of *Palaeospondylus*. Bold lines show ages of fossils of corresponding taxa. Carb., Carboniferous; Eif., Eifelian; Giv., Givetian; Loc., Lochkovian; Miss., Mississippian; Pra., Pragian; Pri., Pridoli; Sil., Silurian. (**b**) Life restorations of Devonian tetrapods. From top to bottom, *Eusthenopteron*, *Palaeospondylus*, *Elpistostege*, and *Acanthostega*.

Tatsuya Hirasawa[a,b]

[a] Department of Earth and Planetary Science, The University of Tokyo
[b] Evolutionary Morphology Laboratory, RIKEN Cluster for Pioneering Research

Email: hirasawa@eps.s.u-tokyo.ac.jp

References

[1] R. H. Traquair: Ann. Mag. Nat. Hist. **6** (1890) 479.
[2] N. H. Trewin: Trans. R. Soc. Edinb. Earth Sci. **77** (1986) 21.
[3] *T. Hirasawa, Y. Hu, K. Uesugi, M. Hoshino, M. Manabe, S. Kuratani: Nature **606** (2022) 109.*

MEM electron density and 3D-ΔPDF study of disorder in thermoelectric InTe

Thermoelectric materials can interconvert heat and electricity, and thus they can harvest waste heat as a contribution to the green transition. The thermoelectric figure of merit is defined as $zT = \alpha^2\sigma\ T/\kappa$, where α, σ, T, and κ are the Seebeck coefficient, electrical conductivity, absolute temperature, and thermal conductivity, respectively. Recently, significant progress in zT values has been achieved, but it is noteworthy that no new materials have reached the market due to problems with materials stability under the harsh operating conditions of a thermoelectric module [1]. A main challenge for developing a high zT is that the physical properties α, σ and κ are inter-connected and many materials design strategies have been introduced over the years to tackle this challenge. The thermal conductivity should be as low as possible and it has two contributions; one from the charge carriers and the other from the crystal lattice. The latter can be lowered through structural disorder due to interstitial, disordered, and diffusive atoms. Disorder is well known in complex thermoelectric materials such as Zn_4Sb_3 [2] but it is rarely seen in simple crystal structures. We have combined single-crystal synchrotron X-ray diffraction, diffuse scattering, the maximum entropy method, the 3D-ΔPDF method, physical property measurements and theoretical calculations, to observe and characterize one-dimensional disordered In^{1+} chains in InTe [3]. The crystal structure contains a significant In^{1+} vacancy along with interstitial indium sites. Intriguingly, the disordered In^{1+} chains undergo a static-dynamic transition with increasing temperature to form a one-dimensional diffusion channel. The present work provides an experimental basis for understanding ultralow thermal conductivity in a broad range of thermoelectric materials.

InTe has ultralow thermal conductivity [3], which is much lower than for famous thermoelectric binary tellurides such as PbTe and Bi_2Te_3. It crystallizes in the TlSe-type structure and it can be described by the formula $In^{1+}In^{3+}Te_2^{2-}$. The In^{3+} ions are tetrahedrally coordinated to Te^{2-} ions forming $(InTe_2)^-$ chains along the c axis while the In^{1+} ions with $5s^2$ lone pair electrons are weakly bound to a cage-like system of eight Te atoms with the square anti-prismatic arrangement (Fig. 1). Using the Bridgman method, we synthesized high quality single crystals and measured accurate single crystal X-ray scattering data at SPring-8 **BL02B1** using a high photon energy of 50.00 keV. X-ray diffraction data at 25 K had a resolution of $\sin\theta/\lambda < 1.67$ Å^{-1} and structure factors were used for Maximum Entropy Method (MEM) calculations to reconstruct the average electron density in the unit cell of the crystal [4].

The MEM electron density reveals two interstitial sites with low occupancy along the c direction, Fig. 1. Since the additional sites are close to the main In^{1+} site, vacancies must also be present on the main site. Structural refinement of a model with In^{1+} vacancies and two interstitial sites lead to an overall composition of $In_{0.98}Te$ in perfect agreement with ICP-OES data. The new structural model leads to a drop in R_F from 2.54% to 1.33%. The observed In^{1+} vacancy agrees with formation energy calculations of native defects in InTe using density functional theory, and it explains the persistent p-type behavior of InTe.

We further conducted MEM calculations based on the single crystals data at 100–700 K, Fig. 2. With increasing temperature, the In^{1+} and interstitial In sites become delocalized and eventually form a continuous 1D channel along the c directions. At 25 and 100 K, two well separated interstitial sites are seen, but at 200 K the In^{1+} density merges with one interstitial.

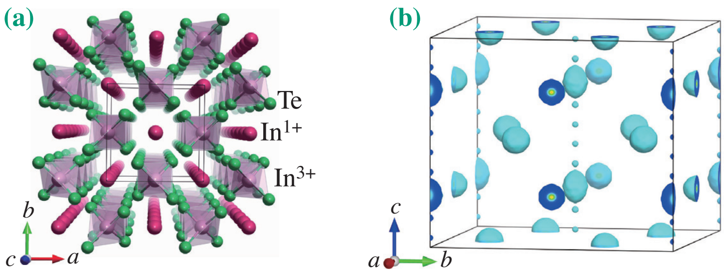

Fig. 1. (**a**) The ideal crystal structure of InTe along the c axis. (**b**) Reconstructed 3D electron density distribution of InTe by the MEM based on the high-resolution single-crystal synchrotron X-ray diffraction data at 25 K. The isosurface value is 15 e Å^{-3}.

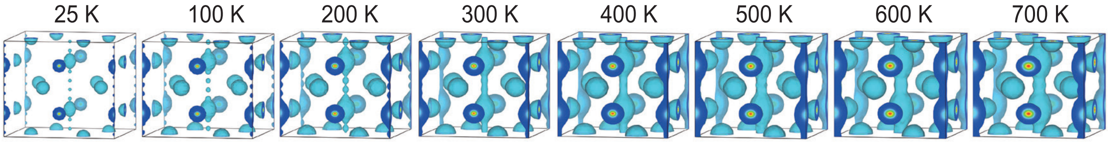

Fig. 2. Temperature-dependent 3D MEM electron density maps of InTe at 25–700 K.

As the temperature increases further a continuous 1D density channel forms along the *c* direction. From the time-space averaged MEM density, we cannot determine whether this dynamic behavior is induced by thermal disorder or dynamic positional disorder. However, the continuous 1D MEM density reveals that In^{1+} can diffuse or hop between sites. The diffusion/hopping increases with increasing temperatures, but it is not very high as the density value at 700 K is only ~5.3% of the maximum In^{1+} peak value.

The local structural order was investigated through diffuse X-ray scattering and 3D-ΔPDF analysis [5]. The 3D-ΔPDF shows which interatomic vectors are more or less present in the real structure compared to the average crystal structure. At 25 K there are strong correlations along *z*, but they become weaker at 300 K. Thus, the defects are strongly correlated along the 1D chains at low temperatures, but less so at higher temperatures, Fig. 3. At 25 K a positive peak observed at 5.8 Å corresponding to the In$_i$(1) and an In$_i$(2) separation, which suggests the Frenkel pairs tend to be separated by this distance at low temperature.

The disordered In^{1+} ions contribute to the ultralow lattice thermal conductivity in InTe. The nearly temperature-independent behavior (~$T^{-0.1}$) in thermal conductivity at ~25–80 K may be attributed to the disorder revealed by the MEM density and 3D-ΔPDF. With increasing temperature the intrinsic phonon-phonon scattering becomes dominant, but the thermal conductivity has a weaker temperature dependence than expected probably due to the tunneling contribution from interstitial, disordered, diffusive In^{1+} ions. The detailed description of structural disorder in InTe is helpful for developing models to understand ultralow thermal conductivity.

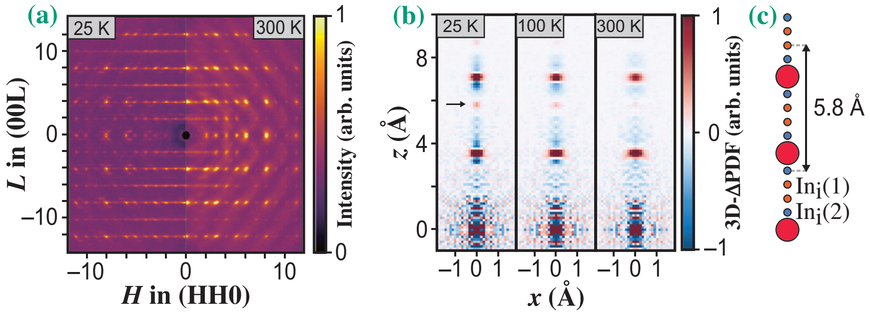

Fig. 3. (**a**) Measured diffuse X-ray scattering of InTe in the *HHL* plane at 25 and 300 K. (**b**) The 3D-ΔPDF along *z* at 25, 100 and 300 K. (**c**) Illustration of the 1D In^{1+} chain with the characteristic distance between interstitial sites marked, corresponding to the positive peak marked in (b) by a black arrow.

Jiawei Zhang[a], Eiji Nishibori[b] and Bo B. Iversen[a,*]

[a] Center for Integrated Materials Research,
Dept. Chemistry and iNANO, Aarhus University, Denmark
[b] Faculty of Pure and Applied Sciences and Tsukuba Research
Center for Energy Materials Science (TREMS),
University of Tsukuba

*Email: bo@chem.au.dk

References

[1] L. R. Jørgensen and B. B. Iversen: Dalton Trans. **51** (2022) 3807.
[2] G. J. Snyder *et al.*: Nat. Mater. **3** (2004) 458.
[3] *J. Zhang, N. Roth, K. Tolborg, S. Takahashi, L. Song, M. Bondesgaard, E. Nishibori and B. B. Iversen: Nat. Commun.* ***12*** *(2021) 6709.*
[4] D. M. Collins: Nature **298** (1982) 49.
[5] N. Roth and B. B. Iversen: Acta Crystallogr. A **75** (2019) 465.

Experimental determination of electron states with orbital degrees of freedom

The orbital degree of freedom plays an important role in strongly correlated materials. Several direct observation methods of electron orbitals have been proposed, but they usually focus on the orbital ordered or stable state, and there are few reports on the observation of the degenerate orbitals. Even first-principles calculations cannot easily determine metastable states at finite temperatures. Therefore, the electron state in degenerate orbitals is only vaguely understood.

Recently, our group has proposed the core differential Fourier synthesis (CDFS) method [1]. It allows the direct observation of the 3D distribution of the valence electron density (VED) by synchrotron X-ray diffraction (XRD). It has been successfully applied to determine the electron density in the orbital ordered state and reported in the Research Frontiers 2020. In the work discussed here [2], we used it to determine the electron state with orbital degrees of freedom through the VED distribution.

We investigated the orbital state of vanadium spinel oxide FeV_2O_4. In this system, despite the lack of charge degrees of freedom due to the Mott insulator, both electronic correlations and geometric frustration are present, resulting in an interplay between the different degrees of freedom, such as spin, orbital, and lattice, which leads to three successive phase transitions with decreasing temperature [3]. Although there has been much discussion on the origin of the phase transition, mainly focusing on the orbital ordered state of V, there are few reports of the definitive determination of the electronic state of the high-symmetry cubic phase.

In FeV_2O_4, because the formal charges of Fe and V are +2 and +3, the electron configurations are $3d^6$ and $3d^2$, respectively. The space group of the cubic phase is $Fd\bar{3}m$, and because FeO_4 is a regular tetrahedron, the electron configuration of Fe^{2+} is $e^3t_2^3$. Owing to the high-spin configuration, one electron on the e orbital is responsible for the orbital degree of freedom (Fig. 1(b)). By contrast, the octahedral site of VO_6 has inversion symmetry, and the $3d$ orbitals of V^{3+} are divided into lower triply degenerate t_{2g} orbitals and higher doubly degenerate e_g orbitals. If VO_6 forms a regular octahedron (O_h), then $3d^2$ electrons occupy t_{2g} in a high-spin configuration (Fig. 1(b)), and V^{3+} has spin and orbital degrees of freedom. Therefore, the FeV_2O_4 system in the cubic phase has spin and orbital degrees of freedom at both the Fe^{2+} and V^{3+} sites. However, the $3d$ state is complicated because of a slight D_{3d} distortion in the VO_6 octahedron.

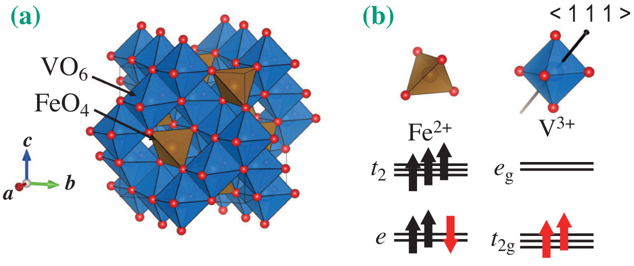

Fig. 1. **(a)** Crystal structure of FeV_2O_4 in the cubic phase. **(b)** Orbital states of V and Fe in the cubic phase. The black arrow in VO_6 indicates the <1 1 1> direction.

The triply degenerate t_{2g} orbitals are further split into one orbital (φ_1) and degenerate orbitals (φ_2 and φ_3) by the crystal field formed by the surrounding oxygen. However, it is not clear which energy level is higher, φ_1 or degenerate orbitals. It is important to note that the triple degeneracy of the t_{2g} orbitals is maintained when the effect of the D_{3d}-type strain is very weak compared with that of the thermal fluctuation. Therefore, we attempted to determine the correct orbital state from the 3D distribution of VED obtained by the CDFS method.

XRD experiments were performed using single crystals at SPring-8 **BL02B1**. Figure 2(d) shows the observed VED around the V (1/2 1/2 1/2) site at 160 K. The VED around the V site is clearly anisotropic. This VED directly reflects the anisotropy of the $3d^2$ electrons.

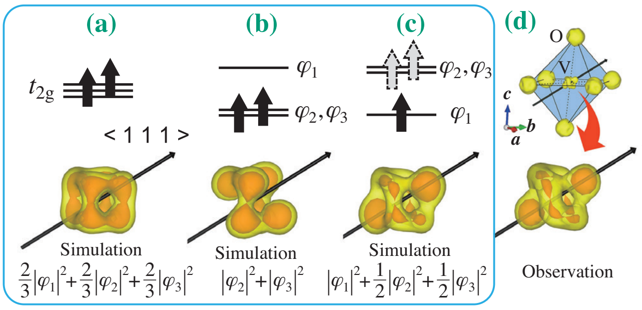

Fig. 2. **(a–c)** Assumed electron configurations and simulated VEDs of V site. The red part of the VED highlights the characteristic components. The gray dotted arrows in (c) indicate that one electron on double degenerate orbitals occupies both orbitals with equal probability. **(d)** (upper panel) Observed VED of VO6 octahedron with internal coordinates (1/2 1/2 1/2) (isosurface level 4.5e/Å^3). The solid line indicates the octahedron and the dotted line indicates the V–O bonds. (lower panel) Observed VED at V site (isosurface level 4.5e/Å^3 (yellow) and 5.3e/Å^3 (orange)).

First, we assumed three orbital states as mentioned above, but the VEDs simulated simply from these states did not reproduce the observed one well (Figs. 2(a,b)). However, we found another possible orbital state where φ_1 was stabilized. In general, the energy gap of the t_{2g} orbitals due to the D_{3d} distortion is small, and Hund's rules are considered. In this case, one electron occupied the lower φ_1 and the other one was lifted to the degenerate orbitals. The simulation $|\varphi_1|^2 + \frac{1}{2}|\varphi_2|^2 + \frac{1}{2}|\varphi_3|^2$ resulted in the VED distribution shown in Fig. 2(c), which perfectly reproduced the experimental result. It is noted that we also succeeded in determining the orbital state at the Fe site. VED analysis by the CDFS method revealed that the degenerate orbitals reflect the anisotropy of their constituent orbitals in the cubic phase.

Here, we reconsider the degenerate orbital. We find that the wavefunctions can also be represented with an arbitrary value of phase θ as

$$\begin{cases} \varphi_2'(\boldsymbol{r}) = \varphi_2(\boldsymbol{r})\cos\theta(\boldsymbol{r},t) + \varphi_3(\boldsymbol{r})\sin\theta(\boldsymbol{r},t) \\ \varphi_3'(\boldsymbol{r}) = -\varphi_2(\boldsymbol{r})\sin\theta(\boldsymbol{r},t) + \varphi_3(\boldsymbol{r})\cos\theta(\boldsymbol{r},t) \end{cases}$$

Orbital degrees of freedom mean that θ fluctuates in space and time. However, from the diffraction data, it is not clear that θ fluctuates in space and time because the VED obtained by XRD measurements is both space- and time-averaged. In fact, assuming an orbital glass state with θ distributed in the whole crystal only spatially, the experimental results can also be reproduced from the θ spatial average.

$$\frac{1}{2\pi}\int_0^{2\pi}\left(|\varphi_1|^2 + |\varphi_2\cos\theta + \varphi_3\sin\theta|^2\right)d\theta = |\varphi_1|^2 + \frac{1}{2}|\varphi_2|^2 + \frac{1}{2}|\varphi_3|^2$$

Therefore, we investigated the dynamics of FeV_2O_4 through phonons to confirm that θ fluctuates in space and time. If θ fluctuates in time, we expect that electron-phonon coupling will allow the electron orbital fluctuations to affect the phonon behavior. In particular, phonon softening might be observed toward the phase transition where orbital fluctuations are eliminated. Therefore, we performed inelastic X-ray scattering (IXS) at SPring-8 **BL43LXU**. The softening of the transverse acoustic (TA) mode dispersing along the [1 1 0] and polarized along [–1 1 0] was clearly observed, as shown in Fig. 3. The symmetry of this TA mode is E_g, which means θ fluctuations. Also, as shown in the dispersion diagram of the E_g TA mode in Fig. 3(c), the softening of the E_g TA mode was observed up to $q \sim 0.7$ r.l.u. This softening is different from the usual precursor phenomenon of structural phase transitions but resembles the nematic state of iron-based superconductors, in which orbital degrees of freedom play an important role [4].

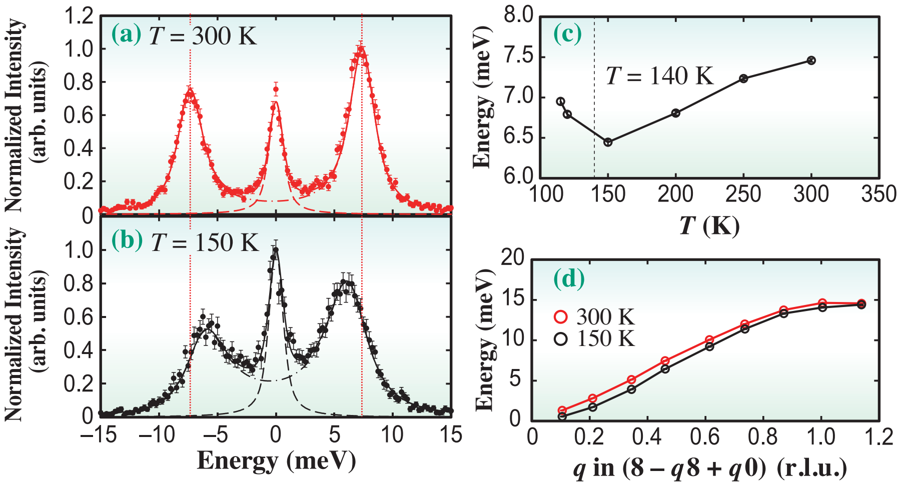

Fig. 3. Energy scan data at Q = (7.54 8.45 –0.03) at **(a)** 300 K and **(b)** 150 K. Phonon peaks correspond to the E_g TA mode. Solid lines indicate the results of fitting using two lines, corresponding to an elastic peak (dashed line) and a pair of phonon peaks (dash-dotted line). The vertical dotted line indicates the phonon energy at 300 K. **(c)** Temperature dependence of the phonon energy at Q = (7.54 8.45 –0.03). **(d)** Phonon dispersions of the E_g TA mode at 300 K and 150 K.

Taishun Manjo[a,*] and Hiroshi Sawa[b]

[a] Japan Synchrotron Radiation Research Institute (JASRI)
[b] Department of Applied Physics, Nagoya University

*Email: manjo.taishun@spring8.or.jp

References

[1] S. Kitou *et al.*: Phys. Rev. Res. **2** (2020) 033503.
[2] *T. Manjo, S. Kitou, N. Katayama, S. Nakamura, T. Katsufuji, Y. Nii, T. Arima, J. Nasu, T. Hasegawa, K. Sugimoto, D. Ishikawa, A. Q. R. Baron and H. Sawa: Mater. Adv.* **3** *(2022) 3192.*
[3] Y. Nii *et al.*: Phys. Rev. B **86** (2012) 125142.
[4] A.M. Merritt *et al.*: Phys. Rev. Lett. **124** (2020) 157001.

Multimodal assessment of mechanically induced transformation in TRIP steel using X-ray micro- and nano-CT and pencil-beam XRD-CT

There has been growing interest in multi-phase steels with meta-stable retained austenite. The retained austenite phase, which is embedded as a minor phase in a ferrite-based microstructure, is stable at room temperature. The retained austenite phase transforms into martensite with volume expansion under external loading, which has a beneficial effect on the strength-ductility balance of multi-phase steels. In retained austenite steels, traditional metallographic preparation, such as cutting and polishing, inevitably introduces austenite-to-martensite transformation due to plastic deformation. A great deal of work has therefore been undertaken employing quantum beams for *in situ* observation. *In situ* diffraction experiments offer a method of measuring morphological and crystallographic characteristics of individual grains in 3D [1]. Remarkable spot blurring and spot overlap however occur during plastic deformation in XRD experiments [1]. Recently, the present authors proposed a multi-modal technique called diffraction-amalgamated grain boundary tracking [2]. In the present study, the technique was used to quantitatively assess the role of individual austenite grains in relation to austenite-to-martensite transformation behavior during plastic deformation. Imaging of the dual phase microstructure has been utilized to directly visualize retained austenite grains by utilizing the phase-contrast X-ray tomography that has recently been improved to 150 nm spatial resolution at 30 keV owing to the development of a type of X-ray Zernike phase-contrast X-ray nanotomography (XNT) by Takeuchi *et al.* at SPring-8 BL20XU [3].

A multi-phase steel consisting of a retained austenite interconnected in a reticulate manner was used (V_f of 22.1%). Both the XNT and XRD experiments were performed at SPring-8 **BL20XU**. A projection-type X-ray micro-tomography (XMT: 1.0 μm in spatial resolution) setup was placed side-by-side with the XRD and XNT setup to switch the three setups repeatedly. A specimen was loaded in tension and its deformation and transformation behavior was observed by the XMT, XNT and XRD techniques. A monochromatic X-ray beam of 20 keV was used for the XMT and XNT experiments. In the XNT Experiment, a large-scale X-ray microscope, which has *L* of 165 m, was used together with Köhler illumination to establish the XNT setup with Zernike phase-contrast mode [4]. A spatial resolution of 0.16 μm was achieved in the reconstructed images. In the XRD experiment, an X-ray pencil beam, which was collimated to 2.0 μm in diameter with a FZP, was raster scanned (50 rows and 50 columns in 1 μm increments) with the sample being rotated over 180° in 1° increments and the raster scan was repeated at each angle, resulting in a total of 450000 diffraction patterns being captured for each loading step. The X-ray energy was tuned to 37.7 keV for XRD.

3D morphology and initial crystallographic orientation of all the retained austenite grains were successfully obtained as demonstrated in Figs. 1 and 2 [5]. Complex austenite morphology was observable with their annihilation behavior during loading. The morphological change in the retained austenite is clearly seen in Fig. 1. The onset of the austenite-to-martensite transformation was seen between the applied strain of 0.3–0.4%. Localized transformation, which is indicated by an arrow in Fig. 1(a), is observed at an applied strain of 1.3% for the green grain. The local transformation then propagated, progressing vertically into a wedge-shape at 2.5%, followed by an abrupt transformation between 2.5 and 3.5%. It is also observed that an upper adjacent gray austenite grain transformed at roughly the same time as the green austenite grain, whereas the lower right gray austenite grain remained up to 3.5%, implying a variety of transformation behaviors for individual grains.

The change in austenite volume fraction was classified according to the initial crystallographic

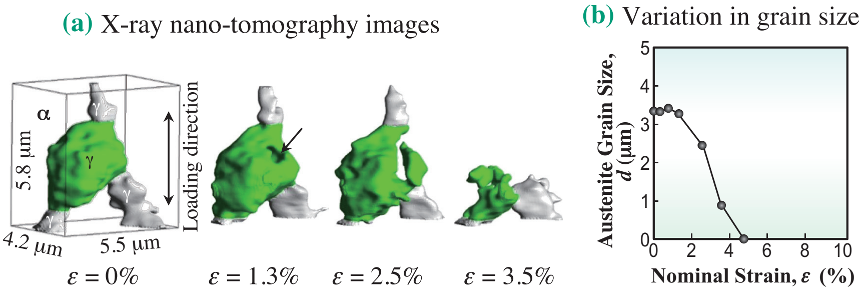
(a) X-ray nano-tomography images
(b) Variation in grain size

Fig. 1. **(a)** Typical example of austenite-to-martensite transformation during loading, together with the variation in grain size of the grain shown in **(b)** expressed in terms of equivalent sphere diameters. The green retained austenite grain was connected to the three adjacent austenite grains highlighted in gray.

orientation, and the annihilation rates were readily comparable among different orientations: retained austenite grains with a tensile axis within 15° of their initial <110> direction exhibit rapid transformation, whereas those within 15° of the initial <111> direction exhibit a low transformation rate.

Figure 2 successfully identifies crystallographic orientations of all 58 austenite grains throughout transformation [5]. The arrows in Fig. 2 indicate rotation paths during transformation. When the transformation is protracted up to 3.5% or above, the majority of the grains are rotated to a non-negligible extent; for example, 2.0° in rotation angle on average for 5.8%. It is also noteworthy that some of the grains reversed their paths in the middle of transformation, for example, the typical reversal by the grain circled in black.

The respective variations in dislocation density in the retained austenite grains are also measured. The dislocation multiplication behavior of austenite grains was strongly affected by their crystallographic orientation; the austenite grains close to the <111> orientation exhibit a gradual increase in dormant dislocation density, whereas those close to the <110> orientation exhibit rapid multiplication. The <100> direction appears to represent an intermediate tendency between the <111> and <110> directions.

Figure 3 illustrates the variety of behaviors observed during the increase in dislocation density and transformation [5]. It is evident that rapid transformation is apt to occur for austenite grains that exhibit abrupt dislocation density increase (grains G1, G3, and G6), whereas those with moderate dislocation density increase (grains G2, G4, and G5) tend to show slow and gradual transformation.

In summary, the gradual transformation, plastic deformation, and rotation behaviors of the individual austenite grains were clearly observed in 3D. It was revealed that the early stage of the transformation was dominated by the stress-assisted transformation that can be associated with measured mechanical driving force, whilst the overall transformation was dominated by the strain-induced transformation that is interrelated with measured dislocation multiplication. The transformation behavior of individual grains was classified according to their initial crystallographic orientation and size. It was conclusively demonstrated that such characteristic behavior partly originated from interactions with surrounding soft and hard phases.

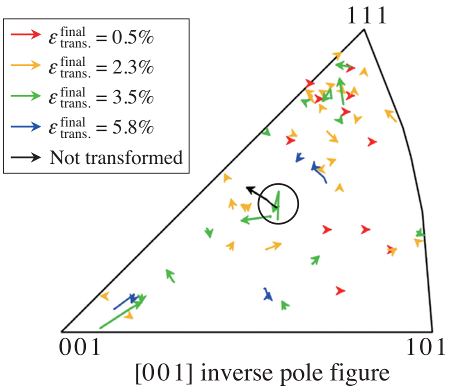

Fig. 2. Crystallographic orientation distribution and rotation behavior on a [001] inverse pole figure. All 58 austenite grains that were successfully identified are color-coded according to the external strain level at which the austenite-to-martensite transformation is completed.

(a) Dislocation density

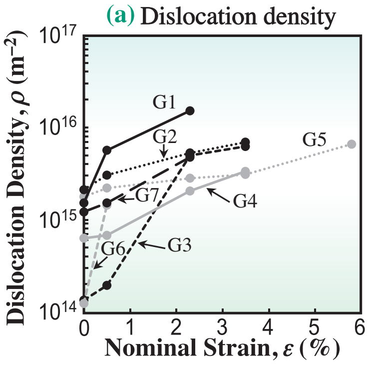

(b) Austenite grain size

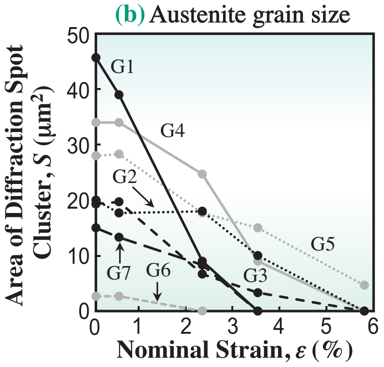

Fig. 3. Changes in **(a)** the dislocation density and **(b)** the retained austenite grain size with applied strain. Seven characteristic grains (G1–G7) have been extracted from the total number of grains obtained. The retained austenite grain size is expressed as the average of the projected spot-cluster areas obtained for three incident beam orientations; diffractions from the {111}, {200}, and {220} planes.

Hiroyuki Toda* and Hiro Fujihara

Department of Mechanical Engineering, Kyushu University

*Email: toda@mech.kyushu-u.ac.jp

References

[1] N. H. Jimenez-Melero *et al.*: Scripta Mater. **56** (2007) 421.
[2] H. Toda *et al.*: Acta Mater. **107** (2016) 310.
[3] A. Takeuchi *et al.*: Rev. Sci. Instrum. **92** (2021) 023701.
[4] H. Toda: X-Ray CT Hardware and Software Techniques (2021) Springer Nature Singapore.
[5] *H. Toda, K. Hirayama, K. Okamura, T. Suzuki, A. Takeuchi, M. Uesugi, H. Fujihara: Acta Mater.* ***234*** *(2022) 117956.*

Nondestructive visualization of inhomogeneous structure inside 40–500 nm single particles using Bragg coherent X-ray diffraction and phase retrieval analysis

Functional materials often have local inhomogeneities that arise in a macroscopically homogeneous structure and play a leading role in various functions. The nature of local inhomogeneities differs depending on the scale at which they occur. For example, impurities change the electrical conductivity by one order of magnitude at the atomic scale. At the *mesoscale* between atomic and macroscopic scales, i.e., over 1 nm but less than 1 μm atomic plane displacements, such as grain and domain boundary arrangements, significantly affect the dielectric and piezoelectric properties. The correlation between such functionalities and inhomogeneous structures is often better understood by visualizing the structures. Electron microscopy observation techniques have been well established for atomic-scale structures; for the mesoscale, however, visualization remained challenging because of the lack of methods. Visualization techniques in a nondestructive manner are essential to precisely capture the actual image of, for example, electric polarization domains, which are mesoscale structures that largely determine the dielectric constant of multilayer ceramic capacitors and the piezoelectric constant of actuators. This is because the domains originate from the electric polarization that spontaneously arises from head to tail of bound charge pairs at the surfaces and grain boundaries of ferroelectric crystals. Ferroelectric materials are primarily used as fine particles of about 100–500 nm in size and ceramics of about 500 nm in size made from these particles. These crystalline sizes are in the mesoscale. Hence, in a nondestructive visualization method for mesoscale structures was long awaited in order to elucidate ferroelectric's functional mechanisms and help material design.

We reconstructed the real-space images of inhomogeneous mesoscale structures inside fine particles in the 40–500 nm range [1]. Figure 1 shows the cross-sectional images of the atomic plane displacements for the following fine particles: 40-nm-sized Pd and 200-, 300-, and 500-nm-sized $BaTiO_3$ (BTO). The color map represents the degree of displacement of the atomic planes. Whereas the structural inhomogeneity of the metallic Pd was small, about π/6, that of the ferroelectric BTO tended to be significant, about π. The visualization of the non-averaged structures for these single particles in the wide size range was made possible by Bragg coherent X-ray diffraction imaging (Bragg-CDI), to which we applied the improvements of a high signal-to-noise ratio and convergence of analysis [1]. Bragg-CDI is a lensless imaging technique consisting of coherent X-ray diffraction and computer-aided image reconstruction. Since this imaging method was proposed [2], it has attracted much attention as a method of observing inhomogeneous structures inside fine crystalline particles and has been further developed at various synchrotron radiation facilities. In Japan, only National Institutes for Quantum Science and Technology has worked on the Bragg-CDI technique [3] and shared it at SPring-8 **BL22XU**, which is now equipped with an undulator source and a Bragg-CDI system.

Below, we describe the present Bragg-CDI system in BL22XU and how to apply Bragg-CDI to samples. Coherent X-ray diffraction (Fig. 2(a)): The three-dimensional (3D) intensity data of Bragg diffraction are recorded using coherent X-rays as a probe. Coherent X-rays in the hard X-ray range focused down to a μm order fully illuminate an isolated crystalline particle in a powder sample. A two-dimensional detector positioned where the camera length and angle satisfy oversampling and Bragg conditions, respectively, records the scattered X-rays from the particle while scanning the ω angle of the sample so that the Ewald sphere goes across one Bragg spot. The recorded scattering pattern consists of an intense spot (yellow in Fig. 2(a)) and faint fringes (light blue in Fig. 2(a)); such a pattern is called a speckle. A speckle pattern contains information on the particle size and mesoscale non-averaged structure; however, such information cannot be directly extracted from the speckle intensity because the phase of the structural factor has been lost.

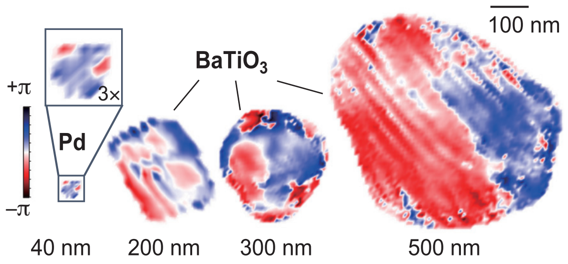

Fig. 1. Color map of atomic plane displacement for a series of samples: 40-nm-sized Pd, and 200-, 300-, and 500-nm-sized BTO. The figure was drawn using VESTA 3 [5].

Phase retrieval analysis (Fig. 2(b)): To reconstruct the real image, one uses Fourier iterative phase retrieval algorithms of hybrid input–output (HIO) and error reduction (ER). Both algorithms have two constraints: speckle intensity data in reciprocal space and support in real space. While the series of HIO–ER is repeated several hundreds of times until the structural factor satisfies the constraints, the support is updated several times by fitting to the reconstructed image in progress; this is called the shrink-wrap (SW) algorithm and increases the oversampling ratio and consequently refines the phase. The image reconstruction in the 40–500-nm-size range, which electron beams and visible light could not achieve, has thus been performed [1].

The advanced Bragg-CDI technique not only reveals the inhomogeneity of structures but also provides more clues to reveal its origin. Recently, the paraelectric (PE) – ferroelectric (FE) phase transition and dislocation at the PE phase for a BTO single particle have been successfully observed with coherent X-ray diffraction and Bragg-CDI, respectively, where a micro-electromechanical system (MEMS) heater chip was used [4]. MEMS devices are easily installed in Bragg-CDI systems because a geometrical change for Bragg-CDI is no more than about 3°, which is 1/100th more minor than that of other imaging techniques e.g., 180° of computer tomography. As shown in Fig. 3(a), the speckle from the BTO splits from 200 reflections (PE phase) to the pair of 200–002 reflections (FE phase) at ~400 K, which corresponds to T_C. The reconstructed 3D image (Fig. 3(b)) exhibits an outer shape with a many-curved surface. The 2D image (Fig. 3(c)) is the cross-section of the 3D image cut by the blue plane, showing an uneven electron density. Focusing on the high crystallinity region surrounded by the dashed line, the phase showed a steep gradient, indicating a dislocation perpendicular to the direction of the black arrow (Fig. 3(d)). Bragg-CDI can thus be used in combination with MEMS devices and other measurement techniques; consequently, one can identify domains and dislocations.

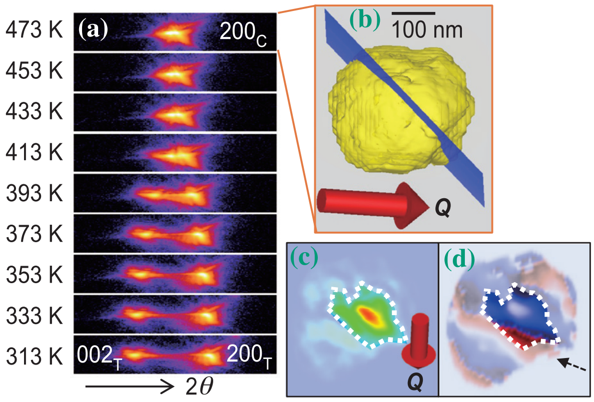

Fig. 3. **(a)** 3D image obtained by applying Bragg-CDI to the speckle at 473 K. **(b)** The cross-sectional view cut by the blue plane in the 3D image. **(c)** Electron density. **(d)** Phase image. The figures were drawn using VESTA 3 [5].

(a) Coherent X-ray diffraction

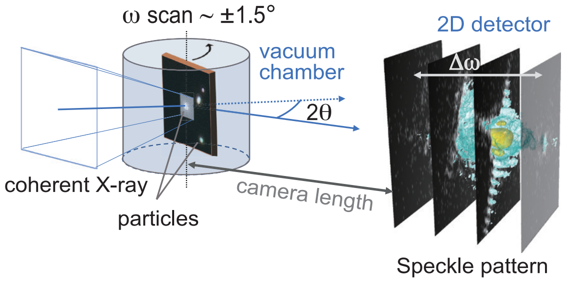

(b) Phase retrieval analysis

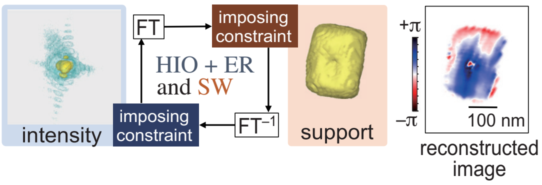

Fig. 2. Schematic diagram of the present Bragg-CDI system. **(a)** Coherent X-ray diffraction. **(b)** Phase retrieval analysis. Part of the figures was drawn using VESTA 3 [5].

Norihiro Oshime

Synchrotron Radiation Research Center, QST

Email: oshime.norihiro@qst.go.jp

References

[1] *N. Oshime, K. Ohwada, K. Sugawara, T. Abe, R. Yamauchi, T. Ueno, A. Machida, T. Watanuki, S. Ueno, I. Fujii, S. Wada, R. Sato, T. Teranishi, M. Yamauchi, K. Ishii, H. Toyokawa, K. Momma, Y. Kuroiwa: Jpn. J. Appl. Phys.* ***60*** *(2021) SFFA07.*
[2] M. Pfeifer *et al.*: Nature **442** (2006) 63.
[3] K. Ohwada *et al.*: Jpn. J. Appl. Phys. **58** (2019) SLLA05.
[4] N. Oshime *et al.*: Jpn. J. Appl. Phys. **61** (2022) SN1008.
[5] K. Momma and F. Izumi: J. Appl. Crystallogr. **44** (2011)1272.

Stress measurements of coarse-grained materials and welded parts by double exposure method with high-energy monochromatic X-rays

In this article, we report the double exposure method (DEM) that was developed at SPring-8 **BL14B1**. The DEM with synchrotron monochromatic X-rays has made it possible to measure residual stresses of coarse-grained materials and welded parts.

Knowledge of the residual stress is indispensable for estimating strength and reliability. Only an X-ray method can nondestructively measure the residual stress of the actual object. In the X-ray method, the change in lattice spacing, Δd, is obtained from the change in diffraction angle, $\Delta\theta$, based on Bragg's law. The residual stress is calculated from the elastic strain $\varepsilon = \Delta d/d_0$, where d_0 is the strain-free lattice spacing. Elastic strain measurements require an accuracy of 5–6 orders of magnitude. For powder diffraction, the residual stress can be measured with sufficient accuracy using a diffractometer.

However, diffraction from the coarse-grained material becomes spotty rather than a continuous ring. This is especially notable in the synchrotron X-ray beam, which is a microbeam with excellent directivity. Therefore, the diffractometer (point detector) cannot be used for coarse-grained materials and an area detector should be used. In the angle measured using the area detector, a center of diffraction, O, is assumed as shown in Fig. 1, and the diffraction angle 2θ is calculated from $\tan^{-1}(r_1/L_0)$. If the sample is small and fined-grained, it is possible to measure the diffraction angle 2θ by this method.

A new problem arises when measuring stress in bulk samples using the strong penetrating power of high-energy synchrotron X-rays. The diffraction from the bulk sample with coarse grains is shown in Fig. 1. The diffraction points differ in accordance with the positions of the grains on the transmitted X-ray beam, as shown in Fig. 1. For example, the diffraction angle, which is calculated using the diffraction center, becomes large for the upstream grain and small for the downstream grain. With this method, the angular variation is too large to measure the elastic strain.

To solve the above problem, we must find a new angle measurement method that does not use the diffraction center. The DEM is proposed as a countermeasure. As shown in Fig. 1, the diffraction spots are measured using the area detector at P1 and P2, and diffraction radii r_1 and r_2 are obtained. The true diffraction radius r is calculated as $r = r_2 - r_1$ and L is the length between P1 and P2. The angle determined from $2\theta = \tan^{-1}(r/L)$ gives the correct diffraction angle regardless of the grain position. This is the principle of the DEM and no diffraction center is required. Also, the diffraction angle and position can be determined from the relationship between the straight lines of the diffracted and incident beams [1].

The nonuniformity of the diffraction ring, which is indicated by the arrow in the images at P1 of Fig. 1, is due to the grain position. The same discrepancy can also be seen in the image at P2 (arrow). The DEM is able to cancel the error due to the grain position. Figure 2 demonstrates the canceling mechanism in the DEM. The fluctuations in the diffraction radii r_1 and r_2 are very large, as shown in Fig. 2, but the fluctuations in both r_1 and r_2 are synchronous. As a result, $r = r_2 - r_1$ gives the accurate diffraction radius.

On the other hand, there is an excellent method called three-dimensional X-ray diffraction microscopy (3DXRD) [2]. It is based on two principles: the use of highly penetrating hard X-rays from a synchrotron source and the application of ‘tomographic’ reconstruction algorithms for the analysis of the diffraction data.

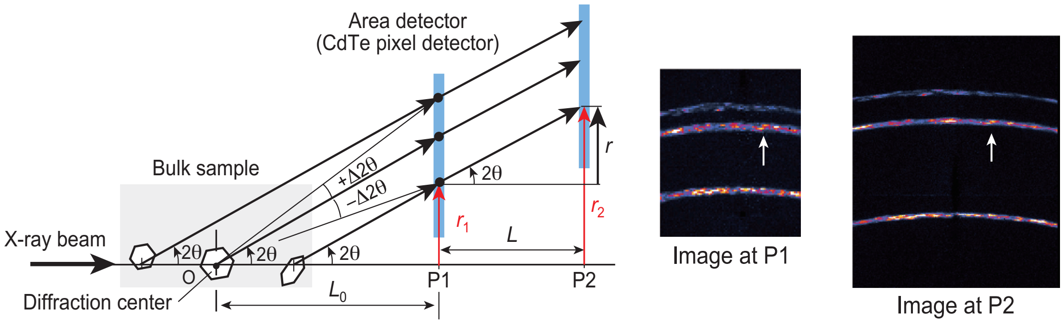

Image at P1

Image at P2

Fig. 1. Diffraction from coarse grains. The difference in the position of coarse grains causes the errors of diffraction angle $\Delta 2\theta$. Using the double exposure method (DEM), angular errors can be canceled.

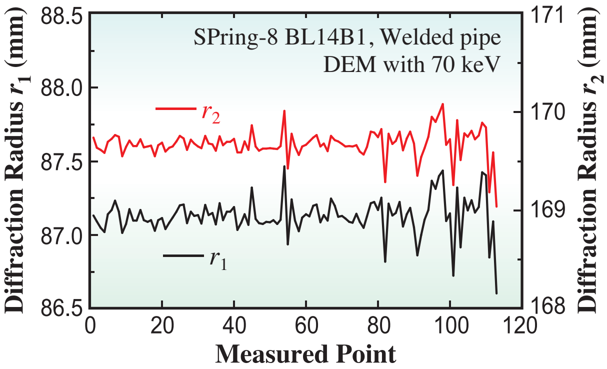

Fig. 2. Fluctuations of the diffraction radii r_1 and r_2 synchronize with each other and cancel the diffraction radius error due to the grain position.

Using 3DXRD, not only the position, morphology and crystallographic orientation but also the elastic strain can be obtained. However, this method cannot be applied to bulk samples. The features of the DEM make it the stress measurement method suitable for bulk materials.

By the DEM, the stress map of coarse-grained materials and welded parts can be obtained; however, a plane stress is estimated without an out-of-plane stress in the DEM. This problem can be solved by combining neutron stress measurement with the DEM, as shown in Fig. 3. For example, the rough hoop stress map is obtained by neutron stress measurement under the triaxial stress state. Combining the out-of-plane stress distribution obtained by neutrons and the detailed two-dimensional stress map obtained by the DEM, a detailed residual stress map of the triaxial stress state can be obtained. The method of analyzing actual stress by using neutrons and the DEM in a complementary manner is called a hybrid actual stress analysis. The maps on the right side in Fig. 3 show the residual stresses of the butt-welded pipe obtained by the hybrid actual stress analysis [3].

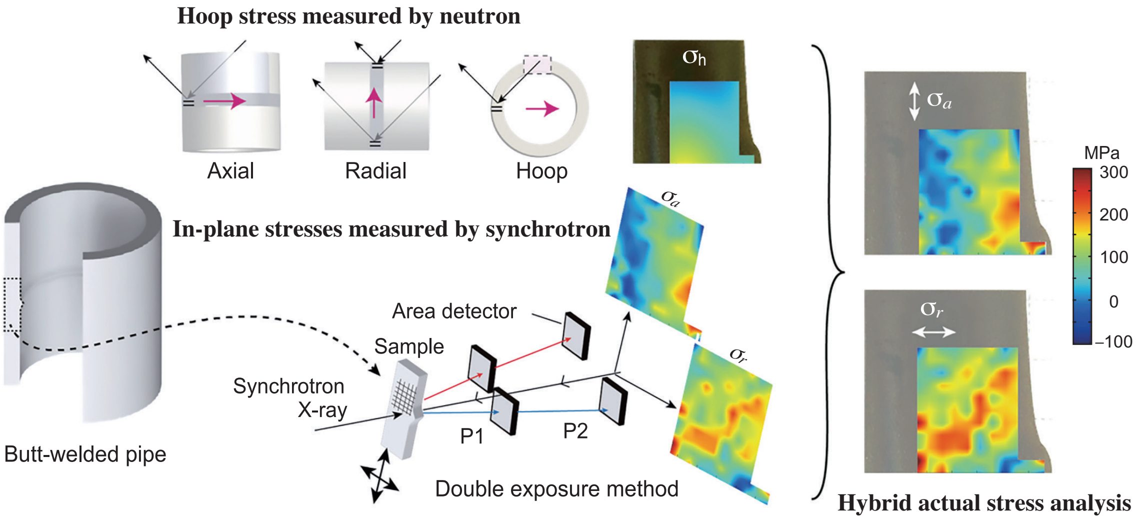

Fig. 3. Hybrid actual stress analysis using hard synchrotron X-rays and neutrons.

Kenji Suzuki

Faculty of Education, Niigata University

Email: suzuki@ed.niigata-u.ac.jp

References

[1] K. Suzuki *et al*.: Mater. Res. Proc. **6** (2018) 69.
[2] H. F. Poulsen: Three-Dimensional X-Ray Diffraction Microscopy, Springer Tracts in Modern Physics **205** (2013).
[3] *K. Suzuki, Y. Miura, A. Shiro, H. Toyokawa, C. Saji, T. Shobu and S. Morooka: J. Soc. Mater. Sci. Jpn.* ***72*** *(2023) 316.*

Critical slowing down in charge fluctuation in a strange metal probed by synchrotron radiation-based Mössbauer spectroscopy

A strange metal (SM) is a ubiquitous state of matter found to develop in quantum materials with strong correlations. It is often linked to quantum criticality (QC) at the border of magnetism. SMs share many commonalities, e.g., anomalous temperature dependences of the specific heat and resistivity. These observed properties are inconsistent with the quasiparticle excitation concept central to the Fermi liquid theory. This universality challenges the conventional wisdom of conductivity based on a momentum ($\boldsymbol{k}$) relaxation of quasiparticles.

Although spin dynamics have been extensively studied, little is known experimentally about charge dynamics. Charge dynamics are studied by optical spectroscopy, but the method only probes the *divergence-free* transverse components of the current $\boldsymbol{J} = \boldsymbol{\sigma E} \perp \boldsymbol{k}$. Mössbauer spectroscopy is a method used to detect low-frequency longitudinal charge dynamics. However, the widespread adoption of Mössbauer methods has been hindered by difficulties in preparing radioisotope sources. To overcome these difficulties, a new generation of Mössbauer spectroscopy has been developed using synchrotron radiation (SR) [1]. The new SR-based Mössbauer spectroscopy approach provides an ideal probe to resolve longitudinal charge dynamics in materials.

Figure 1(a) shows the experimental setup for SR-based ^{174}Yb Mössbauer spectroscopy at SPring-8 **BL09XU** and **BL19LXU**. The monochromatized SR pulse passed through a sample including ^{174}Yb nuclei and then encountered YbB_{12} known as a scatterer. This scatterer was moved using a velocity transducer to create a relative Doppler velocity between the sample and the scatterer. We independently observed weak nuclear resonant scattering delayed by the finite lifetime (τ_0) of the excited nuclear state. Figure 1(c) shows a delay time spectrum after each SR pulse from ^{174}Yb nuclei in the YbB_{12} scatterer. The delayed scattering signals in nuclear recoil-free absorptions were accumulated within the time window from $\tau_s = t_s/\tau_0$ to $\tau_e = t_e/\tau_0$ to measure a SR-based Mössbauer spectrum. As seen in Fig. 1(c), a typical time window in our experiments was in the range from $\tau_s \sim 3.1$ to $\tau_e \sim 6.2$.

Figure 2 shows the SR-based ^{174}Yb Mössbauer spectrum of YbB_{12} at 20 K. The full-width at half-maximum of one absorption component at 0 mm/s was evaluated to be ~1.2 mm/s which is much narrower than that ($2G_0$ = 2.00 mm/s) expected from $\tau_0 = 2.58$ ns. This narrowing phenomenon is related to the time-window effect in the accumulation of the delay time spectrum. A Lorentzian shape with the expected width should be obtained in a spectrum within the time window from $\tau_s \sim 0$ to $\tau_e \sim \infty$. The SR-based ^{174}Yb Mössbauer spectrum is well analyzed using one nuclear transition with this time-window effect.

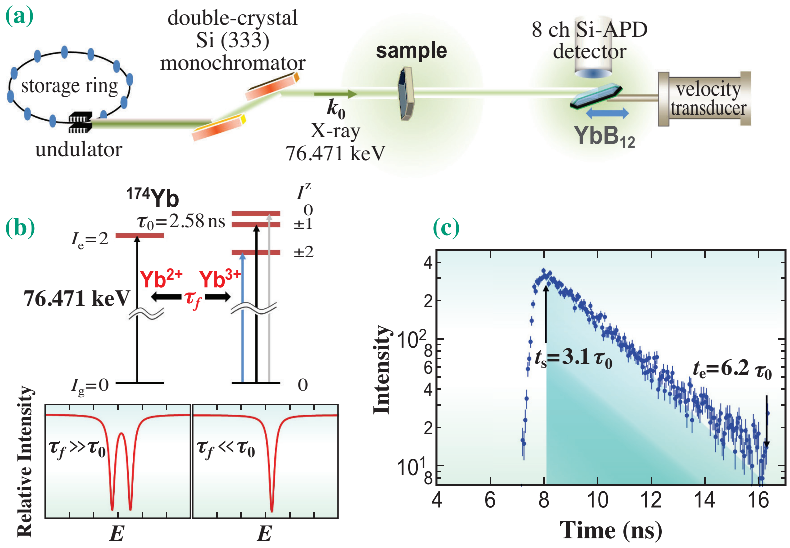

Fig. 1. **(a)** Schematic experimental setup for synchrotron-radiation-based ^{174}Yb Mössbauer spectroscopy. The *c*-axis of the single-crystalline β-$YbAlB_4$ was aligned along $\boldsymbol{k}_0$ of the incident X-ray and YbB_{12} was cooled at 26 K. **(b)** (Top) Energy diagrams of the excited ^{174}Yb (I_e = 2) nuclear state surrounded by different charge configurations. The allowed transitions are indicated by arrows, where the black ones represent the selected transitions for $c // \boldsymbol{k}_0$. (Bottom) Typical Mössbauer spectra at two limiting cases where τ_f is a timescale of fluctuation between two different charge configurations. **(c)** Typical delay time spectrum from YbB_{12}.

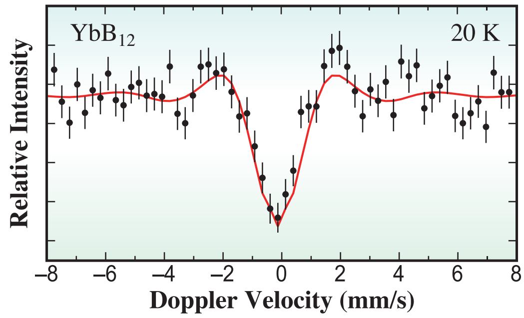

Fig. 2. Synchrotron-radiation-based ^{174}Yb Mössbauer spectrum of YbB$_{12}$ at 20 K. The delayed scattering signals were accumulated within the time window (see Fig. 1(c)). The closed circles and red solid line present the observed and analytical spectra, respectively.

Since τ_s~3.1 is much larger than τ_s~0, an energy resolution higher than that of the conventional ^{174}Yb Mössbauer spectroscopy was achieved.

We report the direct observation of charge dynamics in an SM phase by SR-based Mössbauer spectroscopy. The heavy fermion metal β-YbAlB$_4$ provides an ideal platform to study a SM phase [2]. Accordingly, we have investigated how the QC behavior in the SM phase of β-YbAlB$_4$ affects the charge dynamics. Below T*~8 K, as one enters the QC region, a two-peak structure is observed, as shown in Fig. 3(a). However, above T*, the Mössbauer spectra exhibit a broad-single line feature.

The local symmetry at the Yb site of β-YbAlB$_4$ allows us to rule out a nuclear origin of the double-peak structure. For $c // \boldsymbol{k}_0$, the symmetry selects two degenerate nuclear $I_g = 0 \rightarrow I_e^z = \pm 1$ transitions from the five E2 nuclear transitions of the ^{174}Yb Mössbauer resonance (see Fig. 1(b)). The absence of magnetic order also eliminates magnetic hyperfine interactions. This leaves the electrical hyperfine interactions, linking to the valence state of Yb ions, as the only candidate for the observed splitting. The presence of Mössbauer line splitting then implies a distribution of Yb valences within the crystal. We argue that these result from slow dynamic charge fluctuations.

We have analyzed our Mössbauer spectra applying a stochastic theory with one nuclear transition modulated by two different charge states [3]. Figure 3(a) shows that the predicted spectrum well reproduces the two-peak structure in the spectrum at 5 K and its subsequent collapse into a broad single line with increasing temperature. The extracted fluctuation time τ_f between two different Yb charge states is unusually long compared with the electronic timescales (see Fig. 3(b)). The energy difference between two selected nuclear transitions is almost independent of temperature up to 20 K (see Fig. 3(c)), so that the development of the two-peak structure in the observed spectra must derive from the marked low-temperature growth in τ_f [4]. This consistency leads us to interpret the split line-shape observed in the ^{174}Yb Mössbauer spectra of the SM as unusually slow valence fluctuations between the Yb^{2+} and Yb^{3+} ionic states, on a timescale of τ_f >1 ns that follows a power-law growth with decreasing temperature below T*.

In summary, we have provided direct evidence for unusually slow charge fluctuations in the SM phase of β-YbAlB$_4$ using SR-based ^{174}Yb Mössbauer spectroscopy. An interesting possibility is that these slow charge modes are the origin of the linear resistivity often observed in SMs. Various theoretical approaches [5] have suggested that the novel transport properties of SMs are linked to the universal quantum hydrodynamics of a Planckian metal.

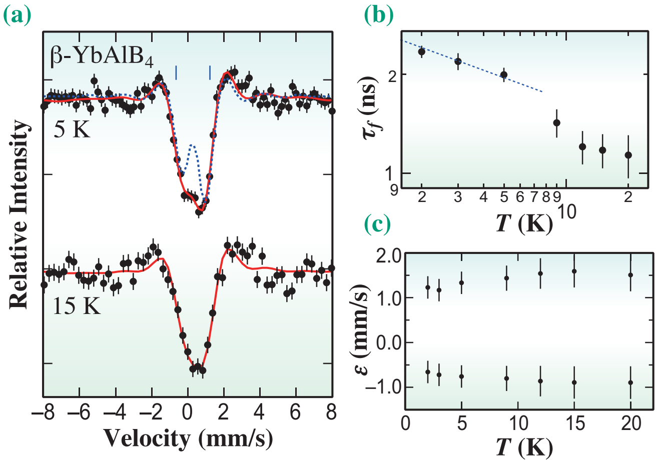

Fig. 3. **(a)** Selected synchrotron-radiation-based ^{174}Yb Mössbauer spectra of β-YbAlB$_4$ and **(b and c)** temperature dependences of the refined fluctuation time τ_f between two different Yb charge states and the refined energy ε values for two nuclear transitions. In (a), the closed circles and red solid line present the observed and the analytical spectra, respectively. The broken blue line in the spectrum at 5 K represents the spectrum with two nuclear transitions expected with our energy resolution. In (b), the broken line represents $\tau_f \propto T^{-0.2}$.

Hisao Kobayashi

Graduate School of Science, University of Hyogo

Email: kobayash@sci.u-hyogo.ac.jp

References

[1] M. Seto *et al.*: Phys. Rev. Lett. **102** (2009) 217602.
[2] S. Nakatsuji *et al.*: Nat. Phys. **4** (2008) 603.
[3] M. Blume: Phys. Rev. **174** (1968) 351.
[4] *H. Kobayashi, Y. Sakaguchi, H. Kitagawa, M. Oura, S. Ikeda, K. Kuga, S. Suzuki, S. Nakatsuji, R. Masuda, Y. Kobayashi, M. Seto, Y. Yoda, K. Tamasaku, Y. Komijani, P. Chandra, P. Coleman: Science* ***379*** *(2023) 908.*
[5] S. A. Hartnoll *et al.*: Holographic Quantum Matter (MIT Press, 2018).

Structural origin of the anomalous properties of SiO_2 glass under pressure reveled by *in situ* high-pressure pair distribution function measurement

Understanding the structural origin of the anomalous properties of tetrahedral liquids and amorphous materials at high pressure and/or high temperature conditions is of great interest in wide range of scientific fields. In particular, since SiO_2 is ubiquitous in the Earth, understanding the SiO_2's anomaly is fundamental not only in physics, but also in geophysics to understand nature of silicate magmas in the Earth and planet, and in materials science as a prototype network-forming glass. It has been reported that SiO_2 liquid shows anomalous density and compressibility behaviors at high temperatures and high pressures [1]. In addition, SiO_2 glass also shows compressibility maximum (bulk modulus minimum) at high pressure of ~2–3 GPa under room temperature condition [2].

Theoretical studies of SiO_2 liquid suggests that the second shell structure of silicon is the key to understanding the anomalous properties of SiO_2 liquid at high temperatures and high pressures. A structural parameter z ($z = \delta_{ji} - \delta_{j'i}$, where δ_{ji} and $\delta_{j'i}$ is the distance from each silicon atom i to the fifth nearest silicon neighbor j and to the fourth nearest oxygen neighbor j') was developed to investigate the second shell structure in SiO_2 liquid [1]. The theoretical study found a bimodal distribution in the structural parameter z with varying temperature, and the S and ρ states are assigned to the high and low distributions in the parameter z, respectively. The low-density S state in SiO_2 liquid consists of four silicon neighbor atoms in the first shell and exhibits high tetrahedral order with clear separation between the first and second shell. The fraction of the S state with high tetrahedrality is considered to be the controlling parameter of the anomalous properties of SiO_2 liquid at high temperatures and high pressures in theoretical study [1]. However, there has been no experimental observation of the structure of the silicon's second shell in SiO_2 liquid and/or glass at *in situ* high pressure and/or high temperature conditions.

In this work [3], we carried out *in situ* high-pressure pair distribution function measurement of SiO_2 glass by utilizing high flux and high energy X-rays from undulator sources at SPring-8 **BL37XU** and **BL05XU** (Fig. 1(a)). The structure of SiO_2 glass was measured at *in situ* high pressure conditions up to 6.0 GPa in a Paris-Edinburgh (PE) cell (Fig. 1(b)) by high-energy X-ray diffraction measurement with a collimation setup to obtain signals only from the SiO_2 glass sample. We obtained the Faber-Ziman structure factor, $S(Q)$, of SiO_2 glass at the wide range of the momentum transfer Q up to 19 $Å^{-1}$ at BL37XU and up to 20 $Å^{-1}$ at BL05XU (Fig. 2), which is almost two times larger than that in conventional high-pressure angle-dispersive X-ray diffraction measurements.

By combining the high-pressure experimental $S(Q)$ precisely determined at a wide range of Q up to 19–20 $Å^{-1}$ with the MD (molecular dynamics simulation)-RMC (reverse Monte Carlo) modeling, we were able to investigate in detail the structural behavior of SiO_2 glass beyond the nearest neighbor distances under *in situ* high pressure conditions. We found bimodal feature in the translational order of the silicon's second shell in terms of the structural parameter z (Fig. 3(c)). The bimodal feature is consistent with that simulated in SiO_2 liquid with varying temperature in the theoretical study [1].

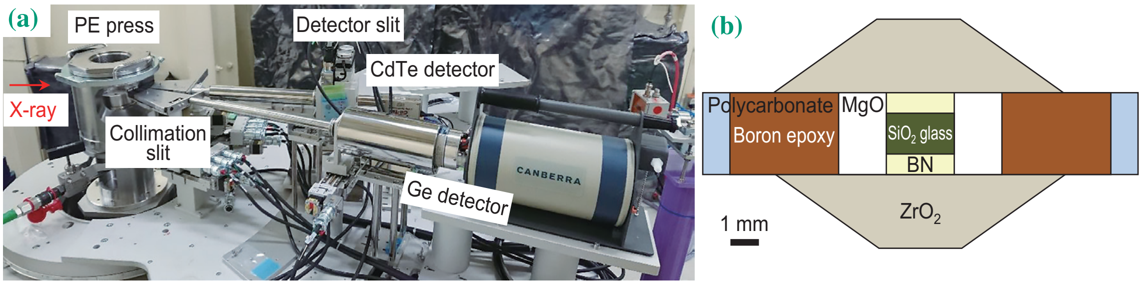

Fig. 1. *In situ* high-pressure pair distribution function measurement at SPring-8 BL05XU **(a)**, and design of the Paris-Edinburgh (PE) cell assembly for the SiO_2 glass experiment up to 6.0 GPa under room temperature condition **(b)**.

The structure of SiO_2 glass with the characteristic distribution of the parameter z at 2.4 Å shows a tetrahedral symmetry structure formed from the nearest four silicon atoms in the first shell, and the first and second shells are clearly separated as the fifth neighbor silicon atom locates in the second shell (Fig. 3(b)). The structural feature corresponds to the low-density *S* state structure reported in the theoretical study of SiO_2 liquid [1]. On the other hand, the structure of SiO_2 glass with the characteristic distribution of z at 1.7 Å shows that the fifth neighbor silicon atom locates in the first shell (Fig. 3(a)), which indicates collapse of the second shell onto the first shell and breaking of local tetrahedral symmetry. SiO_2 glass mainly consists of the low-density *S* state with tetrahedral symmetry structure at low pressures. On the other hand, the local tetrahedral symmetry structure breaks at high pressures, and the fraction of the *S* state in SiO_2 glass decreases under pressure, as well as theoretical observation in SiO_2 liquid at high temperatures and high pressures.

The new experimental technique of high-pressure pair distribution function measurement particularly using the high-flux pink beam at BL05XU beamline opens new way to investigate structural behavior of liquids and amorphous materials at *in situ* high pressure and high temperature conditions. The PE cell enables us to conduct high-pressure experiments not only for glass but also for liquid up to 7 GPa and 2000°C [4]. These techniques would have wide ranging application not only in scientific fields such as physics, chemistry, geoscience, and materials science but also engineering and industry processes.

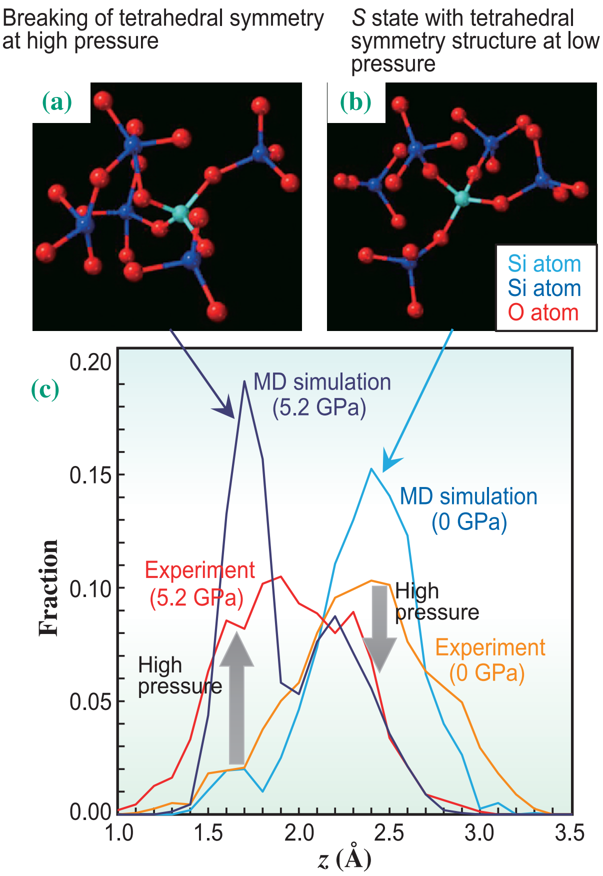

Fig. 3. The structural features in SiO_2 glass with the characteristic distribution of $z = 2.4$ Å **(b)** and $z = 1.7$ Å **(a)**. Translational order in SiO_2 glass as a function of the parameter z obtained in our experiment with MD-RMC modeling and MD simulation with BKS model at 0 and 5.2 GPa **(c)**.

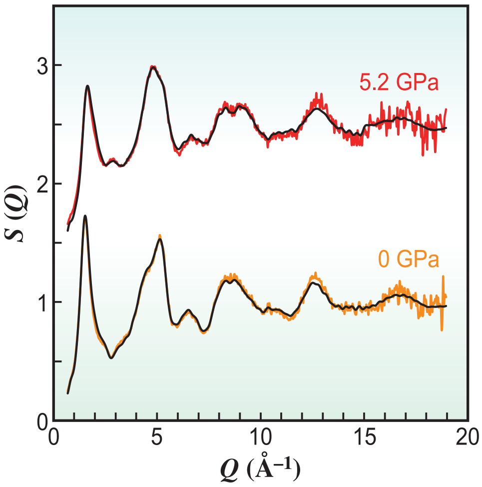

Fig. 2. Structure factor [$S(Q)$] of SiO_2 glass measured at 0 GPa (orange) and 5.2 GPa (red). Black lines show $S(Q)$ of the MD-RMC structure model derived based on the experimentally observed $S(Q)$ at each pressure condition. $S(Q)$ at 5.2 GPa is displayed by a vertical offset of +1.5.

Yoshio Kono

Geodynamics Research Center, Ehime University

Email: kono.yoshio.rj@ehime-u.ac.jp

References

[1] R. Shi and H. Tanaka: Proc. Natl. Acad. Sci. USA **115** (2018) 1980.
[2] A. Yokoyama *et al.*: J. Appl. Phys. **107** (2010) 123530.
[3] *Y. Kono, K. Ohara, N. M. Kondo, H. Yamada, S. Hiroi, F. Noritake, K. Nitta, O. Sekizawa, Y. Higo, Y. Tange, H. Yumoto, T. Koyama, H. Yamazaki, Y. Senba, H. Ohashi, S. Goto, I. Inoue, Y. Hayashi, K. Tamasaku, T. Osaka, J. Yamada and M. Yabashi: Nat. Commun.* ***13*** *(2022) 2292.*
[4] Y. Kono *et al.*: Phys. Earth. Planet. Inter. **228** (2014) 269.

Local structures of hematite-mesocrystal-based photoanodes for efficient and selective solar water splitting

Hydrogen peroxide (H_2O_2) has attracted considerable interest owing to its usefulness as a green oxidant for applications in industrial chemistry and environmental purification, as well as a clean energy source for fuel cells. Solar-driven photoelectrochemical (PEC) water splitting is one of the ideal strategies for the on-site production of H_2O_2 and CO_2-free H_2 gas [1]. PEC H_2O_2 production has been mostly realized by a two-electron pathway of water oxidation using $BiVO_4$-based photoanodes, but these photoanodes are expensive and have low stability. Alternatively, hematite (α-Fe_2O_3) is naturally abundant with good stability and a suitable bandgap (~2.1 eV) for the absorption of sunlight, and has been extensively studied for use in solar-driven water oxidation to generate O_2. However, there are no reports on hematite-based photoanodes for water oxidation to obtain H_2O_2, probably because of their unfavorable surface properties.

A mesocrystal (MC) is an ordered assembly of nanoparticles via oriented attachment and has been applied as a photocatalyst [2]. We have recently discovered that the thermal treatment of hematite MCs at high temperatures (e.g., 700°C) induces the sintering of the interface, which creates numerous interfacial oxygen vacancies (V_O) for the enhanced separation of photogenerated electrons and holes [3,4].

Herein, we present MC-based dopant segregation to effectively modify the hematite MCs surface for highly efficient and selective solar-driven H_2O_2 production (Fig. 1) [5]. The sintering of highly ordered interfaces between the nanocrystal subunits inside the MC eliminates substantial grain boundaries, leading to the efficient segregation of dopants on the external surface, which results in the formation of deficient $SnTiO_x$ overlayers for H_2O_2 production.

The synchrotron-based X-ray total scattering with pair distribution function (PDF) analysis, which is a powerful method of characterizing disordered or amorphous structures, was performed with the incident X-ray energy of 61.4 keV at SPring-8 **BL04B2**. Data were collected using the hybrid detectors of Ge and CdTe. The reduced PDF $G(r)$ was obtained by the conventional Fourier transform (FT) of the Faber–Ziman structure factor $S(Q)$ extracted from the collected data. The as-synthesized Sn- and Ti-doped hematite (SnTi–Fe_2O_3) sample shows a peak shift, along with the broadening of the peaks, towards a larger interatomic distance (r) than the undoped Fe_2O_3 sample (Fig. 2), suggesting the expansion of the hematite lattice due to the replacement of Fe^{3+} sites by the larger Sn and Ti atoms. The thermal treatment at 700°C in air for 20 min leads to a lattice rearrangement in the bulk, as indicated by the peak shifts toward the profile of the undoped Fe_2O_3 sample. Considering that the length of the corner-sharing Ti–Ti (and Sn–Sn) bond of rutile TiO_2 (and SnO_2) is 3.55 Å (and 3.68 Å), the increase in amplitude at 3.5–3.7 Å implies the formation of the dopant oxide overlayers.

To elucidate the local structures of the overlayers, X-ray absorption spectra (XAS) at Ti and Sn K-edges were collected at SPring-8 **BL01B1**. The samples were prepared by pelletizing the uniform mixtures of hematite-based MCs or reference samples with dehydrated boron nitride powders. Figure 3(a) shows the normalized Ti K-edge XANES spectra of the Ti-containing samples. For transition metals in oxides, the threshold energy position of the spectrum is sensitive to their oxidation states, while the shapes of the peaks give information about the local structural environments of the absorbing elements. The peak shapes of the annealed Ti-doped hematite (Ti–Fe_2O_3)

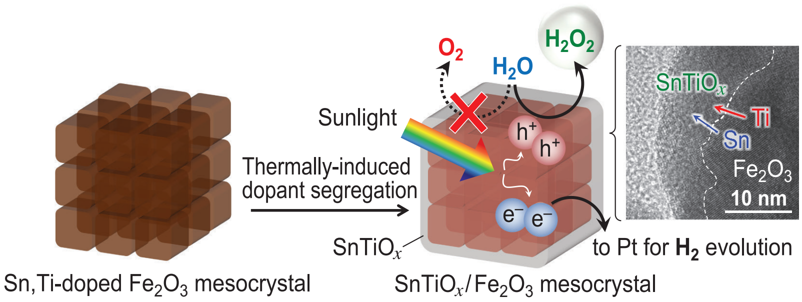

Fig. 1. Hematite-mesocrystal-based photocatalyst for solar H_2O_2 production. A hematite mesocrystal is a superstructure of particles, each around 20 nm in size. The segregation of Sn and Ti atoms doped in the mesocrystal was thermally induced to form a composite oxide ($SnTiO_x$) layer. A transmission electron microscopy image is also shown.

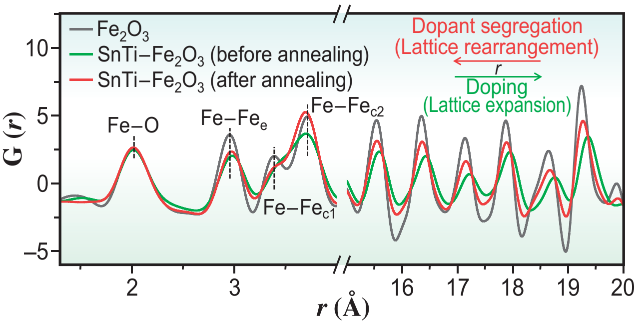

Fig. 2. Synchrotron-based X-ray total scattering measurements with PDF analysis. The peak at approximately 2 Å is composed of shorter Fe–O (1.94 Å) and longer Fe–O (2.12 Å) distances. The peak at approximately 3 Å is composed of the first-neighbor edge-sharing (Fe–Fe$_e$, 2.95 Å) and face-sharing (Fe–Fe$_f$, 2.90 Å) Fe–Fe distances. The first- and second-neighbor corner-sharing Fe–Fe pairs are at 3.39 Å (Fe–Fe$_{c1}$) and 3.72 Å (Fe–Fe$_{c2}$), respectively.

MCs in pre- and post-edge regions are similar to those of rutile TiO_2, suggesting the formation of the rutile overlayer. For the annealed SnTi-Fe_2O_3 sample, the characteristic peak of rutile TiO_2 in the pre-edge region was not clearly observed.

In situ Sn *K*-edge FT-EXAFS measurements helped us to gain more information on the dynamics of thermally induced dopant segregation. For the annealed SnTi–Fe_2O_3 sample, as shown in Fig. 3(b), the second main shell has a shorter radial distance than that of SnO_2 owing to the formation of Sn–Ti coordination. The peak intensity of the Sn–Fe coordination shell gradually decreases with increasing temperature from 48 to 700°C because the Sn coordination becomes disordered as a result of the diffusion of Sn atoms from the hematite lattice. On the other hand, the Sn–Ti coordination peak appears at approximately 700°C and becomes stronger during the heat preservation and cooling stages. From these results, we concluded that Sn atoms initially migrate from the hematite lattice owing to their larger radius and segregate on the surface to form the SnO_2 phase. The deficient $SnTiO_x$ overlayers are then formed when Ti atoms segregate at the surface and react with SnO_2 at 700°C (Fig. 1). The composite overlayers on the hematite MCs could act as co-catalysts for highly selective solar H_2O_2 synthesis.

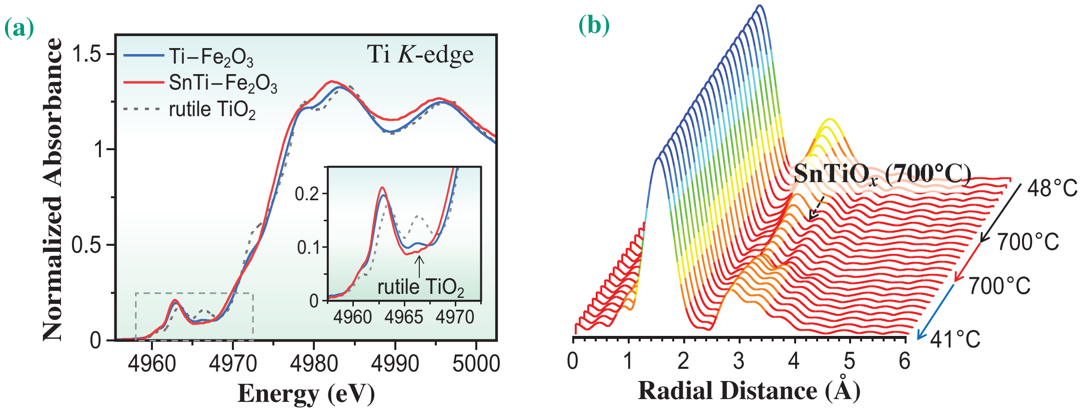

Fig. 3. X-ray absorption spectroscopy (XAS) measurements. (**a**) *Ex situ* Ti *K*-edge XANES spectra of annealed Ti-containing samples and reference samples. (**b**) *In situ* Sn *K*-edge FT-EXAFS spectra of as-synthesized SnTi-Fe_2O_3 measured with a heating procedure similar to that used for electrode preparation.

Takashi Tachikawa

Molecular Photoscience Research Center,
Kobe University

Email: tachikawa@port.kobe-u.ac.jp

References

[1] K. Sayama: ACS Energy Lett. **3** (2018) 1093.
[2] T. Tachikawa *et al.*: NPG Asia Mater. **6** (2014) e100.
[3] Z. Zhang *et al.*: Nat. Commun. **10** (2019) 4832.
[4] Z. Zhang *et al.*: Angew. Chem. Int. Ed. **59** (2020) 9047.
[5] *Z. Zhang, T. Tsuchimochi, T. Ina, Y. Kumabe1, S. Muto, K. Ohara, H. Yamada, S. L. Ten-no and T. Tachikawa: Nat. Commun.* ***13*** *(2022) 1499.*

X-ray Compton scattering reveals electronic motions with a preferred direction in high-temperature cuprate superconductors

An X-ray can be scattered by electrons and lose energy. This process is called X-ray Compton scattering. The scattered X-ray carries information about the momentum distribution $n(\mathbf{k})$ of electrons. In metals, $n(\mathbf{k})$ exhibits a rapid change at the Fermi momentum $\mathbf{k}_F$, above (below) which electron occupation becomes low (high). The surface corresponding to $\mathbf{k}_F$ is called the Fermi surface (FS), the shape of which reflects electron motions inside the metal. The FS is recognized as a fundamental concept in understanding material properties.

High-temperature cuprate superconductors continue to be a central subject in condensed matter physics [1]. They are characterized by a stack of CuO_2 planes, and a vast number of studies using angle-resolved photoemission spectroscopy (ARPES) have confirmed the existence of the two-dimensional (2D) FS at least in the overdoped region — the critical temperature T_c in cuprate superconductors is controlled by the carrier doping rate. In the underdoped region including the optimal doping at which T_c becomes maximal, the FS was observed clearly only around $\mathbf{k} = (0.45\pi, 0.45\pi)$ — the so-called Fermi arcs, which were believed to be a portion of the underlying 2D FS [2].

To reveal the underlying FS, we perform Compton scattering for the La-based cuprate $La_{2-x}Sr_xCuO_4$ with $x = 0.08$ (underdoped sample) at SPring-8 **BL08W** [3]. The obtained momentum distribution $n(\mathbf{k})$ is shown in Fig. 1 in the first Brillouin zone $-\pi < k_x,\ k_y < \pi$. Is Fig. 1 consistent with the conventional 2D FS illustrated in Figs. 2(a) and 2(b)? There are two key criteria: $n(\mathbf{k})$ should be nearly constant along the FS and the derivative of $n(\mathbf{k})$, i.e., $\nabla n(\mathbf{k})$, increases in magnitude there.

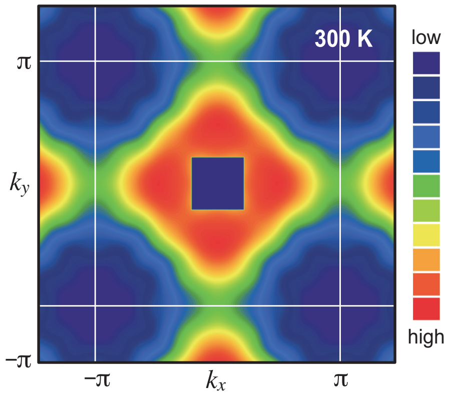

Fig. 1. Electron momentum distribution measured by Compton scattering at 300 K for $La_{2-x}Sr_xCuO_4$ with $x = 0.08$ [3]. Red (blue) indicates a higher (lower) occupation of electrons. Data around $\mathbf{k} = (0,0)$ are removed because of low accuracy. [5]

In Fig. 2(c), we superpose the FS identified by ARPES (dots) [2] by focusing on the first quadrant of the Brillouin zone. Around $\mathbf{k} = (0.45\pi, 0.45\pi)$, $n(\mathbf{k})$ is nearly constant along the FS as expected. However, around $\mathbf{k} = (\pi, 0)$ and $(0, \pi)$, $n(\mathbf{k})$ varies along the FS (from yellow to green), implying that the underlying

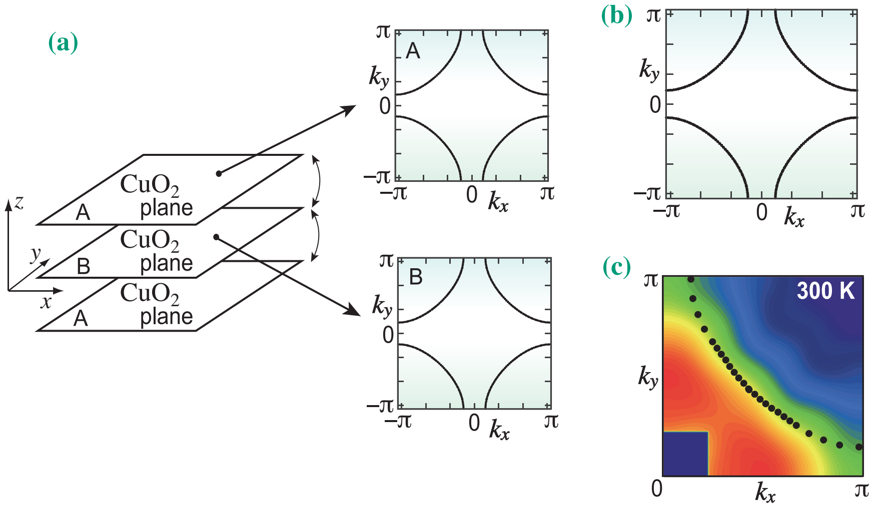

Fig. 2. Conventional idea. **(a)** 2D-like FS is realized in each CuO_2 plane. **(b)** Bulk FS. **(c)** Observed $n(\mathbf{k})$ in the first quadrant of the Brillouin zone. The FS identified by ARPES (dots) is superposed. [5]

FS cannot be the conventional one accepted thus far (Figs. 2(a) and 2(b)). We also examined the data of $\nabla n(\mathbf{k})$, which indicated a curvature qualitatively different from that of the conventional FS [3].

The agreement between the results of the present work and ARPES around $\mathbf{k} = (0.45\pi, 0.45\pi)$ is reasonable because ARPES signals are very clear there. However, the signals become weak and broad upon approaching $\mathbf{k} = (\pi, 0)$ and $(0, \pi)$, which makes it difficult to identify the FS. Hence, the underlying FS was inferred by extrapolating the FS observed clearly around $\mathbf{k} = (0.45\pi, 0.45\pi)$ to a region around $\mathbf{k} = (\pi, 0)$ and $(0, \pi)$, as shown by dots in Fig. 2(c) [2]. However, such a FS cannot be reconciled with our data, especially around $\mathbf{k} = (\pi, 0)$ and $(0, \pi)$.

What does Compton scattering data Fig. 1 then imply? One possibility is an electronic nematic tendency — the electron motion has a preferred direction along the *x*- or *y*-direction in each CuO_2 plane; this tendency is enhanced in the underdoped region in cuprates [4]. For La-based cuprates, this theory [4] predicted that the electronic nematicity yields a quasi-one-dimensional FS in each CuO_2 plane and the direction of nematicity alternates along the *z*-direction through a coupling to the crystal structure; see Fig. 3(a). These FSs are hybridized via weak interlayer coupling, leading to 2D-like FSs, consisting of the inner and outer FS as shown in Fig. 3(b).

We superpose those FSs on the observed $n(\mathbf{k})$ in Fig. 3(c). The inner FS explains $n(\mathbf{k})$, which is essentially constant (yellow) along the FS. Similarly, the outer FS may also explain $n(\mathbf{k})$, although $n(\mathbf{k})$ changes along the FS around $\mathbf{k} = (\pi, 0)$ and $(0, \pi)$ from green to blue. We observed that the value of $\nabla n(\mathbf{k})$ is very small there and thus the actual change in $n(\mathbf{k})$ can be considered to be not sizable. We also performed the same analysis of data at 150 K and confirmed this conclusion. Upon reaching the overdoped region, it is expected that the FS in Fig. 3(a) will lose nematicity and become conventional 2D FS [4]. This expectation was also confirmed by performing Compton scattering at $x = 0.15$ and 0.30 [3].

In summary, X-ray Compton scattering reveals that, in contrast to the common belief (Fig. 2), electrons in La-based cuprates have a preferred direction along the *x*- or *y*-direction in each CuO_2 plane and the preferred direction alternates between the layers (Fig. 3). Compton scattering can be a powerful tool, especially when other probes such as ARPES cannot reveal the whole shape of the FS.

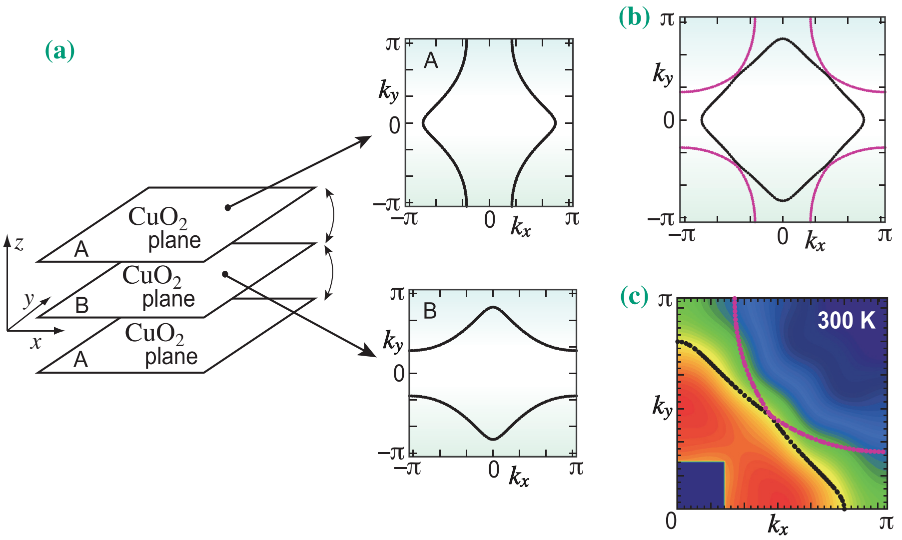

Fig. 3. Electronic nematic scenario. **(a)** FS stacking where the preferred direction of the electron motion is rotated 90 degrees between adjacent layers. **(b)** Bulk FSs consist of the inner (black) and outer (purple) FSs. **(c)** Observed $n(\mathbf{k})$ in the first quadrant of the Brillouin zone. The FS in (b) is superposed. [5]

Hiroyuki Yamase

Research Center of Materials Nanoarchitechtonics (MANA),
National Institute for Materials Science (NIMS)

Email: yamase.hiroyuki@nims.go.jp

References

[1] B. Keimer *et al.*: Nature **518** (2015) 179.
[2] T. Yoshida *et al.*: J. Phys. Soc. Jpn. **81** (2012) 011006.
[3] *H. Yamase. Y. Sakurai, M. Fujita, S. Wakimoto and K. Yamada: Nat. Commun. 12 (2021) 2223.*
[4] H. Yamase and H. Kohno: J. Phys. Soc. Jpn. **69** (2000) 332; *ibid.* 2151.
[5] H. Yamaes and Y. Sakurai: Isotope News **779** (2022) 38.

Effect of impurities on superconductivity in LaH_{10}

Near-room-temperature superconductors are certainly among the most attention-grabbing compounds in materials science. Theoretically, compressed hydrogen should be the best high-temperature superconductor, but it is hard to squeeze it above 450 GPa to turn hydrogen into a metal [1]. Thus instead, scientists are exploring compounds that contain additional elements, besides lots of hydrogen. In that way, some critical temperature (T_C) is sacrificed to reduce the pressures needed to stabilize the superconducting material to 100–200 GPa and into the realm of what is technologically possible. At this moment, lanthanum superhydride LaH_{10} with a well-reproducible critical temperature (T_C) of 250 K is the best-known superconductor [2]. This is very impressive, but to attain even higher critical temperatures, we first had to understand how superconductivity in this material works.

There are multiple microscopic mechanisms of superconductivity. The one best understood is called conventional phonon-mediated superconductivity [3]. The well-established theory of conventional superconductivity can be applied to improve the properties of LaH_{10}, perhaps by introducing some crucial third element to create a novel ternary compound. The problem was, up until now, that no general models of ternary superconducting systems existed determine how much we can improve the properties of polyhydrides by introducing a third element into the system. In this work, we have cleared the way by eliminating this uncertainty. We investigated the La–Nd–H system under pressure and found that the doping of polyhydrides obeys Anderson's theorem proposed for conventional superconductors back in 1959 [4].

Anderson's theorem [4] states that nonmagnetic impurities do not affect the order parameter in the conventional Bardeen–Cooper–Schrieffer (BCS) theory [3], whereas scattering on magnetic centers (e.g., Nd, Eu, Fe, Gd, etc.) is very efficient in destroying electron-electron pairing. Nonmagnetic and magnetic impurities are equally detrimental to the critical temperature T_C of unconventional superconducting states [5]. Therefore, the introduction of such impurities can provide important information on the mechanism of pairing in LaH_{10} under pressure.

The first step in our work [6] was the laser-assisted synthesis of La–Nd polyhydrides in diamond anvil cells (DACs). X-ray diffraction experiments (XRD) at high pressures were performed at SPring-8 **BL10XU**. The analysis of the XRD showed that we successfully synthesized ternary polyhydride $(La, Nd)H_{10}$ containing about 9 at% of Nd atoms, randomly distributed in a LaH_{10}-like metal sublattice (Fig. 1). Transport measurements demonstrated that the addition of magnetic Nd leads to a significant suppression of superconductivity in LaH_{10}: each atomic % of Nd causes a decrease in T_C by 10–11 K (Fig. 2(b)). Superconductivity in the $(La, Nd)H_{10}$ hydrides disappears at a critical concentration of Nd of about 15–20 at%. The pronounced suppression of superconductivity in LaH_{10} by magnetic Nd atoms and the robustness of T_C with respect to nonmagnetic impurities (such as B and N from ammonia borane, C and CH_4 from diamond anvils, Y [7], Al [8], etc.) within Anderson's theorem indicate the isotropic character of electron–phonon pairing in LaH_{10}.

The applicability of Anderson's theorem is limited by the following two conditions:

1. Introduced 3rd element does not change the lattice symmetry of the parent polyhydride and nor lead to the appearance of new phase transitions.
2. Concentration of the doping element remains low (5–15 at%).

For many metal alloys, these conditions are not met. However, they are satisfied in Nb–Ti alloys and T_C almost does not depend on Ti concentration (x) at $x < 0.3$ (Fig. 2(a)) [8]. Surprisingly, La–Y, La–Ce, and La–Nd polyhydrides are one of the best examples of the experimental realization of Anderson's theorem due to the similarity of the physical and chemical properties of La, Y, Ce, and Nd atoms.

From the obtained results, we can draw important conclusions concerning all ternary polyhydrides. As we can see, nonmagnetic impurities do not affect T_C so much. This leads to good reproducibility of the superconducting properties of polyhydrides synthesized in many laboratories around the world. The absence of the effects of C, B and N impurities from NH_3BH_3 also casts doubt on attempts to explain the supposedly huge increase in T_C in experiments with doped H_3S and LaH_{10}. If the leading

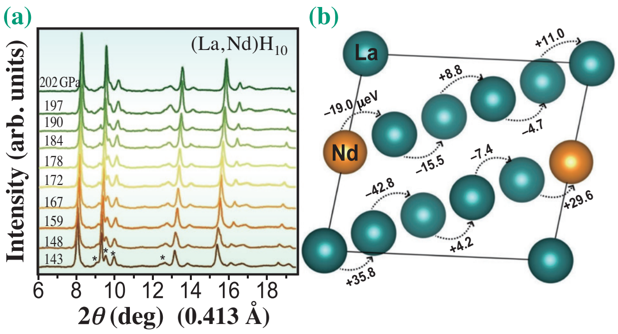

Fig. 1. **(a)** XRD patterns of $(La, Nd)H_{10}$, obtained from $La_{0.91}Nd_{0.09}$ alloy, recorded during decompression from 202 to 143 GPa. Asterisks mark the XRD peaks of an impurity phase. **(b)** Migration (indicated by arrows) of Nd atoms in the LaH_{10} lattice. The values given with the arrows are the formation energy differences ΔH in μeV/atom between the corresponding $P1$-La_9NdH_{100} modifications. For simplicity, hydrogen is not shown. Such low barriers between structures indicate that Nd atoms are randomly distributed in the La sublattice of LaH_{10}.

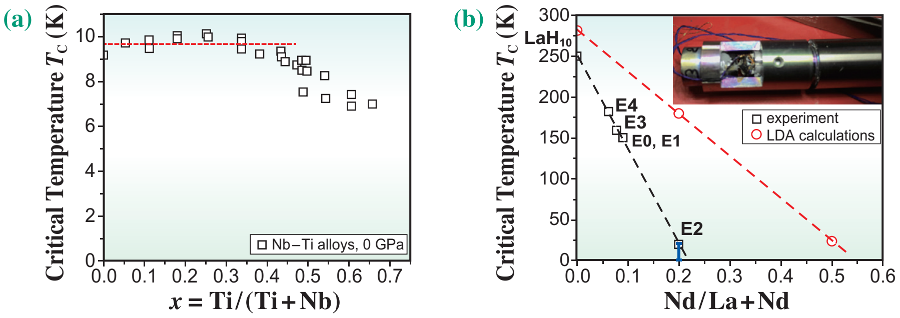

Fig. 2. **(a)** Transition temperature of Nb–Ti alloys *vs* their composition at 0 GPa [9]. Data points are the midpoints of transitions. **(b)** Experimental and calculated (using the local density approximation) dependences of T_C on the concentration of Nd in (La,Nd)H$_{10}$ at 170–180 GPa. Inset: DAC for electrical measurements in pulsed magnetic fields.

mechanism in compressed polyhydrides is the electron–phonon interaction, as most results of experimental and theoretical studies suggest, then it is impossible to expect a significant effect of a small additive, such as carbon or methane in H_3S.

The partial replacement of La atoms by magnetic Nd atoms results in a decrease in not only T_C but also the upper critical field $\mu_0 H_{C2}(0)$, which makes the upper critical field $H_{C2}(0)$ attainable for existing pulse magnets. Using strong pulsed magnetic fields up to 68 T, we constructed the magnetic phase diagram of the (La,Nd)H$_{10}$ superhydride; the magnetic phase diagram appears to be surprisingly linear with $H_{C2} \propto |T - T_C|$. This discovery motivated us to look at the behavior of other hydride superconductors as well. Figure 3 shows that several known superhydrides have a linear $H_{C2}(T)$, and the coefficient $\alpha = -dH_{C2}/dT$ varies in a quite narrow range, $\alpha = 0.9 \pm 0.3$. This leads to the interesting conclusion that the upper critical field in many compressed polyhydrides can be expressed as a linear dependence, $H_{C2}(0) = \alpha T_C$.

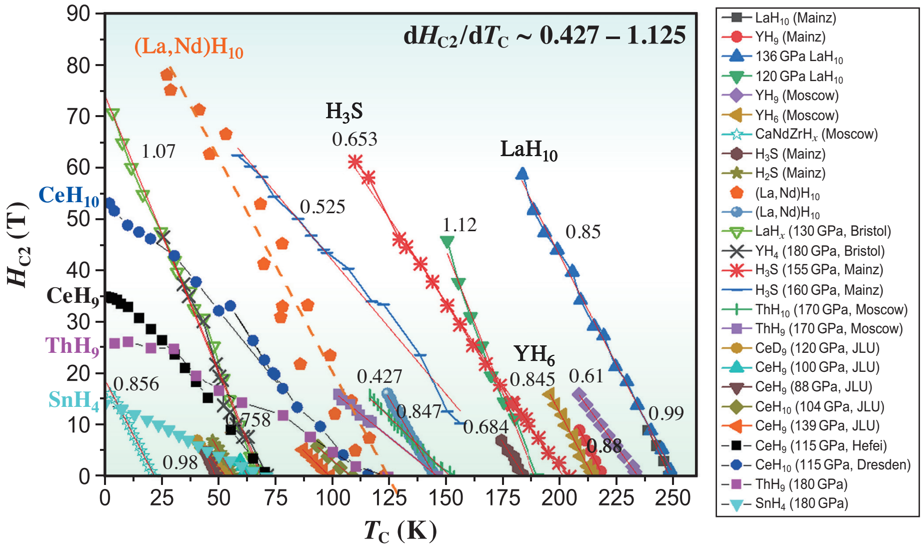

Fig. 3. Magnetic phase diagrams of superhydrides. The legend on the right shows the proposed chemical formula and the research group (city) that investigated the compound.

Dmitrii Semenok

Center for High Pressure Science and Technology
Advanced Research (HPSTAR), China

Email: dmitrii.semenok@hpstar.ac.cn

References

[1] L. Monacelli *et al.*: Nat. Phys. **17** (2021) 63.
[2] A. Drozdov *et al.*: Nature **569** (2019) 528.
[3] J. Bardeen *et al.*: Phys. Rev. **108** (1957) 1175.
[4] P. Anderson *et al.*: J. Phys. Chem. Solids **11** (1959) 26.
[5] J. Bobroff *et al.*: Phys. Rev. Lett. **83** (1999) 4381.
[6] *D. Semenok, I. Troyan, A. Sadakov, D. Zhou, M. Galasso, A. Kvashnin, I. Kruglov, A. Bykov, K. Terent'ev, A. Cherepahin, O. Sobolevskiy, K. Pervakov, A. Seregin, T. Helm, T. Förster, A. Grockowiak, S. Tozer, Y. Nakamoto, K. Shimizu, V. Pudalov, I. Lyubutin, A. Oganov: Adv. Mater.* ***34*** *(2022) 2204038.*
[7] D. Semenok *et al.*: Mater. Today **48** (2021) 18.
[8] S. Chen *et al.*: Natl. Sci. Rev. (2023) nwad107.
[9] R. P. Reed and A. F. Clark: Advances in Cryogenic Engineering Materials, Plenum Press, NY (1980).

Three-dimensional visualization of magnetization reversal behavior inside a high-performance Nd–Fe–B permanent magnet

Technological innovation is strongly required in various fields to achieve carbon neutrality by 2050. To this goal, materials science and material development technology can significantly contribute. For example, high-performance permanent magnets are one of the essential materials for developing environmental and energy-saving technologies, which are used in driving motors for electric vehicles, compressors for air conditioners, wind power generators, and other applications. Further improvement in the magnetic properties of permanent magnet materials, such as coercivity and maximum energy product, can improve the energy efficiency of the environmentally important applications above.

Coercivity is one of the most important measures of magnet performance. Materials with higher coercivity are harder to reverse their magnetization to maintain a strong magnetic force even under high demagnetization fields and high-temperature environments, such as inside a driving motor housing. Moreover, coercivity is closely related to another characteristic called magnetic hysteresis in the magnetization curve. In general, permanent magnet materials have a wide hysteresis loop and, correspondingly, a high coercivity. Nd–Fe–B is a typical material with considerable magnetic hysteresis to exhibit high coercivity as a strong permanent magnet.

Consequently, the development of permanent magnet materials is aimed at increasing the magnetic hysteresis and coercivity further to achieve ultimate performance that exceeds that of currently used Nd–Fe–B magnets. Even though coercivity is a fundamental property of permanent magnets, the mechanism that causes high coercivity has remained unresolved for more than 100 years since the start of magnetism research. It is necessary to clarify the mechanism of high coercivity to develop permanent magnet materials with excellent performance.

One key to understanding the coercivity mechanism is the material's microstructure. Nd–Fe–B sintered magnets are made by sintering $Nd_2Fe_{14}B$ grains with diameters of a few microns or less. The material has a microstructure that consists of $Nd_2Fe_{14}B$ main phase grains, Nd-rich phases containing metallic Nd and Nd oxides of different compositions, and a grain boundary phase containing alloys of Fe, Nd, Cu, and other rare-earth elements. The macroscopic magnetic properties of a bulk Nd–Fe–B magnet are the sum of the magnetization of millions of $Nd_2Fe_{14}B$ grains. Therefore, the microscopic coercivity mechanism can be understood if the magnetization reversal process of individual internal grains can be observed. For this purpose, magnetic microscopy studies have been performed on Nd–Fe–B magnets using different magnetic imaging techniques, including magneto-optical Kerr microscopy (MOKE), magnetic force microscopy (MFM), magnetic scanning electron microscopy (magnetic SEM), scanning X-ray transmission microscopy (STXM), and photoemission electron microscopy (PEEM). However, these conventional magnetic imaging techniques are only applied to the sample surface to obtain two-dimensional (2D) magnetization distribution images, namely, magnetic domains in 2D. They cannot be used to obtain three-dimensional (3D) images of internal magnetic domains.

Recently, several research groups have developed a 3D magnetic microscopy technique called X-ray magnetic tomography [1-4]. In X-ray magnetic tomography measurement, a number of 2D projection images with magnetic contrasts using X-ray magnetic circular dichroism (XMCD) are taken at different sample rotation angles. Then, a dedicated reconstruction algorithm is applied to the magnetic projection data to obtain a 3D image of the magnetization distribution inside the sample. At SPring-8 **BL39XU**, a scanning hard X-ray magnetic tomography technique has been developed [1]. This technique has enabled 3D magnetic domain imaging with a spatial resolution of 360 nm, and the observation is possible under a magnetic field of 1 T.

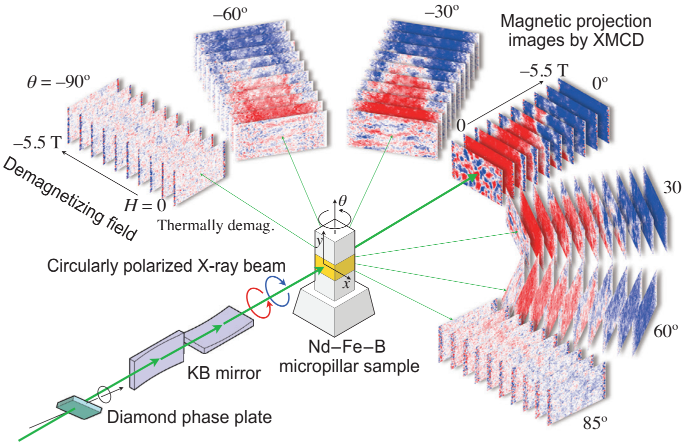

Fig. 1. Schematic of scanning hard X-ray magnetic tomography measurements of high-performance permanent magnet, performed at SPring-8 BL39XU.

In this study, we applied the X-ray magnetic tomography technique to a high-performance permanent magnet material to directly observe magnetic domain structures inside a bulk sample in 3D [5]. Figure 1 shows a schematic of our experiment. The sample was a state-of-the-art fine-grained Nd–Fe–B sintered magnet fabricated by pressless sintering and grain boundary diffusion processes with Tb–Cu eutectic alloy. Its average grain diameter is ~1 μm and its coercivity was 2.7 T. A bulk sample was fabricated into a micropillar with dimensions of 18×18×50 μm^3 by a focused ion beam technique. To study the evolution of internal magnetic domains during the demagnetization process, we used an offline electromagnet and a superconducting magnet to apply a high magnetic field. The sample was initially fully magnetized by applying a +5.5 T field along the easy magnetization direction (parallel to the *c*-axis). X-ray magnetic tomography measurement was performed at the remanent state after the demagnetizing field was applied to the sample, and it was repeated with increasing demagnetizing field from 0 to –5.5 T across the coercivity of 2.7 T.

Figure 2(a) shows the reconstructed 3D density map showing the microstructure and magnetic domain structure in the same observation area of 18×18×10 μm^3, which contains about 4000 grains. The high resolution microstructure image was obtained by 3D scanning electron microscopy (3D-SEM) with by the corresponding image from conventional X-ray tomography, while the magnetic domain image was obtained by X-ray magnetic tomography measurement at the Nd L_2 edge. These 3D images allow us to determine the correlation between the internal microstructure and magnetic domains. Figure 2(b) demonstrates the variation of the internal magnetic domain structures at different demagnetizing fields along the hysteresis curve. We successfully visualized the magnetization reversal behavior of individual magnetic grains with a diameter of ~1 μm. By carefully examining the correlation between the variation of magnetic domains and the microstructure, we have identified some grains that serve as the intrinsic nucleation and annihilation sites of magnetic domains, namely, the departing and terminating points of magnetization reversal, respectively. Moreover, unexpected behaviors of local magnetic domains have been observed, such as magnetic domains formed by chains of reversed magnetic grains connecting perpendicularly to the easy magnetization direction and grains whose magnetization reverses back against the demagnetizing field increase. These unnatural behaviors of the local magnetic domains are probably due to a reformation of the magnetic domains caused by a significant change in the local magnetostatic interaction field.

In summary, our X-ray magnetic tomography study demonstrated an actual microscopic picture of the magnetization reversal behavior in high-performance Nd–Fe–B permanent magnets. The results can provide information useful for clarifying the coercivity mechanism. The observed 3D magnetic and microstructural images will be used as an excellent model in micromagnetic simulations based on our practical experiment to improve calculation accuracy and reliability. The results of this study will open new doors to the study and design of new permanent magnet materials.

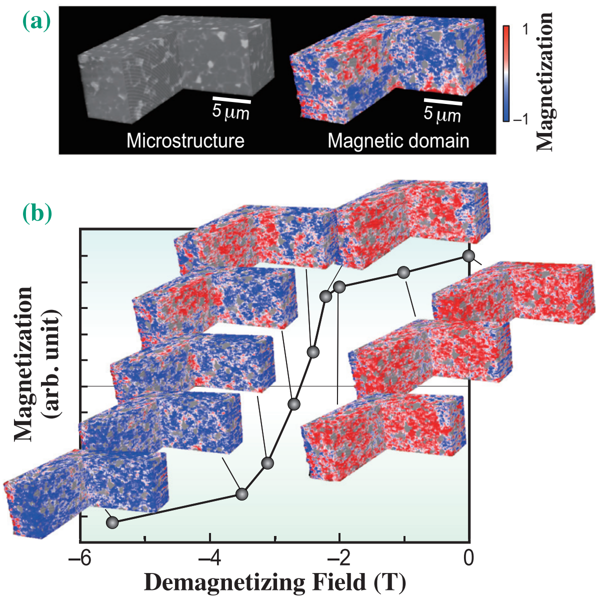

Fig. 2. Three-dimensional reconstructed images of **(a)** microstructure (left) and magnetic domain structure (right) inside a fine-grained Nd–Fe–B sintered magnet. **(b)** Variation of the magnetic domain structure as a function of demagnetizing field along the magnetic hysteresis curve [5].

Motohiro Suzuki[a,*] and Satoshi Okamoto[b]

[a] School of Engineering, Kwansei Gakuin University
[b] Institute of Multidisciplinary Research for
Advanced Materials (IMRAM), Tohoku University

* Email: m-suzuki@kwansei.ac.jp

References

[1] M. Suzuki *et al*.: Appl. Phys. Express **11** (2018) 036601.
[2] C. Donnelly *et al*.: Nature **547** (2017) 328.
[3] A. Hierro-Rodríguez *et al*.: Nat. Comm. **11** (2020) 1.
[4] S. Seki *et al*.: Nat. Mater. **21** (2022) 181.
[5] *M. Takeuchi, M. Suzuki, S. Kobayashi, Y. Kotani, T. Nakamura, N. Kikuchi, A. Bolyachkin, H. Sepehri-Amin, T. Ohkubo, K. Hono, Y. Une and S. Okamoto: NPG Asia Mater.* ***14*** *(2022) 70.*

Direct visualization of three-dimensional shape of magnetic skyrmion string

In recent years, the swirling texture of electron spins, called “magnetic skyrmions”, that appear in magnetic materials has attracted considerable attention. Because of their geometrical stability, extremely small size, and efficient electrical controllability, they are expected to be a promising candidate for information carriers for next-generation ultrahigh density and ultralow power consumption magnetic storage and computation devices [1,2].

Skyrmion is known to have particle-like properties in an ideal two-dimensional system (Fig. 1(a)), and has been experimentally identified using two-dimensional imaging techniques such as Lorentz transmission electron microscopy [1]. On the other hand, recent theoretical studies predict that skyrmions in real three-dimensional systems have the properties of “strings” with spins aligned in a tornado shape (Fig. 1(b)). However, their experimental observation has been considered difficult, because the information along the depth direction is usually lost in the traditional two-dimensional imaging methods. In this context, the development of a novel experimental method to directly visualize three-dimensional shape of skyrmion strings is highly anticipated.

In this study, we focused on a technique called X-ray tomography (which is used in computed tomography (CT) scans for the inspection of the human body), in order to clarify the three-dimensional shape of the skyrmion strings. This approach enables precise reconstruction of the three-dimensional shape of the target object based on two-dimensional transmission images taken from various angles. For this purpose, we constructed an appropriate measurement environment at SPring-8 **BL39XU** (Fig. 1(c)). Here, we employed a circularly polarized X-ray beam to identify the local spin orientation from the X-ray magnetic circular dichroism (XMCD). X-ray energy was tuned at 11.572 keV, in resonance with the L_3 absorption edge of Pt. The X-ray beam was focused to a width of 150 nm for a high spatial resolution, and the sample position was scanned to obtain two-dimensional transmission images. By simultaneously rotating the sample and external magnetic field, such two-dimensional transmission images are taken from various angles, enabling the reconstruction of the three-dimensional distribution of the scalar magnetization component. We applied this technique to a tiny plate-shaped single crystal of non-centrosymmetric magnet $Mn_{1.4}Pt_{0.9}Pd_{0.1}Sn$, which has been reported to produce skyrmions with a diameter of 135 nm at room temperature [3]. As a result, three-dimensional shape of a skyrmion string has been successfully visualized for the first time. This observation experimentally proved the existence of a nearly straight skyrmion string in the sample and also revealed the existence of various defect structures such as interrupted and Y-shaped strings (Fig. 2) [4].

The above results establish a brand new method for the direct observation of the three-dimensional shape of a skyrmion string, which is expected to make a significant contribution to a

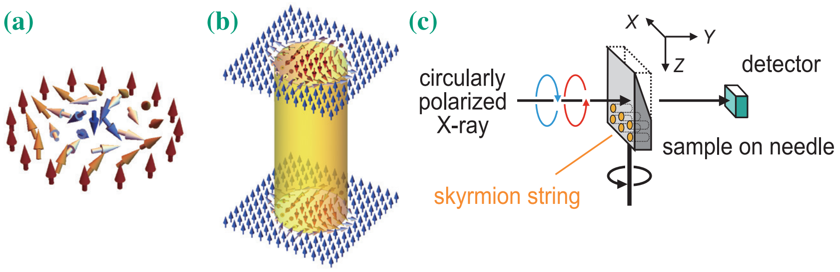

Fig. 1. Schematic illustration of **(a)** a skyrmion particle in a two-dimensional system and **(b)** a skyrmion string in a three-dimensional system, which is characterized by a uniform stacking of two-dimensional skyrmions in the string direction. Arrows indicate the direction of spin. **(c)** Measurement arrangement of the X-ray tomography experiment in this study. Using the two-dimensional XMCD transmission images observed from various angles, we reconstructed the three-dimensional shape of the skyrmion string as shown in Fig. 2.

better understanding of the properties of skyrmions as information carriers. In particular, it is important to understand how a skyrmion string is deformed or pinned in the presence of crystallographic defects in the material when it is driven by an external stimulus such as electric current. The detailed investigation of this process will lead to the elucidation of new guidelines for a more efficient control of skyrmions. According to recent studies, it is also possible to transfer information via the vibration of a skyrmion string, like a tin-can telephone [5]. Since the vibration of such a string does not cause energy loss due to Joule heating (proportional to the square of the current) unlike the current in an electric circuit, skyrmion strings have the potential to be utilized as a rewritable information transmission channel with low power consumption. The present 3D visualization approach allows us to access the unexplored third dimension of skyrmions, which may signal a new phase in the development of skyrmionics.

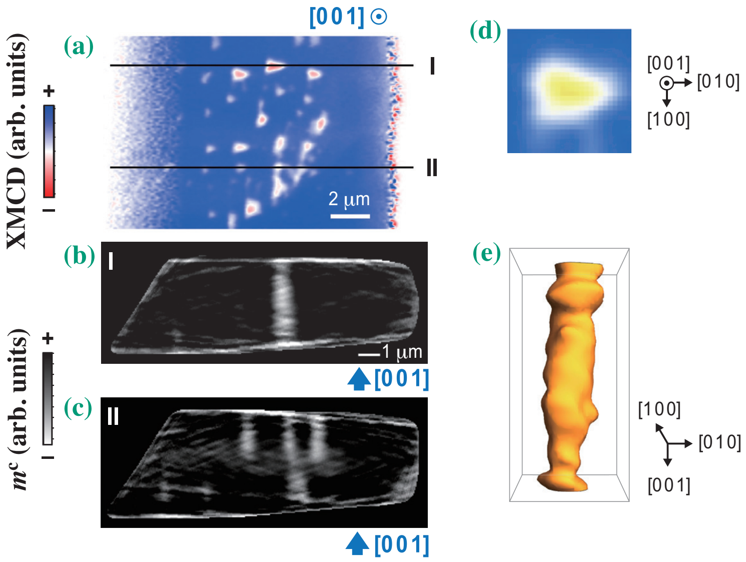

Fig. 2. **(a)** Two-dimensional XMCD transmission image of skyrmion strings in a $Mn_{1.4}Pt_{0.9}Pd_{0.1}Sn$ alloy, observed from the string direction. The background color represents the XMCD intensity and reflects the spin component along the out-of-plane direction. **(b, c)** Cross sections of the three-dimensional spatial distribution of the [001] spin component (m^c) reconstructed from tomographic measurements. In **(b)**, the skyrmion string penetrates from one end of the sample to the other, whereas in **(c)**, the interrupted or Y-shaped skyrmion strings are identified. **(d)** Expanded view of two-dimensional XMCD transmission image of a skyrmion string observed from the string direction. **(e)** Three-dimensional shape of the corresponding skyrmion string obtained from tomographic measurements.

Shinichiro Seki

Department of Applied Physics & Institute of
Engineering Innovation, The University of Tokyo

Email: seki@ap.t.u-tokyo.ac.jp

References

[1] S. Muhlbauer *et al.*: Science **323** (2009) 915.
[2] X. Z. Yu *et al.*: Nature **465** (2010) 901.
[3] A. K. Nayak *et al.*: Nature **548** (2017) 561.
[4] *S. Seki, M. Suzuki, M. Ishibashi, R. Takagi, N. D. Khanh, Y. Shiota, K. Shibata, W. Koshibae, Y. Tokura, T. Ono: Nat. Mater.* ***21*** *(2022) 181.*
[5] S. Seki *et al.*: Nat. Commun. **11** (2020) 256.

Magnetic moments of Fe site in ThMn$_{12}$-type Sm(Fe$_{1-x}$Co$_x$)$_{12}$ compounds and their temperature dependence

With increasing demand for "green technology" to reduce CO_2 emissions, the development of highly efficient electric motors and generators is required. For this, high-performance permanent magnets, especially for traction motors of EVs, HEVs, and turbines of wind power generation, are necessary. Because the working temperature of EV/HEV motors is approximately 150°C, a high coercivity ($\mu_0 H_c$) larger than 0.8 T is necessary at this temperature. Although Nd–Fe–B is the most important permanent magnet material for "green technology," one drawback is its low thermal resistance to $\mu_0 H_c$ owing to its low Curie temperature (T_c) [1]. Therefore, there is a strong demand for the development of new permanent magnets whose magnetic properties are superior to those of Nd–Fe–B, especially at elevated temperatures. One of the candidate materials for the next-generation permanent magnets is an RT$_{12}$-based compound with a ThMn$_{12}$ structure, where R and T represent rare-earth and transition elements, respectively. The RT$_{12}$-based compound is expected to show high saturation magnetization (M_s) owing to its highest Fe composition among rare-earth magnet materials. In addition to the high M_s, it has high Curie temperature (T_c) and high anisotropy (K).

Hirayama *et al*. reported that Sm(Fe$_{0.8}$Co$_{0.2}$)$_{12}$ has the intrinsic magnetic properties of $M_s \sim 1.78$ T, anisotropy field of 12 T and $T_c \sim 859$ K, which are superior to those of Nd$_2$Fe$_{14}$B [2]. Thus, Sm(Fe$_{0.8}$Co$_{0.2}$)$_{12}$ is attracting attention as a new permanent magnetic material. Since these magnets are used in various applications at various temperatures, this study was conducted to clarify the internal magnetic field of Sm(Fe$_{0.8}$Co$_{0.2}$)$_{12}$ thin films and its temperature dependence.

Figure 1 shows (a) magnetization curves, (b) the temperature dependence of the magnetization and (c) the temperature dependence of the normalized magnetization in Sm(Fe$_{1-x}$Co$_x$)$_{12}$ (x = 0, 0.07, 0.2) thin films. All samples show strong perpendicular anisotropy. Saturation magnetization and Curie temperature increase with Co content. The thermal resistance in the saturation magnetization is the highest in the sample with x = 0.2. Figure 2 shows the (a) Mössbauer spectrum and fitting curves, and (b) temperature and (c) Co composition dependences of the Mössbauer spectrum of SmFe$_{12}$ thin films at 300 K. The ^{57}Fe Mössbauer spectra were measured in the temperature range of 80–523 K at SPring-8 **BL11XU**. The Mössbauer spectra were nicely fitted by three different Fe sites of 8i, 8j and 8f. The disappearance of 2nd and 5th absorptions corresponds to the strong (001) texture of SmFe$_{12}$, which shows good agreement with the XRD result [3]. The fitting parameters are summarized in the inset. The hyperfine field decreases with increasing temperature and increases with Co content. Figure 3 shows the temperature dependence of (a) average and (b) normalized magnetic moments in Sm(Fe$_{1-x}$Co$_x$)$_{12}$ (x = 0, 0.07, 0.2) thin films. These temperature dependences well match with those of the magnetization of the sample shown in Fig. 1. Figure 3(c) shows the change in hyperfine field as a function of the Fe–Fe distance. The Fe–Fe distance was estimated by XRD analysis. The magnetic moment of Fe linearly increases with the Fe–Fe distance, and the effect is similar for all Co

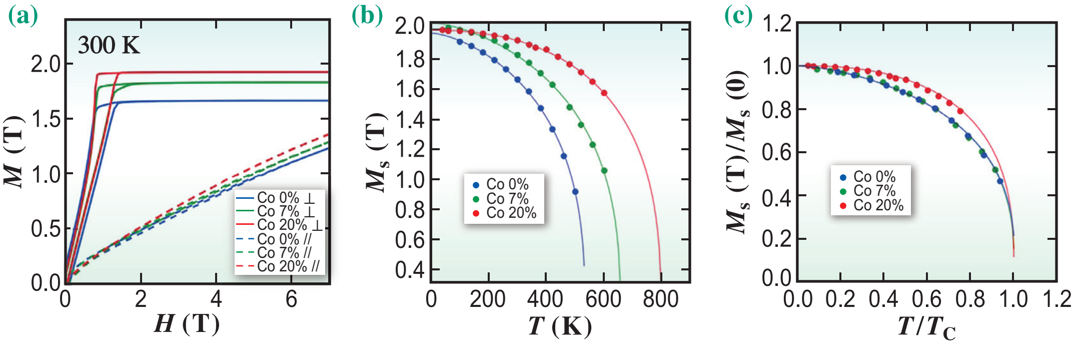

Fig. 1. **(a)** Magnetization curves of Sm(Fe$_{1-x}$Co$_x$)$_{12}$ thin films (x = 0, 0.07, 0.2) measured perpendicular and parallel to film plane at 300 K, **(b)** temperature dependence of spontaneous magnetization, $\mu_0 M_s$, and **(c)** normalized saturation magnetization $\mu_0 M_s/\mu_0 M_s(0)$ *versus* normalized temperature T/T_C of Sm(Fe$_{1-x}$Co$_x$)$_{12}$ (x = 0, 0.07, 0.2) thin films. [3]

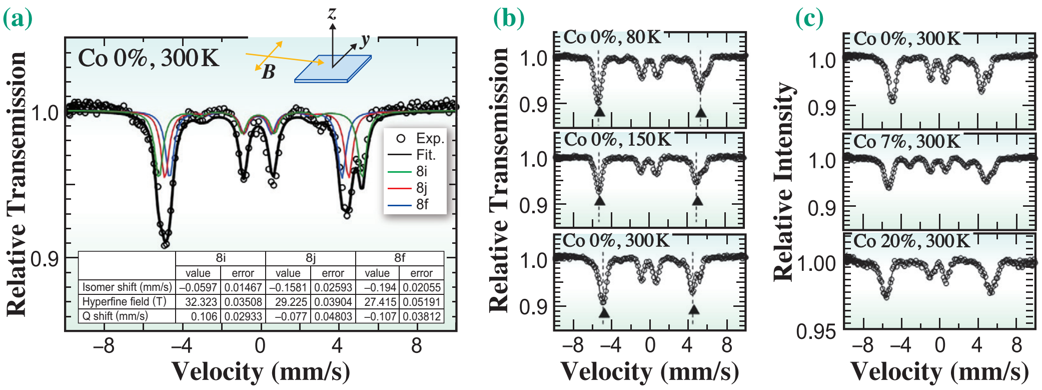

	8i		8j		8f	
	value	error	value	error	value	error
Isomer shift (mm/s)	–0.0597	0.01467	–0.1581	0.02593	–0.194	0.02055
Hyperfine field (T)	32.323	0.03508	29.225	0.03904	27.415	0.05191
Q shift (mm/s)	0.106	0.02933	–0.077	0.04803	–0.107	0.03812

Fig. 2. **(a)** Mössbauer spectrum of $SmFe_{12}$ thin films measured at 300 K with fitting curves using three independent spectra for 8i, 8j, and 8f Fe sites, **(b)** temperature dependence of Mössbauer spectrum of $SmFe_{12}$ thin films, and **(c)** Co content dependence of Mössbauer spectrum of $Sm(Fe_{1-x}Co_x)_{12}$ thin films at 300 K. The dash line and arrows in (b) show the peak positions of 1st and 6th lines at each temperature. [3]

contents; the interdependence of the Fe–Fe distance and Fe magnetic moment is caused by the magneto-volume effect associated with *d*-orbital electrons. The increase in Fe magnetic moment upon Co addition is independent of the Fe–Fe interstitial distance and is similar to the trend shown in Fig. 1.

In conclusion, we first investigated the dependences of temperature and Co composition on the magnetic moment of crystallographically different Fe sites in $Sm(Fe_{1-x}Co_x)_{12}$ (x = 0, 0.07, 0.2) thin films by *in situ* synchrotron Mössbauer spectroscopy. The microscopic origin of the magnetism and temperature dependence of $Sm(Fe_{1-x}Co_x)_{12}$ (x = 0, 0.07, 0.2) thin films is clarified by experiments and theoretical calculations.

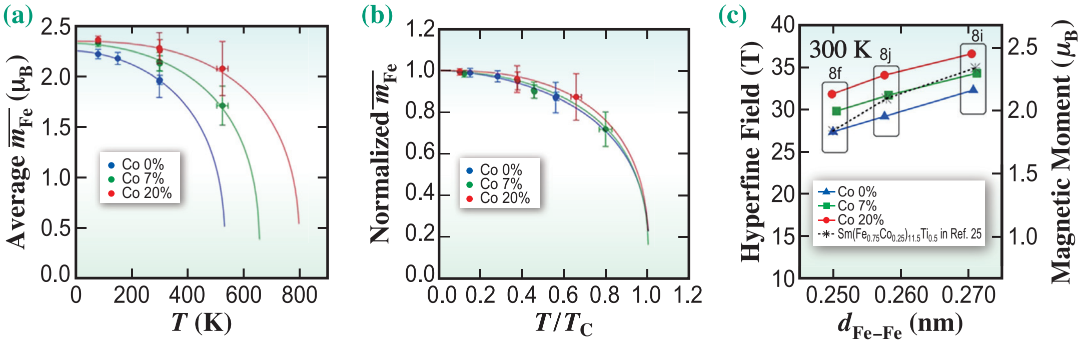

Fig. 3. **(a)** Temperature dependence of magnetic moments at various Co contents and **(b)** normalized magnetic moments at various Co contents site *versus* normalized temperature for $Sm(Fe_{1-x}Co_x)_{12}$ thin films (x = 0, 0.07, 0.2). **(c)** Calculated results of normalized magnetic moments at each Fe site *versus* reduced temperature for $Sm(Fe_{1-x}Co_x)_{12}$ compounds (x = 0, 0.07, 0.2).

Yukiko K. Takahashi

National Institute for Materials Science

Email: TAKAHASHI.Yukiko@nims.go.jp

References

[1] M. Sagawa *et al.*: J. Appl. Phys. **55** (1984) 2083.
[2] Y. Hirayama *et al.*: Scr. Mater. **138** (2017) 62.
[3] *D. Ogawa, T. Fukazawa, S. Li, T. Ueno, S. Sakai, T. Mitsui, T. Miyake, S. Okamoto, S. Hirosawa, Y. K. Takahashi: J. Magn. Magn. Mater.* ***552*** *(2022) 169188.*

Road to X-ray science beyond 100 Tesla

Conventionally, in the research of condensed matter physics, the magnetic field of a few tesla is used as a valuable tool to reveal properties of materials by directly acting on magnetic moments, such as electron spin, orbital motion, and nuclear spins, in a perturbative manner. Using high magnetic fields beyond 10 T, various phase transitions, not only magnetic phase transitions in spin systems but also electronic phases such as superconductivity, charge density wave, multiferroic phase, and metal-insulator transitions, can be induced. This reminds us of the fact that electron spins play crucial roles in the formation of not only magnetic phases but also electronic phases.

On the other hand, condensed matter physics beyond 100 T remains a frontier. It is still unknown what happens to condensed matter when placed under magnetic fields well exceeding 100 T. There are two reasons. One is that the magnetic field is so large that the effects are considered *nonperturbative* in many ways. Hence, theoretical predictions are difficult. The other reason is that, experimentally, producing a magnetic field beyond 100 T requires an uncommon technique called destructive pulse magnets (DPMs). With DPMs, the explosion of coils, pulse durations of a few microseconds, and very large instruments are unavoidable. Currently, a few systems have been installed in large facilities around the world. This situation prevents the casual investigation of material properties above 100 T.

We have made efforts to cultivate the frontiers beyond 100 T and have started to discover marked changes in lattice structures induced at ultrahigh magnetic fields. At the Institute for Solid State Physics, University of Tokyo, we generated 1200 T using the newly developed system based on the electromagnetic flux compression technique in 2018 [1]. Furthermore, we developed techniques to measure the properties of materials such as magnetization, electric conductivity, and magnetostriction [2]. Using those techniques, we revealed exotic phase transitions possibly involving large lattice changes, such as the ferromagnetic phase transition of solid oxygen [3], the metal-insulator transition of VO_2 [4], and possible excitonic phases in $LaCoO_3$ [5,6]. All these findings are based on the measurements of the macroscopic properties of materials. To obtain concrete evidence that we have altered the lattice structures using magnetic fields, we regard complementary microscopic measurements such as X-ray diffraction and spectroscopy measurements to be essential. However, our magnetic field generators are very large and therefore not transportable.

In the present study [7], we devise a new instrument called Portable INtense Kyokugenjiba (PINK-01), as shown in Figs. 1(a-c) and Figs. 2(a-c). PINK-01 is a portable DPM system with a weight of less than 1 ton that is capable of generating pulsed high magnetic fields by the single-turn coil technique. The maximum magnetic field is 77 T in a room temperature bore of 2.5 mm diameter, which is the world's highest field obtained with a portable system. Owing to its portability, we transported PINK-01 to the X-ray free electron laser (XFEL) facility SACLA. At SACLA **BL3**, we carried out the first X-ray diffraction (XRD) experiment at 77 T with XFEL, PINK-01, and a sample of perovskite manganite, $Bi_{0.5}Ca_{0.5}MnO_3$ (BCMO), that shows the charge-ordered phase.

As shown in Figs. 3(a-c), we were successful in observing the lattice changes in the sample of BCMO

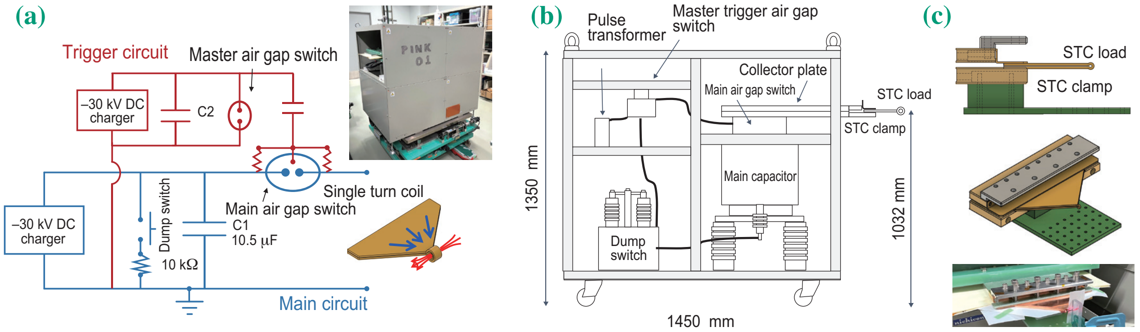

Fig. 1. **(a)** Electric circuit, **(b)** side view of the discharge unit, and **(c)** views of the single-turn coil clamps of PINK-01.

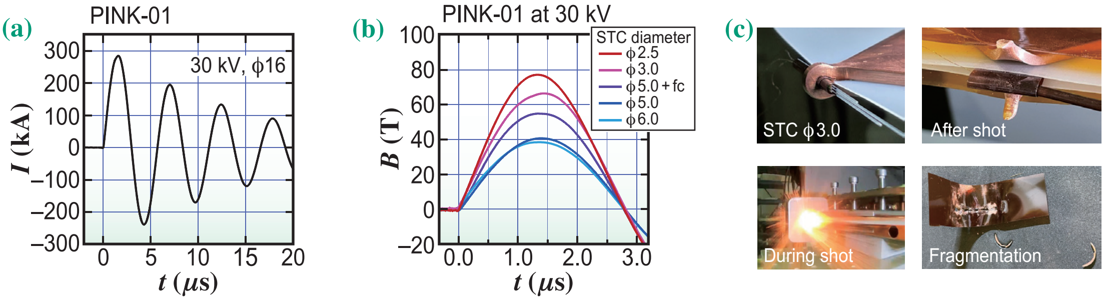

Fig. 2. Waveforms of **(a)** discharged current and **(b)** generated magnetic fields, and **(c)** views of the single-turn coil before, during, and after discharge, obtained using PINK-01.

by using X-rays. The lattice change is considered to be due to the magnetic-field-induced melting of the charge-ordered phase. The result is evidence that we are now capable of the microscopic measurement of materials at high magnetic fields of 77 T, which opens a door to a new era of material science at ultrahigh magnetic fields with microscopic measurements.

As future directions, we are now working on two things. One is the development of a low-temperature environment by means of a small original handmade He flow cryostat to realize XFEL experiments at low temperatures and high magnetic fields. The cryostat must be as small as ϕ4.0 mm including the vacuum shield. The other is the development of PINK-02 with the aim of generating magnetic fields of 100 T and beyond. Armed with such equipment, we play to attempt the structural analysis of the θ phase of solid oxygen, the spin-state crystallization of spin crossover cobaltites, and the valence-induced structural transition of Eu compounds, for starters. As a further goal, we hope to expand our targets to chemistry, biology, plasmas, and quantum vacuums.

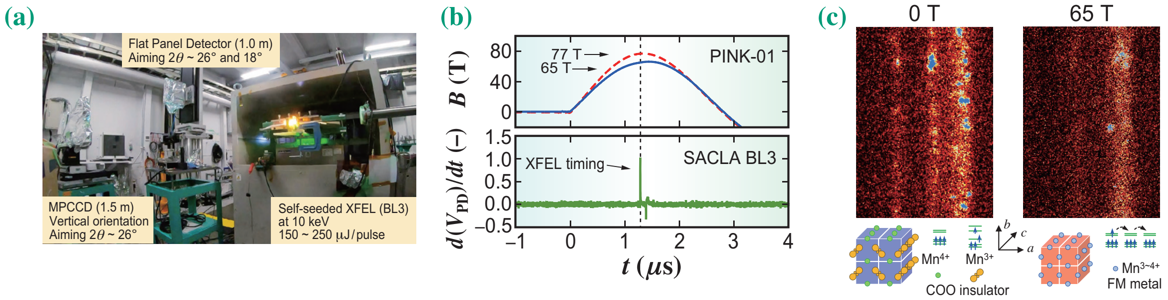

Fig. 3. **(a)** Photograph of PINK-01 in experimental hutch 2 at SACLA BL03 during the simultaneous discharge of magnetic field and XFEL pulses. A flat panel detector and an MPCCD are used as detectors. **(b)** The magnetic field and XFEL timing are well synchronized. **(c)** Part of the Debye-Scherrer rings from BCMO before and during the magnetic field pulse up to 65 T. The marked lattice change is apparent.

Akihiko Ikeda[a,*] and Yasuhiro H. Matsuda[b]

[a] Department of Engineering Science,
University of Electro-Communications
[b] Institute for Solid State Physics, University of Tokyo

*Email: a-ikeda@uec.ac.jp

References

[1] D. Nakamura *et al.*: Rev. Sci. Instrum. **89** (2018) 095106.
[2] A. Ikeda *et al.*: Rev. Sci. Instrum. **88** (2017) 083906.
[3] T. Nomura *et al.*: Phys. Rev. Lett. **112** (2014) 247201.
[4] Y. H. Matsuda *et al.*: Nat. Commun. **11** (2020) 3591.
[5] A. Ikeda *et al.*: Phys. Rev. Lett. **125** (2020) 177202.
[6] A. Ikeda *et al.*: Nat. Commun. **14** (2023) 1744.
[7] *A. Ikeda, Y. H. Matsuda, X. Zhou, S. Peng, Y. Ishii, T. Yajima, Y. Kubota, I. Inoue, Y. Inubishi, K. Tono, M. Yabashi: Appl. Phys. Lett.* ***120*** *(2022) 142403.*

Coherent achromatic rotational reflective optics for ptychography (CARROT) at SPring-8 BL07LSU

With its high spatial resolution and various techniques for analyzing physical properties, X-ray microscopy has been applied in many fields, such as biology and materials science. Soft X-ray microscopy is particularly suited to investigating the physical properties of light-element-rich heterogeneous structures, such as biological cells and polymeric materials. For example, in combination with X-ray absorption spectroscopy, it has been used to map the chemical states of nanoparticles in magnetic bacteria [1] and to visualize the degradation mechanism of Li-ion battery materials [2].

Conventional soft X-ray microscopes have been developed using zone plates [3]. However, chromatic aberration of zone plates makes soft X-ray imaging of multiple elements difficult. In addition, the relatively short working distance makes it a challenge to apply a soft X-ray microscope to various *in situ* /*operando* applications. In this study [4], we developed a new soft X-ray microscope with Wolter mirror optics. The total reflection property of the Wolter mirror is ideal for spectroscopic measurements corresponding to the absorption edges of different elements at multiple wavelengths. We combined the Wolter mirror optics with the ptychography method [5] to achieve a high spatial resolution. Ptychography is a lensless imaging technique for reconstructing sample images from coherent diffraction patterns and can achieve high spatial resolution and sensitivity owing to the redundancy of input information.

Figure 1 shows a photograph and schematic diagram of the developed soft X-ray ptychography system. The system was constructed at the University of Tokyo Materials Science Beamline at SPring-8 **BL07LSU**. The orange cylindrical component in Fig. 1(a) is a 200-mm-long Wolter mirror newly developed as the illumination optics for soft X-ray ptychography. The system is named CARROT after Coherent Achromatic Rotational Reflective Optics for pTychography. The resolution of CARROT was evaluated using a test chart, and it was confirmed that a half-period resolution of 50 nm can be achieved with a broad photon-energy range from 250 eV to 2 keV while maintaining the focal position.

To demonstrate the application of CARROT, biological cell samples were measured with a 600 eV soft X-ray. The samples were Chinese hamster ovarian cancer (CHO-K1) cells grown on a 200-nm-thick silicon nitride thin film and chemically fixed with paraformaldehyde. The cells were approximately 5 μm thick. The internal structures of such thick cells are generally difficult to observe by electron microscopy without thinning. Figure 2 shows a typical example of a cell image observed with CARROT. The absorption and phase images of the cell are shown in the left and right areas of Fig. 2, respectively. The magnified images in the lower row are taken from areas corresponding to the dotted rectangles shown in the upper-right absorption image of the cell. Each magnified image corresponds to a pseudopodal structure of the cancer

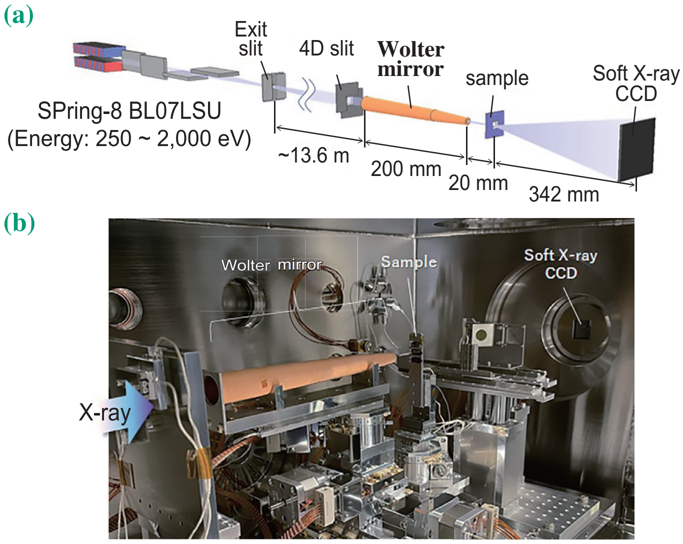

Fig. 1. Schematic diagram **(a)** and photograph **(b)** of CARROT at SPring-8 BL07LSU.

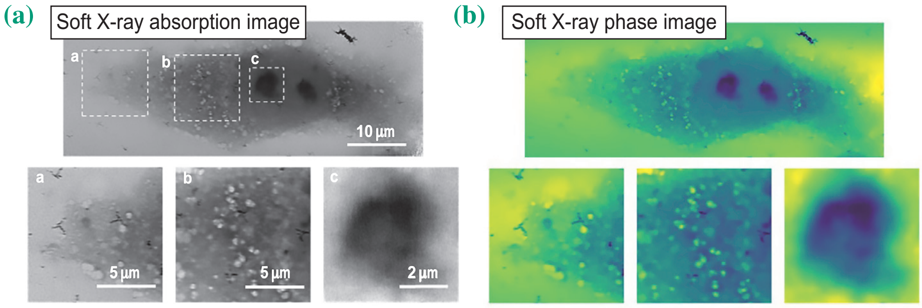

Fig. 2. Retrieved absorption **(a)** and phase **(b)** images of the CHO-K1 cell measured by CARROT. The retrieved image was measured at 600 eV.

cell, organelles such as the endoplasmic reticulum and mitochondria, and the nucleolus. Ptychography can quantitatively determine the amount of phase shift as well as the absorption rate of the sample in response to X-rays. Highly sensitive imaging of both absorption and phase is one of the advantages of ptychography compared with conventional soft X-ray microscopy. Intracellular structures of various thicknesses ranging from micrometers to nanometers, shown in Fig. 2, have been clearly imaged without saturation using highly sensitive absorption and phase imaging of soft X-ray ptychography with CARROT.

Figure 3 shows the phase images of the cell measured at 250 eV, 350 eV, 450 eV, 600 eV, and 1200 eV. Thanks to the achromatic feature of the Wolter mirror optics, we could seamlessly obtain the cell image at largely different wavelengths across the absorption edges of light elements. This demonstration measurement shows the ability to extend CARROT to combine soft X-ray ptychography with absorption spectroscopy of essential elements for biological samples such as carbon, nitrogen, and oxygen.

This element- and molecule-selective, high-resolution imaging technology is expected to be a powerful tool for the analysis of small molecules and other substances that are difficult to image with visible-light fluorescence microscopy.

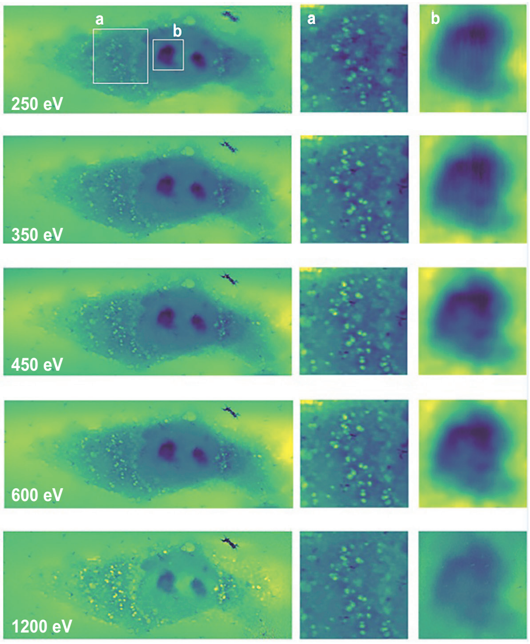

Fig. 3. Phase images of the CHO-K1 cell measured at 250 eV, 350 eV, 450 eV, 600 eV, and 1200 eV.

Takashi Kimura[a,*] and Yoko Takeo[a,b]

[a] The Institute for Solid State Physics,
The University of Tokyo
[b] Japan Synchrotron Radiation Research Institute (JASRI)

*Email: tkimura@issp.u-tokyo.ac.jp

References

[1] X. Zhu *et al.*: Proc. Natl. Acad. Sci. USA **113** (2016) E8219.
[2] T. Sun *et al.*: ACS Nano **15** (2021) 1475.
[3] B. Rösner *et al.*: Optica **7** (2020) 1602.
[4] *T. Kimura, Y. Takeo, K. Sakurai, N. Furuya, S. Egawa, G. Yamaguchi, Y. Matsuzawa, T. Kume, H. Mimura, M. Shimura, H. Ohashi, I. Matsuda, and Y. Harada: Opt. Express **30** (2022) 26220.*
[5] F. Pfeiffer: Nat. Photonics **12** (2018) 9.

Phonon dispersion curve of the organic semiconductor rubrene

Organic semiconductors are now commercially available for electronic devices. The carrier transport mechanism in them is, unlike that in inorganic semiconductors, believed to involve phonons. Local modes that cause molecular deformation alter molecular orbitals, and nonlocal modes alter intermolecular transfer integrals. Both of them break the periodicity, and thus, scatter the carriers. The flexibility of the organic materials makes the importance of lattice vibration prominent. However, experimental observations of the phonon dispersion of organic semiconductors are scarce. There is only one clear report on it: the neutron inelastic scattering measurement on deuterated naphthalene $C_{10}D_8$ single crystal [1]. Although deuteration is needed to perform the neutron inelastic scattering measurements, it alters the lattice vibration frequency as well as the electronic property of molecular crystals. To avoid deuteration, inelastic X-ray scattering (IXS) is employed [2] for the measurement of the phonon dispersion of rubrene $C_{42}H_{28}$, one of the most studied organic semiconductors.

Single crystals of rubrene were grown by the physical vapor transport method. The typical size of the crystals was 4 mm × 1 mm × 0.1 mm along the orthorhombic *a*, *b*, and *c* directions. The lattice parameters were $a = 7.18$ Å, $b = 14.43$ Å, and $c = 26.9$ Å. The large unit cell makes the Brillouin zone small, and the number of phonon branches is 420. These characteristics result in a heavy overlap of the phonon branches, which makes the experimental observation of phonon dispersion difficult. We overcome the difficulties by using density functional theory (DFT) calculations, thermal diffuse scattering (TDS) measurement, and the IXS techniques.

DFT calculation provides the eigenmodes characterized by the wavevector $\boldsymbol{q} = (0, 0, 0)$. The modes were indexed in the order of increasing energy. Modes 1–3 are acoustic modes. We constructed atomic displacement models for the modes characterized by various $\boldsymbol{q}$ vectors using the calculated $\boldsymbol{q} = (0, 0, 0)$ modes to derive the TDS intensity distribution caused by them. The calculated total TDS intensity distribution is obtained as an incoherent sum of the distributions caused by the 25 lowest energy modes. It is presented in Fig. 1 together with the measured value. The TDS intensity distribution at room temperature was measured with an 18 kW Mo $K\alpha$ X-ray generator and a standard four-circle diffractometer. The results appear similar, which validates the mode-discriminated TDS calculation based on $\boldsymbol{q} = (0, 0, 0)$ modes. Since the IXS is a means of measuring the energy spectra of the TDS, we selected the Brillouin zone to measure the IXS to determine the dispersion of specific modes using this information.

The IXS measurements were performed at SPring-8 **BL35XU**, with 1.5 meV resolution optics. Typical inelastic spectra along the $(6, 1+\eta, 0)$-, $(0, 10-\eta, 0)$- and $(0, \eta, 12)$-lines are presented in Fig. 2. There are strong Bragg reflections at $\eta = 0$ positions. Therefore, the signal from acoustic-mode phonons characterized by the wavevector $(0, \eta, 0)$ is observed at the $\eta < 0.5$ regions. Phonon dispersion at $\boldsymbol{q} = (0, 0, 0)$ is directly related to the sound velocity and elastic constants. The elastic stiffness obtained by the present IXS measurement is similar to the values obtained from Brillouin scattering [3], except for the systematic difference of ~25%.

The IXS peak positions in the $\eta > 0.5$ regions show the optical mode phonons characterized by the wavevector $(0, 1-\eta, 0)$. According to the mode-discriminated TDS intensities presented in Figs. 2(a–c), the spectra presented in Figs. 2(d–f) reflect the dispersions of modes 5, 13 and 4, respectively. The phonon dispersion relations of the acoustic modes and some optical modes are derived in the same manner, as shown in Fig. 3. The shape of the Brillouin zone is presented in panel (a), and the dispersions along $\boldsymbol{a}^*$, $\boldsymbol{b}^*$, and $\boldsymbol{c}^*$ directions in the *B*-centered orthorhombic cell are shown in panel (b). There is one interesting finding; the phonon energies measured on the $(0, 10-\eta, 0)$ line, which should reflect the energy of the

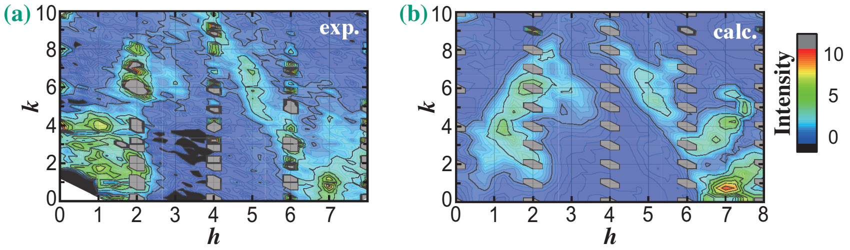

Fig. 1. **(a)** TDS intensity distribution on the $(hk0)$ plane measured with Mo $K\alpha$ X-ray. Reciprocal lattice points were not measured. **(b)** Calculated TDS intensity map on the same plane.

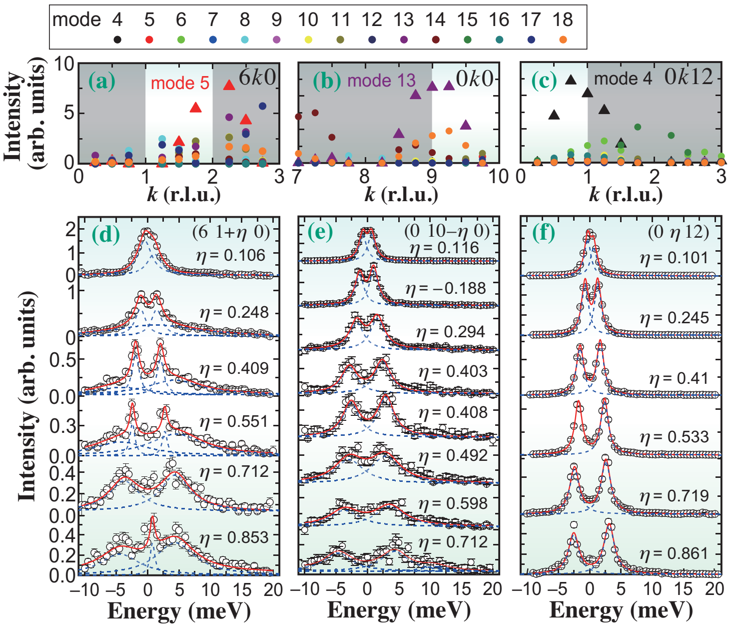

Fig. 2. **(a–c)** Calculated mode-discriminated TDS intensity along the (a) (6, *k*, 0), (b) (0, *k*, 0) and (c) (0, *k*, 12) lines. **(d–f)** IXS spectra measured along (6, 1+η, 0), (0, 10−η, 0), and (0, η, 12) lines.

longitudinal acoustic (LA) mode, are the same as those of the transverse acoustic (TA) mode shown in the Γ-Y line in Fig. 3(b). The energy of the LA mode is usually twice as large as that of the TA mode; thus, this feature appears physically unreasonable. We have interpreted this as the mixing of the local mode with the nonlocal mode. The molecules are significantly deformed by the acoustic mode phonons, which reduces the scattering intensity corresponding to the LA mode on the (0, 10−η, 0) line and increases the signal from the TA mode on the (6, 1+η, 0) line. Such mode mixing is expected in short-wavelength modes, but in the present case, the mixing is observed even in the mode with the wavelength of 14 nm.

The phonon dispersion of the most studied organic semiconductor rubrene was clearly observed experimentally. The procedure for measuring the phonon energies of particular modes was demonstrated. This knowledge provides a robust basis for the study of organic semiconductors.

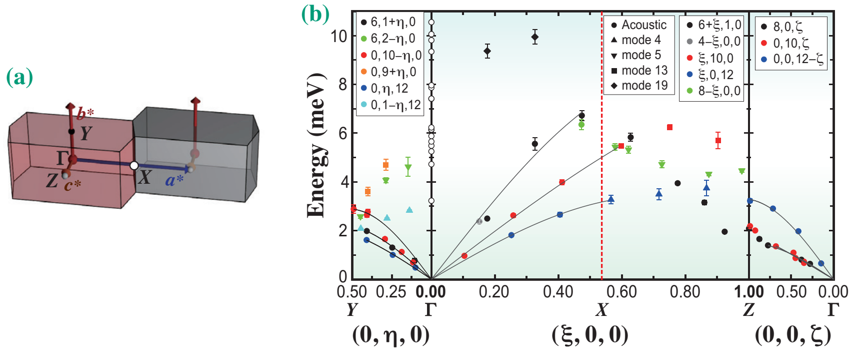

Fig. 3. **(a)** Brillouin zone and **(b)** phonon dispersion relation of rubrene. The closed symbols show the experimentally observed phonon energies. The symbol color represents the measured position in the reciprocal space, and the symbol shape represents the phonon mode. The open symbols on the Γ point show the calculated energies.

Yusuke Wakabayashi

Department of Physics, Tohoku University

Email: wakabayashi@tohoku.ac.jp

References

[1] I. Natkaniec *et al.*: J. Phys. C: Solid State Phys. **13** (1980) 4265.
[2] *K. Takada, K. Yoshimi, S. Tsutsui, K. Kimura, K. Hayashi, I. Hamada, S. Yanagisawa, N. Kasuya, S. Watanabe, J. Takeya and Y. Wakabayashi: Phys. Rev. B **105** (2022) 205205.*
[3] Y. Zhang *et al.*: Appl. Phys. Lett. **110** (2017) 071903.

Direct observation of local structure deformation induced by X-ray irradiation in κ-(BEDT-TTF)$_2$Cu[N(CN)$_2$]Br by X-ray fluorescence holography

κ-(BEDT-TTF)$_2X$, where X is an anion molecule, is a family of organic crystals that has attracted significant attention in strongly correlated electron physics [1]. It is a bandwidth-controlled Mott transition system, where pressure or molecular substitution allows the control of the strength of electron correlation. It was reported that X-ray irradiation induces permanent local defects that affect their electronic properties. In particular, it has been reported that random defects induced by irradiation enhance Anderson-type electron localization in the organic superconductor κ-(BEDT-TTF)$_2$Cu[N(CN)$_2$]Br or κ-Br [1,2]. Contrary to Mott metal-insulator (MI) transitions, the electron localization in Anderson insulators is a result of the interference of electron wave functions due to disorder.

Experimentally, these defects have not been directly observed. No changes were observed in diffraction images even after long irradiation. By infrared optical conductivity spectroscopy, suppression of the vibration modes associated with the C–N and C≡N bonds of the dicyanamide (DCA) molecules in the anion layer was observed in the irradiated κ-Br (Fig. 1(a)) [1], suggesting that these defects are limited to the anion layer. First principles calculations have shown that these can be described by the "bond-shift" (BS) model [3], where irradiation breaks C–N bonds in the DCA molecules, and a C≡N fragment connects with a N–C≡N fragment of an adjacent broken DCA molecule (Fig. 1(c)). Experimentally determining the structure of these defects will be beneficial to our understanding of strongly correlated materials.

These defects, however, are difficult to investigate using conventional X-ray techniques such as X-ray diffraction (XRD) or X-ray absorption spectroscopy. To directly probe the local structure of the defects, we employ X-ray fluorescence holography (XFH). Figure 2(a) shows the principles of XFH, where atoms of a selected element are excited by an incident X-ray and emit fluorescent X-rays, which in turn are scattered by the atoms surrounding the emitter [4]. The interference of the unscattered and scattered fluorescence can be treated as a hologram pattern, where the actual 3D picture of the scatterers around the emitter can be directly reconstructed using reconstruction algorithms. XFH has been extensively used in revealing the local structures around dopants and other defects in various functional materials [4], but work on adapting XFH for organic or protein crystals has only recently begun [5].

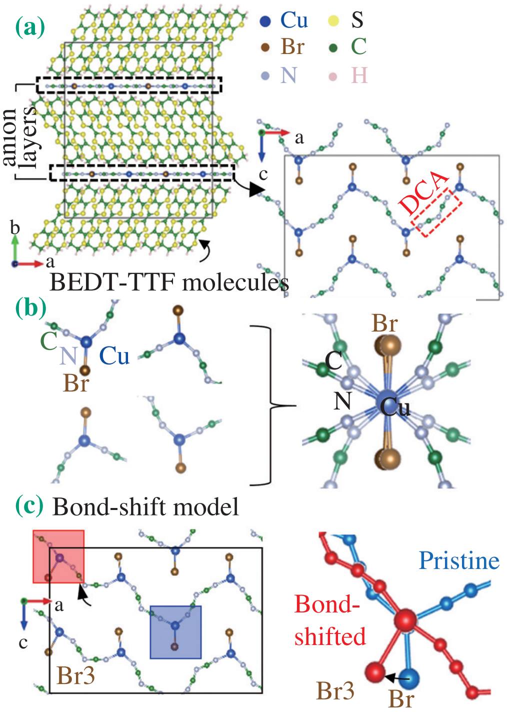

Fig. 1. **(a)** Atomic structure of the κ-Br unit cell and its anion layer, **(b)** the four inequivalent Cu sites, and their superposition, and **(c)** the "bond-shift" model proposed in Ref. 3.

We performed XFH experiments [6] on pristine and irradiated κ-Br crystals at SPring-8 **BL37XU** and **BL39XU**. In these experiments, the crystals were kept at 100 K, and diffraction patterns and resistivity measurements before and after the XFH experiments showed no additional damage due to the irradiation during the XFH experiments. Figure 2(b) shows a schematic of the bioXFH setup [5], where the fluorescent X-ray intensities were recorded as a function of the polar and azimuthal angles as the crystal was rotated relative to the incident X-ray.

From the Cu $K\alpha$ holograms, the atomic images around Cu in the anion layers were reconstructed and are shown in Figs. 3(a) and 3(b). Atomic images coinciding with the Br positions were observed in both the pristine and irradiated samples. The nearest-neighbor N atoms were also observed as weak atomic images in the pristine sample, but were no longer visible in the irradiated crystal. Using the atomic structures of the pristine κ-Br obtained by XRD, and those of the BS model from the calculations, we simulated the Cu $K\alpha$ holograms and reconstructed the atomic images. In these simulations, the reconstruction of the pristine κ-Br agrees with the experiment, but for the BS model, an additional Br image appears at the Br3 position. Furthermore, the intensities of the N atomic images are far higher than those in the experiment for both models. This is because for these hologram simulations, dynamic atomic fluctuations due to thermal vibrations are not taken into account. For organic crystals, the fluctuations due to thermal vibrations are larger than those of inorganic crystals and are expected to affect the reconstructions more.

To address this, we performed molecular dynamics simulations of both the pristine and BS models at 100 K and 300 K. 150 snapshots were taken every 10 fs, where the atomic positions were taken from each frame. The Cu $K\alpha$ holograms were calculated from these atomic positions and the atomic images were reconstructed. Figures 3(c) and 3(d) show that these reconstructions are in better agreement with the experiment. Weak N atomic images were observed in the reconstruction from the pristine model, while they are hardly visible in the BS model. Furthermore, the Br3 atomic image is no longer observed in the BS model. The MD simulations showed that the standard deviation of the angular position distribution σ_A at 100 K is larger for the BS model, especially for the N atoms. The large angular distribution weakens the atomic image in the reconstruction.

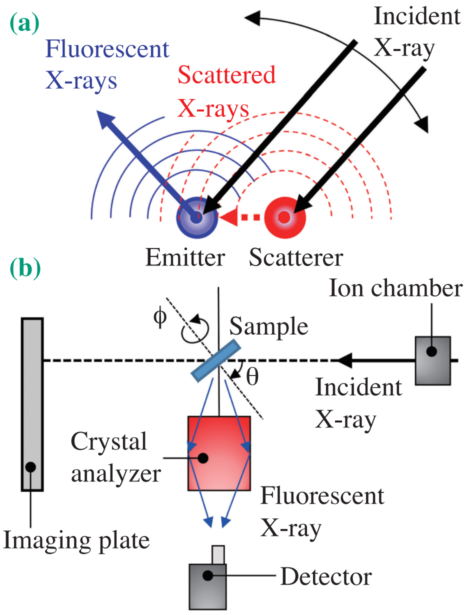

Fig. 2. **(a)** Principles of XFH and **(b)** schematic of the bioXFH experiment.

In summary, our results show experimental evidence supporting the BS model for explaining the MI transition in κ-Br, where defects in the anion layer caused by the irradiation introduce disorder in the system. Furthermore, the clear atomic images obtained from XFH experiments demonstrate that XFH can be a powerful tool in studying the local structures in functional organic crystals and even protein crystals.

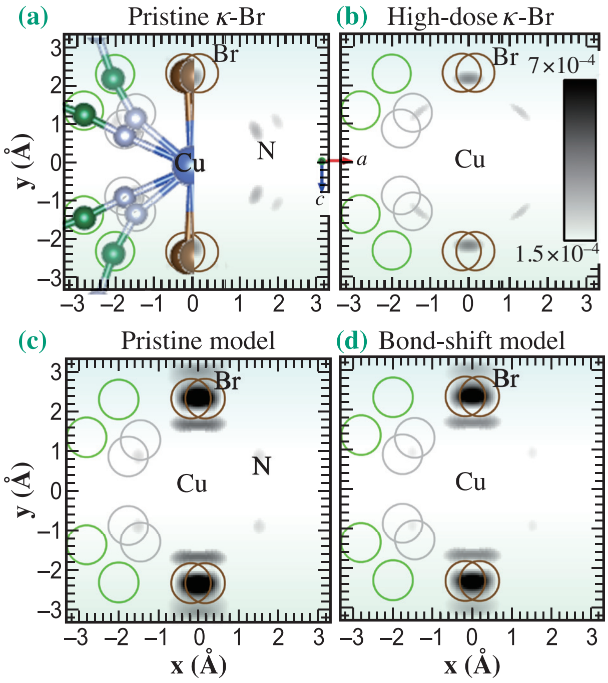

Fig. 3. Reconstructed atomic images from the experiments on the **(a)** pristine and **(b)** irradiated κ-Br samples and from the calculated holograms with the results from MD simulations at 100 K.

Artoni Kevin R. Ang†

Department of Physical Science and Engineering,
Nagoya Institute of Technology

Email: ang.artoni@toyota-ti.ac.jp

† Present address: Toyota Technological Institute

References

[1] T. Sasaki: Crystals **2** (2012) 374.
[2] K. Sano *et al*.: Phys. Rev. Lett. **104** (2010) 217003.
[3] L. Kang *et al*.: Phys. Rev. B. **95** (2017) 214106.
[4] K. Hayashi *et al*.: J . Phys.: Condens. Matter. **24** (2012) 093201.
[5] A. Sato-Tomita *et al*.: Rev. Sci. Instrum. **87** (2016) 063707.
[6] *A. K. R. Ang, R. Marumi, A. Sato-Tomita, K. Kimura, N. Happo, K. Akagi, T. Sasaki and K. Hayashi: Phys. Rev. B.* ***103*** *(2021) 214106.*

Generation of femtosecond X-ray pulse pairs

X-ray free-electron lasers (XFELs), such as SACLA, provide intense, ultrashort X-ray pulses that can probe matter at the atomic length scale and femtosecond time scale. The standard operation of XFELs uses self-amplified spontaneous emission (SASE) pulses that have a ~0.5% relative spectral bandwidth and consist of many random narrow spectral and temporal spikes. Secondary monochromators and new accelerator schemes, such as self-seeding, can provide single-color XFEL pulses with increased temporal coherence, yet, even such pulses limit the applications of XFELs to nonlinear coherent imaging and spectroscopy techniques that, in the optical domain, have revolutionized our understanding of the structures and dynamics of molecules and materials. Extending coherent nonlinear spectroscopies and imaging to the X-ray domain would provide direct insight into the coupled motions of electrons and nuclei, with resolution on the electronic length and time scale and elemental sensitivity. Several approaches have been proposed, but its experimental realization proves very difficult. One big challenge is the generation of intense, coherent, femtosecond X-ray pulses with fixed relative phases. Several groups are currently pursuing the creation and detection of coherent femtosecond X-ray pulse pairs. The work described here focuses on our recently published observation of generating intense phase-stable femtosecond hard X-ray pulse pairs [1].

Our approach for generating such X-ray pulse pairs is based on amplified spontaneous emission (ASE) and seeded stimulated emission (SSE). Both phenomena require intense XFEL pulses and have been observed and explored for various applications at X-ray energies ranging from 850 eV to 8 keV [2-4]. Our experiments were performed at the nanofocus instrument EH5 at SACLA **BL3** XFEL providing highly focused SASE pump and seed pulses. Spectral analysis of the emission signal was performed using a flat Si (220) analyzer crystal dispersing the emission signal onto a two-dimensional CCD. We focus on the 5.9 keV (2.1 Å) Mn $K\alpha_1$ emission line, where we employ an intense XFEL pump pulse at 6.6 keV (above the Mn K-edge) to create many simultaneously excited $1s$ core holes. Stimulated X-ray emission can occur either in the form of ASE, where a randomly emitted X-ray fluorescence photon acts as the seed, or via SSE, where an external second-color XFEL pulse provides the seed. Figure 1 shows the level and state diagrams of stimulated $K\alpha$ X-ray emission (a), the concept of ASE and SSE (b), and the main experimental components (c).

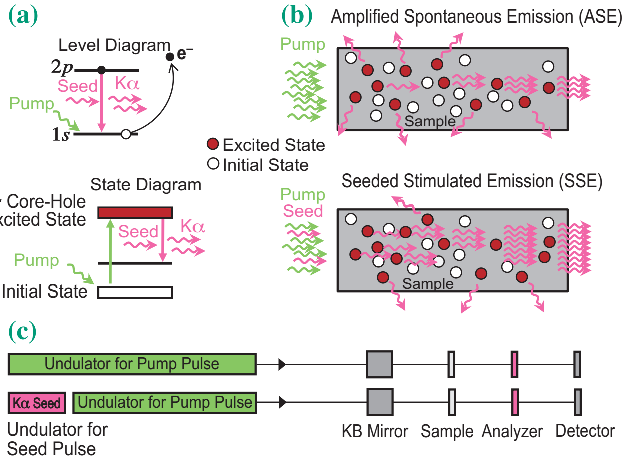

Fig. 1. **(a)** Level and state diagrams for stimulated $K\alpha$ X-ray fluorescence (red) following $1s$ core hole ionization by an incident photon (green) and seeding by either a spontaneously emitted fluorescence photon (ASE) or an external seed photon (SSE). **(b)** Concepts of the two types of stimulated X-ray emission. The pump pulse (green) creates $1s$ core-hole excited states (red). In ASE, a spontaneously emitted $K\alpha$ photon seeds the emission of a second $K\alpha$ photon along the direction of $1s$ core hole-excited states and so on, leading to amplification. In SSE, external seed pulse photons (magenta) stimulate the emission of $K\alpha$ photons from $1s$ core hole excited states along the seeding direction. **(c)** Schematics of the basic components for ASE and SSE experiments showing the undulators for pump and seed pulse generation, the KB focusing mirrors, the sample, the Bragg crystal analyzer, and the 2D detector.

When studying ASE and SSE signals from various Mn compounds at SACLA, we discovered that in some instances the observed spectra show strong interference fringes. Such fringes cannot be caused by any sample-related features in the X-ray emission. After ruling out several possible causes for these fringes, we found the cause: When a SASE XFEL pump pulses has two strong temporal spikes (in addition to many weak ones), each of these strong spikes has enough intensity to generate a very short (1 fs or less) highly directional ASE/SSE signal. The result is an X-ray pulse pair with temporal spacings of ~2–5 fs manifested by spectral interference fringes. The fringes constitute the time-frequency X-ray analogue of Young's double-slit interference allowing for frequency-domain X-ray measurements with attosecond time resolution. The sequence of events for the generation of X-ray pulse pairs and interference fringes is illustrated in Fig. 2.

The relation between the spectral fringe spacings ΔE and temporal pulse spacings Δt is obtained through Fourier analysis via the Planck constant $\Delta t \Delta E = h = 4.136$ fs-eV. Single-shot spectra exhibiting values for ΔE (0.9–2.5 eV) and corresponding values for Δt (1.7–4.6 fs) are shown in Fig. 3. We used the 1-dimensional (1D) semi-classical Maxwell-Bloch theory [5] to simulate the spectra to establish the link between the temporal structure of the SASE pump pulses and the observed fringes.

The fact that stimulated emission is highly nonlinear can explain why in the weaker spikes of the SASE spectrum might not lower the observed contrast of the interference fringes: A temporal spike only generates stimulated emission once it reaches the threshold required for sufficient population inversion. This also explains why fringes are generally rare and their probability depends on the SASE temporal profiles resulting from the electron-bunch compression mode in the linear accelerator.

To conclude, we have experimental evidence that stimulated X-ray emission generated by an XFEL SASE pulse can result in phase-stable fs X-ray pulse pairs. The resulting spectral fringe pattern contains the information about the X-ray pulse pairs, including their temporal spacing, coherence, and relative phase. The spectral fringe separation directly encodes the time delay of these pulses, which can be determined with ~20 attosecond precision for measuring delays of ~4 fs. A future, more robust method for obtaining phase-stable pairs of fs X-ray pulses by stimulated X-ray emission might pave the way to realizing frequency combs in the hard X-ray region.

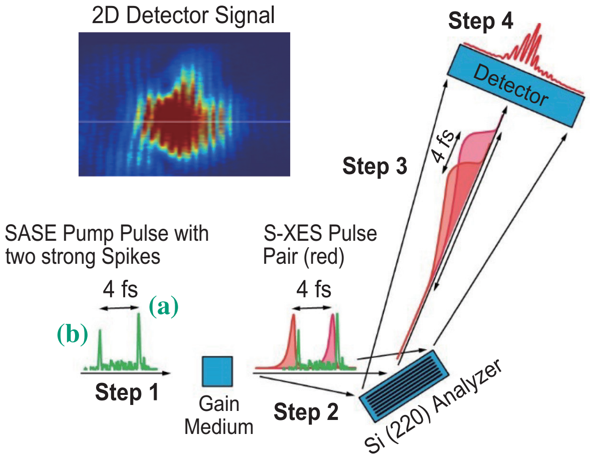

Fig. 2. XFEL SASE pump pulse with two strong temporal spikes **(a)**, **(b)**, impinges on the sample (Step 1), each creating a short superfluorescence burst. The two pulses leave the sample with a slight delay with respect to their respective SASE spikes given by the lifetime of the excited state (Step 2). The two pulses do not overlap temporally until they impinge on the analyzer crystal, where they are spectrally dispersed and temporally stretched to ~22 fs (~8 fs FWHM) corresponding to the ~0.24 eV FWHM Si (220) resolution (Step 3). The two signals then create the frequency interference with the fringe spacings that are inversely proportional to their time delays (Step 4). Inset shows the measured 2D detector signal from a single pulse pair. The white line shows the cut along the dispersive direction resulting in the spectrum shown in Step 4. For more details see [1].

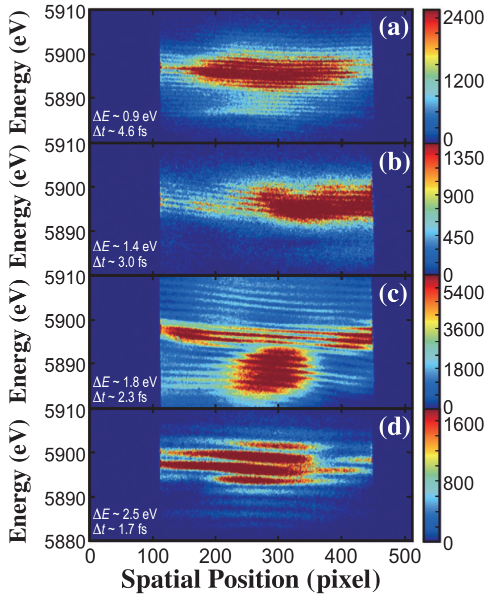

Fig. 3. Selected single-shot ASE spectra of the Mn $K\alpha$ line using MnO_2 films as a gain medium. Spectra with increasing fringe spacings ΔE from ~0.9 to 2.5 eV (**a–d**) are shown, the corresponding time delays Δt between two pulses that cause such interference are also shown in the figure. Each ASE spectrum corresponds to phase-stable femtosecond X-ray pulse pairs with up to ~3×10^7 photons.

Uwe Bergmann

Dept. of Physics, University of Wisconsin-Madison, USA

Email: ubergmann@wisc.edu

References

[1] *Y. Zhang, T. Kroll, C. Weninger, Y. Michine, F. D. Fuller, D. Zhu, R. Alonso-Mori, D. Sokaras, A. Lutman, A. Halavanau, C. Pellegrini, A. Benediktovitch, M. Yabashi, I. Inoue, Y. Inubushi, T. Osaka, J. Yamada, G. Babu, D. Salpekar, F. N. Sayed, P. M. Ajayan, J. Kern, J. Yano, V. K. Yachandra, H. Yoneda, N. Rohringer, U. Bergmann: Proc. Natl Acad. Sci.* ***119*** *(2022) e2119616119.*
[2] T. Kroll *et al.*: Phys. Rev. Lett. **120** (2018) 133203.
[3] N. Rohringer *et al.*: Nature **481** (2012) 488.
[4] H. Yoneda *et al.*: Nature **524** (2015) 446.
[5] C. Weninger and N. Rohringer: Phys. Rev. A **90** (2014) 063828.

Evaluation of dynamical behavior of epoxy resins in the curing process by X-ray photon correlation spectroscopy

Thermoset epoxy resins are indispensable materials for modern industry because of their excellent mechanical properties, high adhesion to various substrates, and excellent heat and chemical resistance. They are used in various materials, such as versatile adhesives, fiber reinforced materials, and high-performance coatings. In the production process, efficient energy use in the thermosetting process is becoming more important, for which optimization of curing conditions is required. Thus, it is necessary to properly understand the kinetics of the thermosetting process.

The thermal curing reaction is typically initiated by mixing two reactive components together and increasing the temperature to induce a cross-linking reaction. The effect of temperature on the isothermal curing reaction is fairly complex. The curing reaction is more likely to occur at high temperatures, thereby resulting in faster curing; however, it does not guarantee the hardness of the cured materials. For certain epoxy resins, when high-temperature curing is preceded by a low-temperature curing process, the cured material has a higher glass transition temperature T_g. Temperature affects the cross-linking network formation, and consequently, density and heterogeneity.

We examined the microscopic dynamics of a catalytic epoxy resin during the isothermal curing process at two different temperatures (100°C and 150°C) by X-ray photon correlation spectroscopy (XPCS) [1]. Previous rheological measurements indicated that both the curing process at 100°C and 150°C reached the gel point within 1 h, and solidification was almost complete. Thus, we focused on the first 2 h of the curing process and investigated its microscopic dynamics by XPCS.

XPCS measurements were performed at SPring-8 **BL03XU**. A sample was irradiated with partially coherent X-rays generated by passing the X-ray beam through a pinhole of 20 μm diameter, and the scattered X-rays were detected using a two-dimensional detector mounted approximately 8 m at the back of the sample. In the XPCS measurements during the curing process, we analyzed the fluctuation of the speckle patterns scattered from the dispersed tracer particles in the epoxy resin, which was a mixture of bisphenol A diglycidyl ether (BADGE) as the base resin and 1-(2-cyanoethyl)-2-undecylimidazole (C11ZCN) as the catalyst. The samples in the liquid state were enclosed in cells designed to have a homogeneous temperature using aluminum foil as window materials [2], placed in a heat bath of 100°C or 150°C, and the change in dynamics during the curing process was measured.

The XPCS results showed that a marked slowing down of dynamics was observed with the progress of thermal curing under both 100°C and 150°C temperature conditions. However, significant differences were observed between the curing process at 100°C and that at 150°C. The time dependence of the characteristic relaxation rate Γ in the 100°C curing process at the scattering wave vector $q = 0.0325$ nm^{-1} is shown in Fig. 1(a). The kinetics were clearly distinguished into regions (I)–(III). This indicates that the thermosetting reaction proceeds in three sequential steps: (I) oligomerization by bonding between monomers, (II) gelation by the cross-linking reaction between oligomers, and (III) densification of the cross-linked structure, which shows a clear difference in dynamics. On the other hand, in the 150°C curing process, there was no clear regional division of dynamics, and a gradual attenuation of dynamics was observed, as shown in Fig. 1(b). In this curing, oligomerization and gelation proceeded simultaneously, and no clear change in dynamics appeared.

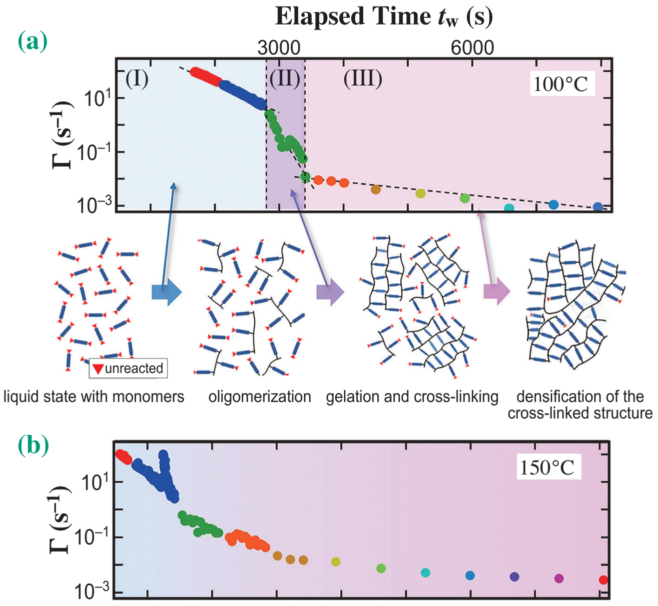

Fig. 1. Time dependence of the characteristic relaxation rate Γ at $q = 0.0325$ nm^{-1} in the 100°C **(a)** and 150°C **(b)** curing processes. The schematic illustrations of the changes in the structure of the epoxy resin during the 100°C curing process are shown in (a).

Furthermore, a significant difference in dynamics fluctuation was observed between the curing process at 100°C and that at 150°C. Figures 2(a) and 2(b) show representative two-time correlation functions at 100°C and 150°C, respectively, which show the time variances of dynamics. In the two-time correlation function, a constant width of the band on the diagonal line indicates that the dynamics is stable. As shown in Fig. 2(a), the function during the 100°C curing process at t_w~1 h shows gradual fluctuation. On the other hand, the function during the 150°C curing process at t_w~1.3 h shows intermittent fluctuations as shown in Fig. 2(b), which indicates that fast and slow dynamics, the difference between which is very large, coexist. Similar intermittent fluctuations were observed for more than an hour during the 150°C curing process, whereas it was observed for about 600 s (Fig. 1(a-II)) of the gelation process during the 100°C curing process. These dynamical behaviors indicate that the 100°C curing process proceeds under relatively dynamically stable conditions, whereas the 150°C curing process proceeds under dynamically unstable conditions. From the instability appearing in the two-time correlation function, the spatial heterogeneity of the dynamics can be quantitatively evaluated as "dynamic heterogeneity" [3,4]. The cured product obtained by curing at 150°C showed a greater dynamic heterogeneity than the cured product obtained by curing at 100°C.

The chemical reactions during the curing process were examined by the Fourier transform infrared (FTIR) spectroscopy, which showed that about 80% of the reactive groups reacted during the 100°C curing process, whereas only 40% reacted during the 150°C curing process. The density of the cross-linking network structure of the resin after curing was also examined by ^{1}H-pulse nuclear magnetic resonance (NMR) spectroscopy, and the results showed that the density of cross-linked components was more than three times higher in the 100°C curing than in the 150°C curing.

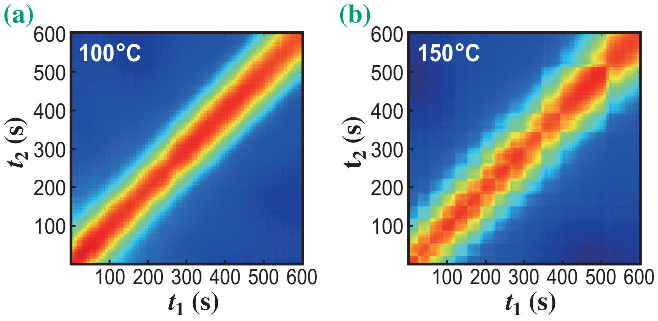

Fig. 2. Two-time correlation function at $q = 0.0325\ \mathrm{nm}^{-1}$ in the 100°C (2825< t_w <3425 s) **(a)** and 150°C (5007< t_w <5607 s) **(b)** curing processes. Both have almost the same time-scale dynamics, but the fluctuations are quite different.

These experimental results showed that in the 100°C curing process, reactions proceeded step by step to form a dense network structure (Fig. 3(a)), whereas in the 150°C curing process, the formation of chemical bonds at an early stage prevents molecular motion, resulting in curing with many unreacted groups remaining (Fig. 3(b)). These differences in the network formation should lead to the difference in glass transition temperature.

The dynamical behaviors observed in this study have not been observed in macroscopic rheological measurements. There are various materials produced by the formation of cross-linked networks. Similar analysis can be applied to the curing process using ultraviolet light as well as heat, and similar principles are also used to mold many three-dimensional printing materials. By focusing on the dynamic fluctuations during the curing process, we expect to produce high-performance materials by more efficient molding methods.

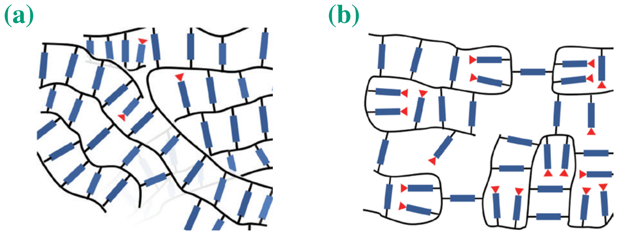

Fig. 3. Schematic illustration of the structure of the epoxy resin obtained by the 100°C **(a)** and 150°C **(b)** curing processes.

Taiki Hoshino[a,b,*], Yasushi Okamoto[c]
and Atsushi Yamamoto[c]

[a] International Center for Synchrotron Radiation Innovation Smart, Tohoku University
[b] RIKEN SPring-8 Center
[c] DENSO CORPORATION

*Email: taiki.hoshino.c7@tohoku.ac.jp

References

[1] *T. Hoshino, Y. Okamoto, A. Yamamoto and H. Masunaga: Sci. Rep.* ***11*** *(2021) 9767.*
[2] T. Hoshino *et al.*: Polymer J. **45** (2012) 94.
[3] T. Hoshino *et al.*: Phys Rev Lett **124** (2020) 118004.
[4] K. Kanayama *et al.*: Phys. Rev. Research **4** (2022) L022006.

Kinetics of denaturation and renaturation processes of double-stranded helical polysaccharide, xanthan, in aqueous sodium chloride

Multiple helices are important secondary structures in biological molecules, such as DNA, collagen, and polysaccharides. Since the rodlike conformation of multiple helices makes a solution highly viscous even at quite low concentrations of such molecules, these molecules can be applied as food additives. Xanthan, a double helical polysaccharide (Fig. 1(a)) [1], is one of the most useful rheology control materials because of its high solubility in water. Furthermore, unlike flexible polyelectrolytes in aqueous media, the viscosity of an aqueous xanthan solution is insensitive to changes in salt concentration. This is because the high chain stiffness of a rodlike double helical structure determines the solution viscosity.

The double helical structure of xanthan in aqueous sodium chloride was confirmed by the weight-average molar mass in a solvent, that is, the molar mass of xanthan was twice that in dimethyl sulfoxide. However, this finding of a double helical structure was not accepted at that time because the optical rotation of xanthan solution in the salt-jump experiments showed the first-order reaction [2]. On the other hand, this double helical structure was found by atomic force microscopy techniques, which is widely accepted. There have only been a few research studies to clarify this inconsistency. Another interesting feature of xanthan is its hairpin-like conformation and branched complexes (Figs. 1(b,c)) [3], which may have unique rheological properties. Time-resolved measurement of the chain conformation is desired to clarify the denaturation and renaturation processes and to control the renatured conformation of xanthan.

Small-angle X-ray scattering (SAXS) is a powerful tool to determine the molecular conformation of polymers and macromolecular assemblies in solution. In particular, the conformational change from a single chain to a double helix can be detected as a significant increase in scattering intensity at the magnitude q of the scattering vector between 0.3 and 2 nm^{-1}. We thus conducted time-resolved SAXS measurements of double helical xanthan to observe the conformational change processes using the synchrotron radiation at SPring-8 **BL40B2**. Time-resolved circular dichroism (CD) measurement was also conducted since CD signals reflect the chiral structure of chromophores; therefore, the temperature change of the CD signal of xanthan reflects the conformational change of side groups. Although this is consistent with the double helix content at the equilibrium state, we found that clear differences were found immediately after the temperature change. The specific ellipticity $[\theta']_{210}$ detected by CD measurement at λ_0 = 210 nm with λ_0 being the wavelength of incident light in a vacuum and the weight fraction α of double helix determined by SAXS measurement are plotted in Fig. 2.

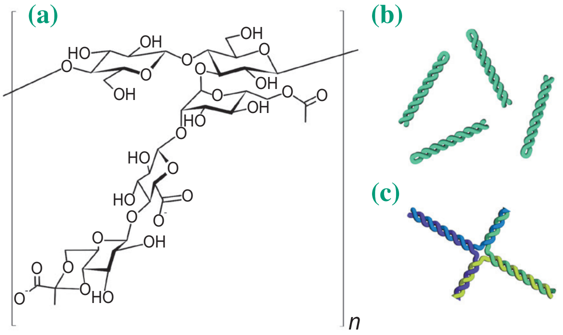

Fig. 1. **(a)** Chemical structure of xanthan [1]. **(b)** Hairpin-like conformation. **(c)** Branched complex.

As shown in the figure, the $[\theta']_{210}$ value immediately reaches the denatured (red line in Fig. 2(a)) for the single chain after rapid heating, whereas the α value reaches zero after more than 1000 s, clearly indicating that after rapid heating, the side chains in xanthan immediately fluctuate markedly as observed by CD, whereas that of the rodlike double helical conformation was maintained for least several minutes. On the other hand, in the rapid cooling process, the α value immediately reaches an asymptotic value, whereas the $[\theta']_{210}$ value gradually increases. This shows that the rodlike double helix forms in a short time range after rapid cooling, whereas it took more than one day to recover the CD signal. This change can be regarded as the first-order process as in the case of the rapid heating process. Another interesting point is that the α values after cooling are however smaller than unity for the renatured samples. This is most likely due to the fact that the complete double helical conformation cannot be formed by materials with the hairpin-like conformation or branching complexes.

The above-mentioned results of the time-resolved CD and SAXS measurements indicate that both the denaturation and renaturation processes consist of at least two steps, and hence the existence of some intermediate species, as shown in Fig. 3. The initial change after the rapid heating is recognized as

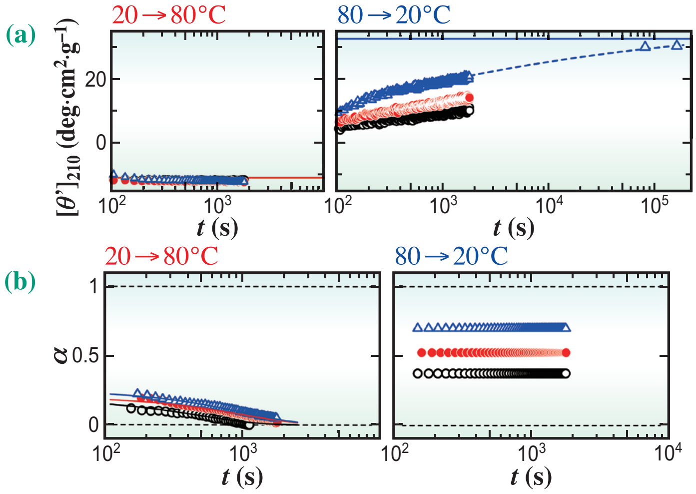

Fig. 2. Time course of **(a)** $[\theta']_{210}$ and **(b)** α for X341k in aqueous NaCl. Left, abruptly heated from 20 to 80°C. Right, abruptly cooled from 80 to 20°C. Black unfilled circles, red filled circles, and blue unfilled triangles denote $C_S = 5$ mM and $c = 3$ mg·mL^{-1}, $C_S = 5$ mM and $c = 6$ mg·mL^{-1}, and $C_S = 10$ mM and $c = 6$ mg·mL^{-1}, respectively. The solid blue line indicates the $[\theta']_{210}$ value for the as-prepared solution at 20°C. [1]

the melting of the side chain. The resulting double helix can be looser than that at low temperatures. In contrast, the formation of the loose double helical structure is quite rapid, whereas the reaction leading to the formation of the native double helix takes more than 24 h. These kinetic characteristics of xanthan in the solution can be related to the formation of a higher-order structure shown in Fig. 1, showing that not only static properties but also kinetic properties play important roles in realizing the higher-order structure and rheological properties of renatured xanthan. The current procedure to determine the helical structure can be utilized for various multiple helical polysaccharides [4] and the complex formation behavior of polysaccharides with other materials [5].

In this study, we clearly showed that the SAXS profile is a direct measure of the helical structure of multiple helical biopolymers. Not only spectroscopic methods but also elastic scattering measurements including SAXS, light scattering, and neutron scattering play a decisive role in elucidating the conformational feature of biopolymers in solution. Since time-resolved SAXS measurements are available using a synchrotron light source, it is an indispensable method to clarify the kinetics of conformational change of multiple helical polymers in solution.

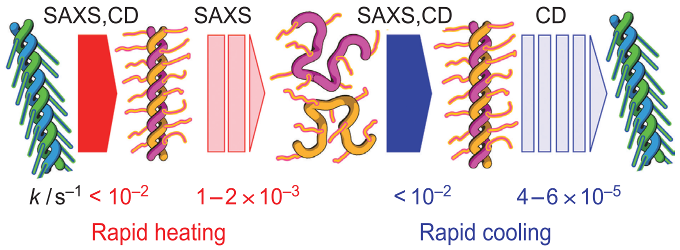

Fig. 3. Schematic representation of denaturation and renaturation processes of xanthan in aqueous NaCl. [1]

Ken Terao* and Yu Tomofuji

Department of Macromolecular Science,
Osaka University

*Email: terao.ken.sci@osaka-u.ac.jp

References

[1] *Y. Tomofuji, K. Matsuo, K. Terao: Carbohydr. Polym.* ***275*** *(2022) 118681.*
[2] E. R. Morris: Food Hydrocolloids **86** (2019) 18.
[3] Y. Matsuda *et al.*: Polym. J. **41** (2009) 526.
[4] Y. Meng *et al.*: Biomacromolecules **21** (2020) 1653.
[5] Y. Tomofuji, K. Terao: Macromol. Symp. (2023) - in press.

Nanoscale subsurface plasma dynamics observed by single pulse GISAXS

When an intense femtosecond laser pulse far above the material damage threshold is irradiated on a solid, the atoms are immediately ionized, and a dense plasma is created. The laser field interacts with electrons around the surface up to tens of nanometers limited by the skin depth. After the laser pulse, several physical processes occur inside the material leading to thermalization, diffusion, compression, and ablation and finally resulting in a new surface structure [1]. A deeper understanding of these processes will enable better control of high-precision material processing and functional surfaces production.

Up to now, we are missing methods for observing these complex density dynamics with sufficient spatial and temporal resolution which prevented us from obtaining a quantitative understanding of the underlying physics. Here, we demonstrated for the first time the feasibility of single pulse grazing-incidence X-ray diffuse scattering experiments from laser-excited solids employing single XFEL pulses.

The experiment was performed at SACLA **BL2** EH6. A metallic multilayer (ML) sample consisting of five layers of tantalum (Ta) and copper nitride (Cu_3N) was irradiated by an optical laser with 800 nm wavelength, 3.6×10^{14} W/cm^2 intensity and 40 fs pulse duration (Fig.1(a)) [1]. After a variable delay, the sample was irradiated with 8.81 keV X-rays at a grazing-incidence angle of 0.64° and the scattered X-ray photons around the specular reflection were recorded by an MPCCD area detector [2]. To cover the X-ray footprint on sample (4 μm for 0.64° grazing incidence yields 360 μm), the laser beam was defocused to a diameter of ~500 μm. The intense specular reflection was blocked by a beam stop.

Figure1(b) shows the time evolution of the signal within the scattering plane at $Q_y = 0$ for time delays up to 4.0 ps. The intense peak at $Q_z = 1.33$ nm^{-1} represents the typical length scales of each Ta/Cu_3N double layer. The Kiessig fringes, represented as small peaks between $Q_z = 1.0$ and 1.33 nm^{-1}, are a fingerprint of the number of double-layer repeats in the ML sample [3].

Upon interactions with the laser, we observe drastic changes in the X-ray scattering profiles. We notice a progressive reduction of the number of Kiessig fringes with time and simultaneously, a broadening and reduction in intensity of the peak at 1.33 nm^{-1} both indicating a receding surface and a loss of correlation within the double-layer structure. The scattering signal at exit angles below the incident angle ($Q_z < Q_{\mathrm{specular}}$) in the range of the critical angles of total external reflection (so-called Yoneda peaks) are originating predominantly from the interference of the topmost surface layers and are a sensitive marker for the structure of the uppermost layers. Even at the delay time of 4 ps, where the Kiessig fringes had disappeared, the Yoneda peaks are still present thus revealing important information for the density reconstruction.

We reconstructed the density profiles of the scattering signals using the state-of-the-art GISAXS analysis program BornAgain. Circular dots in Figs. 2(a) and 2(b) show the in-plane scattering signal obtained at −0.5 and 2.0 ps after the laser intensity peak. The solid lines in Figs. 2(a) and 2(b) represent refinements of the scattering data leading to the corresponding electron density profile shown in Fig. 2(c). While the density profile at −0.5 ps is identical to that of the cold sample, at 2.0 ps delay the density profile is strongly modulated although the periodic double-layer structure is still existing. A reduced number of layers or reduced homogeneity in layer thickness corresponds to the disappearance of Kiessig fringes between $Q_z = 1.0$ and 1.33 nm^{-1}. Furthermore, the reduced density of the uppermost Ta layer in Fig. 2(c) is corroborated by the reduction of the $Q_z = 0.87$ nm^{-1} peak.

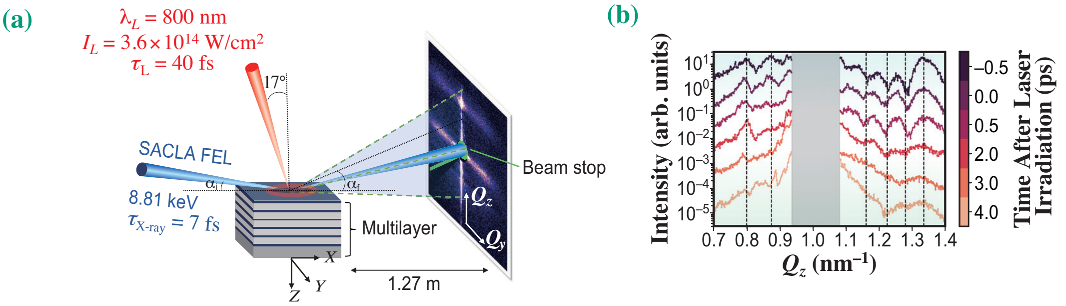

Fig. 1. **(a)** Experimental setup at SACLA BL2 EH6. **(b)** In-plane scattering signal for different time delays between laser and XFEL.

The reconstructed density profiles for different delays have been compared to two simulation codes: MULTI-fs, designed for femtosecond laser-solid interactions in a nonrelativistic regime [4] and PICLS, typically used for the modeling of relativistic plasmas in the context of, e.g., laser particle acceleration [5].

For both, simulations and experiment we observe an immediate expansion of the top layer into the vacuum due to high surface pressures (Fig. 3). Subsequently, the electron heat wave propagates into the bulk to heat the ML above 10 eV (~10^5 K) which modulates the ML structures. The observed ML dynamics in MULTI-fs appeared very different from our experiment which we attributed to the intermixing of particles between layers that is missing in the Lagrangian code. On the contrary, although kinetic PIC simulations have been considered inadequate for a relatively low temperature and highly collisional plasmas, the overall shape of the density profiles and the number of density peaks shows good qualitative agreements. This was achieved by implementing atomic-scale collisions into our PIC code. The agreement is however lost after ~2 ps due to the current limitations of the code: missing physics of radiation transport, multidimensional atomic mixing, recombination, large-angle many-body collisions, and degeneracy. This will motivate the development of new models which can now be tested by using our experimental method.

In summary, we demonstrated for the first time a new experimental capability of studying nanoscale surface and sub-surface dynamics upon high-intensity laser irradiation by grazing-incidence X-ray scattering with picosecond time resolution. Our result will allow the benchmarking of physics models and simulations with relevance to laser material processing and high-energy-density science.

For future experiments, having a larger detection area would be beneficial to provide additional constraints on the density retrieval. Additionally, a nanofocused X-ray beam would yield better time resolution to also observe femtosecond density dynamics.

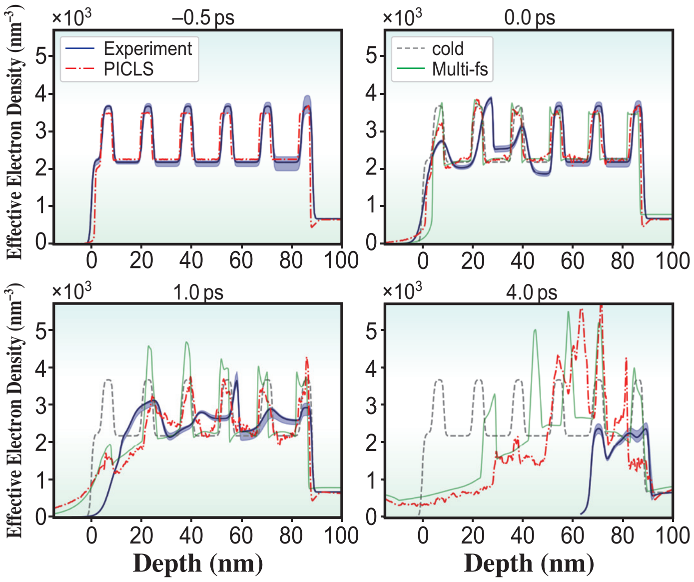

Fig. 3. Evolution of the electron density profiles with various pump-probe delays. Comparison between the experiment and simulations. Blue solid lines display experimental results, red dashed-dotted lines are simulation results from PICLS, and green solid lines are results from MULTI-fs.

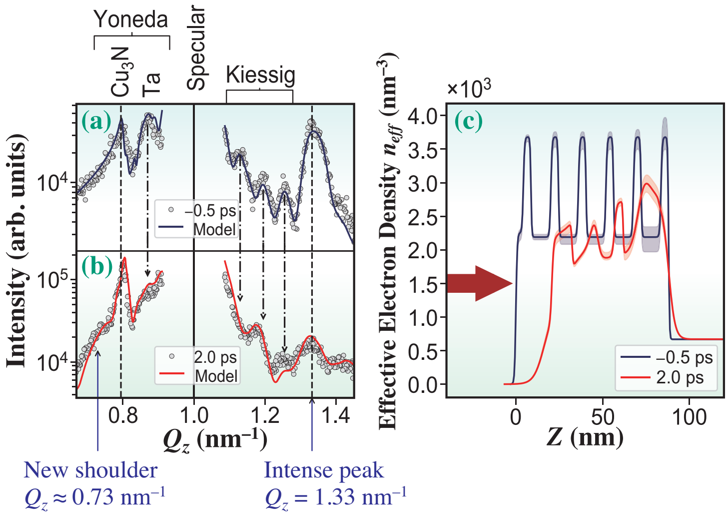

Fig. 2. GISAXS signals and corresponding electron density profiles. Lineout of the in-plane scattering at **(a)** 0.5 ps before and **(b)** 2 ps after the laser. **(c)** Retrieved electron density profile as a function of the depth.

L. Randolph[a,b,*], M. Banjafar[b], C. Gutt[a]
and M. Nakatsutsumi[b]

[a] University of Siegen, Germany
[b] European XFEL, Germany

*Email: lisa.randolph@xfel.eu

References

[1] *L. Randolph, M. Banjafar, T. R. Preston, T. Yabuuchi, M. Makita, N. P. Dover, C. Rödel, S. Göde, Y. Inubushi, G. Jakob, J. Kaa, A. Kon, J. K. Koga, D. Ksenzov, T. Matsuoka, M. Nishiuchi, M. Paulus, F. Schon, K. Sueda, Y. Sentoku, T. Togashi, M. Bussmann, T. E. Cowan, M. Kläui, C. Fortmann-Grote, L. Huang, A. P. Mancuso, T. Kluge, C. Gutt and M. Nakatsutsumi: Phys. Rev. Res.* **4** *(2022) 033038.*
[2] T. Kameshima *et al.*: Rev. Sci. Instrum. **85** (2014) 033110.
[3] V. Holý *et al.*: Phys. Rev. B **47** (1993) 15896.
[4] R. Ramis *et al.*: J. Comput. Phys. **227** (2008) 6846.
[5] Y. Sentoku and A. J. Kemp: J. Comput. Phys. **227** (2008) 6846.

Formation mechanism of high-entropy alloy nanoparticles assisted by hydrogen spillover effect

High-entropy alloys (HEAs) have recently received significant attention in various research fields. These alloys represent a new class of metallic materials in which more than five near-equimolar components are mixed to form single-phase solid solutions with high mixing entropy values, rather than intermetallic phases. Various unique synergistic effects result from such mixtures, including high configuration entropy, lattice distortion, sluggish diffusion and cocktail effects, and endow HEAs with high mechanical strength, good thermal stability and superior corrosion resistance. However, the development of HEA nanoparticles (NPs) with a mean diameter of less than 10 nm lags significantly behind, despite the potential practical applications of these NPs in catalysis, nanoelectronics and material science.

Hydrogen spillover is a fascinating phenomenon that occurs in sensors, hydrogen storage materials and heterogeneous catalysis. In this process, dissociated H atoms migrate to adjacent hydrogen-poor metal oxide surfaces via coupled proton/electron transfer. We demonstrate that titanium dioxide (TiO_2) is a promising platform for the low-temperature synthesis of supported CoNiCuRuPd HEA NPs driven by the pronounced hydrogen spillover effect on TiO_2. This study also revealed the specific mechanism responsible for the formation of HEA NPs, on the basis of *in situ* characterization techniques.

CoNiCuRuPd HEA NPs supported on TiO_2 (CoNiCuRuPd/TiO_2) were synthesized by a simple impregnation method, employing an aqueous solution of the corresponding precursors. This was followed by reduction under a H_2 atmosphere at 400°C. *In situ* X-ray absorption fine structure (XAFS) analyses were acquired at SPring-8 **BL01B1** in conjunction with a Si (111) monochromator under a H_2 atmosphere at elevated temperatures (Fig. 1). X-ray absorption near-edge structure (XANES) spectra confirmed the reduction of all the precursors at 200°C. The intermediate shapes and edge positions at the Co and Ni *K*-edges indicated the presence of a mixture of cations and zero-valent ions at 200°C, because of their relatively low reduction potentials. In contrast, all spectra acquired at 400°C resembled those of the corresponding foils, suggesting that all the elements were in a metallic state.

Fourier transforms of extended X-ray absorption fine structure (FT-EXAFS) data further clarified

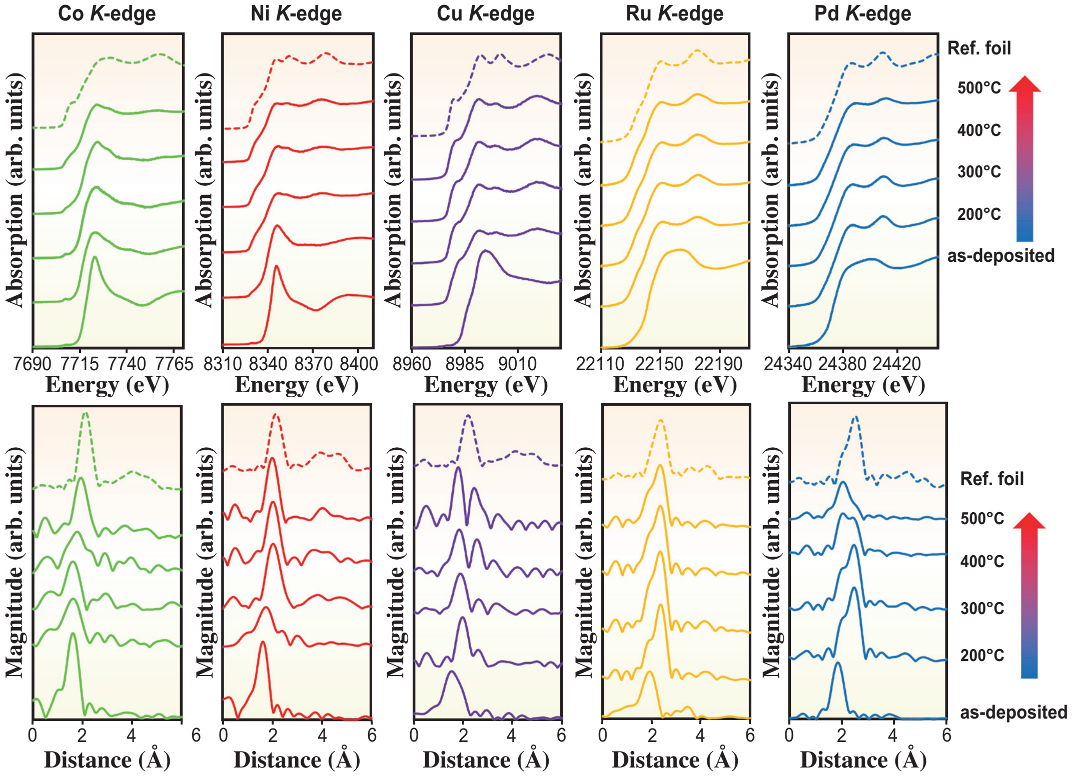

Fig. 1. *In situ* XANES and FT-EXAFS spectra at the Co, Ni, Cu, Ru, and Pd *K*-edges of CoNiCuRuPd/TiO_2 acquired during reduction in H_2 from room temperature to 500°C, and the corresponding reference foil materials (dotted line).

the structural transformation during the reduction sequence. The spectra of the as-deposited sample produced a sharp singlet peak in the *K*-edge region that was attributed to M–O bonds with lengths of approximately 1.7–1.9 Å. In the case of Co and Ni, the peak intensity due to the M–O bonds decreased at 200°C, whereas another peak attributed to metallic M–M bonds with longer interatomic distances appeared for Cu, Ru and Pd. These transitions demonstrated the reduction of M^{n+} ions on the TiO_2 support. The bond structure after the completion of the reduction revealed that the interatomic metallic M–M bond lengths were significantly different from those for the corresponding bulk references. In the case of the Ru *K*-edge, the shouldered peak was observed at around 1.9 Å, which is suggestive of the formation of Ru–M with shorter interatomic distances. These results suggest that all elements were surrounded by different metallic atoms.

Considering *in situ* XAFS results as well as the result of other characterization methods, such as STEM and H_2-TPR, we propose a mechanism for the formation of the HEA NPs on the TiO_2 support in conjunction with hydrogen spillover (Fig. 2). In a H_2 atmosphere, the Pd^{2+} precursors are first partially reduced to generate nuclei. Following this, H_2 is dissociated on the surfaces of these Pd nuclei to form Pd–H species (**Step 1**). The reduction of Ti^{4+} to Ti^{3+} together with the transfer of H atoms from Pd nuclei at the metal-support interfaces (**Step 2**) is accompanied by the migration of electrons from Ti^{3+} ions to neighboring Ti^{4+} ions. This promotes the subsequent simultaneous transfer of protons to O^{2-} anions attached to these adjacent Ti^{4+} ions (**Step 3**). In this manner, the hydrogen atoms rapidly reach all metal ions by moving over the TiO_2 surface (**Step 4**), such that these ions are all reduced at the same time to form the HEA NPs (**Step 5**) accompanied by the regeneration of Ti^{4+}. The *in situ* XRD pattern of CoNiCuRuPd/TiO_2 after reduction in H_2 at 200°C, which was conducted at BL01B1, showed the broad peak due to Pd (111). This peak disappeared with increasing reduction temperature, accompanied by the appearance of new peaks due to the formation of HEA NPs. *In situ* FT-EXAFS spectra at the Pd *K*-edge of CoNiCuRuPd/TiO_2 acquired in H_2 at 200°C showed a strong peak due to the contagious Pd–Pd bond, which slightly shifted toward a shorter interatomic distance with increasing temperature. These are clear evidence of the formation of Pd nuclei in the early stage, which act as uptake sites to enhance the migration of active hydrogen atoms. These results also indicated the initial formation of a Pd_{core}–M_{shell} (M represents Co, Ni, Cu, or Ru metal) structure, which finally forms HEA NPs via atomic diffusion with increasing reduction temperature, owing to the increase in configuration entropy.

A CoNiCuRuPd/TiO_2 catalyst synthesized in this manner exhibited high activity, different selectivity, and significantly improved stability compared with Pd/TiO_2 during the hydrogenation of CO_2. Theoretical investigations also emphasized that the sluggish diffusion in these CoNiCuRuPd HEA NPs is caused by the combination of multiple metals, and that lattice distortion plays a crucial role in the superior robustness of this material. Further investigation to demonstrate the applicability of the present synthetic method is now under way.

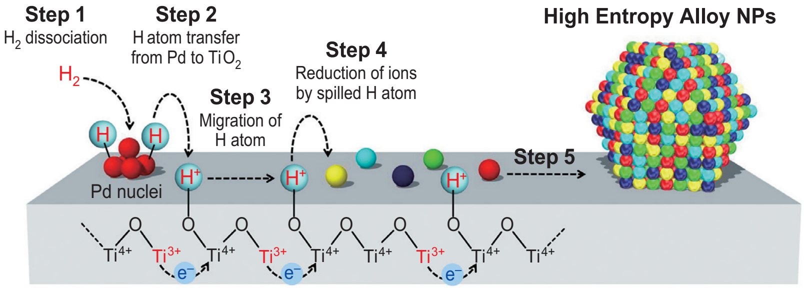

Fig. 2. Schematic illustration of the elementary steps in the formation of HEA NPs on a TiO_2 support assisted by hydrogen spillover.

Kohsuke Mori*, Naoki Hashimoto and Hiromi Yamashita

Graduate School of Engineering, Osaka University

*Email: mori@mat.eng.osaka-u.ac.jp

References

[1] J.-W. Yeh *et al.*: Adv. Eng. Mater. **6** (2004) 299.
[2] S. Masuda *et al.*: Chem. Sci. **11** (2020) 4194.
[3] K. Mori *et al.*: ACS Catal. **6** (2016) 3128.
[4] K. Shun *et al.*: Chem. Sci. **13** (2022) 8137.
[5] *K. Mori, N. Hashimoto, N. Kamiuchi, H. Yoshida, H. Kobayashi, H. Yamashita: Nat. Commun.* ***12*** *(2021) 3884.*

Chemical crystallography by serial femtosecond X-ray diffraction: XFEL as a tool for accelerating materials discovery

Single-crystal crystallography is one of the most important tools for the characterization of a newly synthesized material. Given a large enough crystal, precise information about the atomic-level structure can be extracted, and from that, a wealth of theoretical tools can be applied to understand its function. Unfortunately, some materials resist our efforts to grow large enough crystals for analysis. This dramatically chills the pace of material discovery in the hybrid material class and lowers the quality of structural data for the theoretical understanding of their properties.

Recently, metal-organic chalcogenolates (MOChas) have emerged as a new category of self-assembling two-dimensional material with potential applications in energy science, display technology, and photocatalysis [2]. However, the material family is plagued by small crystal sizes that make analysis challenging. We, therefore, developed a new approach to perform small-molecule serial femtosecond crystallography (smSFX) using the XFEL and first validated the approach at SACLA **BL2** [2]. The experiment is outlined in Fig. 1 along with images of the typical MOCha samples employed for this work. Crystals are suspended in a solvent and subjected to the XFEL beam. We arrive at a complete diffraction dataset by measuring ~10^6 frames containing ~10^4 indexable patterns.

A key difference between traditional single-crystal crystallography and SFX is the unknown orientation matrix for the crystal. In a single-crystal crystallography experiment, a crystal is rotated on a goniometer, bringing reflections into the diffracting condition through the X-ray beam, where the orientation is recorded per rotation. In SFX, each crystal is randomly oriented, so the crystal orientation for each recorded frame is unknown and must be deduced. Frames collected for a protein crystal have numerous indexable reflections, so Fourier methods are applicable to solve index the frames. However, comparable frames of hybrid materials have only 3–10 reflections, a result of its small unit cell! This sparsity makes it impossible to use traditional indexing methods which rely on the periodicity of the lattice seen in the diffraction pattern to determine the reciprocal basis vectors that define the crystal orientation.

To index the frames collected from small-molecule crystals, we developed and employed the program *cctbx.small_cell* using a maximum clique algorithm that finds three-dimensional reciprocal space relationships in a sparse pattern [3]. This algorithm requires a unit cell candidate. However, this poses several problems. First, we found that relying on literature values collected at different temperatures resulted in poor indexing rates because of the small changes to the unit cell. Second, such an approach would require additional experiments conducted outside the XFEL experiment to obtain the structure of the compound.

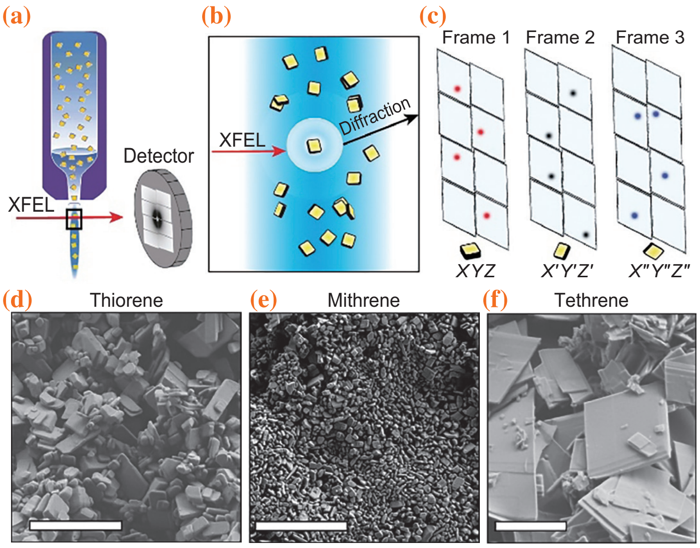

Fig. 1. **(a)** Schematic of the smSFX experiment. **(b)** Randomly oriented microcrystals are delivered to the XFEL interaction point. 30-fs XFEL pulses interact with the microcrystals to produce diffraction images before destruction by the XFEL pulse. **(c)** Individual frames from randomly oriented mithrene crystals are sparse. **(d–f)** Scanning electron micrographs of all three silver benzenechalcogenolates, where some size heterogeneity and morphological divergence is noted. Scale bars are 5 μm.

We devised an alternate approach to obtain the unit cell details of the experiment at the beamline. Unit cells can be extracted from 1-dimensional 'powder' diffraction patterns, a common approach for materials science. This technique generally requires highly accurate *d*-values. We exploited the XFEL experiment to extract this data from individual crystal frames. Our method enabled us to derive high-resolution powder patterns by constructing a composite (or virtual powder pattern) over numerous XFEL diffraction patterns. By extracting only the centroid position of a given diffraction spot, we were able to locate spots with sub-pixel accuracy thereby eliminating sample- and instrument-based peak broadening. Our approach is therefore to collect data until a sufficient quantity of frames is collected to obtain a high-resolution powder diffraction pattern from XFEL data before generating unit cell candidates.

The results of the smSFX validation and experimental datasets are shown in Fig. 2. The smSFX technique provided a key structural basis for understanding the properties of the materials studied. We previously demonstrated that excitons in mithrene, delocalized in two-dimensions across the argentophilic network of Ag–Ag bonds, give rise to its visible absorption and emission spectra. Our further study here demonstrated that thiorene's argentophilic interactions are marked by linear Ag–Ag chains, which do not support the two-dimensional delocalization of excitons observed in mithrene and tethrene. Therefore, this smSFX study resolves the long-standing puzzle of thiorene's optoelectronic divergence from its homologs mithrene and tethrene. This work demonstrates that smSFX is a general technique for chemical crystallography on microcrystalline samples and can be employed to obtain high-quality structural data for obligate nanocrystals.

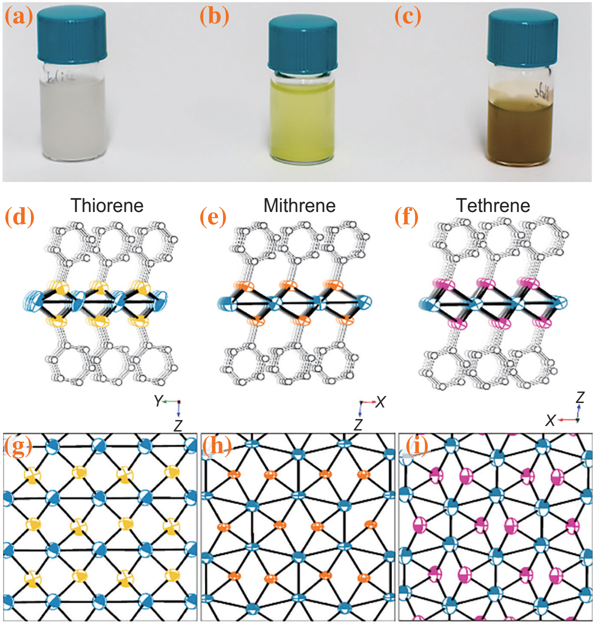

Fig. 2. **a**–**c**, Suspended microcrystals of thiorene (**a**), mithrene (**b**) and tethrene (**c**) show their respective milky white, yellow and deep orange colors. **d**–**f**, Side and top views of crystal structures from smSFX for thiorene (**d**), mithrene (**e**) and tethrene (**f**). Thermal ellipsoids for Ag (blue), S (yellow), Se (orange) and Te (magenta) are drawn at the 50% probability level. Hydrogen atoms and one position of disordered C_6H_5 (for mithrene) are omitted for clarity. **g**–**i**, Models of thiorene (**g**), mithrene (**h**) and tethrene (**i**) with the view oriented down the *c* axis of the unit cell, with the carbon and hydrogen atoms omitted, displaying the divergence in the thiorene Ag–Ag bonding environment compared to that in mithrene and tethrene.

J. Nathan Hohman[a,*] and Aaron S. Brewster[b]

[a] Institute of Materials Science and Department of Chemistry, University of Connecticut, USA
[b] Molecular Biophysics and Integrated Bioimaging Division, Lawrence Berkeley National Laboratory, USA

*Email: james.hohman@uconn.edu

References

[1] B. Trang *et al.*: J. Am. Chem. Soc. **140** (2018) 13892.
[2] *E. A. Schriber, D. W. Paley, R. Bolotovsky, D. J. Rosenberg, R. G. Sierra, A. Aquila, D. Mendez, F. Poitevin, J. P. Blaschke, A. Bhowmick, R. P. Kelly, M. Hunter, B. Hayes, D. C. Popple, M. Yeung, C. Pareja-Rivera, S. Lisova, K. Tono, M. Sugahara, S. Owada, T. Kuykendall, K. Yao, P. J. Schuck, D. Solis-Ibarra, N. K. Sauter, A. S. Brewster and J. N. Hohman: Nature **601** (2022) 360.*
[3] A. S. Brewster *et al.*: Acta Crystallogr. D **71** (2015)357.

Intact sea-island nanostructures of solid-state electrolytes snapshotted with a femtosecond X-ray laser

All-solid-state batteries are promising as next-generation batteries for electric vehicles, so applications and fundamental research have been intensively active in both industry and academia in recent years. Solid electrolytes can replace the conventional liquid electrolytes, which are highly reactive and flammable; thus, solid electrolytes can improve the safety, lifetime, and energy density of batteries. Glass-ceramics, which have an amorphous phase and one or more crystalline phases, have attracted significant interest as a solid electrolyte material. In particular, sulfide glass-ceramics have achieved ionic conductivity at room temperature equivalent to or higher than that of liquid electrolytes [1]. Knowledge of the relationship between the structural information of sulfide glass-ceramics and its battery performances will accelerate further improvement of solid electrolytes towards widely practical use. So far, various methods such as Raman spectroscopy, nuclear magnetic resonance, transmission electron microscopy (TEM), and molecular dynamics simulation have provided new insights into the structure of sulfide glass-ceramics. Among them, high-resolution TEM is a powerful tool that enables direct observation of the sea-island (amorphous-crystal) structure of sulfide glass-ceramics with nanometer spatial resolution and *in situ* measurement [2]. However, imaging intact nanostructure is still challenging because the crystal grains become amorphous during the observation owing to electron beam damage.

In the current study [3], we visualized the structure of an intact sulfide glass-ceramic electrolyte particle using pulsed coherent X-ray solution scattering (PCXSS). Additionally, we suggested an image processing method that makes use of morphological operations to obtain crystal images and the volume ratio of the amorphous to crystalline phases from the two-dimensional projection image produced via PCXSS (Fig. 1). PCXSS is a coherent diffractive imaging technique based on the X-ray free-electron laser (XFEL) and micro-liquid enclosure array (MLEA). Since XFEL pulses are extremely short (in the femtosecond range), it is possible to collect diffraction data from samples before radiation damage sets in. MLEA integrates many small solution wells into a single device and makes it possible to hold specimens in a vacuum environment with control over parameters such as temperature and solvent.

PCXSS measurements of $(Li_2S)_{70}$–$(P_2S_5)_{30}$ glass-ceramic particles were carried out at SACLA **BL2** EH3. The incident XFELs with a photon energy of 4 keV were focused to ~1 μm on the sample using total reflection mirrors. Immediately prior to the PCXSS measurement, the particles dispersed in a heptane solvent were enclosed in the MLEA (Fig. 2) using a semiautomated assembly system. Heptane solvent prevented the deliquescence of sulfide glass-ceramics and enhanced the slight image contrast between the amorphous and crystalline phases, as previously described [3]. Figure 3(a) shows a single-shot X-ray laser diffraction pattern from a glass-ceramic particle. The diffraction pattern reached the edge of the detector with a good signal-to-noise ratio, though the presence of the solvent generally reduces diffracted intensities from the sample. The maximum spatial frequency was 0.105 nm^{-1}. Figure 3(b) is a projection image reconstructed by applying the phasing method to the diffraction pattern (Fig. 3(a)). The spatial resolution was 14.5 nm, as evaluated by the phase retrieval transfer function. The particle size was approximately 300 nm, and there were many bright spots all throughout the

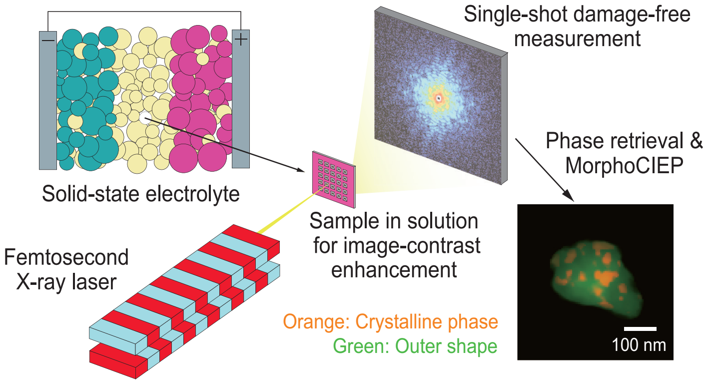

Fig. 1. Schematic of a femtosecond X-ray laser and cutting-edge image-processing technique that reveal intact sea-island nanostructures of fragile solid-state electrolytes for batteries. [3]

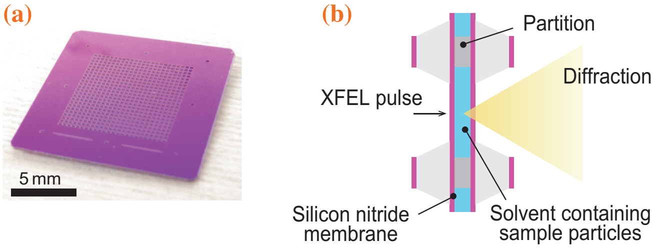

Fig. 2. **(a)** Photograph of an MLEA. The MLEA comprises 576 micro-liquid enclosures. **(b)** Schematic of the cross-section of an MLEA chip. The micro-liquid enclosures are separated from each other by epoxy grid partitions. [3]

particle. Because the outer shape of the particle is smooth, these bright spots can be attributed to crystal grains with higher electron densities rather than to the roughness of the particle surfaces.

We applied a newly developed image processing technique, morphological crystal-image-extraction processing (MorphoCIEP), to the reconstructed image in Fig. 3(b) to quantitatively extract the outer shape and crystal images. Figure 3(c) shows the superposition of the crystal (orange) and outer shape (green) images. The extracted crystal image clarified the sea-island nanostructures. MorphoCIEP consists of several steps, including high-pass filtering (HPF), rotational morphological processing (RMF) [4], and interpolation processing. HPF and RMF act complementarily in the reciprocal and real spaces to effectively emphasize crystal grains. Parameters in each image processing step can be optimized by repeatedly performing the process while feeding back the output results. The sizes of the crystal grains were approximately 10–50 nm, which is consistent with observations of the TEM images. There were 23 crystal grains in total, and they covered the entire particle, from the edge to the center. Furthermore, the volume ratio of amorphous to crystalline phases in the particles was determined to be approximately 2.5:1 using the intensity values of the extracted images and known electron densities of amorphous and crystalline phases of $(Li_2S)_{70}$–$(P_2S_5)_{30}$. The proportion and distribution of crystalline grains in the particles are related to the lithium-ion conductivity, which is essential to battery performance.

The quantitative morphological information obtained via PCXSS with MorphoCIEP will guide the optimization of various properties of solid electrolytes, including thermal stability, moisture resistance, potential window, interface resistance, and ionic conductivity. In future work, we aim to perform *in situ* temperature-controlled PCXSS measurements to observe the dynamics of structural changes during the annealing process in the synthesis of sulfide solid-state electrolytes. The studied sulfide solid-state electrolyte is a kind of metastable material. With the progress of materials informatics [5], metastable materials have been found to be innovative materials with unprecedented functions. However, as the name implies, the low thermodynamic stability of metastable materials makes it difficult to fully analyze their structures by conventional measurement methods. PCXSS with MorphoCIEP has the potential to contribute to the development of reliable, safer, and higher-performance batteries and advanced metastable materials for realizing a sustainable society.

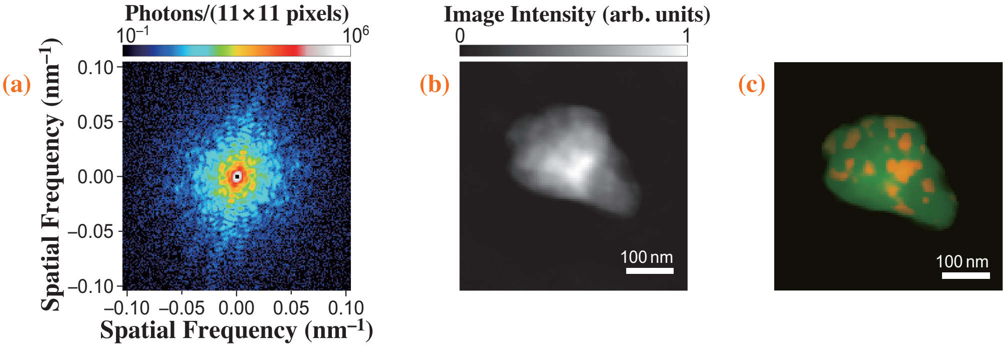

Fig. 3. **(a)** Measured diffraction pattern from a glass-ceramic particle. **(b)** Reconstructed image obtained via phase retrieval. **(c)** Superposition of crystal (orange) and outer-shape (green) images after applying MorphoCIEP to the reconstructed image in Fig. 3(b). [3]

Akihiro Suzuki* and Yoshinori Nishino

Research Institute for Electronic Science,
Hokkaido University

*Email: akihiro.suzuki@es.hokudai.ac.jp

References

[1] A. Hayashi *et al*.: Nat. Commun. **10** (2019) 5266.
[2] H. Tsukasaki *et al*.: Sci. Rep. **7** (2017) 4142.
[3] *A. Suzuki, H. Tanaka, H. Yamashige, Y. Orikasa, Y. Niida, T. Kimura, K. Tono, M. Yabashi, T. Ishikawa, Y. Bessho, Y. Joti, Y. Nishino: Nano Lett.* ***22*** *(2022) 4603.*
[4] Y. Kimori: J. Synchrotron Rad. **20** (2013) 848.
[5] D. P. Tabor *et al*.: Nat. Rev. **3** (2018) 5.

Hydrogen storage by earth abundant metals – high-pressure synthesis of Al_3FeH_4

Compounds of metal and hydrogen are called metal hydrides, and among them, alloys that can easily release and absorb hydrogen near ambient pressure–temperature conditions are called hydrogen storage alloys. There are well-known guidelines for obtaining hydrogen storage alloys. These guidelines concern alloying metals with high and low hydrogen affinities [1]. Here, metals with high hydrogen affinities refer to elements that can easily form metal hydrides with hydrogen-to-metal atomic ratios (H/M ratios) of 0.5 or higher near ambient pressure. In contrast, metals with low hydrogen affinity refer to elements that cannot form such hydrides near ambient pressure.

It is also known that hydrogen affinity can be well classified on the basis of the periodic table. Figure 1 shows the relationship between a certain part of the periodic table and hydrogen affinity. It is clear from Fig. 1 that elements in groups 1 through 5 have high hydrogen affinities, while those in groups 6 through 13 have low hydrogen affinities. It has been reported that the hydrogen affinity of metals is related to their softness [2].

Hydrogen storage alloys must contain at least one metal with a high hydrogen affinity. However, as shown in Fig. 1, except for Mg, all metals with high hydrogen affinities are expensive, making it difficult to reduce costs. In addition, the choice of lightweight elements is also limited, making it difficult to increase the hydrogen density per weight. Thus, under the conventional search guidelines for hydrogen storage alloys, it is considered difficult to obtain a material that can solve the problems of hydrogen storage alloys, such as gravimetric hydrogen density and cost.

With the aim of realizing hydrogen storage alloys that do not contain expensive rare metals, we have been searching for hydrides consisting only of metals with low hydrogen affinities, which do not follow the synthesis guidelines for hydrogen storage alloys, under high pressures. We found that an alloy of aluminum and iron can form hydrides under high pressures and that the resulting hydride has the potential to absorb hydrogen even near ambient pressure [3].

The starting material was the $Al_{13}Fe_4$ alloy prepared by arc melting at ambient pressure. The obtained ingot was crushed into a coarse powder and compacted into a disk shape. The disk-shaped sample was placed in a sample capsule made of boron nitride. The sample was pressurized to 9 GPa at room temperature and then heated to 750°C in fluid hydrogen. The sample was kept in hydrogen for 2 h, cooled to room temperature, and depressurized to the ambient pressure.

The hydrogenation of the sample was achieved using a high-pressure cell developed by Fukai and Okuma [4]. A capsule made of NaCl was used for hydrogen sealing. An internal hydrogen source made of NH_3BH_3 was placed in the hydrogen sealing capsule along with the sample. The sample in the boron nitride capsule, through which hydrogen can permeate but not other byproducts from the internal hydrogen source, was hydrogenated. We observed structural changes of the sample during the hydrogenation reaction *in situ* using synchrotron radiation X-ray diffraction (SR-XRD) measurement at SPring-8 **BL14B1** to detect the occurrence of a novel hydrogenation reaction.

Figure 2 shows the X-ray powder diffraction profiles obtained when the $Al_{13}Fe_4$ alloy was kept in a hydrogen fluid under high pressures. Figure 2(a) shows the change in the profile when the alloy was kept at 600°C at 6 GPa. The bottom profile was obtained after the alloy was pressurized to 6 GPa at room temperature. Excluding diffraction lines from high-pressure cell parts, all peaks can be indexed to the ambient-pressure phase of the $Al_{13}Fe_4$ alloy, indicating that no pressure-induced structural phase transition occurred. When the alloy was heated, no significant structural changes were observed except for peak sharpening and increases in the intensities of some peaks owing to the relaxation of anisotropic strain introduced by solid compression. $Al_{13}Fe_4$ alloy cannot be hydrogenated at 600°C and 6 GPa.

Figure 2(b) shows X-ray diffraction profiles of the alloy hydrogenated at 750°C and 9 GPa. Decreases in the intensities of Bragg peaks from the alloy and the appearance of new peaks were observed above

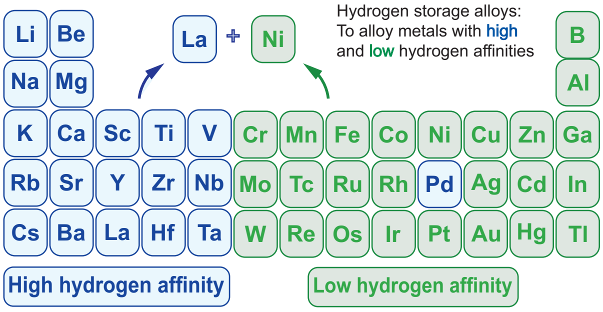

Fig. 1. Relationship between hydrogen affinities of metallic elements and the periodic table, where elements in groups 1 to 5 have high hydrogen affinities and those in groups 6 to 13 have low affinities. Hydrogen storage alloys are obtained by alloying metals with high and low hydrogen affinities.

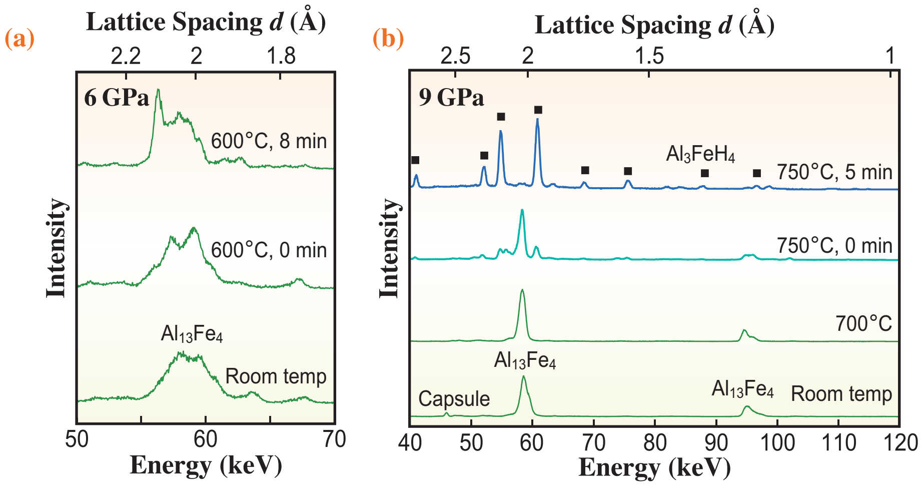

Fig. 2. *In situ* powder X-ray diffraction profiles measured when $Al_{13}Fe_4$ alloys were hydrogenated at **(a)** 6 GPa and **(b)** 9 GPa.

650°C. When the alloy was kept at 750°C, the peaks from the alloy disappeared after 5 min, and only the peaks from the new structural phase appeared. It was determined that the new structural phase was the new hydride Al_3FeH_4 on the basis of the results of characterizing the recovered hydride under ambient conditions. The schematic of the crystal structure of Al_3FeH_4 is shown in Fig. 3.

It was also clarified that Al_3FeH_4 is thermodynamically stable under near-ambient conditions by the analysis of the recovered sample. In other words, $Al_{13}Fe_4$ alloy can absorb hydrogen at around ambient pressure and has potential for hydrogen storage application. In contrast to its thermodynamical stability, a high pressure above 7 GPa is currently necessary to hydrogenate the alloy. This is because a chemically stable oxide layer on the alloy prevents the hydrogenation reaction. Now, we are attempting to hydrogenate the alloy at around ambient pressure by suppressing the effect of the surface oxide layer.

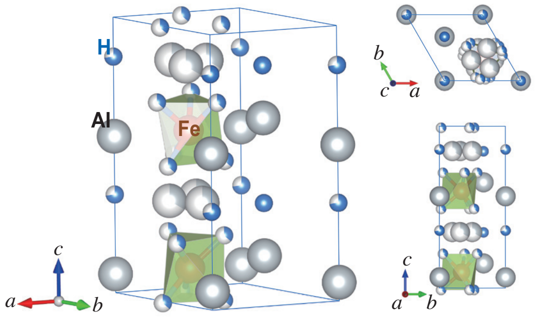

Fig. 3. Schematic of the crystal structure of Al_3FeH_4. The crystal structure was drawn using the VESTA program [5].

Hiroyuki Saitoh

Synchrotron Radiation Research Center, QST

Email: saito.hiroyuki@qst.go.jp

References

[1] A. Züttel: Mater. Today **6** (2003) 24.
[2] H. Mizoguchi *et al.*: J. Am. Chem. Soc. **143** (2021) 11345.
[3] *H. Satioh, T. Sato, M. Tanikami, K. Ikeda, A. Machida, T. Watanuki, T. Taguchi, S. Yamamoto, T. Yamaki, S. Takagi, T. Otomo and S. Orimo: Mater. Des.* ***208*** *(2021) 109953.*
[4] Y. Fukai and N. Okuma: Jpn. J. Appl. Phys. **32** (1993) L1256.
[5] K. Momma and F. Izumi: J. Appl. Crystallogr. **41** (2008) 653.

Spin tube oxide obtained by topochemical dehydration

Dehydration is an essential reaction for maintaining biological functions such as maintaining a constant body temperature and is also involved in other simple organic reactions such as the synthesis of ethers from alcohols [1]. In the case of inorganic materials, dehydration reactions can be seen, for example, in the processes of molding and baking clay during which our ancestors made earthenware and pottery. The Hayabusa2 spacecraft, which succeeded in its mission in 2020, has shown that the near-Earth asteroid Ryugu has an unexpectedly low water content resulting from its surface material being composed of carbonaceous chondrites that have undergone heating and dehydration [2].

Oxides, which represent inorganic materials, exhibit various properties that make them function as magnets, batteries, catalysts, and superconductors among others. Interestingly, functionalities of oxide materials can be achieved through the successful control of oxygen content. For example, in the high-T_c oxide superconductor $YBa_2Cu_3O_{7-x}$, the transition temperature of superconductivity can be tuned by adjusting the oxygen content x [3]. The main method of controlling the oxygen content of oxides has been to adjust the gas atmosphere during synthesis at high temperatures. Recently, however, it has been reported that low-temperature topochemical reactions using metal hydrides such as CaH_2 are powerful methods to remove oxygen ions from oxides during reduction reactions [4].

In this study, we have succeeded in obtaining a new material, $SrCoO_2$, by electrochemical insertion of a proton (H^+) into the oxide $SrCoO_{2.5}$, followed by heating and a dehydration reaction (Fig. 1(a)) [5]. Here, the cobalt valence is reduced from trivalence in the starting material $SrCoO_{2.5}$ to divalence in the reactant $SrCoO_2$, indicating that this method of combining protonation and dehydration is a powerful reduction reaction process. Note that $SrCoO_2$ cannot be obtained by the reduction reaction using metal hydrides, which have been known as the strongest reducing agent.

We have performed soft X-ray absorption spectroscopy (sXAS) experiments at SPring-8 **BL25SU** to investigate the local structure and valence state of $SrCoO_{2.5}$ and materials obtained by our developed new reduction reaction method using protonation and dehydration. Figure 1(b) shows the sXAS spectra around the Co *L*-edge for the samples before and after protonation and after subsequent dehydration in a vacuum. The electrochemical protonation of $SrCoO_{2.5}$ results in $HSrCoO_{2.5}$, indicating that the Co *L*-edge shifts to a lower energy accompanied by the reduction from Co^{3+} to Co^{2+}. On the other hand, after $HSrCoO_{2.5}$ is dehydrated at a high temperature, the position of the Co *L*-edge does not change, indicating that the divalent state Co^{2+} is retained during the dehydration reaction. However, the spectral shape changed significantly, indicating a significant change in the local structure around Co cations after dehydration. That is, the spectrum of $HSrCoO_{2.5}$ before dehydration contains a mixture of spectra corresponding to both octahedral and tetrahedral coordination around Co cations, but after heating and dehydration, the former spectrum

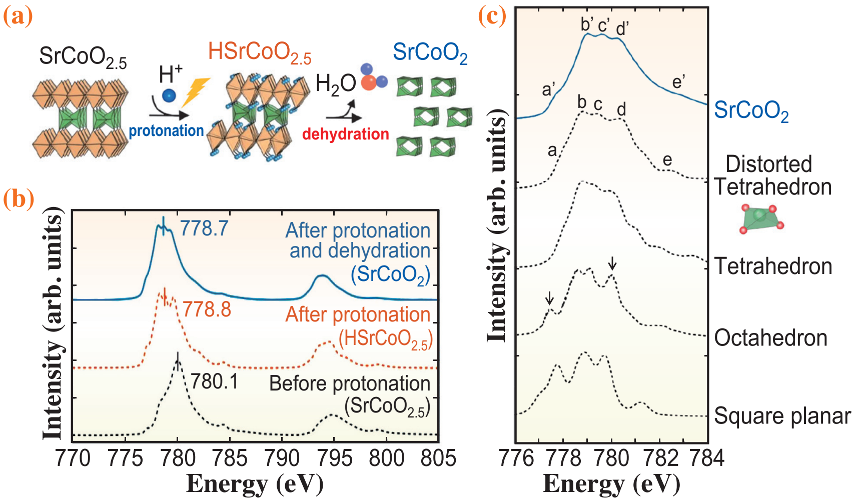

Fig. 1. **(a)** New reduction process using the combination of electrochemical protonation and subsequent dehydration discovered in this study. **(b–c)** Experimental results of sXAS measurements performed at SPring-8 BL25SU.

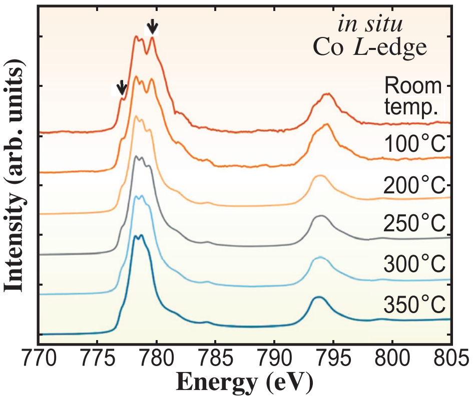

Fig. 2. *In situ* sXAS spectra of the Co *L*-edge of $HSrCoO_{2.5}$ during heating in a vacuum. Arrows indicate the characteristic peaks of the CoO_6 octahedron, which disappear at high temperatures in a vacuum.

corresponding to octahedral coordination disappears and the only that corresponding to the distorted tetrahedral coordination is observed (Fig. 1(c)). This result was also confirmed by the results of *in situ* sXAS experiments (Fig. 2). This means that a large number of oxygen ions can be removed from $HSrCoO_{2.5}$ at about 300°C during the dehydration reaction ($HSrCoO_{2.5} \rightarrow SrCoO_2 + 0.5H_2O$). $SrCoO_2$ obtained through this reaction is a new material, and its crystal structure was also determined by scanning transmission electron microscopy (STEM) experiments and complemental theoretical calculations (Fig. 3(a)).

The feature of this new reduction reaction method is the existence of a protonated intermediate $HSrCoO_{2.5}$ (Fig. 1(a) center), in which the CoO_6 octahedron is distorted upon protonation and destabilized under local strain. It is therefore considered that stable water (H_2O) can be removed along with oxygen ions from the crystal lattice of $HSrCoO_{2.5}$ by heating and dehydration, resulting in $SrCoO_2$ (Fig. 1(a) right). Thus far, in perovskite-related ABO_2 (A, alkaline-earth metal ions or rare-earth metal ions; B, transition metal ions) compounds, only those with iron (Fe), copper (Cu), and nickel (Ni) at the B site are known to exist. Therefore, it is interesting and important to note that a new variation of cobalt Co was obtained in this study by a new reduction process in which the oxide is protonated followed by a dehydration reaction.

The insertion of H^+ into oxide thin films using the ionic liquid gating technique is a recent subject of research worldwide. However, there has been no research on the concept of using an electrochemically protonated material as a precursor for a dehydration reaction to synthesize a new material with low oxygen content, as in this study. Therefore, this study is the first demonstration that the dehydration reaction after protonation is a powerful method of reduction reaction to remove many oxygen ions from an oxide. In the future, it is expected that this reducing reaction will be used to develop new oxide functional materials. For example, it will be interesting to apply this method to powder samples and to develop reduced oxides with new structures in combination with the substrate strain arising from the thin film growth. In terms of applications, the potential utilization in the development of hydrogen storage materials holds promise. Moreover, $SrCoO_2$ obtained in this study has a unique crystal structure called a four-leg spin tube (Fig. 1(a) right and Fig. 3(b)). This structure closely resembles the "spin ladder structure" that has attracted attention in the field of condensed matter physics since the discovery of high-T_c cuprate superconductors. Therefore, it is expected to be a new platform for the emergence of novel quantum magnetism and superconductivity, and it will be interesting to see the future experimental and theoretical development of this research.

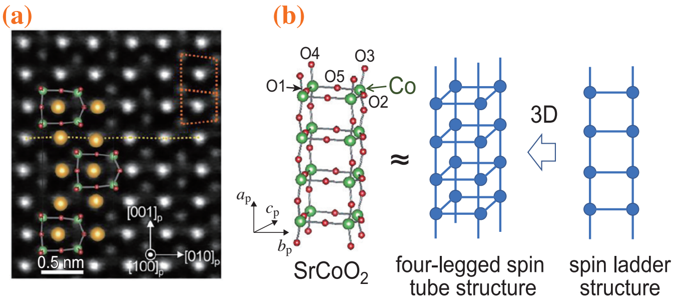

Fig. 3. **(a)** High-angle annular dark-field STEM image of $SrCoO_2$. **(b)** Schematic view of the relationship between tour-legged spin tube structure of $SrCoO_2$ and spin ladder structure.

Hiroshi Takatsu*, Hao-Bo Li† and Hiroshi Kageyama

Graduate School of Engineering, Kyoto University

*Email: takatsu@scl.kyoto-u.ac.jp

† Present address: SANKEN, Osaka University

References

[1] A. D. McNaught and A. Wilkinson: Compendium of Chemical Terminology, 2nd ed. (Blackwell Science: Oxford, UK, 1997).
[2] T. Yokoyama *et al*.: Science **379** (2022) 6634.
[3] R. J. Cava *et al*.: Phys. Rev. B **36** (1987) 5719.
[4] e.g., M. Hayward *et al*.: J. Am. Chem. Soc. **121** (1999) 8843.
[5] *H.-B. Li, S. Kobayashi, C. Zhong, M. Namba, Y. Cao, D. Kato, Y. Kotani, Q. Lin, M. Wu, W.-H. Wang, M. Kobayashi, K. Fujita, C. Tassel, T. Terashima, A. Kuwabara, Y. Kobayashi, H. Takatsu and H. Kageyama: J. Am. Chem. Soc.* ***143*** *(2021) 17517.*

Phonon-assisted proton(deuteron) transfers leading the antiferro-electric ordering in superprotonic conductors $Cs_3H(D)(SeO_4)_2$

Proton conduction is a key functionality to improve a high-performance fuel cell that is a fundamental technology to reduce CO_2 emissions and to achieve a hydrogen society. In general, proton conduction is phenomenologically discussed with activation-type motions as a diffusion process. In crystalline proton conductors, a proton–phonon (PP) interaction is significant to understand microscopic-transfer mechanisms because the proton never transfers individually but interacts with a lattice system. Nevertheless, little knowledge on PP interactions has been obtained so far in protonic systems. Among a variety of proton conductors, we have focused on $Cs_3H(D)(SeO_4)_2$ that exhibits superprotonic conduction above T_{spc} and antiferroelectric (AF) ordering below T_{AF} (Fig. 1 (a)), because the good single crystal is obtained.

The crystal structure on the *ab* plane of localized phases III and IV is shown in Fig. 1(b), where the lattice constant is summarized in the table. Two SeO_4 tetrahedra are connected through a hydrogen bond between apical O(2) and O'(2) in the form of dimer (Fig. 1(c)). The proton and deuteron possess two equivalent sites in between O(2) and O'(2). A remarkable isotope effect relevant to the AF ordering was known about 40 years ago (Fig. 1(a)); T_{AF} = 50 K ($Cs_3H(SeO_4)_2$) and 168 K ($Cs_3D(SeO_4)_2$). Similar isotope effects are observed in the corresponding systems such as $Rb_3H(D)(SeO_4)_2$, and ferroelectric materials like potassium dihydrogen phosphate (KDP). Employing a wide range of infrared spectroscopies combined with first principles calculations and ^{1}H-NMR experiments, we have clarified the difference of AF-ordering mechanisms and the role of PP interactions in $Cs_3H(SeO_4)_2$ and $Cs_3D(SeO_4)_2$ [1,2].

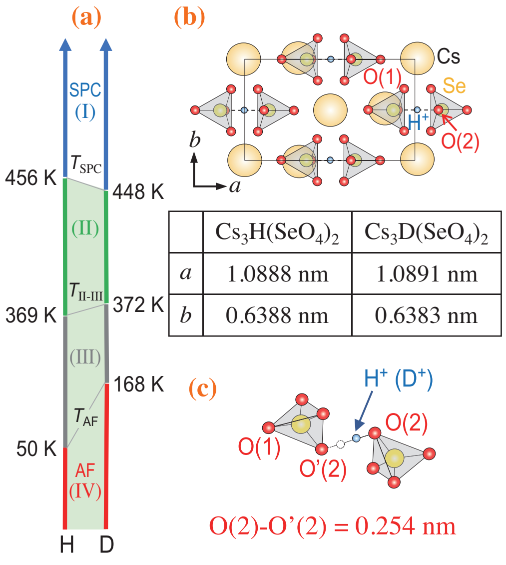

	$Cs_3H(SeO_4)_2$	$Cs_3D(SeO_4)_2$
a	1.0888 nm	1.0891 nm
b	0.6388 nm	0.6383 nm

Fig. 1. **(a)** Transition temperatures in $Cs_3H(SeO_4)_2$ and $Cs_3D(SeO_4)_2$. **(b)** Crystal structure on the *ab* plane and lattice constants. **(c)** Two equivalent sites in O(2)-O'(2) of the dimer.

Absorbance spectra below 300 K were measured at 5–8000 cm^{-1} utilizing a terahertz time-domain spectrometer, and a FT-IR spectrometer equipped with a Cassegrain microscope. Especially in far-infrared range, the single-domain crystal with about 1 mm in diameter is quite difficult to measure with usual spectrometers. Thanks to the microscopic spectrometer facilitated at SPring-8 **BL43IR** providing strong far-infrared light, we have successfully detected the polarized absorbance spectra.

In the far-infrared spectra of $Cs_3H(SeO_4)_2$ (Fig. 2(a)) and $Cs_3D(SeO_4)_2$ (Fig. 2(b)), a libration and SeO_4-tetrahedral deformations accompanied with a O-Se-O bending (def$_{bend}$ mode) appear at 180 and 300 – 450 cm^{-1}, respectively [1,2]. The libration in $Cs_3H(SeO_4)_2$ exhibits a spectral splitting at 30–70 K, while such anomaly is never observed in $Cs_3D(SeO_4)_2$. In Fig. 2(c), the splitting for *a* polarization at T_{AF} in $Cs_3H(SeO_4)_2$ is reproduced with two Lorentzian curves. The vibrational motif of libration illustrated in Fig. 2(d) induces a characteristic modulation of O(2)-O'(2) distance. From the mid-infrared spectrum, anomalous OH stretching mode proves that the proton anharmonically couples to the libration, and thereby the PP interaction plays the important role to generate the AF ordering [1]. In $Cs_3D(SeO_4)_2$, anomalous enhancements of the integrated absorbance (Fig. 2(e)) are observed at around T_{AF} in the 310-cm^{-1} def$_{bend}$ mode that is painted in blue in Fig. 2(b), and the vibrational motif is depicted in Fig. 2(f). Taking the anharmonicity of OD stretching mode into account, the deuteron is found to couple to the 310-cm^{-1} def$_{bend}$ mode [2]. Therefore, the proton and deuteron interact to the different phonon modes.

The proton and deuteron have to transfer between the equivalent sites to achieve the AF arrangement. According to the ^{1}H-NMR measurements, conventional thermal hopping in a rigid double-minimum potential (Fig. 3(a)) diminishes below 150 K [1]. As the modulation of O(2)-O'(2) distance is huge enhanced through fluctuations towards the AF ordering in

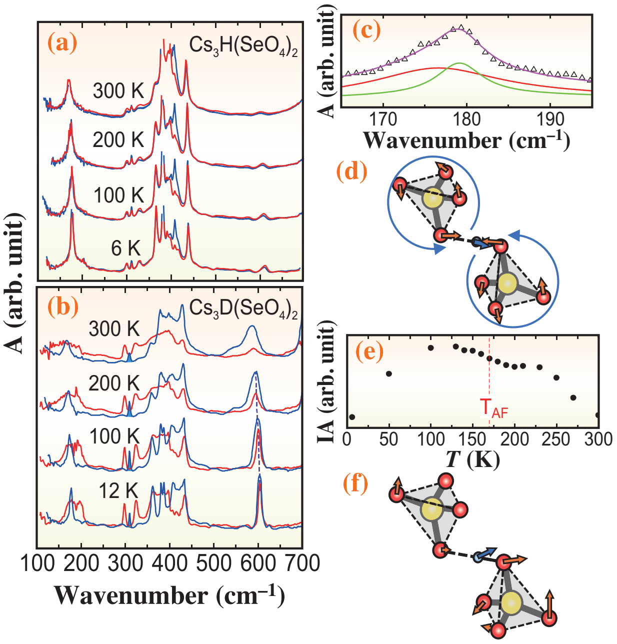

Fig. 2. **(a, b)** Absorbance (A) of $Cs_3H(SeO_4)_2$ and $Cs_3D(SeO_4)_2$ in far-infrared range. **(c, d)** Splitting and vibrational motif of the libration in $Cs_3H(SeO_4)_2$. **(e, f)** Integrated absorbance (IA) and vibrational motif of the 310-cm^{-1} def$_{str}$ mode in $Cs_3D(SeO_4)_2$.

$Cs_3H(SeO_4)_2$, the wave functions of two equivalent sites can overlap, and simultaneously a dynamical proton tunneling yields the splitting of the ground state as shown by red lines in Fig. 3(b). Since each level strongly couples to the libration, the split bands emerge in the far-infrared time scale. This phenomenon corresponds to a phonon-assisted proton tunneling (PAPT) associated with the libration, and hence quantum fluctuations conduct the AF ordering.

A splitting is never observed in the spectra of $Cs_3D(SeO_4)_2$, though the anomalous integrated absorbance of 310-cm^{-1} def$_{bend}$ mode represents the increase of oscillator strength through huge modulations of the O(2)-O'(2) distance [2]. The modulation dynamically suppresses the potential-barrier height (Fig. 3 (c)), and then a phonon-assisted deuteron hopping (PADH) associated with the 310-cm^{-1} def$_{bend}$ mode generates classical fluctuations to lead the AF ordering. The isotope effect is concluded to change the phonon that helps the transfer. Since the 310-cm^{-1} def$_{bend}$ mode is energetically larger than the libration, $Cs_3D(SeO_4)_2$ possesses higher T_{AF} than $Cs_3H(SeO_4)_2$.

Finally, we would like to mention the 610-cm^{-1} band that exhibits the most remarkable isotope effect. The absorbance spectrum obtained by the first principles calculation has no bands at 500~700 cm^{-1}. The 610-cm^{-1} band is not attributed to phonons and molecular vibrations, but to a collective excitation relevant to a classical hopping, because the barrier height coincides with the result evaluated from the ^{1}H-NMR measurement [1]. The intensity in $Cs_3D(SeO_4)_2$ (Fig. 2(b)) is about ten times as large as one in $Cs_3H(SeO_4)_2$ (Fig.2(a)) [2]. In $Cs_3H(SeO_4)_2$, the PAPT associated with the 440-cm^{-1} def$_{bend}$ mode becomes dominant at 70–250 K, so that very few protons contribute to the classical hopping. On the other hand, all the deuterons contribute to the classical hopping, and consequently the 610-cm^{-1} band in $Cs_3D(SeO_4)_2$ has large intensity compared to $Cs_3H(SeO_4)_2$.

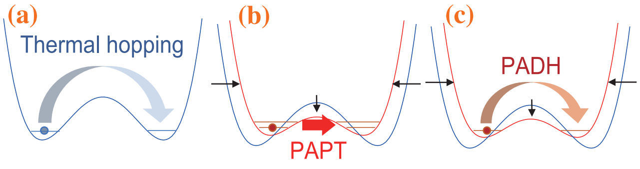

Fig. 3. Schematic illustrates of double minimum potential for thermal hopping **(a)**, PAPT **(b)** and PADH **(c)**.

Hiroshi Matsui

Department of Physics, Tohoku University

Email: hiroshi.matsui.b2@tohoku.ac.jp

References

[1] H. Matsui *et al.*: J. Chem. Phys. **152** (2020) 154502.
[2] *H. Matsui, K. Fukuda, S. Takano, Y. Ikemoto, T. Sasaki and Y. Matsuo: J. Chem. Phys.* ***156*** *(2022) 204504.*

Unraveling the resistive switching mechanisms in $LaMnO_{3+\delta}$-based memristive devices by *operando* hard X-ray photoemission

Oxide-based resistive random-access memories (OxRRAMs) are promising candidates for the next generation of non-volatile memories. The data storage principle is based on the switching, upon applied electrical bias, of the resistivity of an oxide between high (HRS) and low (LRS) resistive states. Devices based on a transition metal oxide, such as the $LaMnO_{3+\delta}$ (LMO), have shown interesting electrical properties such as multi-level data storage [1]. Their resistive switching mechanism is related to the formation and partial rupture of a conductive filament.

Further information concerning chemical changes governing the conduction mechanism are needed to efficiently control and optimize the devices performances. In the past, HAXPES was used to study the critical metal/oxide interfaces of such oxide-based memristive devices [2]. However, standard measurements only provide a static view of the involved phenomena whereas *operando* measurements can bring a more dynamic picture of the mechanisms governing the device behavior [3].

Operando HAXPES under *in situ* electrical biasing has thus been developed to investigate the behavior of memory devices during operation and based on the M/LMO/Pt stack, with M = Au or Pd [4]. We focus here on memory cells fabricated with a chemically inert top electrode, compared to an active TiN electrode [5]. HAXPES measurements were performed at SPring-8 **BL15XU** with a photon energy of 7933 eV.

In order to both match the HAXPES requirements and allow *in situ* electrical activation, the device depicted in Fig. 1(a) was fabricated. The active region consists of a thin (~7 nm) metal layer (Au or Pd) deposited directly on a 100×100 μm² LMO surface. Outside this region, the top electrode was electrically isolated from LMO by a 50 nm-thick Si_3N_4 insulating layer. A thick current collector was deposited away from the active area and connected to a sourcemeter (Keithley 2635B).

Figure 1(b) shows the characteristic hysteretic current-voltage (I-V) curve measured *in situ* for the Au top electrode-memristive device, exhibiting an asymmetric bipolar counter-clockwise-type switching. An abrupt RESET from LRS to HRS occurs around 2 V while the SET process requires higher negative voltage (–8 V) and presents several consecutive steps starting at –6 V. The compliance current was set to 10 mA in negative polarity in order to avoid the oxide electrical breakdown at high voltage.

HAXPES measurements were carried out on the Pd/LMO/Pt device after *in situ* switching. By comparing the O 1*s* spectra measured in LRS and HRS (see Figs. 2(a) and 2(b)), noticeable differences are observed, though partly screened by the large Si–O signal coming from the partially oxidized Si_3N_4 layer. Two other contributions are identified corresponding to lattice oxygen from LMO ($O_{latt.}$) and to interfacial oxygen ($O_{inter.}$) ascribed to oxygen inserted at the metal/oxide interface. From LRS to HRS, the $O_{inter.}$ contribution slightly increases (from 20.5% to 21.6% of the total area) with respect to the $O_{latt.}$ one (from 7.7% to 6.6%). This result indicates that oxygen is released from the LMO lattice and drifts towards the top electrode during the RESET step ($V_{RESET} > 0$).

Figures 2(c) and 2(d) show the La $3d_{5/2}$ spectra recorded in LRS and HRS, respectively. Both spectra exhibit a main peak (cf^0) and two satellite peaks (cf^1L), resulting from core-hole screening processes. In our previous study [5], we demonstrated the direct relationship between the oxygen content in the surrounding of La atoms and the ratio of the satellites/main peak areas. From LRS to HRS, a slight decrease of the main peak intensity is observed, thus indicating an increase of the oxygen content in the La

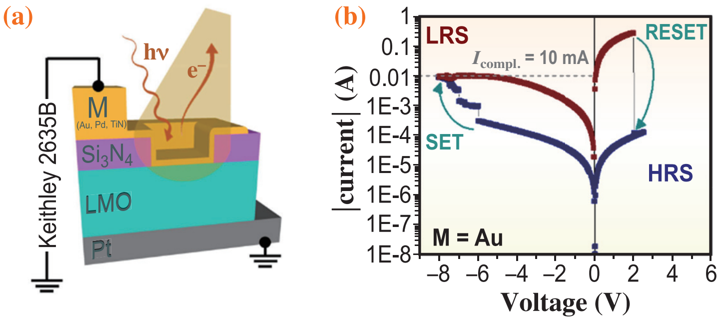

Fig. 1. **(a)** Sketch of the memristive device for operando measurements. **(b)** *In situ* I–V characteristics obtained for an Au/LMO/Pt stack. [4]

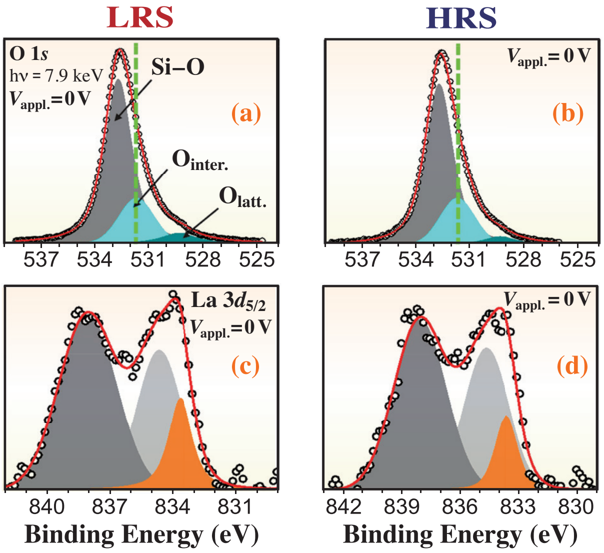

Fig. 2. O 1s and La 3$d_{5/2}$ spectra for the Pd/LMO/Pt stack in **(a)**, **(c)** LRS, and **(b)**, **(d)** HRS at 0V. [4]

neighborhood. The La spectra indicate that, in addition to the oxygen release, an oxygen-rich region is formed at the top LMO interface.

Based on these results, we suggest a model of the resistive switching mechanism in the Pd/LMO/Pt system as depicted in Fig. 3. We assume that the conduction in the LMO is related to the formation of filaments with an oxygen-rich composition (see Fig. 3(a)). When a positive voltage is applied (RESET, see Fig. 3(b)), oxygen from the filament drifts towards the top electrode, thus reducing the LMO conductivity. The device is switched to the HRS state. When a negative voltage is applied (SET, see Fig. 3(c)), oxygen is drifting back into the material and conductive paths can be formed again: the device is then set back in its LRS.

In summary, we demonstrated that the switching mechanism of the Pd(Au)/LMO/Pt devices is triggered by oxygen drift phenomena between the LMO and the top electrode, thus locally modifying the conductivity of oxygen-rich regions, so-called filaments. The oxygen is accumulated at the interface with the top Pd(Au) electrode, both in a top LMO oxygen-rich layer, and in the form of gas pockets under the metal electrode.

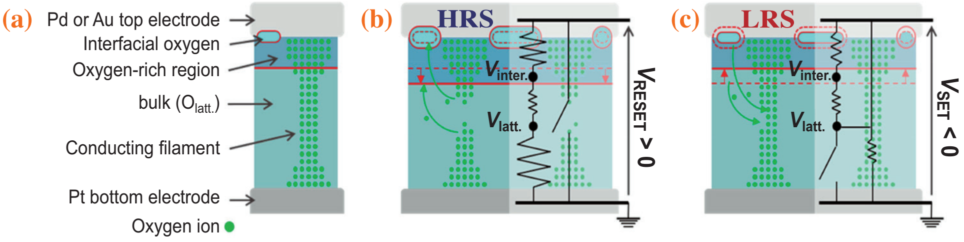

Fig. 3. Sketch of the proposed physical model used to describe the M/LMO/Pt devices (M = Au, Pd) studied by operando HAXPES. [4].

Benjamin Meunier, Eugénie Martinez and Olivier Renault*

University Grenoble Alpes, CEA, France

*Email: Olivier.Renault@cea.fr

References

[1] P. Stoliar *et al.*: IEEE Trans. Circuits Syst. II **61** (2014) 21.
[2] P. Calka *et al.*: J. Appl. Phys. **109** (2011) 124507.
[3] M. Sowinska *et al.*: J. Appl. Phys. **115** (2014) 204509.
[4] *B. Meunier, E. Martinez, R. Rodriguez-Lamas, D. Pla, M. Burriel, C. Jimenez, Y. Yamashita, S. Ueda, O. Renault: ACS Appl. Electron. Mater.* ***3*** *(2021) 5555.*
[5] B. Meunier *et al.*: J. Appl. Phys. **126** (2019) 225302.

Observation of rapid lift-up behavior of acetate-intercalated layered yttrium hydroxide interlayer in water: Application for heterogeneous Brønsted base catalysts

Due to their unique characteristics combined with their host–guest properties and rare-earth cations, layered rare-earth hydroxides (LRHs) are receiving much attention as a new type of anionic layered compound [1]. The general formula of LRHs is $Ln_2(OH)_5X{\cdot}nH_2O$, where Ln and X are a trivalent rare-earth metal cations and anions, respectively. There are two kinds of coordination polyhedra, such as a dodecahedron and a monocapped square antiprism, linked through μ^3-hydroxy groups in the cationic layer of LRHs, $[Ln_4(OH)_{10}(H_2O)_4]^{2+}$. Numerous studies by use of various types of LRHs applied as the functional materials have been reported, however, there are few examples of the application of LRHs as catalyst materials.

We have reported successful Knoevenagel condensation with various anion-exchanged layered yttrium hydroxides (Y-LRHs) as solid base catalysts [2]. Catalytic condensation in water proceeded efficiently in the presence of acetate-intercalated Y-LRH (CH_3COO^-/Y-LRH). In this catalysis, the specific lift-up behavior of the basal spacing of CH_3COO^-/Y-LRH in the presence of excess water was confirmed by time-resolved synchrotron-radiation X-ray diffraction (*t*-SXRD) profiles.

A novel *t*-SXRD measurement system was developed at SPring-8 **BL02B2** [3]. The measurement system consisted of a diffractometer equipped with a sample stage, an auto-titrator, and multiple MYTHEN detectors at room temperature. The sample stage contained a glass tube holder (ϕ10 mm) was set with a magnetic stirrer. A constant solution volume was remotely and promptly transferred from the auto-titrator to the sample glass tube through a fluorinated ethylene propylene (FEP) tube. The *t*-SXRD patterns were acquired over 360 s with accumulation time of 0.5 s per diffraction pattern and an X-ray wavelength of 0.08 nm (15.5 keV) was selected.

According to the report by Sasaki *et al.* [4], the parent chloride-intercalated Y-LRH (Cl^-/Y-LRH; $Y_2(OH)_5Cl{\cdot}1.43H_2O$) was synthesized by the homogeneous precipitation method. The treatment of Cl^-/Y-LRH with various sodium acetate yielded CH_3COO^-/Y-LRH catalyst in the form of white powders. The Cl^-/Y-LRH was dispersed in water set on the glass tube with vigorous stirring, and then the SXRD pattern of the aqueous dispersion of the sample was collected. The aqueous sodium acetate solution was immediately added at once using the auto-titrator.

Figure 1(a) shows the 2D maps of the *t*-SXRD profiles for Y-LRH during the anion exchange reaction from chloride into acetate. This anion-exchange reaction rapidly occurred. After the addition of aqueous sodium acetate into the solution of Cl^-/Y-LRH dispersed in water, the d_{00l} peak at 5.51° (0.85 nm) disappeared immediately, a new peak based on the formation of CH_3COO^-/Y-LRH in water appeared at 3.45° (1.33 nm), and the FWHM value of the newly appeared peak was constant. From the time profile of the peak area at 3.45° (Fig. 1(b)), two steps, fast and slow increment behavior, were clearly observed. In contrast, anion-exchange ratio of 91 and 93%,

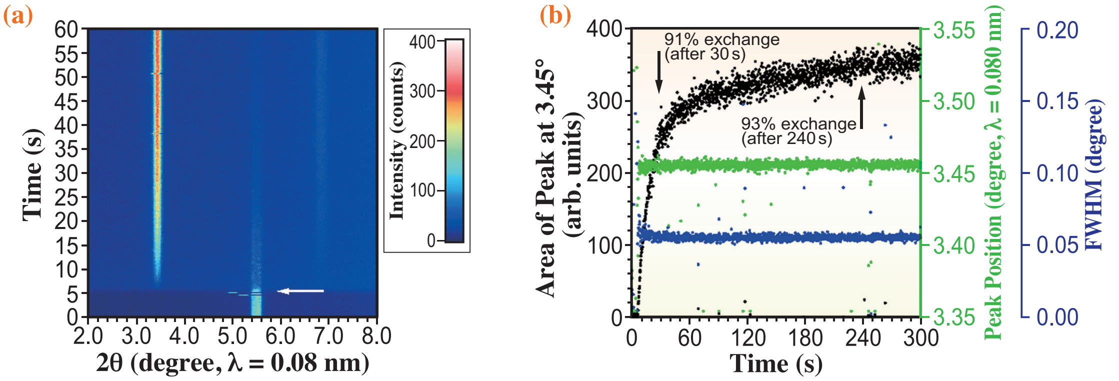

Fig. 1. **(a)** 2D mapping plots of the *t*-SXRD patterns of Y-LRH during the anion-exchange reaction from chloride into acetate. The arrow indicates the starting point of the addition of aqueous sodium acetate solution. **(b)** Time profile of the newly appeared peak area at 3.45°, peak position, and FWHM value in *t*-SXRD.

confirmed by ion chromatography of the liquid phase, were obtained after 30 and 240 s, respectively. From these results indicate, it can be speculated that anion-exchange from Cl^- into CH_3COO^- occurred rapidly and that diffusion and rearrangement of the anion species in the Y-LRH interlayer space took place relatively slowly, accompanied by the formation of a stacked structure. In the previous studies of ion exchange behavior, the structures after ion exchange reaction, i.e., after an ion exchange equilibrium, have been discussed. By use of this measurement technique in liquid phase, the structural change of solid materials until reaching ion exchange equilibrium was able to be discovered.

Interestingly, the basal spacing of the CH_3COO^-/Y-LRH catalyst increased from 1.00 nm to 1.35 nm only in the addition of water. The isolated interlayer acetate by electrostatic interaction between the layered host might interact with *ca.* four water molecules by hydrogen bonds to form acetate–water composites in the interlayer. To the best of our knowledge, this is the first example showing the lift-up behavior of LRH interlayers in aqueous media. During the water-swelling process of the CH_3COO^-/Y-LRH catalyst, the d_{00l} peaks of the nonhydrated matrix, observed at 4.70° (1.00 nm), immediately disappeared, and new peaks based on the lifted-up CH_3COO^-/Y-LRH were appeared at 3.47° (1.32 nm), shown in Fig. 2(a). The *t*-SXRD measurement was conducted with the addition of water into nonswelling CH_3CN in the presence of the CH_3COO^-/Y-LRH catalyst. From the time profile of the peak area at 3.47°, the expanded layered structure increased rapidly, and a newly arranged interlayer was formed within a minute (Fig. 2(b)). The time scale of the expansion of the interlayer spacing due to the formation rate of the acetate–water composite in the Y-LRH interlayer was faster than that of the catalytic Knoevenagel condensation.

The CH_3COO^-/Y-LRH catalyst was able to be applied for gram-scale Knoevenagel reaction, and an almost quantitative amount of corresponding analytically pure grade product was obtained. The CH_3COO^-/Y-LRH catalyst was reusable without any loss of its catalytic activity and selectivity. We expect that the proposed characterization method will contribute to the understanding the relationship between dynamical structural change of layered compounds as a catalyst material and their catalytic properties.

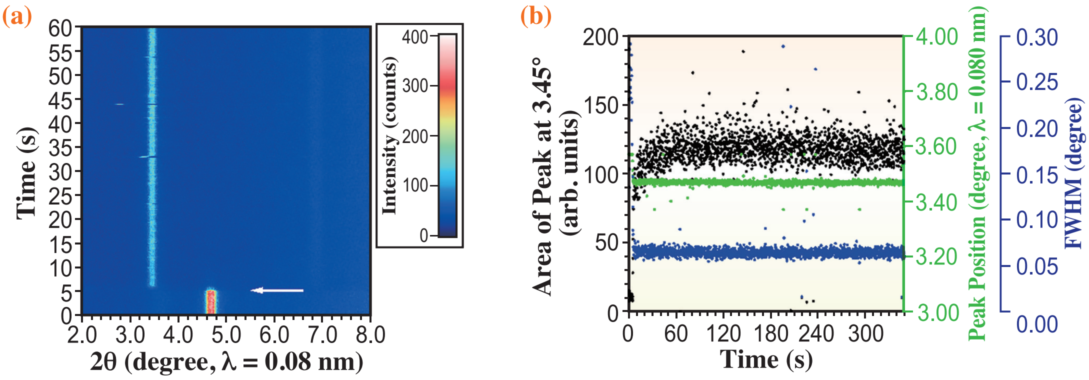

Fig. 2. **(a)** 2D mapping plots of the *t*-SXRD patterns of CH_3COO^-/YLRH during the interlayer lift-up process. The arrows indicate the starting point of the addition of water into a solid dispersion in acetonitrile solution. **(b)** Time profile of the newly appearing peak area at 3.45°, peak position, and FWHM value in *t*-SXRD.

Takayoshi Hara* and Nobuyuki Ichikuni

Department of Applied Chemistry
and Biotechnology, Chiba University

*Email: t_hara@faculty.chiba-u.jp

References

[1] J.-G. Li *et al*.: J. Adv. Ceram. **6** (2017) 177.
[2] *T. Hara, M. Habe, H. Nakanishi, T. Fujimura, R. Sasai, C. Moriyoshi, S. Kawaguchi, N. Ichikuni and S. Shimazu: Catal. Sci. Technol.* ***12*** *(2022) 2061.*
[3] K. Sugimoto *et al*.: Rev. Sci. Instrum. **88** (2017) 085111.
[4] T. Sasaki *et al*.: J. Am. Chem. Soc. **130** (2008) 16344.

In situ X-ray and acoustic observations of deep seismic faulting upon phase transitions in mantle olivine

The surface of the Earth consists of plates, which move and subduct along with the flow of the mantle beneath the plates. Earthquakes occur upon the collision and subduction of plates, even at depths of several hundred kilometers in the mantle, which are called "deep-focus earthquakes." Such earthquakes occasionally result in serious disasters as shown, for instance, by the 1994 Bolivian earthquake that occurred at a depth of 638 km with a magnitude of 8.3. The cause of deep-focus earthquakes, however, has been a mystery, because the occurrence of earthquakes requires the rapid sliding of the fault, which is difficult under great pressures in the deep mantle. It is well recognized that the frequency of earthquakes monotonically decreases with depth. However, an increase in the frequency of earthquakes at depths from ~400 km to ~600 km seems to be linked to the phase transitions of olivine to high-pressure phases (i.e., wadsleyite at ~400 km; ringwoodite at ~500 km) [1]. Attempts have been made to understand the mechanism behind the occurrence of deep-focus earthquakes through laboratory deformation experiments, but such experiments under deep mantle conditions have not been performed owing to technical difficulty. In most of the previous studies, a germanate analog (Mg_2GeO_4), which transforms directly to the spinel phase at 1 to 2 GPa without passing through the modified spinel phase (i.e., wadsleyite), has been used. Moreover, the net temperature increment due to the release of latent heat across the phase transition of the germanate analog is much lower than that of mantle olivine [2], implying that this might not be a perfect analog of mantle olivine [3]. Here, we, for the first time, performed deformation experiments on natural olivine, which is the major mineral of the mantle and subducting oceanic lithosphere (slab), using a state-of-the-art large-volume deformation apparatus combined with synchrotron X-ray observations [4].

We have conducted uniaxial deformation experiments on mantle olivine samples combined with synchrotron *in situ* X-ray observations at pressures of 11–17 GPa, temperatures of 860–1350 K, and strain rates of 10^{-5} – 10^{-4} s^{-1} using a deformation-DIA apparatus at SPring-8 **BL04B1**. These temperature and pressure ranges are equivalent to the conditions in deep subducted slabs. Acoustic emissions (AEs) were monitored using six piezoceramic lead-zirconate titanate transducers that were attached to the side of each second-stage anvil. Our AE monitoring technique allowed us to evaluate the three-dimensional location and magnitude of microcracks (i.e., hypocentres of AEs) in a deforming sample. The mechanical and statistical similarities between AEs and earthquakes have been verified in terms of the Gutenberg-Richter relationship and other models.

Within a narrow temperature window (~800°C), the semi-brittle flow of olivine resulted in formation of throughgoing faults (Fig. 1). At the timing of faulting, one or two large AEs occurred inside the sample, followed by relatively large AEs outside the sample, radiated around the fault plane crossing the sample. This suggests that the occurrence of a throughgoing fault slip caused by rupture was followed by rupture propagation outside the sample. After careful analyses of the recovered sample, we found that faulting was induced by the growth of 'new' olivine/wadsleyite with diameters of tens of nanometers upon the phase transition of 'old' olivine. The gouge layer, which consists of the nanograins of olivine/wadsleyite, acts as a lubricant for the rapid sliding of the fault.

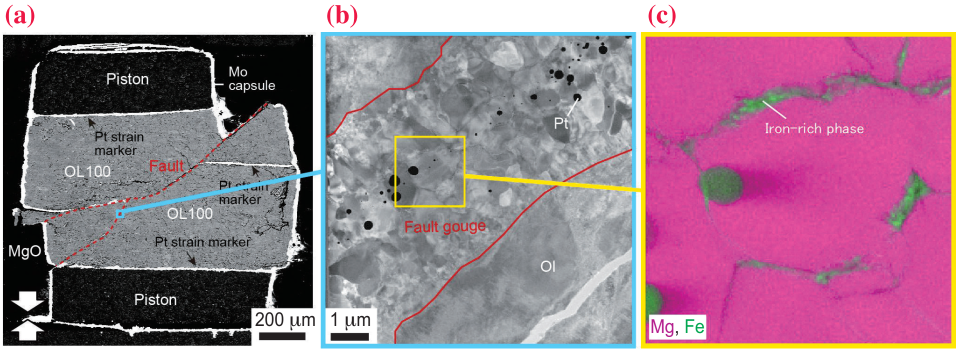

Fig. 1. Faults developed in the olivine aggregate deformed at 15.5 GPa and 850°C. **(a)** The recovered sample. Red dashed lines represent faults. **(b)** The fault filled with nanocrystalline olivine and wadsleyite. **(c)** A close-up view of the fault gouge. The iron-rich phase (a product of partial melting of olivine: green) is distributed along the grain boundaries of nanocrystalline olivine.

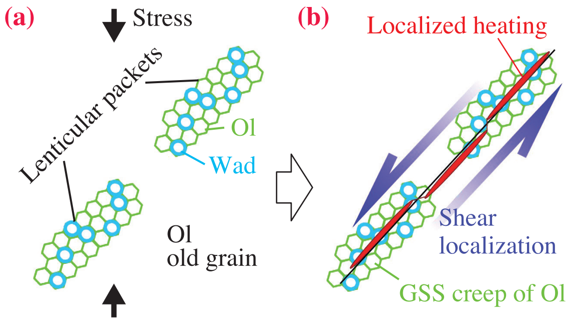

Fig. 2. Faulting triggered by the phase transition of olivine. **(a)** Formation of lenticular packets filled with nanocrystalline olivine (Ol)/wadsleyite (Wad). **(b)** Shear localization on the weak layer formed by the coalescence of the lenticular packets. This results in shear heating followed by faulting (i.e., deep-focus earthquakes).

Platinum-iron alloy blobs with a diameter of 10–200 nm and an interconnected iron-rich silicate phase (FeO = 20–37 wt%) are also observed in the gouge core (Fig. 1), showing the melting of the platinum strain marker and olivine during throughgoing faulting. The melting curves for the platinum-iron alloy and olivine polymorphs constrains the peak temperature during throughgoing faulting to the range of ~1900–2200°C or higher.

In a few runs deformed at 600–800°C without throughgoing faulting, the formation of lenticular packets filled with nanocrystalline olivine and wadsleyite (20–300 nm in diameter: Fig. 2) was observed, showing the grain size reduction of olivine and the nucleation of wadsleyite induced by the olivine-wadsleyite transition. The lenticular packets are aligned with high angles (~30°) to the compression direction and have a width of 2–3 μm. The linking-up of the lenticular packets should be the cause of weak fault gouge layers observed in the faulted samples (Figs. 1 and 2).

Our model based on the results of laboratory experiments well explains the distribution of the deep-focus earthquakes, which increase with depth from ~400 km to ~600 km, where the metastable 'old' olivine is expected to form ultrafine-grained 'new' olivine/wadsleyite. The seismic imaging of the deep mantle demonstrates the presence of the metastable olivine wedge (MOW), accompanied by deep-focus earthquakes, in a low-velocity zone with a thickness of tens of kilometers inside the subducted slabs (Fig. 3). The results of the present study suggest that a deep-focus earthquake nucleates when the temperature of the MOW becomes close to 800°C at pressures of the mantle transition region. The nanocrystallization of olivine occurs upon the phase transition (i.e., formation and linking-up of the lenticular packets filled with nanocrystalline olivine/wadsleyite) followed by throughgoing faulting due to shear instability (Fig. 2), although this critical temperature may be lower on the geological time scale. In fact, the observed deep-focus earthquakes are reported to be located along an isotherm of ~700°C in subducted slabs [5]. The shear zones filled with nanocrystalline olivine required for throughgoing faulting would not be preserved in subducted slabs at depths beyond this kinetic boundary of ~630 km, which is consistent with the abrupt decrease in seismicity at depths below ~600 km [1].

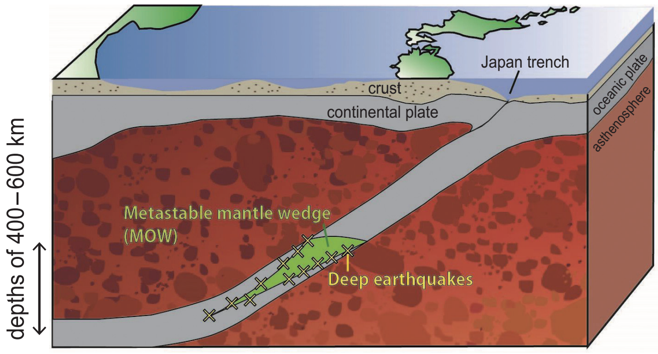

Fig. 3. Deep-focus earthquakes occurring in the subducted slab underneath Honshu Island. Our results suggest that hypocenters of deep-focus earthquakes are preferentially distributed around the surface of the metastable olivine wedge (MOW), which forms the central part of the subducted slab.

Tomohiro Ohuchi

Geodynamics Research Center, Ehime University

Email: ohuchi@sci.ehime-u.ac.jp

References

[1] C. Frohlich: Ann. Rev. Earth Planet. Sci. **17** (1989) 227.
[2] S. Kirby *et al.*: Rev. Geophys. **34** (1996) 261.
[3] H. W. Green II *et al.*: Nature **348** (1990) 720.
[4] *T. Ohuchi, Y. Higo, Y. Tange, T. Sakai, K. Matsuda and T. Irifune: Nat. Commun.* ***13*** *(2022) 5213.*
[5] D. A. Wiens *et al.*: Nature **264** (1993) 790.

Viscosity measurements of bridgmanite by *in situ* stress and strain observations

The Earth's mantle, which is a layer of silicate rock between the crust and the metallic core, is convective, which causes the volcanic and seismic activities and thermal evolution of the Earth through plate subduction and hot plumes. Our knowledge of the rheological properties of mantle constituent minerals, including viscosity, is fundamental to comprehending the dynamics of the Earth's mantle. The Earth's mantle consists of the upper mantle (depth: > 410 km), transition zone (depth: 410–660 km) and lower mantle (depth: 660–2900 km), which were distinguished by seismological and mineralogical studies. The lower mantle occupies ~65 vol% of the Earth's mantle. The viscosity-depth models of the Earth's mantle proposed on the basis of many geophysical observations [e.g., 1,2] indicate that the lower mantle has the highest viscosity, which is assumed to be 10^{19}–10^{21} Pa·s, among all the mantle layers. In addition, the viscosity difference between the transition zone and the top of the lower mantle has been assessed to be 1–2 orders of magnitude. Therefore, it is important to know the viscosity of the Earth's lower mantle to understand the Earth's mantle dynamics.

In the pyloritic mantle model, the lower mantle constituent minerals are bridgmanite (77 vol%), which is $(Mg,Fe)SiO_3$ perovskite with the space group *Pbnm*, ferropericlase (16 vol%) and $CaSiO_3$ perovskite (7%). The contribution of $CaSiO_3$ perovskite to viscosity is negligible because of the low abundance in the lower mantle. The viscosity of ferropericlase is considered to be much lower than that of bridgmanite. If an interconnected weak layer of ferropericlase was formed by a large shear strain such as a shear in a localized area, ferropericlase could be the dominant contributor to the lower mantle viscosity. In other cases, bridgmanite would govern the lower mantle viscosity because it is the most abundant mineral in the lower mantle.

In the Earth's mantle, the dominant deformation mechanisms are generally considered to be diffusion creep and/or dislocation creep. The total strain ($\varepsilon_{\mathrm{total}}$) during deformation is the sum of the strains of diffusion creep ($\varepsilon_{\mathrm{dif}}$) and dislocation creep ($\varepsilon_{\mathrm{dis}}$), and viscosity ($\eta$) is defined as $\eta = \sigma/\dot{\varepsilon}_{\mathrm{total}}$, where σ and $\dot{\varepsilon}_{\mathrm{total}}$ are the stress and total strain rate, respectively. The diffusion creep of bridgmanite has been studied mainly by diffusion experiments under deep mantle conditions, whereas the dislocation creep of bridgmanite is still unclear. Therefore, it is essential to quantitatively investigate the flow laws of mantle minerals in the dislocation creep regime through direct measurements. To determine the viscosity of bridgmanite in the dislocation creep region, the *in situ* stress and strain measurements of $MgSiO_3$ bridgmanite during uniaxial deformation at temperatures of 1473–1673 K and pressures of 23–27 GPa were conducted using the Kawai-type cell assembly with both the deformation-DIA-type apparatus (D-DIA), which was called "KATD," at SPring-8 **BL04B1** and the deformation-111 (D111)-type apparatus at KEK, PF-AR, NE7A [3]. Stress and strain rate in the deformation experiments are under conditions of 0.25 to 4.5 GPa and 1.6×10^{-6} to 1.5×10^{-4} s^{-1}, respectively. The maximum strain of bridgmanite using KATD was 6.8% (Fig. 1), whereas it reached 30.1% using the D111-type apparatus.

Figure 2 shows the creep strengths in the dislocation creep of bridgmanite and other mantle minerals obtained in the uniaxial deformation geometry in the D-DIA apparatus. These creep strength data were obtained under nominally dry conditions, although ringwoodite and wadsleyite, which are olivine polymorphs at the mantle transition zone, contained small amounts of water (0.029–0.1 wt%). The creep strength of bridgmanite is the highest among those of olivine, its high-pressure polymorphs, and periclase. This result is also supported by the additional experiment on deformation in a serial arrangement of bridgmanite and ringwoodite along the deformation axis using KATD to observe the direct viscosity contrast between them under nominally dry conditions [3]. Quantitatively, Fig. 2 shows that the creep strength of bridgmanite is approximately one order of magnitude larger than that of ringwoodite. Therefore, the observed viscosity variation between the mantle transition zone and the top of the lower mantle would be explained by the creep strength

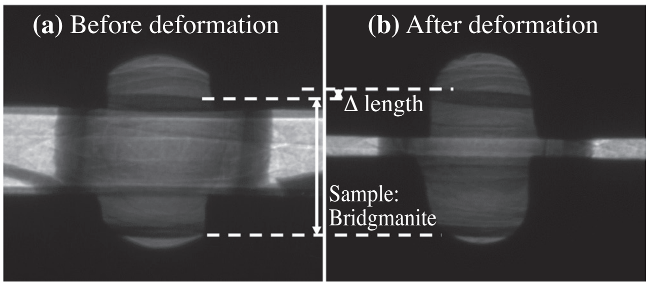

Fig. 1. X-ray radiographs before deformation **(a)** and after deformation **(b)** in M2344 using KATD. Total strain was 6.8%. Δ length is the difference between the sample lengths obtained before and during deformation.

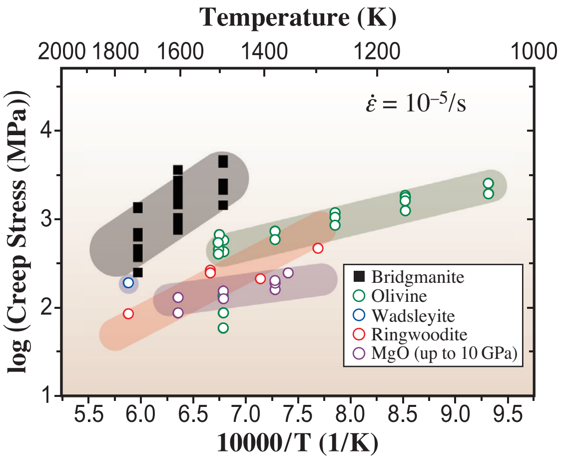

Fig. 2. Creep strength of bridgmanite at strain rate of 10^5/s in dislocation creep and those of other mantle minerals determined using the D-DIA-type apparatus. Solid black squares represent the strength of bridgmanite. Open green, blue, red and purple circles show the strengths of olivine, wadsleyite, ringwoodite and MgO, respectively.

contrast between bridgmanite and ringwoodite in the dislocation creep region even under nominally dry conditions.

The deformation mechanism map of bridgmanite at 1900 K and 25 GPa shown in Fig. 3 was also constructed using the flow law of the dislocation creep of bridgmanite [3] and the diffusion coefficients reported by annealing experiments [4] for diffusion creep. The temperature dependence of the strain rate is mainly derived from those of lattice and grain-boundary diffusion coefficients, which are the most important parameters in the diffusion creep regime. To realize a viscosity of 10^{21}–10^{22} Pa·s for the top of the lower mantle, the stress magnitude and strain rate are required to be 2×10^4 to 3×10^5 Pa and 2×10^{-18} to 3×10^{-16} s^{-1} in the grain-size-insensitive dislocation creep regime, respectively, whereas a grain size of 3–8 mm is necessary in the stress-independent diffusion creep regime shown as the yellow region in Fig. 3. These stress magnitudes of bridgmanite are consistent with those in the upper mantle estimated from the flow laws of olivine. Therefore, it is concluded that the rheology of the lower mantle is dominated by bridgmanite, which means that bridgmanite forms the load-bearing framework in the lower mantle rocks to control the lower mantle viscosity.

It is considered that the depth dependence of the diffusion coefficient for bridgmanite calculated by homologous temperature scaling with the adiabatic temperature gradient is consistent with the depth profiles of the observed lower mantle viscosity. Therefore, the observed viscosity profiles of the whole lower mantle can be explained by that of bridgmanite with constant stress and grain size conditions that correspond to the yellow region in Fig. 3. The required grain size of bridgmanite in the whole lower mantle is found to be several millimeters from the deformation mechanism map of bridgmanite. On the other hand, the grain size of bridgmanite after phase transition from the transition zone with a normal geotherm is estimated to be less than several hundred micrometers even over one billion years [5], because the grain growth rate of bridgmanite in a multiphase system is characteristically reduced. This indicates that the lower mantle materials, which have viscosities comparable to that of the lower mantle, would not have experienced the phase transition during mantle convection. Therefore, the main portion of the lower mantle would have been isolated from mixing by mantle stirring after crystallization from the magma ocean and remained as an ancient mantle.

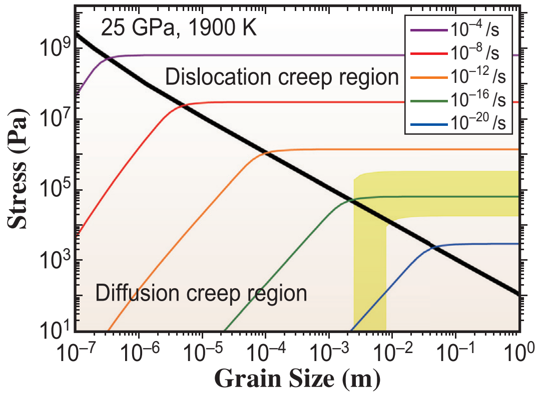

Fig. 3. Deformation mechanism maps for bridgmanite at 25 GPa and 1900 K with stress exponent n of 3 constructed using the parameters for dislocation creep [3] and diffusion creep [4]. The yellow area denotes the region dominated by diffusion creep and dislocation creep with an observed viscosity range of 10^{21}–10^{22} Pa·s.

Noriyoshi Tsujino

Japan Synchrotron Radiation Research Institute (JASRI)

Email: noriyoshi.tsujino@spring8.or.jp

References

[1] Y. Ricard, B. Wuming: Geophys. J. Int. **105** (1991) 561.
[2] J. X. Mitrovica, A. M. Forte: Earth Planet. Sci. Lett. **225** (2004) 177.
[3] *N. Tsujino, D. Yamazaki, Y. Nishihara, T. Yoshino, Y. Higo, Y. Tange: Sci. Adv.* ***8*** *(2022) eabm1821.*
[4] D. Yamazaki *et al.*: Phys. Earth Planet. Int. **119** (2000) 299.
[5] D. Yamazaki *et al.*: Science **274** (1996)2052.

Equation of state of iron and nickel to 370 gigapascals

The Earth's inner core is the deepest region and at 3.30–3.65 million atmospheres of pressure (330–365 gigapascals, GPa). It is mainly made of solid iron (Fe), and according to cosmochemical and geochemical studies, it contains a substantial (5 to 15%) amount of nickel (Ni) as the second component. Experimental measurements of the Earth's core material properties combined with seismic observations indicate that the inner core is a few percent less dense than pure iron. This implies that a light component is probably present in the inner core, such as sulfur, silicon, oxygen, carbon, and hydrogen. The description of the Earth's inner core, thus, highly depends on the compression property of Fe under high-pressure, high-temperature conditions determined experimentally.

Numerous works on Fe have continued for half a century through static and dynamic experiments and theoretical calculations, including those on the equation of state (EOS) and the phase relation in a high-pressure, high-temperature regime. Modeling the interior structure of the Earth's inner core requires an accurate determination of the EOS from the experimental data obtained at pressures corresponding to the inner core and then a direct comparison with the densities obtained from the seismological model. However, the maximum pressure achieved in static compression experiments has been limited to 300 GPa for iron [1-3] and below 160 GPa for nickel [4], and accurate experimental data of density that enable a direct comparison for the inner core region have remained elusive. The pressure–volume data collection through the inner core to the Earth's center has been one of the most significant challenges in deep Earth mineralogy.

We focused on the experimental investigation of the compression behavior of Fe and Ni at Earth's inner core pressures. High-pressure powder X-ray diffraction in diamond anvil cells was carried out at SPring-8 **BL10XU** and **BL04B2**. Using high-energy microfocused X-ray beams at 30 keV (or 28 and 37.8 keV), we succeeded in generating high pressures of up to 370 GPa corresponding to the central region of the Earth [5]. The compression data at 165 points for Fe and 103 for Ni were collected over the experimental pressure range. The isothermal EOSs of Fe and Ni were then determined at 298 K using quasi-absolute EOS pressure scale of platinum (Pt) proposed recently on the basis of high-precision measurements by a ramp (shockless) dynamic compression technique.

We observed that Fe underwent a phase transition from the body-centered cubic (bcc-Fe, or α-Fe) phase to the hexagonal close-packed (hcp-Fe, or ε-Fe) phase at ~15 GPa, and then the hcp-Fe phase remained stable up to a maximum pressure of 354 GPa at 298 K, as shown in Fig. 1(a). Seven diffraction lines were identified for hcp-Fe, from which the lattice constants *a*, *c*, and *c*/*a* were estimated to be 2.1294(17) Å, 3.390(5) Å, and 1.592(4), respectively. The volume at 354 GPa had shrunk to ~56.3% of that at ambient pressure.

Ni has a face-centered cubic (fcc) structure at ambient pressure and does not show any structural phase transition up to 368 GPa, indicating that the fcc structure is stable up to the maximum pressure investigated in this study (Fig. 1(b)). At 368 GPa, six diffraction lines were observed for fcc-Ni, and eight diffraction lines were identified for Pt. The lattice constant *a* of fcc-Ni was estimated to be 2.9521(10) Å, and the volume compression ratio V/V_0 was 0.5880. Our pressure–volume data of Fe and Ni, plotted in Fig. 2, were analyzed using a Vinet EOS, a universal formalism shown to be widely applicable to solids of different bonding types:

$$P = 3K_0\,(1-x^{1/3})\,x^{-2/3}\,\exp\left[\tfrac{3}{2}(K_0'-1)(1-x^{1/3})\right],$$

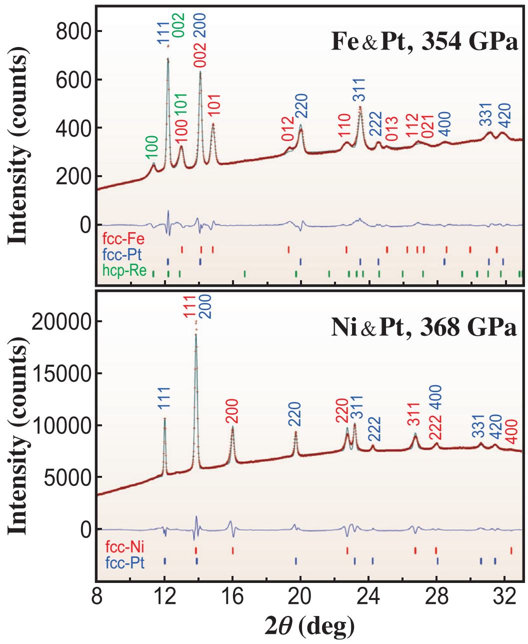

Fig. 1. Representative X-ray diffraction pattern (red crosses) and Rietveld simulation (green lines) for hcp-Fe at 354 GPa and Ni at 368 GPa. Blue lines show the difference between the observed and calculated patterns.

where $x = V/V_0$, V_0 is the ambient atomic volume, and K_0 and K'_0 are the bulk modulus at ambient pressure and its pressure derivative. The EOS parameters of K_0 and K'_0 were estimated to be 159.27(99) GPa and 5.86(4) for hcp-Fe, and 173.5(1.4) GPa and 5.55(5) for Ni, respectively.

At 365 GPa (the pressure of the center of the Earth), by comparing the present EOS to EOS extrapolated from the recent compression curve [3,4], the present volumes of Fe and Ni are found to be 2.3% and 1.5% larger than those estimated from the extrapolation, respectively. When the pressure values in the literature curve are corrected using the latest Pt-EOS pressure scale, the volume difference in Fe is within ±0.7% at 365 GPa. Our compression curve for Ni also is in perfect agreement with the literature curve with corrected pressure values. We conclude that these discrepancies are due to the pressure scale.

Generally, a sample compressed between two anvils without any pressure-transmitting medium is under non-hydrostatic stress conditions. We examined the non-hydrostatic pressure effect in the diffraction data by analyzing the *d*-spacing using the lattice strain equations. The difference between the axial and radial stress components in the diamond anvil sample, referred to as the differential or uniaxial stress component, is a measure of non-hydrostaticity. The uniaxial stress component was estimated under the isostrain (Voigt) condition, giving the lower bound. The obtained values for fcc-Pt at 354 GPa and 368 GPa and fcc-Ni at 368 GPa were all below 0.9 GPa and within the uncertainty of pressure, suggesting that the uniaxial stress effect is negligible.

Figure 3 shows the room-temperature densities of hcp-Fe and fcc-Ni as functions of pressure in the Earth's core, along with the seismic Preliminary Reference Earth Model (PREM) density profile. The new static compression data allow the density to be constrained directly at inner core pressures without the extrapolation of the data. As both Fe and Ni have a close-packed structure under high compression, we also expect that the density of the Fe–Ni alloy can be estimated from our EOSs of Fe and Ni using the mass fraction of Ni in Fe. The present data covering the entire pressure range of the Earth's inner core will provide a better understanding of the solid inner core's interior structure and composition, including light element(s).

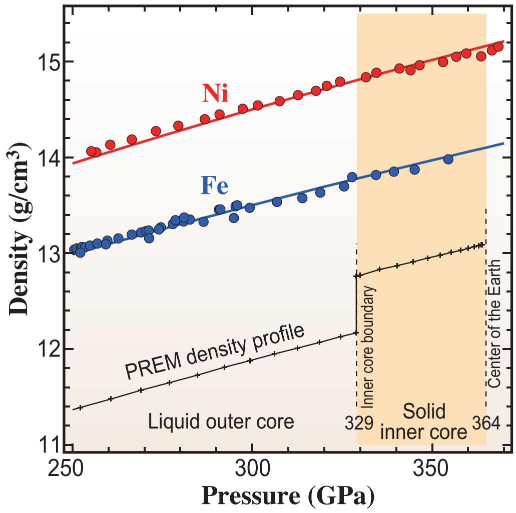

Fig. 3. Densities of Fe and Ni at 298 K as functions of pressure. Circles, experimental data points. Circles, experimental data points; curves, calculated profiles using isothermal EOSs. The seismic Preliminary Reference Earth Model (PREM) is also shown for comparison.

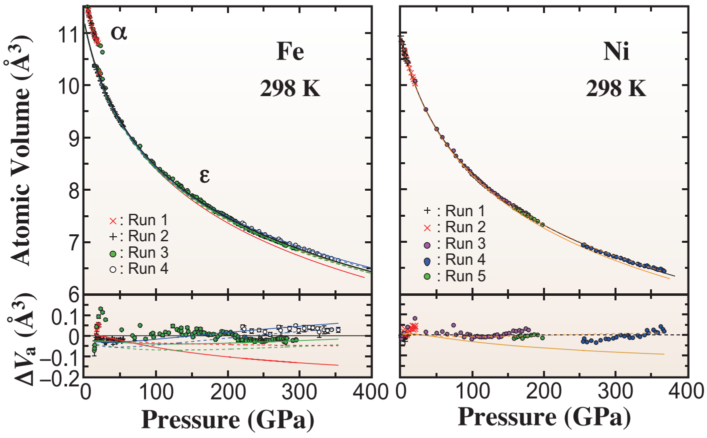

Fig. 2. Pressure–volume curves for Fe and Ni, along with literature data. Black (this work), green [1], blue [2], red [3], and orange [4]. Dashed curves show pressure-corrected EOSs based on the latest Pt scale. ΔV_a denotes the deviations of the atomic volume between the measured and fitted volumes.

Naohisa Hirao[a,*,†] and Yuichi Akahama[b]

[a] Japan Synchrotron Radiation Research Institute (JASRI)
[b] Graduate School of Science, University of Hyogo

*Email: naohisa.hirao@j-tec.co.jp

[†] Present address: JTEC Corporation

References

[1] H. K. Mao *et al*.: J. Geophys. Res. **95** (1990) 21737.
[2] L. S. Dubrovinsky *et al*.: Phys. Rev. Lett. **84** (2000) 1720.
[3] A. Dewaele *et al*.: Phys. Rev. Lett. **97** (2006) 215504.
[4] A. Dewaele *et al*.: Phys. Rev. B **78** (2008) 104102.
[5] *N. Hirao, Y. Akahama, Y. Ohishi: Matter Radiat. Extremes* ***7*** *(2022) 038403.*

Stratification in planetary cores by liquid immiscibility in Fe–S–H

The InSight (Interior Exploration using Seismic Investigations, Geodesy and Heat Transport) mission conducted by NASA recently detected seismic waves from the interior of Mars and found that Mars has a large and light liquid core [1]. A large and light core implies that there are substantial amounts of light elements in the core. Sulfur has been a widely accepted candidate light element in the Martian core on the basis of studies on Martian meteorites. However, the low density of the core requires the presence of other light element(s) such as oxygen, carbon, and hydrogen in addition to sulfur. In particular, hydrogen could be another major light element in the core of Mars because of its abundance in planetary building blocks and strong siderophile behavior at high pressures. Since light elements change the chemical and physical properties of the metallic core, their amounts affect core dynamics such as core convection and dynamo action, which generate a planetary magnetic field. While Earth currently has a magnetic field, the Martian magnetic field was lost ~4 billion years ago, which led to the loss of the ocean on Mars. Despite its importance, the property of Fe–S–H liquids has rarely been studied because of experimental difficulties in treating Fe–H alloys. Since hydrogen escapes from an iron lattice at ambient pressure and room temperature, the quantification of the hydrogen content in iron alloys requires X-ray diffraction (XRD) measurements at high pressures.

In the present study [2], we conducted high-pressure melting experiments using a diamond-anvil cell (DAC) technique and XRD measurements at SPring-8 **BL10XU**. We loaded a foil of Fe–S alloy and paraffin (C_nH_{2n+2}) as a hydrogen source into a cell assembly. After compression to high pressures, the sample was heated to higher than its melting temperature using a laser-heating system installed at BL10XU (Fig. 1). We collected XRD patterns before, during, and after heating at the center of a heating spot (Fig. 2). The disappearance of XRD peaks of iron alloys during heating was used to confirm melting. The XRD profiles collected after heating indicate volumes of iron alloy crystals that crystallized upon quenching the temperature. Such crystals preserve the composition of the liquid during heating. Because hydrogen expand the lattice volume of iron alloys, we determined the hydrogen content in the liquid from the volumes of hydrogen-bearing Fe and FeS at high pressures. Combining the XRD profiles at high pressures and textural/chemical observations on sample cross sections at ambient pressure, we determined the composition of Fe–S–H liquid at high pressures and temperatures.

Cross sections of recovered samples showed a homogeneous single liquid or two separate Fe–S and Fe–H liquids. Pressure (P)–temperature (T) conditions in the experiment indicate that Fe–S–H liquids show immiscibility (separation into two liquids) at relatively low temperatures (e.g., <3000 K at 40 GPa) (Fig. 3(a)). We also conducted silicon- or oxygen-bearing experiments. Silicon and oxygen were preferentially incorporated into S-rich liquids, while carbon from paraffin was included predominantly in H-rich liquids. We observed immiscible S-rich and H-rich liquids to ~120 GPa, while immiscibility gaps in other iron-light element liquids close below 10–30 GPa.

The present-day P–T conditions of the Martian core (~20–40 GPa and ~2000–2500 K) are fully within the ranges required for liquid immiscibility to occur in the

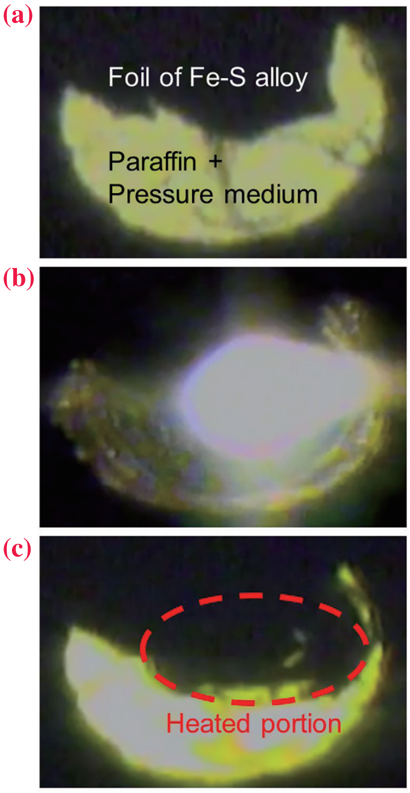

Fig. 1. Microscopy images of a sample chamber **(a)** before, **(b)** during, and **(c)** after heating. Change in the shape of Fe–S alloy between (a) and (c) indicates the melting of the heated portion.

Fe–S–H system (Fig. 3(b)). Also, the compositions of liquids in the present experiments, including hydrogen contents revealed by XRD measurements, are similar to that in one of the Martian core composition models [3]. Therefore, the Martian core may have separated into two liquids as it cooled. The light liquid released by the separation of the liquid core could have driven the core convection and generated the planetary magnetic field. At the same time, separated light and heavy liquids could have formed gravitationally stable layers that halted the core convection. In this way, the Fe–S–H liquid immiscibility may have been responsible for both the onset and termination of the Martian core convection and planetary magnetic field.

On the other hand, *P*–*T* conditions of the Earth's outer core overlap the conditions of immiscibility only at its top (Fig. 3(b)). This implies that the Earth's uppermost core is stratified. Indeed, seismology indicates a low-sound-velocity layer at the top of the outer core [4]. While the layer is required to be light to remain at the top of the core, alloying more light elements causes a higher sound velocity. However, since the effect of H on the sound velocity of iron alloy is less than those of other light elements, the low-velocity layer could be formed by the enrichment of H and the depletion of S, Si, and O. Such a compositional anomaly can be formed by immiscibility in Fe–S–H liquid because Si and O are preferentially incorporated into S-rich liquids.

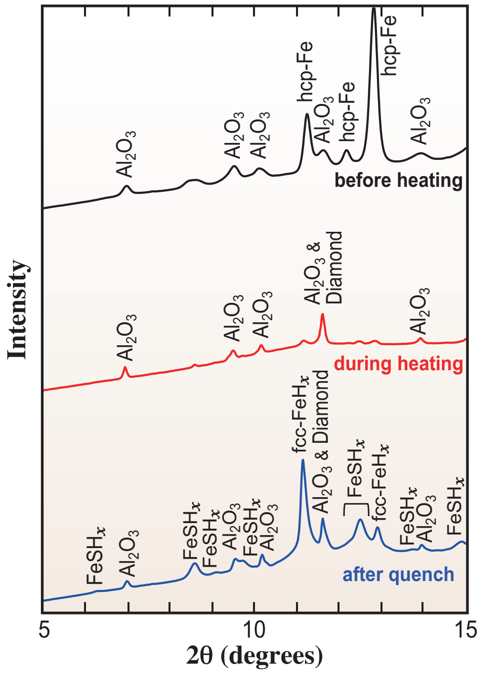

Fig. 2. X-ray diffraction patterns collected before, during, and after heating. Peaks of iron alloys and pressure medium (Al_2O_3) are labeled.

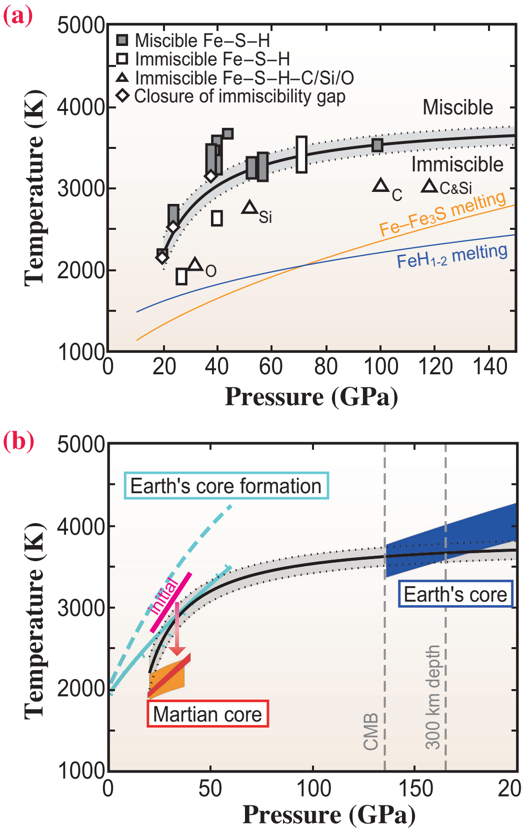

Fig. 3. Pressure-temperature conditions for immiscibility in liquid Fe–S–H. **(a)** Experimental results showing a homogeneous single liquid (filled) and two immiscible liquids (open) in Fe–S–H (rectangles) and Fe–S–H–C/Si/O (triangles). Elements other than Fe, S, and H are indicated. The miscible/immiscible boundary (black line) and its uncertainty band (dashed lines) are based on the *P*–*T* conditions of the miscible/immiscible border in a sample (diamonds) and those of miscible/immiscible liquids obtained near the boundary. Yellow and blue lines are melting curves in the Fe–Fe_3S and Fe–FeH_x ($x > 1$) systems, respectively. **(b)** The blue band indicates the isentropic temperature profile of the Earth's core with the core-mantle boundary temperature $T_{CMB} = 3600$ K. Light-blue lines are the pressure–temperature paths for the segregation of core-forming metals from silicate. Temperature profiles of the initial (pink) and present-day Martian cores (orange and red) are also given.

Shunpei Yokoo

Department of Earth and Planetary Science,
The University of Tokyo

Email: shunpei@eps.s.u-tokyo.ac.jp

References

[1] S. C. Stähler *et al.*: Science **373** (2021) 443.
[2] *S. Yokoo, K. Hirose, S. Tagawa, G. Morard, Y. Ohishi: Nat. Commun.* ***13*** *(2022) 1.*
[3] T. Yoshizaki and W. McDonough: Geochim. Cosmochim. Acta **273** (2020) 137.
[4] S. Kaneshima: Phys. Earth Planet. Inter. **276** (2018) 234.

Sound velocity of hexagonal close-packed iron to the Earth's inner core pressure

Despite the fact that space probes can now reach outside the solar system and humans can directly observe many planets/asteroids, the interior of the Earth, our home planet, is still shrouded in mystery. The main reason is that humans cannot observe it directly. Therefore, the most reliable information about the Earth's interior is based on observation of seismic waves propagating inside the Earth. The seismic model of the Earth's interior, the Preliminary Reference Earth Model (PREM) [1], tells us the density (ρ) and the sound velocity, specifically the compressional (v_p) and shear (v_s) wave velocities, as a function of depth. It is also widely accepted that the main component of the core of the Earth is iron, based on the solar abundance of elements and research on meteorites.

Determining a core structure that is consistent with PREM has been the subject of many experiments, since the exact core composition has important implications for understanding the formation and evolution of the Earth in the solar system. These experiments, with great effort, have suggested that there must be something more than just iron in the core to match PREM, and, in particular, that Earth's core contains light elements [2]. However, the investigations rely on *extrapolations of the sound velocity of iron and iron alloys measured at low pressure*. This is because it is difficult to reach core pressures, and to measure the sound velocity, in a laboratory: even using the hardest material, diamond, as an anvil, achieving core pressures is challenging. However, it is very important that such measurements be done, as the use of different methods to extrapolate the relation between sound velocity and density, lead to significant uncertainties in discussing the Earth's core [3].

In this work [4], we were able to measure the sound velocity, v_p, of hexagonal close-packed (hcp) iron up to a density ρ of 13.87 g/cm^3 using inelastic X-ray scattering (IXS) at SPring-8 **BL43LXU** [5]. This density is larger than that of the inner core, about double that of ambient iron, and corresponds to a pressure of 310–327 GPa (depending on the pressure scale). Measurement at such extreme pressure — approximately double that previously achieved with IXS, world-wide — was made possible by taking advantage of several technical developments including an improved design of the diamond anvil cell using a "stepped-bevel" anvil combined with sophisticated optics and the strong source at BL43LXU. Even so, count rates were only ~0.01–0.02 cps at the highest pressure. Figure 1 shows a typical spectrum collected at the highest ρ of 13.87 g/cm^3 corresponding to 310–327 GPa. We identified the IXS peaks for the longitudinal acoustic (LA) mode of hcp-iron and the transverse acoustic (TA) and LA modes of diamond.

The v_p of hcp-iron determined in this work is plotted in Fig. 2(a). It is clear that a linear v_p–ρ relation, Birch's law, is valid for hcp-iron up to 13.87 g/cm^3 which covers inner core density regions of 12.8–13.1 g/cm^3. Combining the present results and those of previous work we found the Birch's law for hcp-iron as:

$$v_p \text{ [km/s]} = 1.162\,\rho \text{ [g/cm}^3\text{]} - 3.450 \qquad (1)$$

Figure 2(b) shows the pressure dependence of v_p of hcp-iron using pressures determined by the equation of state (EoS) by Dewaele *et al.* [2]. The effect of temperature on the v_p–ρ relation of hcp-iron at high temperature was then evaluated by combining the present results with previous measurements at high temperature. We parameterized the temperature

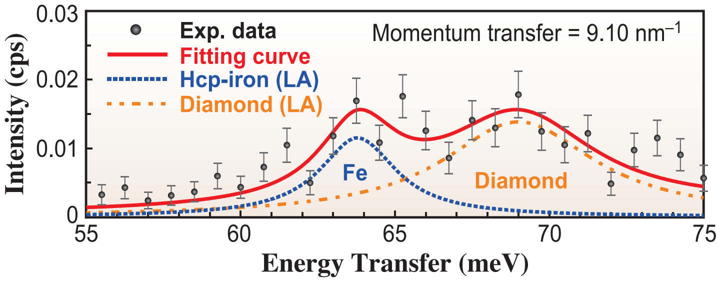

Fig. 1. An IXS spectrum of hcp-iron at 13.87 g/cm^3 corresponding to 310–327 GPa [4]. The experimental data (black dot with 1σ error bar) was fit (red solid line) with peaks for the IXS signal of LA mode from iron (blue dotted line) with TA mode from diamond (orange dashed line).

dependence of the Birch's law for hcp-iron as:

$$v_p\ [\mathrm{km/s}] = 1.162\,\rho\ [\mathrm{g/cm^3}] - 3.450 - 2.5\times10^{-5}\ (T\ [\mathrm{K}] - 300)\ (19.2 - \rho\ [\mathrm{g/cm^3}]), \qquad (2)$$

where T is temperature in kelvin.

Figure 3 shows the $v_p-\rho$ and $v_s-\rho$ relations for hcp-iron at pressures varying from 330 GPa (inner core boundary, ICB) to 365 GPa (center of the Earth/core, COE) at temperatures of 300 K and 6000 K, compared to the values of the PREM inner core [1]. The v_p at high pressure and temperature is derived from equation (2) with the pressures and temperatures based on the EoS of Dewaele *et al.* [2]. The v_s is derived from the v_p of the present results and the adiabatic bulk modulus (K_S) of the EoS as follows: $K_S = \rho\ (v_p^2 - 4/3\ v_s^2)$. Pure hcp-iron has 2±2% higher v_p and 29±17% higher v_s at the ICB, and 4±2% higher v_p and 36±17% higher v_s at the COE, respectively, compared to those of the PREM inner core with a typical estimated inner core temperature of 6000 K [4]. A large v_s deficit compared to the v_p deficit of the PREM inner core relative to hcp-iron is an important constraint on the sound velocity deficits determined by direct static measurements at core densities. This provides a strong constraint for estimation of the light element contents in the inner core.

The present result combined with previous work at high pressure and temperature for iron-silicon alloy, iron sulfide, and iron oxide suggests the Earth's core may be enriched in 3±1 wt% silicon and 3±2 wt% sulfur with ~5 wt% nickel with negligible amount of oxygen, consistent with the existing outer core model with oxygen, as the growth of the inner core from the outer core may have created a secular enrichment of oxygen in the outer core [4].

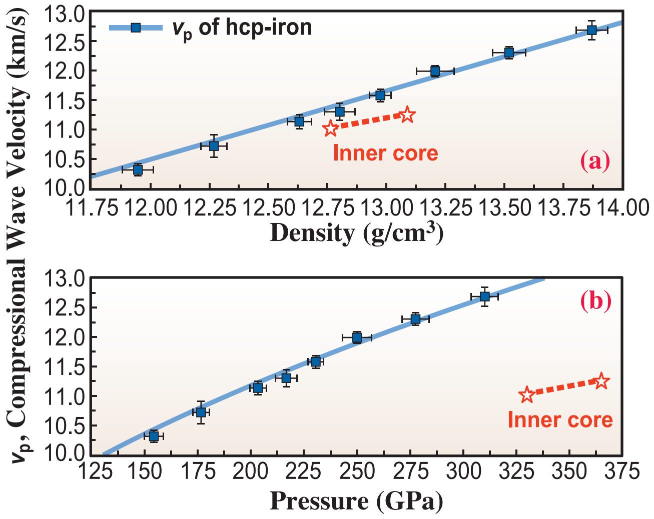

Fig. 2. Density–v_p **(a)** and pressure–v_p **(b)** of hcp-iron at high pressure determined by the present work (blue square symbols with 1σ error bars and light blue solid line) compared with the PREM inner core (red dashed line with stars). Pressure in (b) is evaluated by Dewaele *et al.* [2].

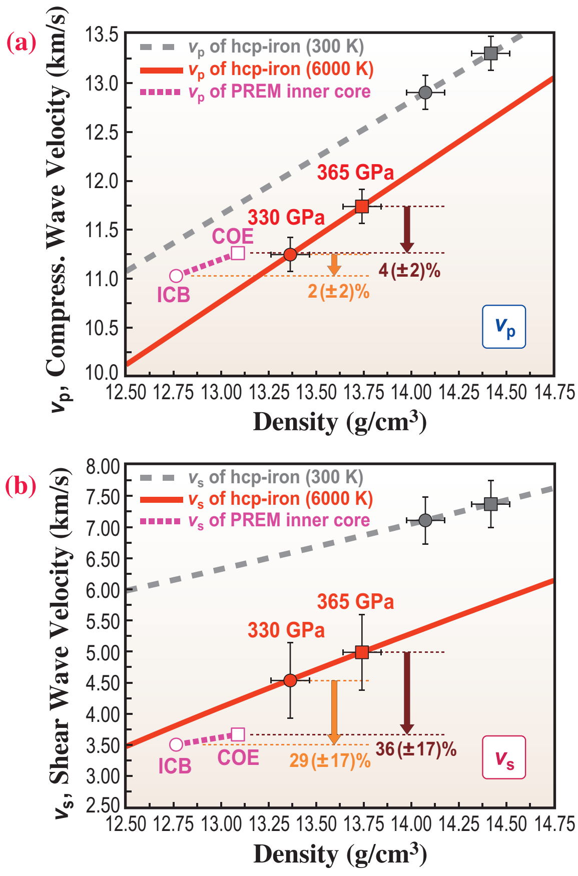

Fig. 3. Density–v_p **(a)** and density–v_s **(b)** relations of hcp-iron under the inner core pressures (330–365 GPa) at 300 K and 6000 K compared with the PREM inner core. The relations at 300 K are shown as gray symbols and dashed lines, and those at 6000 K are shown as red symbols and solid lines. The error bars represent 1σ uncertainties. The relation for the PREM inner core is given as the magenta open symbols with dotted lines.

Daijo Ikuta[a,b,*], Eiji Ohtani[b] and Alfred Q. R. Baron[c,d]

[a] Institute for Planetary Materials, Okayama University
[b] Department of Earth Science, Tohoku University
[c] RIKEN SPring-8 Center
[d] Japan Synchrotron Radiation Research Institute (JASRI)

*Email: dikuta@okayama-u.ac.jp

References

[1] A. M. Dziewonski and D.L. Anderson: Phys. Earth Planet. Inter. **25** (1981) 297.
[2] A. Dewaele *et al.*: Phys. Rev. Lett. **97** (2006) 215504.
[3] D. Antonangeli and E. Ohtani; Prog. Earth Planet. Sci. **2** (2015) 3.
[4] *D. Ikuta, E. Ohtani, H. Fukui, T. Sakai, D. Ishikawa and A. Q. R. Baron: Nat. Commun.* ***13*** *(2022) 7211.*
[5] A. Q. R. Baron: SPring-8 Inf. **15** (2010) 14.

Operando X-ray diffraction and X-ray absorption spectroscopy of zero-strain lithium-ion battery material $Li[Li_{1/3}Ti_{5/3}]O_4$

For lithium insertion materials for lithium-ion batteries (LIBs), the lattice dimensions are usually altered during the charge and discharge reactions owing to changes in the ionic radius of the redox species, Coulomb repulsion between O^{2-} ions, etc. Among various lithium insertion materials, $Li[Li_{1/3}Ti_{5/3}]O_4$ (LTO) and related compounds are regarded as zero-strain materials because their cubic lattice parameter (a_c) is maintained at ~8.36 Å throughout the electrochemical reaction [1,2]. This zero-strain character is essential for long-cycle-life LIBs and is currently employed in all-solid-state LIBs, which require a robust interface between the electrodes and electrolyte. However, because of this zero-strain character, the reaction mechanisms of LTO, especially those underlying detailed structural transformations, have not been fully understood for approximately the past thirty years [1].

In contrast to conventional *ex situ* analyses, state-of-the-art *in situ* and *operando* techniques are powerful tools for monitoring electrode materials under operating conditions. Since the early 2010s, we have been developing both a Li cell and an experimental setup to perform a series of *operando* X-ray diffraction (XRD) and X-ray absorption (XAS) spectroscopy at the Toyota beamline, SPring-8 **BL33XU** [3,4]. The *operando* XRD/XAS system consists of a specially designed tapered undulator and servo-motor-driven Si channel-cut monochromator, which enables rapid switching to the desired X-ray energy within ~20 s. We applied the *operando* XRD/XAS technique to LTO together with chemometric analyses and the multivariate curve resolution by alternating least squares (MCR-ALS) method.

Figure 1(a) shows the Rietveld analysis results of the pristine LTO sample. The crystal structure can be assigned to a spinel structure with the $Fd\bar{3}m$ space group, in which Li^+ ions occupy tetrahedral 8*a* and octahedral 16*d* sites and Ti^{4+} ions occupy the 16*d* site (see the inset of Fig. 1(a)). Figure 1(b) shows the discharge and charge curves of the LTO/Li cell for the *operando* XRD/XAS measurements. The cell voltage (E) rapidly drops from ~2.8 V to ~1.5 V at the beginning of the discharge reaction and then remains constant (~1.5 V) up to a capacity (Q) of 150 $mAh{\cdot}g^{-1}$. The flat E is the signature of a two-phase reaction scheme, although only a linear change in a_c was observed in previous *ex situ* XRD analyses [1]. These electrochemical properties are consistent with those of previous studies [1,2], confirming a homogeneous electrochemical reaction even in the LTO/Li cell for *operando* XRD/XAS measurements.

Figure 2(a) shows the bond length between Ti and O atoms during the discharge and charge reactions, which were determined by *operando* XRD measurements ($d_{Ti\text{-}O}{}^{XRD}$). During the discharge reaction, $d_{Ti\text{-}O}{}^{XRD}$ monotonically decreases from ~1.986 Å at 0 $mAh{\cdot}g^{-1}$ to ~1.984 Å at ~170 $mAh{\cdot}g^{-1}$ and then rapidly increases to ~1.990 Å at ~220 $mAh{\cdot}g^{-1}$. During the charge reaction, $d_{Ti\text{-}O}{}^{XRD}$ almost traces with $d_{Ti\text{-}O}{}^{XRD}$ during the discharge reaction at $Q \geq 170$ $mAh{\cdot}g^{-1}$. However, the difference in $d_{Ti\text{-}O}{}^{XRD}$ between the discharge and charge reactions ($\delta d_{Ti\text{-}O}{}^{XRD}$) clearly appears below 170 mAh g^{-1}. By contrast, the bond lengths between Ti and O atoms determined by *operando* XAS measurements ($d_{Ti\text{-}O}{}^{XAS}$) are almost the same between the discharge and charge reactions (Fig. 2(b)), i.e., $d_{Ti\text{-}O}{}^{XAS}$ linearly increases from ~1.95 Å at 0 $mAh{\cdot}g^{-1}$ to ~2.15 Å at ~170 $mAh{\cdot}g^{-1}$, corresponding to the change in the ionic radius of Ti ions. Other differences in the results between XRD and XAS measurements are also observed in the normalized concentration (c) profile obtained by the MCR-ALS analyses. For the *operando* XRD measurements shown in Fig. 2(c), the c profile of LTO-1 (or LTO-2) during the discharge reaction differs from that during the charge reaction, whereas for the *operando* XAS measurements shown in Fig. 2(d), the c profile of LTO-1 (or LTO-2) during the discharge reaction is similar to that during the charge reaction. Here, LTO-1 and LTO-2 represent $Li[Li_{1/3}Ti_{5/3}]O_4$ and $Li_2[Li_{1/3}Ti_{5/3}]O_4$, respectively. The difference in c between the discharge and charge reactions (δc) is related to $\delta d_{Ti\text{-}O}{}^{XRD}$.

To summarize the differences in the results between XRD and XAS measurements, we schematically illustrate the reaction mechanisms occurring in LTO

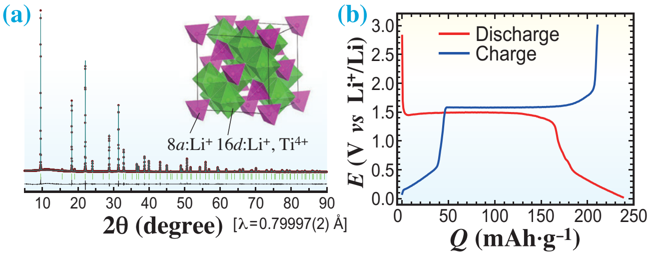

Fig. 1. **(a)** Rietveld analysis results of the pristine LTO sample and a schematic of the crystal structure (inset) and **(b)** discharge and charge curves of the Li/LTO cell for the *operando* XRD/XAS measurements.

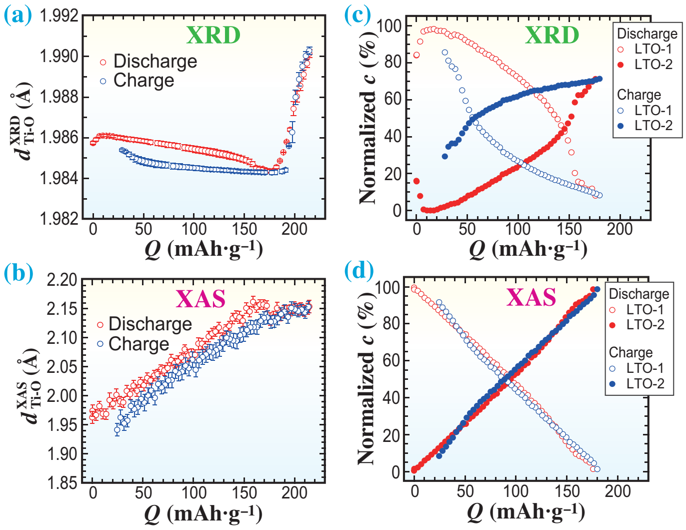

Fig. 2. **(a)** d^{XRD}_{Ti-O} and **(b)** d^{XAS}_{Ti-O} during the discharge and charge reactions. Normalized *c* profiles of the LTO-1 ($Li[Li_{1/3}Ti_{5/3}]O_4$) and LTO-2 ($Li_2[Li_{1/3}Ti_{5/3}]O_4$) components obtained by the MCR-ALS analyses of *operando* **(c)** XRD and **(d)** XAS measurements.

at both the micro- (XRD) and atomic (XAS) scales (Figs. 3(a) and 3(b), respectively). The presence of δd_{Ti-O}^{XRD} and δc indicates the difference in the distribution of the LTO-1 (or LTO-2) phase in an LTO particle. During the discharge reaction, Li^+ ions are inserted into the surface, forming a core–shell structure, with the core and shell being LTO-1 and LTO-2, respectively (Fig. 3(a)). During the charge reaction, Li^+ ions are extracted from the surface, forming the opposite core–shell structure. Because the XRD measurements correspond to the core (bulk) structure, δd_{Ti-O}^{XRD} and δc were observed below ~170 mAh·g^{-1}. On the other hand, at the atomic scale (Fig. 3(b)), Li insertion/extraction proceeds along the two-phase reaction scheme, wherein the amount of LTO-1 (or LTO-2) phase linearly decreases/increases during the discharge and charge reactions.

As described above, we first unveiled the dynamic structural transformations of LTO using this *operando* XRD/XAS technique. The present results would be useful for not only further improving the rate capability of LTO but also clarifying the reaction mechanisms of $LiFePO_4$ and $Li[Ni_{1/2}Mn_{3/2}]O_4$, both of which undergo two-phase reactions. Such studies are underway in our laboratory, and the results will be presented in a forthcoming paper.

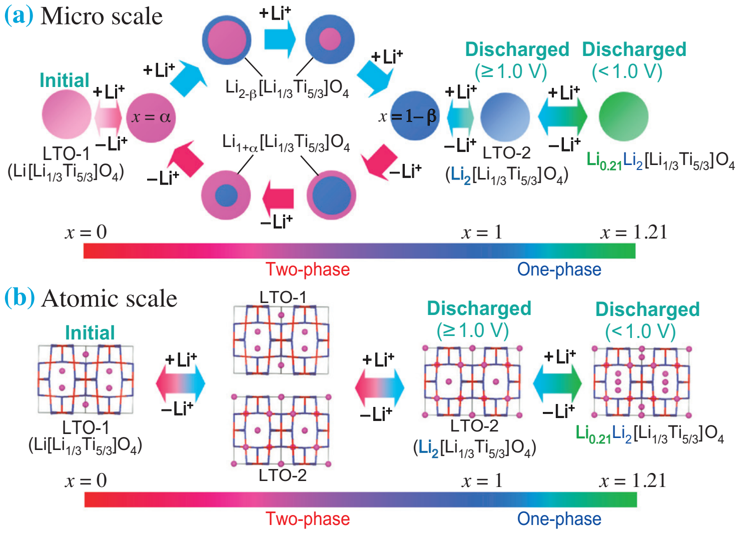

Fig. 3. Schematics of the reaction scheme of LTO at the **(a)** micro- (< 120 nm) and **(b)** atomic scale (<1 nm) scales. For both scales, the two-and one-phase reaction models are applicable in the *x* ranges of $0 \leq x \leq 1$ and $1 < x \leq 1.21$, respectively. At the microscale, the $Li_{1+\alpha}[Li_{1/3}Ti_{5/3}]O_4$ (or $Li_{2-\beta}[Li_{1/3}Ti_{5/3}]O_4$) phase is distributed differently in the particle between the discharge and charge reactions, providing δa_c (δd^{XRD}_{Ti-O}) and δc.

Kazuhiko Mukai*, Takeshi Uyama and Takamasa Nonaka

Toyota Central R&D Labs., Inc.

*Email: e1089@mosk.tytlabs.co.jp

References

[1] T. Ohzuku *et al.*: J. Electrochem. Soc. **142** (1995) 1431.
[2] K. Mukai: Inorg. Chem. **58** (2019) 10377.
[3] T. Nonaka *et al.*: Rev. Sci. Instrum. **83** (2012) 083112.
[4] K. Mukai *et al.*: Inorg. Chem. **59** (2020) 16882.
[5] *K. Mukai, T. Nonaka and T. Uyama: Energy Storage Mater.* ***44*** *(2022) 547.*

ACCELERATORS & BEAMLINES FRONTIERS

SPRING-8
BEAM PERFORMANCE

Recent update of accelerators

A new undulator, referred to as Helical-8 undulator, which facilitates operation mode can be switched between helical and figure-8 modes, has been proposed and developed at SPring-8. For soft X-ray (SX) undulators, a large K value is required for the high electron energy of SPring-8, that is, 8 GeV, and typically polarization control is necessary. One solution for this may be the APPLE-type undulator that can provide both linear and circular polarized radiation; however, it is unsuitable to SPring-8 because of its large on-axis heat load in a linearly polarized radiation mode. Another solution is the Figure-8 undulator, which has a considerably lower on-axis heat load than that of the APPLE-type undulator. However, circularly polarized radiation cannot be obtained from the Figure-8 undulator. Thus, one of the SX beamlines in SPring-8, BL25SU is equipped with twin helical undulators with a fast helicity switching function and is devoted only to experiments using circular polarized radiation. Another SX beamline, BL27SU, used to provide only linearly polarized radiation along the horizontal or vertical axis from a Figure-8 undulator. The newly developed Helical-8 undulator can be switched between helical and figure-8 modes, thus providing both circularly and linearly polarized radiations. For the circular polarization mode, both right and left polarization are available. Whereas, for the linear mode, both horizontally and vertically polarized radiation can be produced. Further, for all the polarization modes, the on-axis heat load is well suppressed. Such an undulator with an undulator period of 120 mm and a minimum gap of 20 mm has been constructed during the period of FY2021 to 2022. Consequently, it was verified that the magnetic field distributions inside the undulator were consistent with the designated ones. Spatial radiation patters of radiation generated from the undulator were also consistent with those expected from the design. The undulator was installed in BL17SU in the summer of 2022, and user experiments have already started.

In-vacuum undulators (IVU) are key insertion devices in SPring-8. Most of the currently operated insertion devices in SPring-8 are standard IVUs. We have developed a new IVU, referred to as IVU-II, for a future major upgrade, SPring-8-II. Since the installation of the first type of IVU-II in BL10XU in 2019, various improvements have been made. The latest design of IVU-II offers many new features compared with the conventional IVU, such as, avoiding demagnetization of permanent magnets, reducing manufacturing costs, etc. The strong attractive force between the upper and lower magnet arrays of an undulator is canceled via the addion of two more pairs of magnetic arrays such that the additional magnet arrays generate repulsive forces that are identical to the attractive force for any gap length [1]. Thus, the mechanical supports for the undulator can be simplified considerably, reducing the manufacturing cost. The manufacturing process of the permanent magnet, configuration of the permanent magnet pieces, and others such as a mechanical structure for assembling magnet pieces have been extensively improved. We plan to begin the replacement of the present IVUs with the latest design of IVU-II anticipating the future upgrade, SPring-8-II.

In addition to the insertion devices, other components of accelerators have also been updated anticipating SPring-8-II. One of the recent developments for present SPring-8 is the replacement of all the conventional low-level RF (LLRF) systems based on NIM modules with a new technology mTCA.4 [2]. Most of the replacements have already been completed, and the new system has been improved for the daily operation of SPring-8. To date, reliable user operations have been conducted without severe problems, and the new mTCA.4 based LLRF and other systems have been modified as needed.

Other recent updates such as the replacement of the injector based on a combination of the 1 GeV linac and the 8 GeV booster to the SACLA linac [3], the new bunch cleaner in the storage ring, and the adaptive feedforward control of electron beam orbit [4] have all worked smoothly, providing reliable and stable beam operations [2]. The future plan has not been officially approved yet; however, once it is funded and the storage ring is upgraded, the new generation storage ring will benefit from these machine upgrades.

Shiro Takano and Takahiro Watanabe*

Japan Synchrotron Radiation Research Institute (JASRI)

*Email: twatanabe@spring8.or.jp

References

[1] R. Kinjo *et al.*: Rev. Sci. Instrum. **88** (2017) 073302.
[2] SPring-8/SACLA Research Frontiers 2021.
[3] T. Hara *et al.*: Phys. Rev. Accel. Beams **24** (2021) 110702.
[4] M. Masaki *et al.*: J. Synchrotron Rad. **28** (2021) 1758.

SACLA
BEAM PERFORMANCE

Recent update of accelerator

In the time-resolved beam injection from the SACLA linac (hereafter, referred to as “beam injection from SACLA”) to the storage ring, the most severe issue affecting the reliable and steady beam operations is the reduction of the downtime upon the failure of the electron gun system at SACLA. Installing a spare electron gun next to the existing gun is not feasible because passage of emission electron beams from the gun cathode through the non-straight line by kicking the beam results in the fatal deterioration of the beam quality. Thus, such a spare gun adjacent to the existing gun cannot provide experimental users with high-performance XFELs. To solve this problem, the gun system was heavily modified in the summer shutdown period of 2022. The entire gun system, including the high voltage tank and gun cathode was constructed as an exchangeable module to facilitate quick recovery from any fatal problem that may occur in the gun system. Figure 1 shows the two module-typed gun systems in the test stand. The spare gun is always ready in case of the requirement for replacement at the gun conditioning bench. This system has significantly reduced the downtime owing to the gun cathode exchange module and facilitated quick restart of user operations at both SACLA and SPring-8. Figure 2 shows the recovery example of the

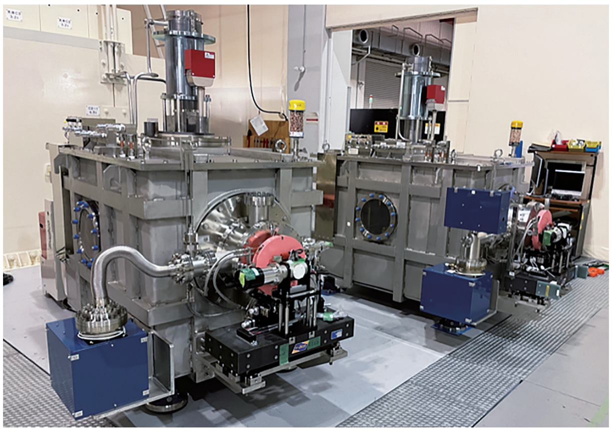

Fig. 1. Two developed module-typed gun systems in the test stand. One of the two is used for the beam operation in the tunnel and the other is on stand-by in the gun conditioning bench.

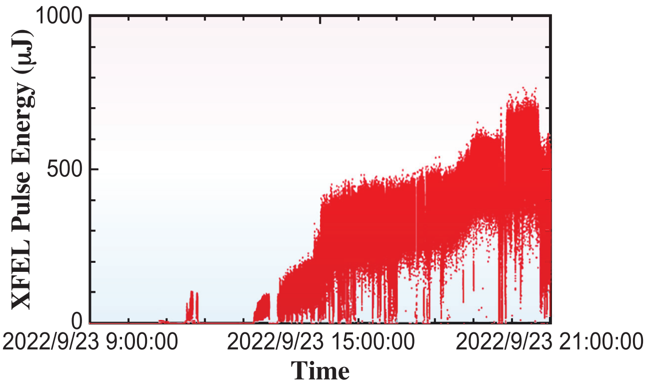

Fig. 2. Recovery example of pulse energy of XFEL after the gun exchange.

pulse energy of XFEL after the gun exchange. The XFEL pulse energy could be smoothly increased up to an intensity level of approximately 0.5 mJ in half a day.

Multi-beamline operations with pulse-by-pulse route switching have been routinely used for user experiments at SACLA. To maximize the XFEL performance and beam injection stability during this operation, a pulsed quadrupole focusing system has been developed to set pulse-by-pulse optimum focusing parameters according to the selected beam route. In the fiscal year of 2022, the new pulsed AC magnets replaced seven existing quadrupole DC magnets in the summer shutdown period. The necessary replacement work will be continued through the next year and the full pulsed quadrupole focusing system will be completed at the end of the fiscal year of 2023. Figure 3 shows the newly installed quadrupole laminated magnet.

A tube-type RF source referred to as inductive output tube (IOT) has been used as the RF source for the 476 MHz booster cavity in the buncher section of the SACLA linac. As the IOT tube used in SACLA was discontinued, we began to develop a new 476 MHz RF source by using the recent advancement of power semiconductor technology for reliable and steady operations. In 2022, newly developed RF source was installed near the old IOT coupled with a switcher to facilitate quick switching between the two sources. Figure 4 shows the newly installed 476 MHz RF source. The basic source performance was experimentally confirmed and now the 476 MHz new source is ready for routinary use. The switch from the old source to new one is scheduled for 2023.

Fig. 3. Quadrupole laminated magnet newly installed to realize pulse-by-pulse beam optimal focusing.

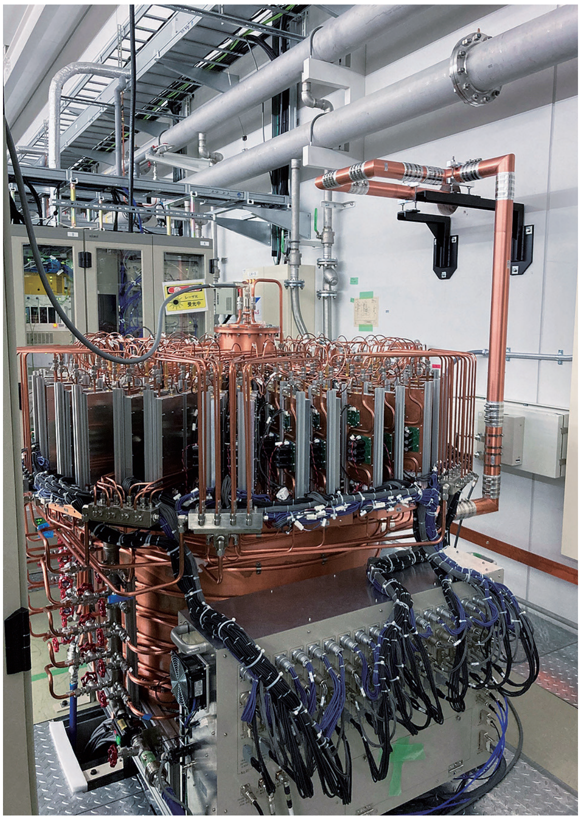

Fig. 4. New 476 MHz RF source installed at the klystron gallery of SACLA.

Hitoshi Tanaka

RIKEN SPring-8 Center

Email: tanaka@spring8.or.jp

High-fluence multilayer focusing optics attaining 2 nm spatial resolution in XFEL based coherent diffractive imaging

Femtosecond coherent diffractive imaging (CDI) is an analytical technique made possible by X-ray free electron lasers (XFELs). This is a microscopic technique in which an object image is reconstructed using an iterative algorithm from a coherent diffraction pattern obtained by illuminating a sample with a femtosecond XFEL pulse. Compared with CDI using synchrotron radiation, CDI using XFEL allows us to detect information under the native states of samples before radiation damage. On the basis of the theoretical calculations, femtosecond CDI is anticipated to take snapshots of biological molecules with a spatial resolution approaching an atomic resolution.

Various efforts have been made to achieve a high resolution; however, the spatial resolution of CDI in single-XFEL-pulse exposure has been limited to ~5 nm. A higher fluence to illuminate samples is required to obtain a higher spatial resolution in femtosecond CDI, because the signal-to-noise ratio obtained on a detector, i.e., a low amount of signal from a very small sample, is a critical problem. Our group has developed XFEL focusing mirrors to obtain a high fluence focus by solving technical problems in the fabrication of ultrahigh-precision mirrors with atomic-level precision. The developments have enabled us to realize an extremely high fluence focus at a beam size of 100 nm and to improve the spatial resolution of femtosecond CDI to an unprecedented 2 nm with single-XFEL-pulse exposure [1].

Our group designed a focusing optical system that matches CDI optics and includes X-ray energy. Our group employed multilayer focusing mirrors in the Kirkpatrick–Baez (K–B) geometry to focus X-rays efficiently with high demagnifications. A higher fluence at the focus can be produced by utilizing higher demagnification with smaller focal lengths, because multilayer mirrors can be designed to have larger glancing angles than general total reflection mirrors. However, multilayer focusing mirrors have steeply curved aspheric substrates, making them difficult to fabricate. The fabrication of the X-ray focusing mirrors requires extremely high precision technologies of a surface measurement system at the atomic level as well as an aspheric processing method.

Our group developed, in particular, a new high-precision surface measurement system of zero-method surface profilometry (ZSP) (see Supplementary Information in Ref. 1.) in addition to an ultraprecise processing technology used in the fabrication of X-ray mirrors at SPring-8 [2]. Using these fabrication technologies, substrates of the X-ray focusing mirrors with an elliptical-cylinder shape were finished with a precision of 0.2 nm in root mean square at the SPring-8 site. The mirror surfaces were then coated with $(Cr/C)_{30}$ multilayers in a lateral graded structure using a multilayer deposition system at SPring-8. The design of the focusing optics at an optimized X-ray energy of 4 keV is as follows. The focal length is 190 mm (110 mm) in the horizontal (vertical) direction, the two mirrors are 80 mm long, the two incident angles are 25 mrad, and the working distance is 60 mm. The mirrors have a large spatial aperture of 1850 μm square compared with the incident X-ray beam size of ~550 μm in full width at half maximum (FWHM).

Our group developed a femtosecond CDI instrument using the fabricated multilayer focusing mirrors at SACLA **BL2**. This system is called MAXIC-S. A photograph of the main vacuum chamber, which is equipped with X-ray focusing mirrors, an alignment mechanism, and sample scanning stages, is shown in Fig. 1. To avoid contaminants on the mirrors, air absorption, and unwanted scattering, all of the components, including the focusing mirrors, the sample, and the multiport charge-coupled device (MPCCD) detector to record diffraction patterns, are enclosed in a vacuum environment. The MPCCD detector can obtain diffraction signals at a full-period resolution of 2 nm at the edge.

Our group evaluated the focused beam produced by the multilayer mirrors using the knife-edge

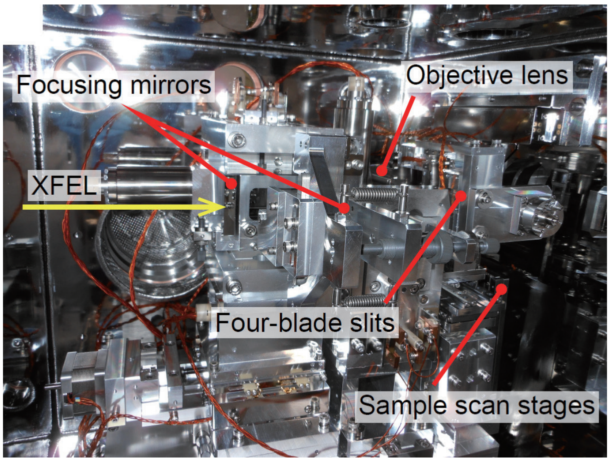

Fig. 1. Photograph of the CDI instrument at SACLA. [1]

scanning method at SACLA. Measured beam sizes were 110 nm and 60 nm (FWHM) in the horizontal and vertical directions, respectively, which are in agreement with the design. The reflectivity of the double reflection by the multilayer focusing mirrors was 52%, while the theoretical reflectivity is 62%. The optics achieved an extremely high fluence focus at 3×10^5 J/cm^2/pulse with the evaluated beam sizes and a pulse energy of 61 μJ. The photon density was 4×10^{12} photons/μm^2/pulse, and the intensity was 3×10^{19} W/cm^2 at a pulse duration of 10 fs. The photon density of XFEL was enhanced by a factor of 2×10^6 compared with the unfocused beam. This focus has a 50-times-higher photon density than the 1 μm focus [3] used for CDI at SACLA.

The CDI instrument utilizing the developed high-fluence beam was applied to observe Au nanoparticles (AuNPs) in water (Fig. 2). The sample AuNPs have a bipyramidal shape with a volume of ~20 nm cube, which includes electrons as small as the same order of magnitude as that of biological particles, such as a virus particle of ~70 nm diameter. As a result of the observation by single-XFEL-pulse exposure, the CDI system attained an unprecedented high spatial resolution of 2 nm (full-period resolution). Au particles become a highly functional material with unique physical and chemical properties when its size is reduced to the nanometer scale. In water, which is applicable to biological samples, the observation before changing with XFEL illumination was successfully demonstrated at this extremely high spatial resolution using ultrafast XFEL exposure. The observed result was a native structure of the material showing important information for elucidating the relationship between the structure and function of nanoparticles. In addition, the validity of the fluence at the focus evaluated by the knife-edge scanning method was confirmed by the agreement with the fluence estimated from the measured coherent diffraction pattern.

The CDI system developed in this study has been applied to observe biological samples and functional materials. The microscope is expected to be utilized for the ultrahigh-resolution and ultrahigh-speed observation of the native state of samples that has never been seen previously.

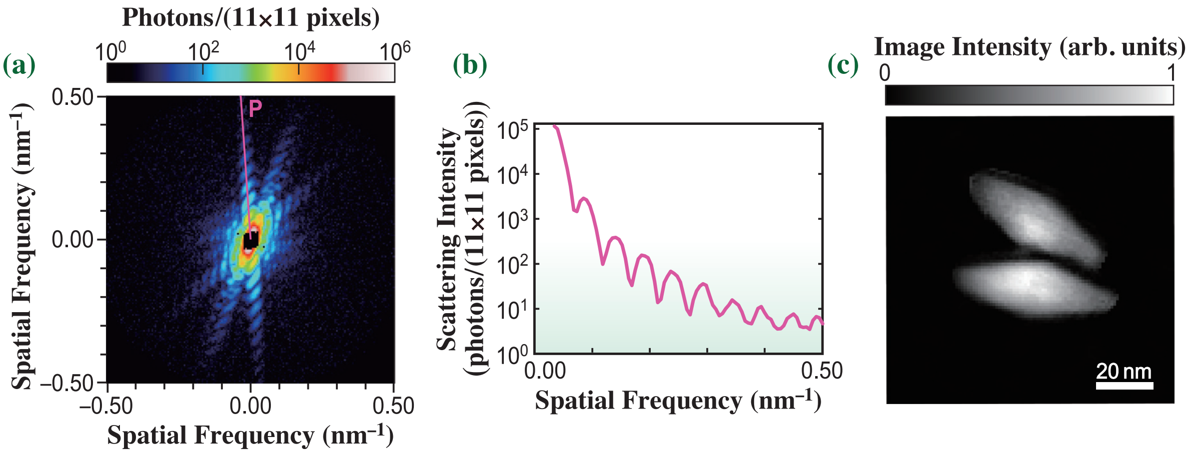

Fig. 2. Demonstration of femtosecond coherent diffractive imaging. **(a)** Measured coherent diffraction pattern. (**b**) Profile along line P in (a). (**c**) Reconstructed image. [1]

Hirokatsu Yumoto

Japan Synchrotron Radiation Research Institute (JASRI)

Email: yumoto@spring8.or.jp

References

[1] *H. Yumoto, T. Koyama, A. Suzuki, Y. Joti, Y. Niida, K. Tono, Y. Bessho, M. Yabashi, Y. Nishino and H. Ohashi: Nat. Commun.* ***13*** *(2022) 5300.*
[2] H. Yumoto *et al*.: Proc. of SPIE **9206** (2014) 920605.
[3] H. Yumoto *et al*.: Nat. Photonics **7** (2013) 43.

FACILITY STATUS

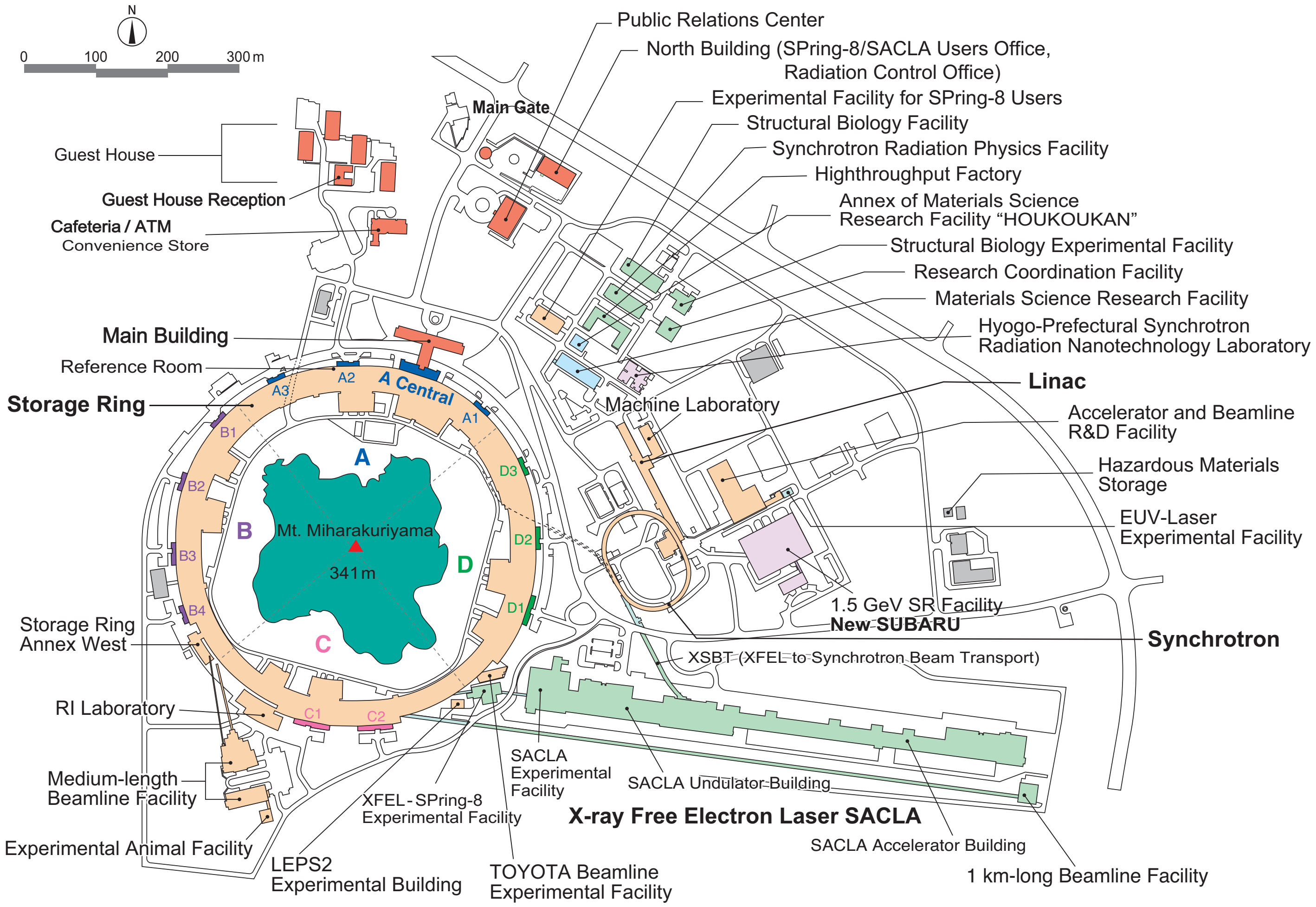

SPring-8

I. Introduction

SPring-8 was stably operated throughout FY2022 achieving a total accelerator complex operation time and user beam time of 5259.3 h and 4416.0 h, respectively, and a downtime of 19.7 h. SPring-8 completed all its operations by the middle of February 2023.

For the contract beamlines, interim reviews were conducted at QST Quantum Dynamics I (BL11XU, National Institutes for Quantum Science and Technology), QST Quantum Dynamics II (BL14B1, National Institutes for Quantum Science and Technology), JAEA Actinide Science I (BL22XU, Japan Atomic Energy Agency), JAEA Actinide Science II (BL23SU, Japan Atomic Energy Agency), Advanced Softmaterial (BL03XU, Advanced Softmaterial Beamline Consortium), NSRRC ID (BL12XU, National Synchrotron Radiation Research Center), and NSRRC BM (BL12B2, National Synchrotron Radiation Research Center). Subsequently, these beamlines projects were authorized to continue.

Following the contract cancellation, a post-evaluation was conducted for the University-of-Tokyo Outstation Beamline for Materials Science (BL07LSU) in August 2022. At present, the number of SPring-8 users is as high as 14,000, all of whom are members of the SPring-8 Users Community (SPRUC).

To facilitate dialogue between users and facility staff, it is important for SPring-8 to organize scientific events in collaboration with SPRUC, such as the SPring-8 Symposium. In 2022, the SPring-8 Symposium was held online on September 25–26, with 497 participants. SPring-8 also facilitates communication between users and industry. The Joint Conference on Industrial Applications of SPring-8 was held in Hyogo Prefecture from August 31 to September 1, 2022, with 214 participants. Moreover, as part of its continuous effort towards fostering human resources in synchrotron sciences, SPring-8 organized the 22nd SPring-8 Summer School with 77 students of graduate schools nationwide, in cooperation with the University of Hyogo, Kwansei Gakuin University, the University of Tokyo, Okayama University, Osaka University, Ibaraki University, Japan Atomic Energy Agency, National Institutes for Quantum and Radiological Science and Technology, and RIKEN. Furthermore, SPring-8 and SPRUC organized the 6th SPring-8 Autumn School with 60 participants, which included university students and corporate researchers.

II. Machine Operation

The operation statistics for the last five fiscal years are shown in Fig. 1. In FY2022, the operation time of the storage ring was 5259.3 h, 84.0% of which (4416.0 h) was devoted to the SR experiments. This excellent figure for the user time represents a storage ring availability of 99.5%. The total downtime caused by failures amounted to 19.7 h accounting for 0.45% of the total user time. For 99.4% of the user time in FY2022, the stored beam current was maintained at 100 mA via the top-up operation wherein the stored beam was filled up on demand at any time. Extreme stability of the light source intensity better than 0.1% was provided by the top-up operation.

The variety of operation modes for SR experiments is one of the characteristics of SPring-8. The operation modes are classified into two types: several-bunch and hybrid-filling modes. The several-bunch mode comprises equally spaced bunches or trains of bunches such as 203 bunches or 29 trains of 11 bunches. Whereas, the hybrid-filling mode is composed of a long train of bunches and isolated single bunches. Sufficient isolated bunch purity is maintained by the SACLA linac's spurious bunch sweeper and the storage ring's bunch cleaning system. The operation modes of SPring-8 are listed in Table 1, along with a share of each operation mode for FY2022. Table 2 summarizes the beam parameters of the storage ring.

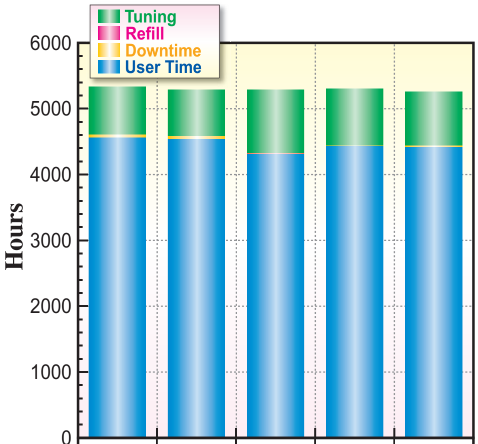

	FY2018	FY2019	FY2020	FY2021	FY2022
Accelerator Operation Time	5329.8	5285.7	5284.6	5300.2	5259.3
Storage Ring Operation Time	5316.7	5271.2	5274.8	5300.2	5259.3
Tuning & Study (Acc. & BL)	721.8	701.7	964.6	860.2	819.3
Refill	5.3	5.6	3.6	3.1	4.3
Downtime	43.1	40.5	7.4	10.0	19.7
Mean Time Between Failures	168.9	206.3	718.2	553.4	232.4
Achieved User Time	4559.6	4537.9	4309.0	4426.9	4416.0
Planned User Time	4608.0	4584.0	4464.0	4440.0	4440.0
Availability (%)	98.9	99.0	99.7	99.7	99.5

Fig. 1. Operation statistics for five most recent fiscal years.

Table 1. Operation modes in FY2022

	Single bunch current (mA)	Share of operation time (%)
203 bunches		39.5
4 bunch-train × 84		7.0
11 bunch-train × 29		17.8
1/7-filling + 5 single bunches	3	6.5
2/29-filling + 26 single bunches	1.4	0
1/14-filling + 12 single bunches	1.6	6.5
4/58-filling + 53 single bunches	1.0	3.2
406 × 11/29-filling + 1 single bunch	5	19.5

Table 2. Beam parameters of SPring-8 storage ring

Energy [GeV]	**8**
Number of buckets	**2436**
Tunes (ν_x / ν_y)	**41.14 / 19.325**
Current [mA]:	
single bunch	**12**
multi bunch	**100**
Bunch length (σ) [psec]	**13**
Horizontal emittance [nm·rad]	**2.4 ***
Vertical emittance [pm·rad]	**4.8 ***
Coupling [%]	**0.2**
RF Voltage [MV]	**14.4 ** ~ 16**
Momentum acceptance [%]	**3.2 (~256 MeV)**
Beam size (σ_x / σ_y)* [μm]	
Long ID section	**333 / 7**
ID section	**316 / 5**
BM1 section	**94 / 12**
BM2 section	**100 / 12**
Beam divergence (σ_x' / σ_y')* [μrad]	
Long ID section	**8 / 0.7**
ID section	**9 / 1.0**
BM1 section	**58 / 0.5**
BM2 section	**68 / 0.5**
Operational chromaticities (ξ_x / ξ_y)	**+2 / +2 *****
Lifetime [hr]:	
100 mA (multi bunch)	**~ 250**
1 mA (single bunch)	**~ 30**
Horizontal dispersion [m]:	
Long ID section	**0.153**
ID section	**0.146**
BM1 section	**0.039**
BM2 section	**0.059**
Fast orbit stability (0.1 – 200 Hz) [μm]:	
horizontal (rms)	**~ 4**
vertical (rms)	**~ 1**

---

* Assuming 0.2% coupling
** Power saving mode
*** With bunch-by-bunch feedback

III. Beamlines

The SPring-8 storage ring can accommodate up to 62 beamlines: 34 insertion devices, 4 long undulators, and 24 bending magnets. At present, 54 beamlines are in operation, covering a wide variety of research fields involving synchrotron radiation science and technology. The beamlines are classified into the following three types.

(1) Public Beamlines (26 beamlines operating),
(2) Contract Beamlines (15 beamlines operating), and
(3) RIKEN Beamlines (13 beamlines operating).

Currently, 26 public beamlines are fully operating. Beamlines that have been proposed and constructed by external organizations, such as universities, research institutes, private companies and consortiums, are referred to as contract beamlines and these are used exclusively by contractors for their own research purposes. Currently, 15 contract beamlines are operational. Beamlines constructed by RIKEN or transferred to RIKEN, except for public beamlines, are referred to as RIKEN beamlines and are primarily used for RIKEN's own research activities, with partial availability for public use. RIKEN operates 13 beamlines. To illustrate the beamline portfolio of SPring-8, a beamline map is shown in Fig. 2 along with the beamline classification. The research fields for each beamline are listed in Table 3.

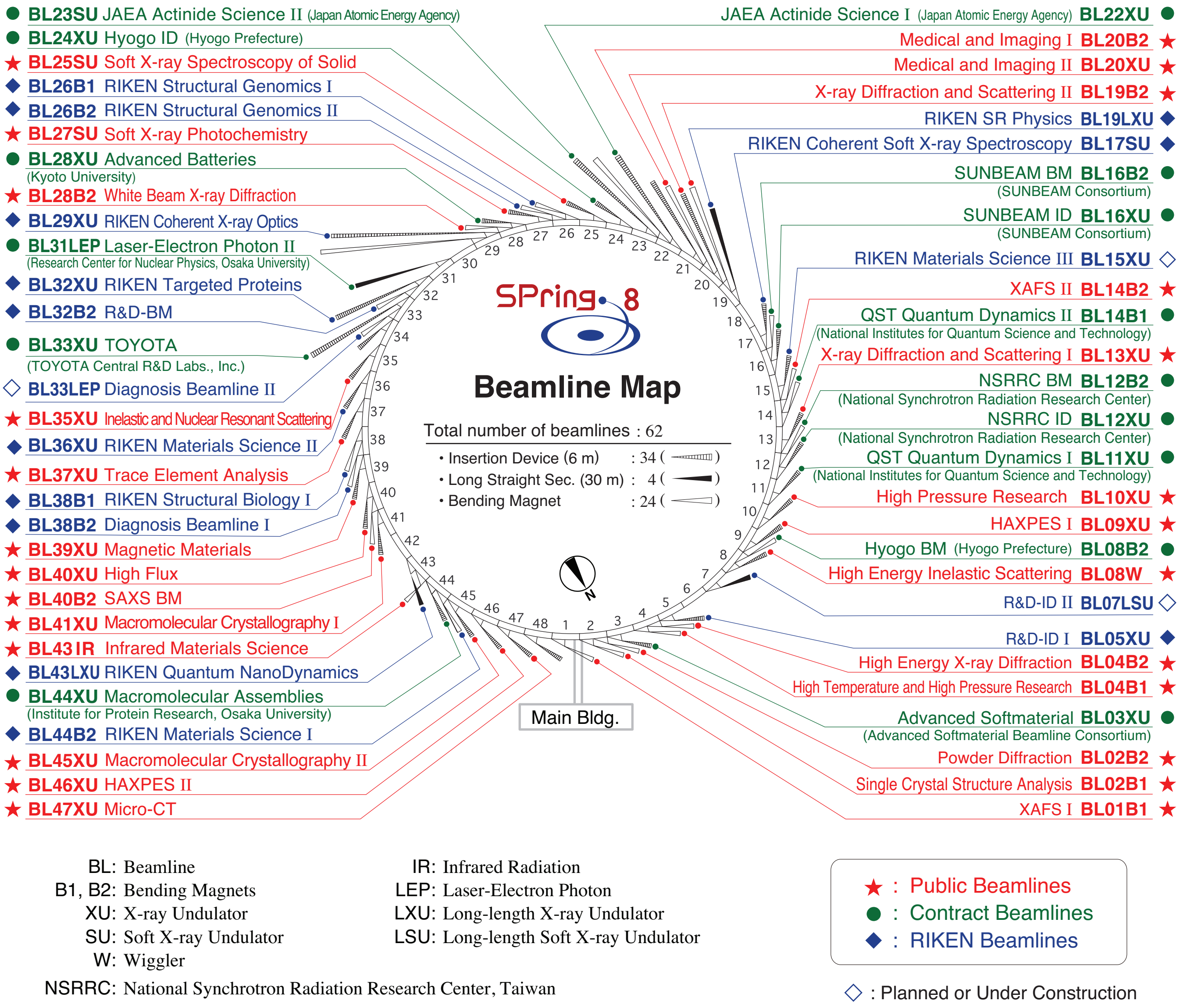

BL: Beamline
B1, B2: Bending Magnets
XU: X-ray Undulator
SU: Soft X-ray Undulator
W: Wiggler
IR: Infrared Radiation
LEP: Laser-Electron Photon
LXU: Long-length X-ray Undulator
LSU: Long-length Soft X-ray Undulator
NSRRC: National Synchrotron Radiation Research Center, Taiwan

Fig. 2. Beamline map.

Table 3. List of beamlines

BL #	Beamline Name	(Public Use) or (First Beam)	Areas of Research and Available Techniques
★ Public Beamlines			as of April 2023
BL01B1	XAFS I	(Oct. 1997)	Wide energy range (3.8 – 113 keV), XAFS of dilute systems and thin films, time-resolved XAFS by quick scan (time-resolved QXAFS), depth-resolved XAFS, XAFS at low and high temperatures, simultaneous XAFS and XRD measurements, simultaneous XAFS and IR measurements.
BL02B1	Single Crystal Structural Analysis	(Oct. 1997)	Charge density study using high energy X-ray, *in situ* single crystal experiments, microcrystal structure analysis.
BL02B2	Powder Diffraction	(Sep. 1999)	Charge density study from powder diffraction, structural phase transition, *ab initio* structure determination from powder diffraction, crystal structure refinement by Rietveld method, *in situ* powder diffraction experiment under gas and vapor adsorption/desorption.
BL04B1	High Temperature and High Pressure Research	(Oct. 1997)	X-ray diffraction measurements and radiography under extreme conditions using large-volume press.
BL04B2	High Energy X-ray Diffraction	(Sep. 1999)	Structural analysis of glass, liquid, and amorphous materials.
BL08W	High Energy Inelastic Scattering	(Oct. 1997)	Magnetic Compton scattering, high-resolution Compton scattering, Compton scattering imaging, high-energy X-ray scattering, high-energy X-ray fluorescence analysis (XRF), time-resolved pair distribution function analysis (PDF).
BL09XU	HAXPES I	(Oct. 1997)	Resonant hard X-ray photoelectron spectroscopy (HAXPES), polarization-dependent HAXPES using diamond phase retarder, depth analysis of electron state, materials science, and applied materials science.
BL10XU	High Pressure Research	(Oct. 1997)	Crystal structure analysis under high pressure using diamond-anvil cells, *in situ*/*operando* observation of phase transition and compression behavior under extreme conditions, material sciences under extreme conditions, high pressure Earth and planetary science.
BL13XU	X-ray Diffraction and Scattering I	(Sep. 2001)	X-ray diffraction and reflectivity measurements, atomic-scale structural analysis of crystal surfaces and interfaces, ultrathin films, and nanostructures, residual stress measurement, time-resolved X-ray diffraction, *in situ* process observation using X-ray diffraction, *operando* X-ray diffraction, high-resolution powder X-ray diffraction and X-ray total scattering, structural refinement using Rietveld analysis, *in situ*/*operando* powder X-ray diffraction, time-resolved powder X-ray diffraction, analysis of local structures using nanodiffraction.
BL14B2	XAFS II	(Sep. 2007)	X-ray imaging, XAFS in a wide energy range (3.8 – 72 keV), XAFS of dilute systems and thin films, time-resolved XAFS by quick scan (time-resolved QXAFS), XAFS at low and high temperatures.
BL19B2	X-ray Diffraction and Scattering II	(Nov. 2001)	Residual stress measurement, structural analysis of thin film, surface and interface, powder X-ray diffraction, X-ray topography, ultrasmall-angle X-ray scattering.
BL20B2	Medical and Imaging I	(Sep.1999)	Micro-radiography, micro-angiography, micro-tomography, and refraction-contrast imaging are the mainly used techniques. BL20B2 is also applicable to small-animal experiments for medical research. Research and development of basic techniques for evaluation of optical devices and X-ray imaging.
BL20XU	Medical and Imaging II	(Sep. 2001)	X-ray micro-/nano-imaging: micro-tomography (micro-CT), nano-CT (15 – 37.7 keV), refraction/phase contrast imaging, X-ray diffraction tomography (XRD-CT), microbeam/scanning X-ray microscope, research and development of X-ray optics and optical elements, coherent X-ray optics, ultrasmall-angle X-ray scattering (USAXS, 23 keV).
BL25SU	Soft X-ray Spectroscopy of Solid	(Apr. 1998)	Research on electronic states by photoemission spectroscopy (PES), Research on electronic band structures by angle-resolved photoemission spectroscopy (ARPES), study of magnetic states by magnetic circular dichroism (MCD) of soft X-ray absorption, analysis of surface atomic arrangement by photoelectron diffraction (PED), nano-spectroscopic analysis using low-energy/photoemission electron microscope (SPELEEM).
BL27SU	Soft X-ray Photochemistry	(May 1998)	Soft X-ray photoabsorption spectroscopy of dilute samples in partial fluorescence yield mode, surface and interface analysis using depth-resolved soft X-ray photoabsorption spectroscopy, soft X-ray photoabsorption spectroscopy underambient atmospheric pressure, spectroscopy using soft X-ray microbeam, observation of electron state in solids by soft X-ray emission spectroscopy.
BL28B2	White Beam X-ray Diffraction	(Sep. 1999)	White X-ray diffraction: X-ray topography, energy-dispersive strain measurement, high energy (~200 keV) X-ray microtomography, high-speed X-ray imaging.
BL35XU	Inelastic and Nuclear Resonant Scattering	(Sep. 2001)	Phonons in solids and atomic dynamics in disordered materials by inelastic X-ray scattering, atomic and molecular dynamics by nuclear resonant inelastic scattering and quasi-elastic scattering, synchrotron-radiation-based Mössbauer spectroscopy, nuclear excitation.
BL37XU	Trace Element Analysis	(Nov. 2002)	X-ray microbeam/nano-beam spectrochemical analysis, X-ray spectroscopic imaging, ultratrace-element analysis, high-energy X-ray fluorescence analysis. Projection/scanning/imaging XAFS microscopy, high brightness XAFS, coherent diffraction imaging XAFS microscopy.
BL39XU	Magnetic Materials	(Oct. 1997)	X-ray magnetic circular dichroism (XMCD) spectroscopy and element-specific magnetometry (ESM), XAFS and XMCD spectroscopy under extreme conditions (high pressure, high magnetic field, and low/high temperature), XAFS and XMCD spectroscopy using micro/nanobeam and variable X-ray polarization (horizontally/perpendicularly linear or circular), scanning XAFS and XMCD microscopy using micro/nanobeam, X-ray emission spectroscopy (XES) and high-energy resolution fluorescence detected (HERFD) XAFS spectroscopy.
BL40XU	High Flux	(Apr. 2000)	Fast time-resolved X-ray diffraction and scattering experiments, X-ray photon correlation spectroscopy, X-ray fluorescence analysis, microbeam X-ray diffraction and scattering experiments, micro-crystallography.
BL40B2	SAXS BM	(Sep. 1999)	Small-angle X-ray scattering (SAXS).
BL41XU	Macromolecular Crystallography I	(Oct. 1997)	Macromolecular crystallography, micro-crystallography, ultrahigh resolution structural analysis.
BL43IR	Infrared Materials Science	(Apr. 2000)	Infrared microspectroscopy.
BL45XU	Macromolecular Crystallography II	(Apr. 2019)	Macromolecular crystallography, micro-crystallography, automation and high throughput data collection for protein crystallography.
BL46XU	HAXPES II	(Nov. 2000)	Hard X-ray photoemission spectroscopy, ambient pressure hard X-ray photoemission spectroscopy.
BL47XU	Micro-CT	(Oct. 1997)	X-ray micro-/nano-imaging including CT (7 – 15 keV), refraction/phase contrast imaging, high speed X-ray imaging, microbeam/scanning X-ray microscope.

BL #	Beamline Name	(Public Use) or (First Beam)	Areas of Research and Available Techniques
			● **Contract Beamlines** as of April 2023
BL03XU	**Advanced Softmaterial** (Advanced Softmaterial Beamline Consortium)	(Nov. 2009)	Structural characterization of softmaterials using small- and wide-angle X-ray scattering, grazing-incidence small- and wide-angle X-ray scattering for thin films.
BL08B2	**Hyogo BM** (Hyogo Prefecture)	(Jun. 2005)	XAFS in a wide energy region, small angle X-ray scattering, X-ray topography, imaging, X-ray diffraction for multipurpose.
BL11XU	**QST Quantum Dynamics I** (National Institutes for Quantum Science and Technology)	(Oct. 1998)	Nuclear resonant scattering, surface and interface structure with MBE, resonant inelastic X-ray scattering, X-ray emission spectroscopy.
BL12B2	**NSRRC BM** (National Synchrotron Rad. Res. Center)	(Oct. 2000)	X-ray absorption spectroscopy, powder X-ray diffraction, high resolution X-ray scattering, protein crystallography.
BL12XU	**NSRRC ID** (National Synchrotron Rad. Res. Center)	(Dec. 2001)	Non-resonant or resonant inelastic X-ray scattering, hard X-ray photoemission spectroscopy.
BL14B1	**QST Quantum Dynamics II** (National Institutes for Quantum Science and Technology)	(Dec. 1997)	Materials science at high pressure, XAFS, time-resolved energy-dispersive XAFS (DXAFS).
BL16B2	**SUNBEAM BM** (SUNBEAM Consortium)	(Oct. 1998)	Characterization of various industrial materials for secondary batteries, fuel cells, catalysts, steels, semiconductors, optical and magnetic devices and others using X-ray absorption fine structure, X-ray diffraction (including X-ray reflectivity technique), X-ray topography and computed tomography/laminography.
BL16XU	**SUNBEAM ID** (SUNBEAM Consortium)	(Oct. 1998)	Characterization of various industrial materials for secondary batteries, fuel cells, catalysts, steels, semiconductors, optical and magnetic devices and others using X-ray diffraction, X-ray microbeam based evaluation techniques, hard X-ray photoelectron spectroscopy and X-ray fluorescence analysis.
BL22XU	**JAEA Actinide Science I** (Japan Atomic Energy Agency)	(May 2002)	HAXPES, microbeam XAFS, residual stress/strain distribution analysis, X-ray imaging, time-resolved X-ray diffraction, surface X-ray diffraction, high-energy X-ray diffraction, high-pressure science, coherent X-ray diffraction.
BL23SU	**JAEA Actinide Science II** (Japan Atomic Energy Agency)	(Feb. 1998)	Surface chemistry with supersonic molecular beam, photoelectron spectroscopy, magnetic circular dichroism, STXM.
BL24XU	**Hyogo ID** (Hyogo Prefecture)	(May. 1998)	Microbeam small- and wide-angle X-ray scattering for local structure analysis, scanning and imaging microscope, micro-tomography, coherent diffractionm, microbeam X-ray diffraction and bright field X-ray topography for electronic device materials, near-ambient pressure hard X-ray photoelectron spectroscopy.
BL28XU	**Advanced Batteries** (Kyoto University)	(Apr. 2012)	Characterization of rechargeable battery reactions and battery related materials by resonance X-ray diffraction, X-ray absorption spectroscopy (XAS), X-ray diffraction spectroscopy (XDS), and hard X-ray photoemission spectroscopy (HAXPES).
BL31LEP	**Laser-Electron Photon II** (RCNP, Osaka University)	(Oct. 2013)	Production of high intensity GeV photon beam by laser-backward Compton scattering, hadron physics via photonucleon and photonuclear reactions, test and calibration of detectors with GeV gamma-ray and converted electrons/positrons.
BL33XU	**TOYOTA** (TOYOTA Central R&D Labs., Inc.)	(Apr. 2009)	Time-resolved XAFS. 3DXRD, characterization of industrial materials and devices (e.g., catalysts, lightweight bodies, secondary batteries, fuel cells, and power modules).
BL44XU	**Macromolecular Assemblies** (IPR, Osaka University)	(May 1999)	Crystal structure analysis of biological macromolecular assemblies (e.g., membrane protein complexes, protein complexes, protein-nucleic acid complexes, and viruses).
BL05XU	**R&D-ID I**	(Mar. 2004)	R&D of high-energy X-ray optics, instruments, and applications; structural and dynamical research using small and wide angle scattering.
BL07LSU	**R&D-ID II**	(Oct. 2009)	R&D of soft X-ray optics, instruments, and applications.
BL15XU	**RIKEN Materials Science III**	(Oct. 2021)	Advanced diffraction and scattering with high-energy X-rays.
BL17SU	**RIKEN Coherent Soft X-ray Spectroscopy**	(Sep. 2003)	High resolution photoemission spectroscopy; soft X-ray emission spectroscopy; soft X-ray diffraction spectroscopy; soft X-ray microspectroscopy.
BL19LXU	**RIKEN SR Physics**	(Oct. 2000)	SR science with highly brilliant X-ray beam.
BL26B1	**RIKEN Structural Genomics I**	(Apr. 2002)	Structural biology research based on single crystal X-ray diffraction.
BL26B2	**RIKEN Structural Genomics II**	(Apr. 2002)	Structural biology research based on single crystal X-ray diffraction.
BL29XU	**RIKEN Coherent X-ray Optics**	(Dec. 1998)	X-ray optics, especially coherent X-ray optics.
BL32XU	**RIKEN Targeted Proteins**	(Oct. 2009)	Protein microcrystallography.
BL32B2	**R&D-BM**	(May 2002)	X-ray computed tomography; X-ray diffraction; X-ray absorption fine structure; R&D of SR instruments.
BL36XU	**RIKEN Materials Science II**	(Mar. 2020)	Time resolved XAFS and X-ray diffraction; 2D/3D scanning XAFS imaging; 3D computed tomography/laminography XAFS imaging; X-ray emission spectroscopy; ambient pressure hard X-ray photoelectron spectroscopy; pink beam experiments.
BL38B1	**RIKEN Structural Biology I**	(Oct. 2000)	Structure study of non-crystalline biological materials using small-angle scattering and diffraction techniques.
BL38B2	**Diagnosis Beamline**	(Sep.1999)	Accelerator beam diagnostics.
BL43LXU	**RIKEN Quantum NanoDynamics**	(Oct. 2011)	High resolution inelastic X-ray scattering for investigating atomic and electronic dynamics.
BL44B2	**RIKEN Materials Science I**	(Feb. 1998)	Structural materials science research using powder X-ray diffraction.

IV. User Program and Statistics

In principle, SPring-8 calls for public use proposals twice a year. Since the 2022B term, nine public beamlines have started inviting proposals six times annually, including the beamlines previously intended for industrial applications. Submitted proposals are reviewed by the SPring-8 Proposal Review Committee (SPring-8 PRC). Since 1997, SPring-8 has accepted a variety of proposals. For the promotion of research on industrial applications at SPring-8, currently, Industrial Application Proposals account for approximately 16%–19% of the total number of proposals conducted at various public beamlines. Certain companies and research institutes find retaining specialized staff and accommodating the need for quick access to SPring-8 difficult. The SPring-8 Measurement Service has been provided to appropriately respond to these circumstances.

In this framework of service, JASRI staff members perform measurements on behalf of users. Users may visit SPring-8 and be present during the measurements or simply send their samples to SPring-8. BL28XU was added to the Measurement Service BL in 2022B. JASRI expanded the purview of the SPring-8 Measurement Service to include five measurement methods (XAFS, Powder X-ray Diffraction, Small Angle X-ray Scattering, High energy X-ray CT, Hard X-ray Photoemission Spectroscopy). In addition, JASRI provides Protein Crystallography Automatic Data Collection at the Macromolecular Crystallography beamlines. Therefore, users can choose to be present at SPring-8 during the measurements or simply send their samples to SPring-8. Since 2022A, JASRI has begun suggesting Hour-based usage at most public beamlines as part of its proprietary time-designated proposals. According to this change, the feasibility study proposals for industrial applications have been integrated into this proposal program. Further, SPring-8 is developing a remote operation system that allows users to control the experimental instruments from outside to promote remote access. The numbers of experiments conducted and user visits to public and contract beamlines are presented in Fig. 3. Part of the proposals are for proprietary use, and do not require refereed reports. Figures 4 to 13 show information related to the user programs.

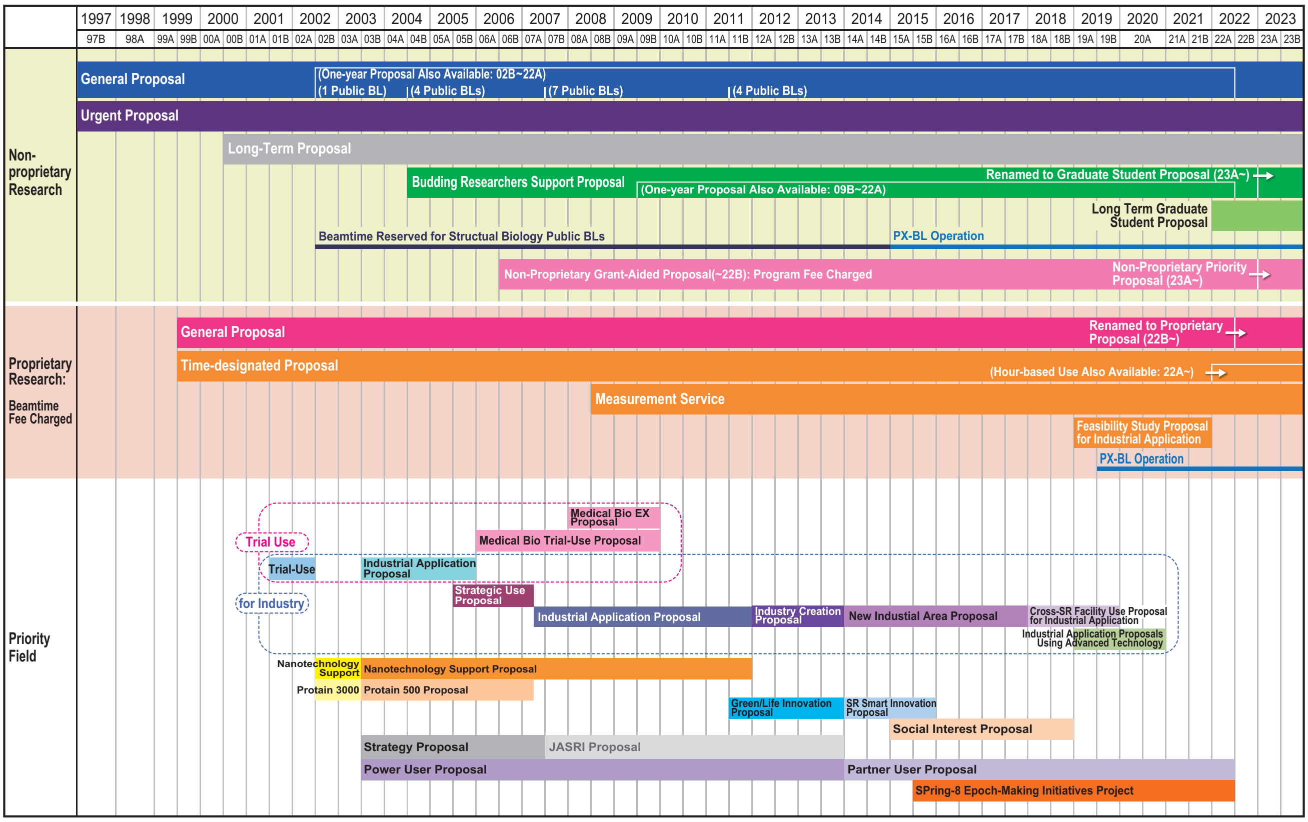

Fig. 3. Categories of proposals for the public beamlines.

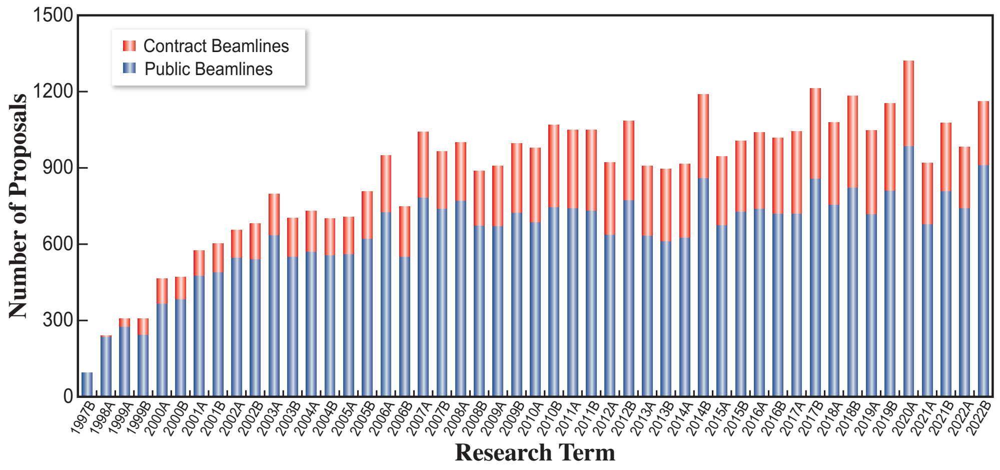

Fig. 4. Numbers of conducted experiments.

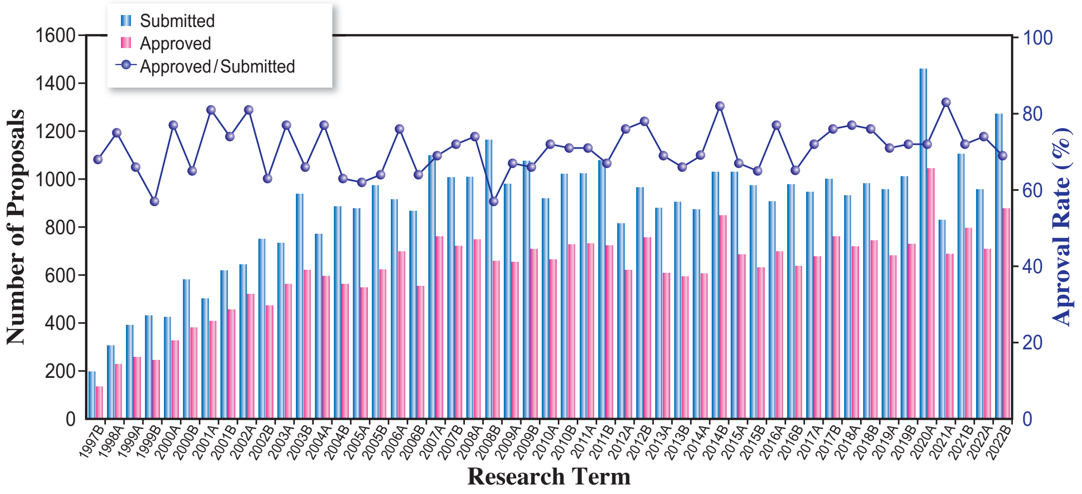

Fig. 5. Numbers of submitted proposals and approved proposals by research term (public beamlines).

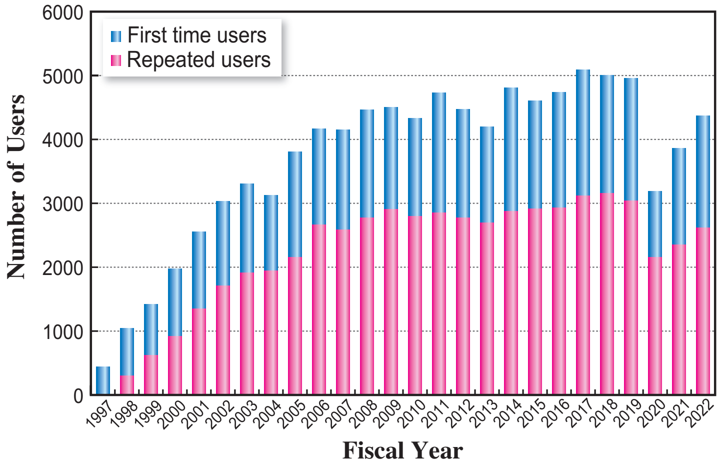

Fig. 6. Numbers of users by fiscal year.

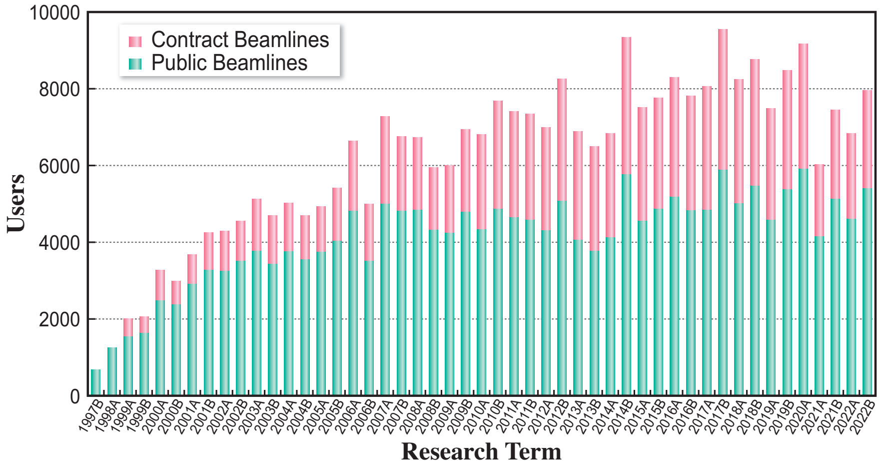

Fig. 7. Numbers of users visits by research term.

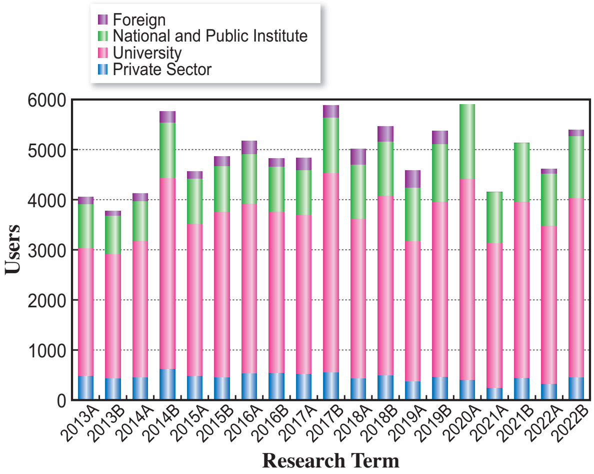

Fig. 8. Numbers of users by affiliation categories (public beamlines).

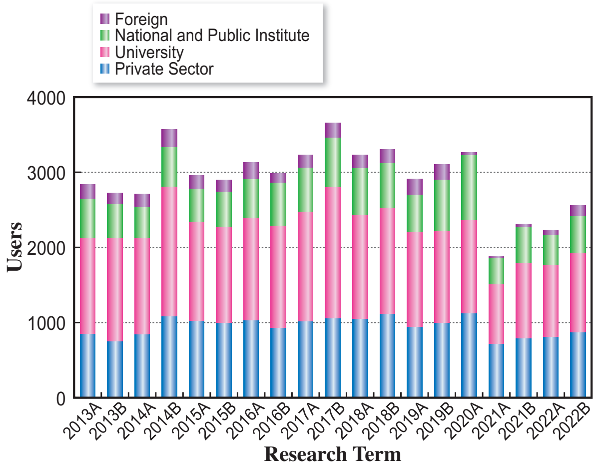

Fig. 9. Numbers of users by affiliation categories (contract beamlines).

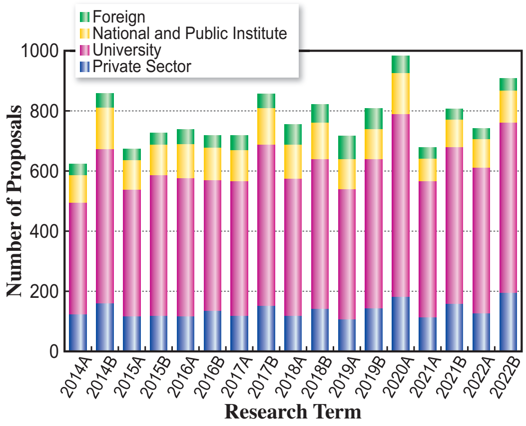

Fig. 10. Numbers of conducted proposals by affiliation (public beamlines).

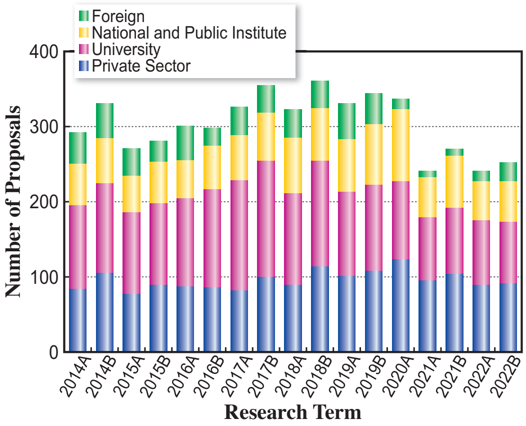

Fig. 11. Numbers of conducted proposals by affiliation categories (contract beamlines).

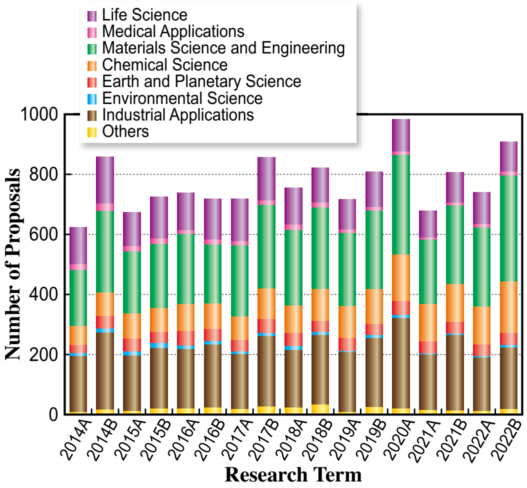

Fig. 12. Numbers of conducted proposals by research area (public beamlines).

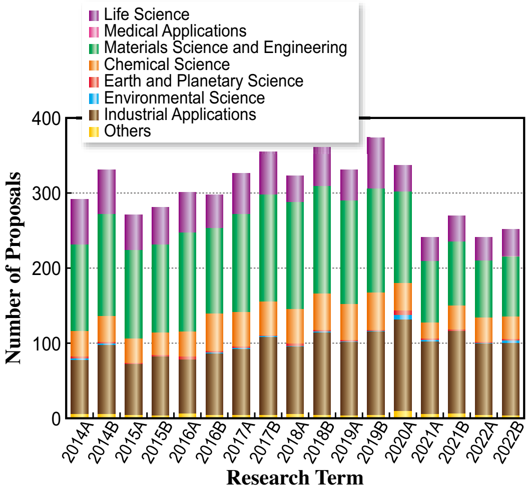

Fig. 13. Numbers of conducted proposals by research area (contract beamlines).

V. Research Outcome

As of March 2023, the total number of registered refereed papers from SPring-8 is 21,044. Figure 14 shows the annual statistics of refereed papers.

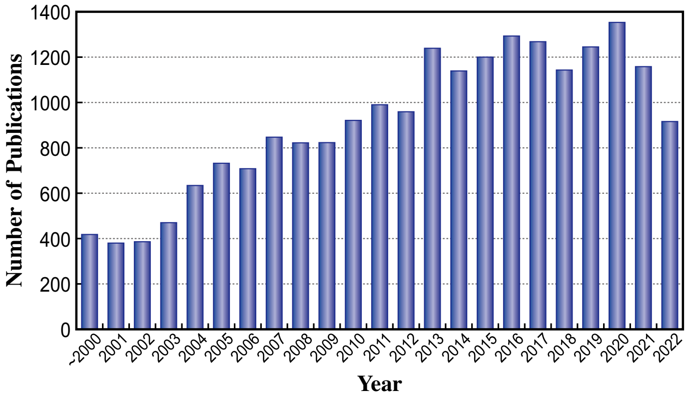

Fig. 14. Number of refereed publications.

VI. Research Complex

The facilities of SPring-8, SACLA, and NewSUBARU form the Center of Excellence (COE) on the SPring-8 campus where JASRI, public beamline users, contractors of contract beamlines, RIKEN, and the University of Hyogo work in close cooperation. Thus, a research complex has been formed, where each member has their own role in achieving high-quality results in the field of synchrotron radiation science and technology. The organizational charts of RIKEN and JASRI, which are at the center of this research complex, are shown in Figs. 15 and 16, respectively.

Fig. 15. RIKEN Harima Campus chart as of April 2023.

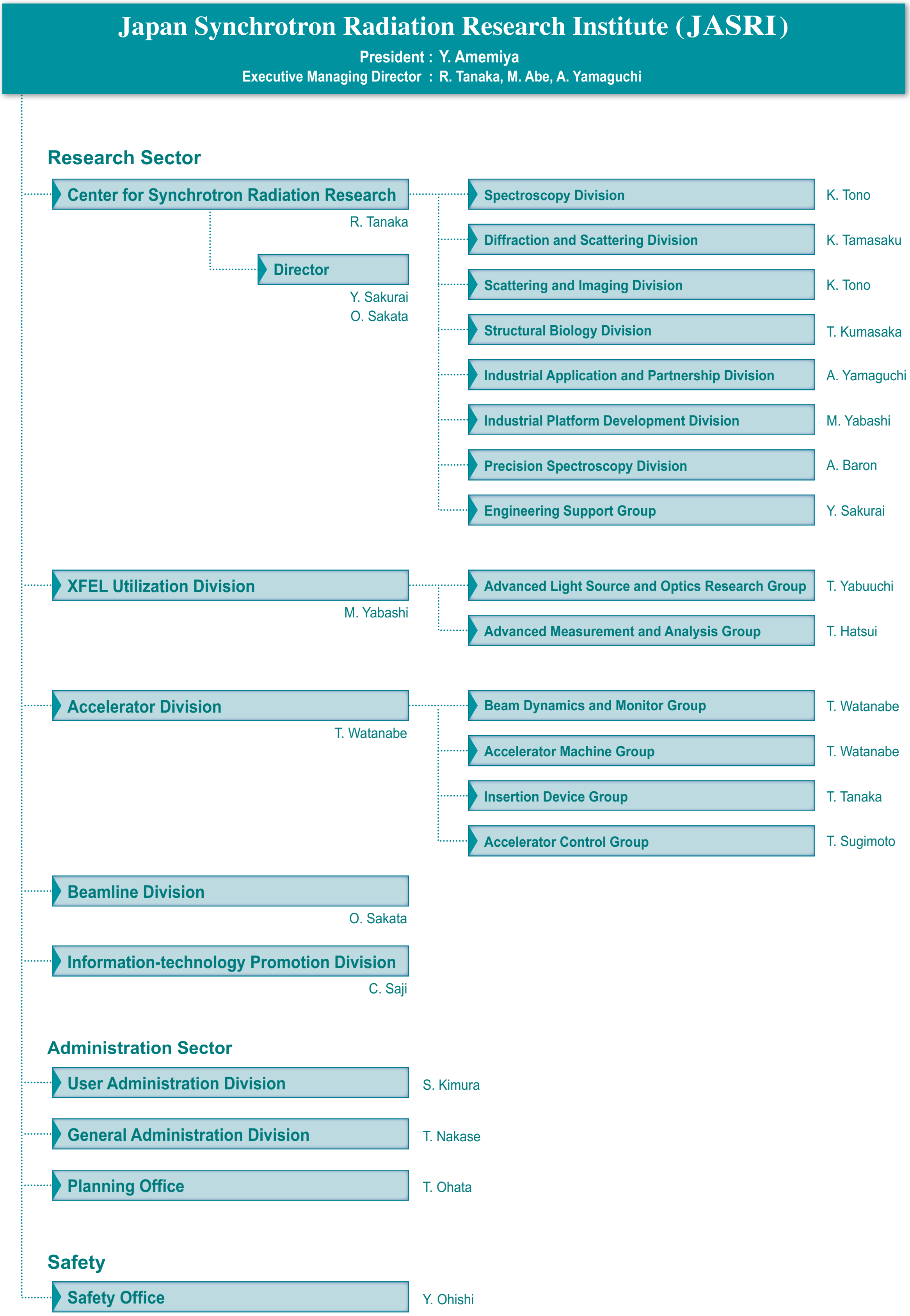

Japan Synchrotron Radiation Research Institute (JASRI)

President : Y. Amemiya
Executive Managing Director : R. Tanaka, M. Abe, A. Yamaguchi

Research Sector

- **Center for Synchrotron Radiation Research** R. Tanaka
  - **Director** Y. Sakurai, O. Sakata
  - **Spectroscopy Division** K. Tono
  - **Diffraction and Scattering Division** K. Tamasaku
  - **Scattering and Imaging Division** K. Tono
  - **Structural Biology Division** T. Kumasaka
  - **Industrial Application and Partnership Division** A. Yamaguchi
  - **Industrial Platform Development Division** M. Yabashi
  - **Precision Spectroscopy Division** A. Baron
  - **Engineering Support Group** Y. Sakurai
- **XFEL Utilization Division** M. Yabashi
  - **Advanced Light Source and Optics Research Group** T. Yabuuchi
  - **Advanced Measurement and Analysis Group** T. Hatsui
- **Accelerator Division** T. Watanabe
  - **Beam Dynamics and Monitor Group** T. Watanabe
  - **Accelerator Machine Group** T. Watanabe
  - **Insertion Device Group** T. Tanaka
  - **Accelerator Control Group** T. Sugimoto
- **Beamline Division** O. Sakata
- **Information-technology Promotion Division** C. Saji

Administration Sector

- **User Administration Division** S. Kimura
- **General Administration Division** T. Nakase
- **Planning Office** T. Ohata

Safety

- **Safety Office** Y. Ohishi

Fig. 16. JASRI chart as of April 2023.

VII. SPring-8 Users Community (SPRUC)

Professor E. Nishibori
University of Tsukuba
SPRUC Chairman FY2022

The SPRUC is a user society comprising of all users of SPring-8/SACLA. In addition to individuals, representative organizations comprising 26 institutes (principal universities, national/international research institutes, industries, and beamline consortiums) participate in the SPRUC to discuss strategies and perspectives to promote the utilization of SPring-8 and SACLA.

The SPring-8 Symposium is an important annual event of the SPRUC. SPring-8 Symposium 2022 was jointly organized by the University of Tokyo, RIKEN, and JASRI and held on September 25–26 in a hybrid manner on-site (the SPring-8 campus) and online presentations. The symposium theme was "Linkages between Academia and Society at SPring-8." Approximately 500 people attended the symposium, and many topics related to industry-academia collaboration were presented and discussed. In addition, a ceremony was held for the SPRUC 2022 Young Scientist Award, during which the award selection committee conferred the award to Dr. Ichiro Inoue from RIKEN SPring-8 Center, and Dr. Yoshihiko Furuike from Institute for Molecular Science. The upcoming SPring-8 Symposium 2023 is scheduled for September 26–27 at Osaka University.

The SPRUC supported the "SPring-8 Summer School" held in July for the enhancement of research competency of users, and hosted the "SPring-8 Autumn School" on September 4–7 in collaboration with JASRI for acquiring new users and human resource development. The Autumn School was postponed to December 2021 owing to COVID19, however, it was held in September 2022 for the first time in three years. The SPRUC research groups contributed to the planning of lectures at the Autumn School. To facilitate easier participation people from companies and students who were not yet affiliated with a laboratory, the school was opened to them without the requirement of registration as radiation workers.

SPRUC2022 Young Scientist Award
Dr. I. Inoue, Prof. E. Nishibori, and Dr. Y. Furuike

The SPRUC cohosted the 5th Beamlines Upgrade Workshop on March 10 with RIKEN and JASRI, as it did in previous years. The workshop was held to enhance information exchange between members of the SPRUC and the facility, focusing mainly on the progress of each beamline upgrade such as the diffraction and scattering beamlines, X-ray micro-CT beamlines, and HAXPES beamlines. In addition, the progress of automated measurements, renewal of the proposal systems at SPring-8, and development of light sources and accelerators for SPring-8-II were described and discussed.

The 6th SPRUC research groups were voluntarily organized in each research field and comprised 35 research groups. In 2022, the 6th SPRUC research groups welcomed a new addition, the angle-resolved scattering spectroscopy group. The research groups actively held meetings to collect ideas and determine the need for beamline upgrades in each research field.

SPring-8 Symposium 2022

VIII. Outreach Activities

To reach new users in unexplored application fields, SPring-8 holds various serialized seminars named “Workshop on Advanced Techniques and Applications at SPring-8.” Representative examples are as follows:

◆ 77th: Collaborative usage of Synchrotron Radiation and Neutron Beam Advances in Measurement Informatics and Data Processing Using External Computational Resources
May 20, 2022 • Video conference

◆ 81st: Current Status and Future of Protein Structural Biology Research at SPring-8
September 15, 2022 • Osaka University and Video conference

◆ 84th: Cutting-Edge of Silicon Semiconductor Manufacturing Technology and Ceramic Device Development in Synchrotron Radiation
December 20, 2022 • AP Shinagawa

In addition, by exploring the advantages of video conferencing, we have been holding a “Seminar on Advanced Techniques and Applications at SPring-8” every Tuesday evening since January 2021. Over 2000 participants have been involved in the eight seminars conducted during the period of May 11 to June 28, 2022.

SACLA

I. Machine Operation & Beamlines

Our eleventh year of operations proceeded without any significant issues. Operation statistics are summarized in Table 1. The ratio of downtime to user time was kept below 4%, a reasonably low rate for linac-based light sources.

Table 1. Operation Statistics for FY2022

		Time (h)
Total operation time		5789.4
User time		
	BL1	1380
	BL2	2022
	BL3	2748
Facility tuning time		864
Downtime		178.1

In 2012, two beamlines, BL3 for XFEL and BL1 for broadband spontaneous light, were opened for users, while all experiments were conducted at BL3. As the newest beamline, construction of BL2 was completed during the summer shutdown of 2014, and first laser amplification was achieved on October 21. An upgraded beamline for soft X-ray FEL, BL1, which combines the prototype accelerator of SACLA (SCSS), started operation in 2016. Parallel user operation of BL2 and BL3 started in 2018.

II. User Program and Statistics

SACLA normally calls for public user proposals twice per year. Moreover, SACLA Feasibility Study Program has started since 2021A to provide an opportunity to experience the use on a trial basis for the purpose of dissemination and enlightenment.

In FY2016, JASRI introduced the proprietary research of General Proposals and the Proprietary Time-Designated Proposals. The project leaders of these proprietary proposals are not required to publish their research results, but required to pay each beamtime fee. In addition, to apply for the proprietary research the project leaders should be affiliated with a corporate enterprise located and registered in Japan.

Figures 1 and 2, and Table 2 provide statistics on proposals, users, and beamtime.

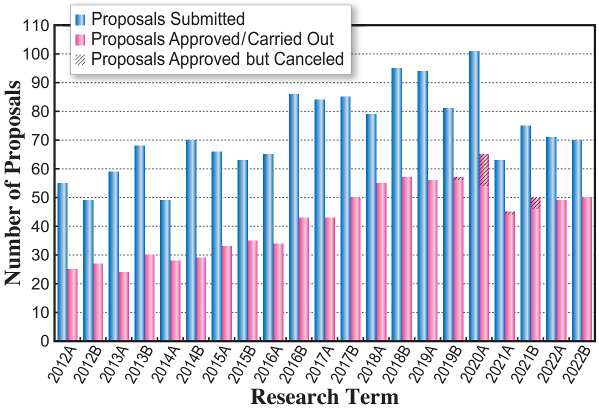

Fig. 1

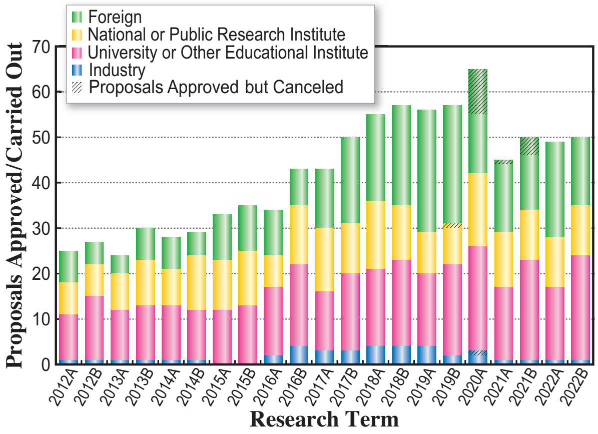

Fig. 2

Table 2. Number of proposals submitted, proposals approved/carried out, cumulative users, and beamtime available by research term

Half-year Research Term	Proposals Submitted	Proposals Approved / Carried Out					Cumulative Users	Beamtime Carried Out (Shifts)
			Priority Strategy Proposals	Non-proprietary	Proprietary			
				General Proposals	General Proposals	Time-Designated Proposals		
2012A	55	25	(12)	(13)	–	–	297	126
2012B	49	27	(19)	(8)	–	–	461	154
2013A	59	24	(15)	(9)	–	–	268	117
2013B	68	30	(19)	(11)	–	–	410	139
2014A	49	28	(20)	(8)	–	–	400	147
2014B	70	29	(17)	(12)	–	–	430	140
2015A	66	33	(23)	(10)	–	–	527	144
2015B	63	35	(23)	(12)	–	–	552	152
2016A	65	34	(21)	(12)	(1)	–	538	158
2016B	86	43	(21)	(20)	(1)	(1)	650	197
2017A	84	43	–	(43)	(0)	(0)	577	210
2017B	85	50	–	(50)	(0)	(0)	642	244
2018A	79	55	–	(55)	(0)	(0)	643	257
2018B	95	57	–	(56)	(0)	(1)	653	264
2019A	94	56	–	(55)	(0)	(1)	564	259
2019B	81	57	–	(56)	(0)	(0)	650	266
2020A	101	65	–	(54)	(0)	(0)	461	276
2021A	63	45	–	(44)	(0)	(0)	465	248
2021B	75	50	–	(46)	(0)	(0)	468	254
2022A	71	49	–	(49)	(0)	(0)	570	249
2022B	70	50	–	(50)	(0)	(0)	588	259

One shift = 12 hours at SACLA beamlines

SPring-8/SACLA

Budget and Personnel

When SPring-8 started operations in 1997, it was jointly managed by RIKEN, JAERI (now JAEA), and JASRI. However, JAEA withdrew from the management of SPring-8 on September 30, 2005. Currently, SPring-8 is collaboratively administered by RIKEN and JASRI.

RIKEN established specific synchrotron radiation facilities (i.e., SPring-8 and SACLA) and is responsible for their operation and maintenance. JASRI selects and supports users of these facilities under the "Act on the Promotion of Public Utilization of the Specific Advanced Large Research Facilities."

Figure 1 shows government subsidy. Figure 2 shows the manpower of JASRI and RIKEN.

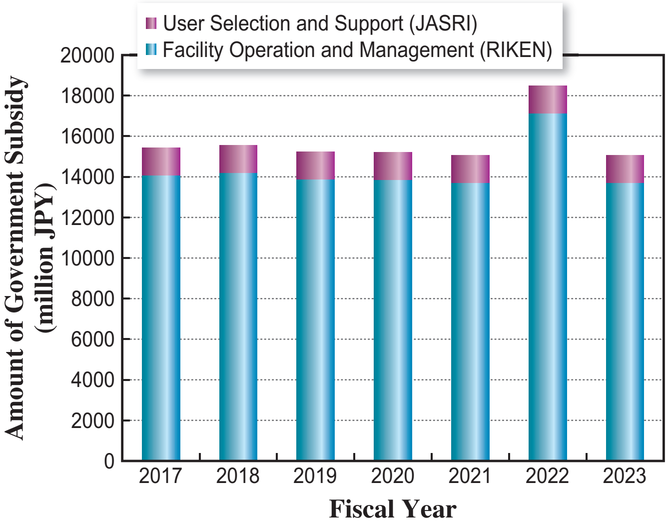

Fig. 1

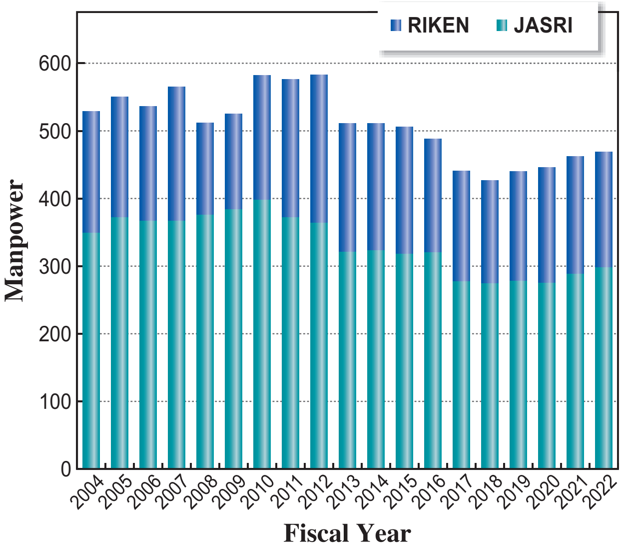

Fig. 2. Manpower at SPring-8: JASRI and RIKEN.

Editor
Toyohiko Kinoshita
Japan Synchrotron Radiation Research Institute (JASRI)

Editing, Design & Layout
Marcia M. Obuti-Daté
Japan Synchrotron Radiation Research Institute (JASRI)

Printing
Hokuoh Printing Co.

JASRI
Information & Outreach Section
Users Administration Division

1-1-1 Kouto, Sayo-cho, Sayo-gun
Hyogo 679-5198 • JAPAN
Tel: +81-(0)791-58-2785 Fax: +81-(0)791-58-2786

Email: frontiers@spring8.or.jp
http://www.spring8.or.jp/

August 2023

http://www.spring8.or.jp

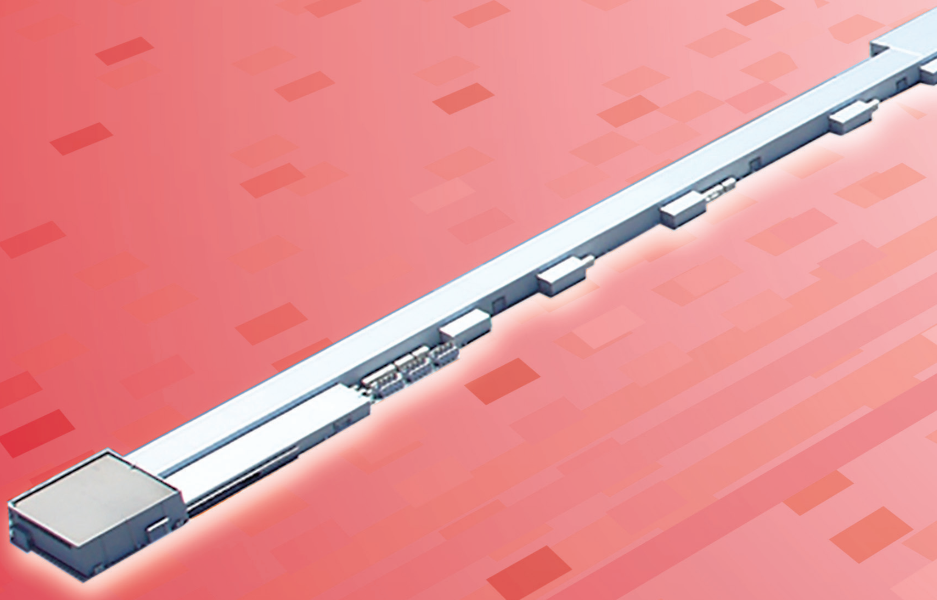

Japan Synchrotron Radiation Research Institute (JASRI)
1-1-1 Kouto, Sayo-cho, Sayo-gun, Hyogo 679-5198, Japan